Terms and Conditions of Use of Digitised Theses from Trinity College Library Dublin

Copyright statement

All material supplied by Trinity College Library is protected by copyright (under the Copyright and Related Rights Act, 2000 as amended) and other relevant Intellectual Property Rights. By accessing and using a Digitised Thesis from Trinity College Library you acknowledge that all Intellectual Property Rights in any Works supplied are the sole and exclusive property of the copyright and/or other IPR holder. Specific copyright holders may not be explicitly identified. Use of materials from other sources within a thesis should not be construed as a claim over them.

A non-exclusive, non-transferable licence is hereby granted to those using or reproducing, in whole or in part, the material for valid purposes, providing the copyright owners are acknowledged using the normal conventions. Where specific permission to use material is required, this is identified and such permission must be sought from the copyright holder or agency cited.

Liability statement

By using a Digitised Thesis, I accept that Trinity College Dublin bears no legal responsibility for the accuracy, legality or comprehensiveness of materials contained within the thesis, and that Trinity College Dublin accepts no liability for indirect, consequential, or incidental, damages or losses arising from use of the thesis for whatever reason. Information located in a thesis may be subject to specific use constraints, details of which may not be explicitly described. It is the responsibility of potential and actual users to be aware of such constraints and to abide by them. By making use of material from a digitised thesis, you accept these copyright and disclaimer provisions. Where it is brought to the attention of Trinity College Library that there may be a breach of copyright or other restraint, it is the policy to withdraw or take down access to a thesis while the issue is being resolved.

Access Agreement

By using a Digitised Thesis from Trinity College Library you are bound by the following Terms & Conditions. Please read them carefully.

I have read and I understand the following statement: All material supplied via a Digitised Thesis from Trinity College Library is protected by copyright and other intellectual property rights, and duplication or sale of all or part of any of a thesis is not permitted, except that material may be duplicated by you for your research use or for educational purposes in electronic or print form providing the copyright owners are acknowledged using the normal conventions. You must obtain permission for any other use. Electronic or print copies may not be offered, whether for sale or otherwise to anyone. This copy has been supplied on the understanding that it is copyright material and that no quotation from the thesis may be published without proper acknowledgement.

A STUDY ON HYDRODYNAMICS OF GRIT PARTICLES IN CURVED OPEN CHANNELS USING PHYSICAL AND COMPUTATIONAL MODELLING

A STUDY ON HYDRODYNAMICS OF GRIT PARTICLES IN CURVED OPEN CHANNELS USING PHYSICAL AND COMPUTATIONAL MODELLING

by

Titiksh Patel

A thesis submitted for the Degree of Doctor of Philosophy
to Trinity College, University of Dublin.

October 2007

Department of Civil, Structural and Environmental Engineering
Trinity College
University of Dublin

DECLARATION

I hereby declare that this thesis is entirely my own work unless otherwise stated and that it has not been submitted for a degree at any other university. I agree to permit the library to lend or copy this thesis upon request.

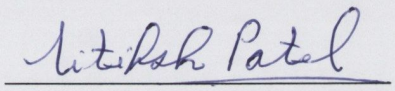

Titiksh Patel

SUMMARY

An investigation has been made of the secondary flow phenomenon in curved open channels and the hydrodynamics of grit particles as they pass around a bend by using a combination of a physical modelling and mathematical Computational Fluid Dynamics (CFD) modelling. The basic principle is that when water passes round a bend in a channel, secondary currents are induced due to the centrifugal force which tends to push any particles moving along the base of the channel to the inside of the bend. This phenomenon can be employed to remove grit from wastewater entering a treatment works in the inlet-channel by placing a sump at the inside of the bend with the advantage that the process has no significant head loss nor requires any extra operating cost.

Initially, a previously published case study was investigated in order to verify the ability of CFD software FLUENT® to simulate secondary flow in a curved open channel flow. The same methodology was then adopted to model secondary currents in the curved grit channel. The movement of grit particles was modelled using a Discrete Phase Model (DPM) where each grit particle was treated as a discrete entity. Benchmark experimental results of grit removal efficiencies by a physical model of a curved grit channel in the laboratory for various particle sizes ranging from 63μm to 2000μm were attained in order to calibrate the computational model. The computational model was then calibrated against different parameters such as the shape factor of grit particle, particle behaviour near the wall and particle injection location. Once the calibration of the computational model was done, detailed parametric investigations were undertaken on the curved grit channel where the effect of angle of bend (15°, 30° and 45°), flow rate (ranging from 4l/s (0.48m/s) to 15l/s (0.74m/s) or corresponding depth of flow/curvature ratio from 0.038 to 0.096), radii of curvature (0.78m, 1.56m and 2.34m) and channel widths (0.13m, 0.19m and 0.25m) on secondary flows and subsequently grit removal efficiencies were assessed.

A reasonably good agreement was found between the experimental data and the computational model of the case study and all the main flow features within the curved domain could be well simulated. The computational predictions of secondary flow within

the curved grit channel indicated that the magnitude of the secondary flow tends to increase with an increase in the angle of bend and tends to decrease with an increase in the radius of curvature. An interesting phenomenon was also observed for the cases analyzed for angle of bend of 30° and 45° at 15l/s (0.74m/s) or the corresponding depth of flow/curvature ratio (H/R_c) of 0.096, where an outer bank circulation cell was also formed in addition to the main circulation cell at the intersection of the free surface and the outer bank. This outer bank cell also has as a protective effect to the outer bank as it maintains the maximum longitudinal velocity contour away from the outer bank, thus minimising scour. An analytical model has also been suggested in which magnitude of secondary flow is predicted by a relation consisting of angle of bend, average velocity and radius of curvature to width ratio.

Grit removal efficiencies tend to decrease with the increase in the magnitude of the secondary flow as it also results in the increase of the uplift velocity at the inside of the bend and hence preventing the grit from entering into the sump. It should be noted that the extent of grit removal is decided by the location of the particles hitting any θ° (15°, 30° or 45°) vertical plane (just preceding the sump). It is then the vertical position of the particles rather than their respective horizontal position when they strike at any plane which remains the critical issue in deciding the grit removal efficiency for particles of size ranging from 63μm to 2000μm. The introduction of baffles within the sump results in increase of grit removal efficiency, increasing from approximately 60% to 90% at 4l/s (0.48m/s) for grit particles of 150μm size. It is also found that the settling velocity to average velocity ratio of 0.148 results in 100% removal of grit particles irrespective of the flow rate, angle of bend or particle diameter. Overall, It was found with the increase in the magnitude of the secondary flow, that the grit removal efficiency for various particle sizes tends to decrease due to the increased uplift velocity (of secondary flow currents) at the inside of the bend which brings into question the rationale behind the design of grit channels with bends for the removal of grit particles. It is also recommended to investigate secondary flow especially outer bank cell in more detail using high resolution experimental techniques and also to assess full scale performance of straight grit channel and curved grit channel.

ACKNOWLEDGEMENTS

I would like to take this opportunity to extend my deepest gratitude to my supervisor, Dr. Laurence Gill for his constant understanding, invaluable support and encouragement during this research. His sharp eye for details and excellent analytical skill has greatly enhanced the quality of this work. I am also grateful to my mates Niall, Omran, Aonghus and all other colleagues for their assistance and companionships throughout my stay at the Dublin University. I specially thank Patrick, George and all other technical staff in Department of Civil Engineering for their help during the experimental work. My sincere thanks to Trinity Centre for High Performance Computing (TCHPC) for allowing access to their computing facilities, without it many of the simulations would not be possible. Special acknowledgment is also given to RPS Consulting Engineers for funding this research project.

My gratitude goes to my former colleagues of Jodhpur University and IIT Delhi, India. They show concern for my progress and my well being. Some of whom, over the years have become my friends. Special thanks to Barry (Bharath) from Mechanical Engineering Department, who has been very supportive during my research.

I am greatly indebted to my family for their understanding, patience and support during the entire period of my study. Last but not least, I am thankful to God for giving me courage and determination to complete this research.

CONTENTS

LIST OF FIGURES

LIST OF TABLES

1. INTRODUCTION

This chapter provides an introduction to the thesis in which the motivation and objectives of the thesis are first highlighted, followed by a discussion on the modelling strategy adopted in the curved grit channel. Thereafter, a brief overview of all the chapters is presented.

1.1 Motivation of the Study

Grit removal from municipal wastewater is a critical process at the front of a treatment plant. If the grit is not removed, it can cause damage to downstream mechanical components such as aeration diffusers and pumps, and/or can settle out and accumulate in pipes, channels and process tanks reducing hydraulic capacity, decrease retention time and increase friction losses. Grit is generally removed in a primary treatment process via grit removal devices as detritus tanks, aerated grit chambers (AGCs), vortex grit chambers (VGCs) and constant velocity (C.V.) channels (Imhoff and Imhoff, 1979; Metcalf and Eddy, 1991; Rupke, 1994; USEPA, 2003; Hydro International Plc., 2007; Smith and Loveless Inc., 2007 and Eutek Systems, 2007). However, each of these grit removal devices has advantages and disadvantages associated with them, with one of the major drawbacks (especially of AGCs and VGCs) being operation and maintenance costs (Metcalf and Eddy, 1991 and USEPA, 2003). The thesis intends to analyze the flow behaviour within a curved open (grit) channel and subsequently the movement of grit particles as they pass around a bend in a potentially simple and efficient grit removal device (i.e. curved grit channel). As such, it is envisaged that this type of grit removal device will have a minimum energy requirement apart from pumping out the grit from the sump (as for all devices), a minimum maintenance cost and will provide cleaner grit which will contain relatively less organics. The grit removal device contains a curved open channel and a sump, and is designed in such a way that secondary flows are

generated within the channel by providing a curvature in the alignment. This causes all the grit particles carried in the flow to accumulate at the inside of bend where they are subsequently removed by a sump placed at this location. Concurrently, such analysis will also enable secondary flows to be studied in detail as they are considered to be vital in curved open channel processes, being fundamental to the evolution of natural rivers and estuaries with time (Rozovskii, 1957; Bathurst *et al.* 1977, 1979; Hicks, *et al.*, 1990; Naot, *et al.*, 1993; Ye and McCorquodale, 1998 and Blanckaert, 2003). The prediction of the same is also considered to be important in the stabilisation and design of natural rivers and man-made channels. Thus, such an exclusive study includes an analysis of the phenomenon of secondary flows for various geometrical and dynamical parameters. This has subsequently been used to model their effect on the behaviour of grit particles in curved open channels.

1.2 Aims and Objectives

The main aims of the thesis are twofold which are as follows:

1) to investigate the effects of various geometrical and dynamical parameters (flow rate, angle of bend, radius of curvature and width of the channel, etc.) on the development of secondary flow currents.
2) to investigate the effects of secondary flow on the movement of grit particles (trajectories) within a curved grit channel and consequently evaluate the grit removal efficiency of the device at various geometrical and dynamical parameters.

These aims will be achieved by the following objectives:

- Construction of a physical model of the curved grit channel in order to attain benchmark experimental results of grit removal efficiency at various flow rates for various particle sizes.

- Calibration of a computational model with the experimental results using the Computational Fluid Dynamics (CFD) software FLUENT®.
- Investigations on the various geometrical and dynamical parameters using the calibrated model of the curved grit channel in order to establish their effects on secondary flows and subsequently the behaviour of grit particles (i.e. grit removal efficiency).
- Modifications to the physical model based on the above investigations and physical experiments carried out again to ascertain the accuracy of the CFD model.

Such detail investigations for various geometrical and dynamical parameters are not reported in previous studies and will provide, (a) a realistic scenario of the phenomenon of the secondary flows for such parameters, (b) a detailed presentation of the effect of secondary flows on behaviour of grit particles in curved grit channel, and (c) the practicality of usage of the curved grit channel as a potential grit removal device in wastewater treatment plants.

1.3 Modelling Strategy

Both physical and computational modelling approaches were undertaken in order to establish the grit removal efficiencies of various particle diameter sizes ranging from 63μm to 2000μm by the curved grit channel. Initially, benchmark experimental results of grit removal efficiencies were attained on a physical model of a curved grit channel (fabricated in the Civil Engineering laboratory) at various flow rates using particle size distribution and standard sieve analysis procedures (BS:1377, 1990). Once the experimental results were obtained, computational investigations were performed using the CFD software FLUENT®. An overview of the modelling strategy is shown in Figure 1.1. The computational investigations also included the CFD analysis of a case study (Blanckaert, 2003) which had used high resolution instrumentation on the physical model to ascertain the ability of CFD software to simulate secondary flows accurately and to develop a methodology of the same which could be incorporated in the curved grit

channel study. The measurement of secondary flows in the curved open channel by high resolution experimental techniques (such as Acoustic Doppler Velocimeter (ADV), Laser-Doppler Anemometer or Velocimeter (LDA or LDV) and Particle-tracking and Particle-image Velocimeter (PTV and PIV)) was not possible in the present study and hence such comparison between computational and experimental results was used to aid in the understanding of the phenomenon of secondary flows. The computational model was calibrated against the experimental data of grit removal efficiencies for various grit particle sizes and based on that, detailed parametric investigations were undertaken.

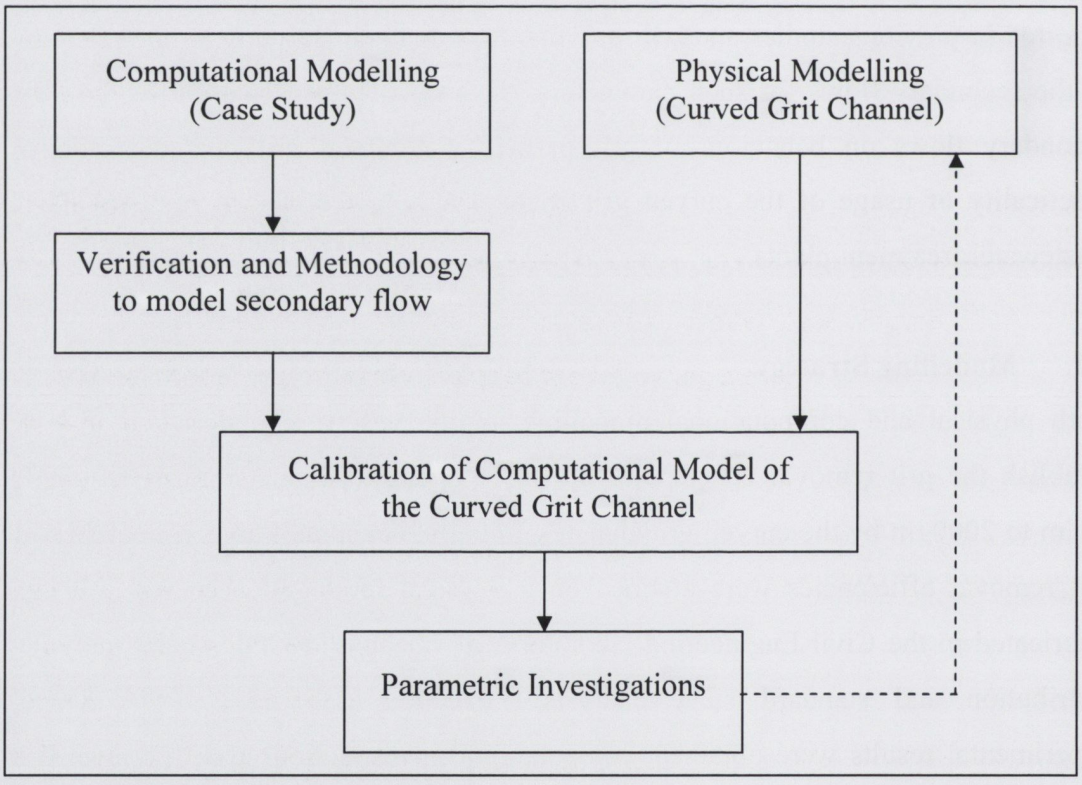

Figure 1.1: Modelling Strategy Adopted in Curved Grit Channel

Finally, some of the modifications made during the parametric investigations were incorporated back into the physical model which underwent further trials to ascertain the accuracy of the predictions by the computational model (see Figure 1.1.). The computational modelling primarily included the following steps:

(i) the fluid flow field was solved using the governing flow equations and turbulence models with the numerical solver.

(ii) grit particles of known physical properties (diameter, particle density, etc.) were injected into the domain and their trajectories and fates tracked using the Discrete Phase Model (DPM).

(iii) the flow fields were analyzed by plotting velocity contours, secondary flows and particle fates using user defined functions (carried out using MS Excel, Matlab and Surfer).

1.4 Outline of the Thesis

Chapter 2 reviews the literature regarding the classification of open channel flows, laminar and turbulent flows, secondary flows and their modelling approach. The chapter also highlights the fundamental difference between the modelling technique adopted in simulating sediment-laden rivers and other environmental flows (such as wastewater and storm water flows). The chapter then discusses the nature of grit, and its characteristics and loading rates found in a typical wastewater treatment plant. Various grit removal devices which are being used worldwide and their on and off-site performance are also discussed. Thereafter, an introduction to computational fluid dynamics (CFD) software and detailed theory associated with computational modelling is discussed. Methods used for the simulation of the free surface and movement of grit particles are also presented.

Chapter 3 presents the methodology adopted during the physical modelling of the curved grit channel and the characteristics of grit particles (particle size distribution and particle density). The design guidelines of the physical model of the curved grit channel including various geometrical characteristics (such as angle of bend, radius of curvature, channel width, etc.) are also discussed. Thereafter, a detailed analysis of experimental results of grit removal efficiencies for various grit particles sizes ranging from 63μm to 2000μm at different flow rates is presented.

Chapter 4 discusses the methodology adopted in computational modelling, creation of the geometry (curved grit channel), numerical grid and its characteristics, boundary conditions employed, interpolation schemes and iterative solver. The steps involved during the numerical solution of the case study and the curved grit channel are also discussed.

Chapter 5 presents the detailed computational results of the case study and their comparison with the experimental results. Thereafter, it presents a detailed analysis of the results on secondary flows and their effect on velocity redistribution and subsequent grit removal efficiency for the grit channel. The detailed parametric investigations (in which the effect of different angles of bend, radii of curvature, channel widths, flow rates, etc. is observed) are presented where their effect on secondary flows and subsequently grit removal efficiency to various geometrical and dynamical parameters are investigated. The computational results are shown in the form of the longitudinal velocity contours, cross-flow velocity vectors and scatter plots of particles using the DPM.

Chapter 6 is comprised of the revised experimental results performed after the modifications made on the curved grit channel during the computational (parametric) investigations on the curved grit channel.

Chapter 7 summarizes the conclusions of the study and presents recommendations for future work.

2. LITERATURE REVIEW: FLOW AND SEDIMENT DYNAMICS OF OPEN CHANNELS AND INTRODUCTION TO COMPUTATIONAL MODELLING

The objective of this chapter is to introduce the fundamentals of open channel flow and to review the flow and sediment dynamics in open channels. Methods for interpreting secondary flows in curved channels and ways of modelling various types of flows in the field of environmental engineering are also discussed. A review on grit characteristics and grit removal devices which are being used worldwide is also presented. Thereafter, an introduction to computational fluid dynamics (CFD) software and detailed theory associated with computational modelling is discussed. Methods used for the simulation of the free surface and movement of grit particles are also presented.

Sections 2.1 and 2.2 are based on Chow (1973); Chadwick and Morfett (1993); Chanson (1999) and MIT OCW (2004).

2.1 Hydraulics of Open Channels

The term 'hydraulics' is related to the application of Fluid Mechanics principles to water engineering structures, and civil and environmental engineering facilities, especially hydraulic structures (e.g. canals, rivers, dams, reservoirs, and water treatment plants). Canals, natural streams and rivers are examples of open channels in which water flows with a free surface under the driving force of gravity. Natural open channels include streams and rivers, while man-made channels include irrigation and navigation canals, drainage ditches, sewer and culvert pipes running partially full, and spillways. In addition, open-channel bends are ubiquitous in alluvial lowland rivers, but they also occur in mountain-rivers and in manmade channels. They influence the conveyance capacity of the channel, may lead to undesired erosion/deposition and enhanced mixing, and they provide a place for the intake of relatively clear water.

From an ecological point of view, meander migration is an important agent in floodplain rejuvenation. Hence, there are many good reasons to investigate flow behaviour and sediment dynamics in open-channel bends.

2.1.1 Flow with Free Surface

Open channel flow is characterized by the existence of a free surface which is the interface between air and water. The pressure on the free surface is constant and equal to atmospheric pressure and as the driving force is gravitational, the pressure distribution along any cross-section of the channel is generally hydrostatic. The free surface rises and falls in response to the perturbations to the flow (e.g. change in the bed slope or discharge) making the flow conditions more complex than closed pipe flow, and the solutions are more varied in spatial and temporal scales, creating the study of such problems both interesting and challenging. A fundamental difference between open and closed-conduit channel flow is that the area of the cross-section is variable in open channels and is not controlled by the fixed boundaries.

2.2 Flow Classification

2.2.1 Spatial and Temporal Classification

Open channel flows can be fundamentally classified by two parameters - spatial and temporal which are variation in space (distance) and time respectively. These are the basic criteria adopted for classification of all types of fluid flows including open channels. If the flow depth (d) or hydraulic radius (R_h) varies with distance $\partial(d)/\partial x = 0$ or $\partial(d)/\partial x \neq 0$; then the flow is known as uniform or non-uniform flow and similarly if $\partial(d)/\partial t = 0$ or $\partial(d)/\partial t \neq 0$; then the flow is known as steady or unsteady flow.

Based on the above parameters, the majority of the flow will fall into one of the following combined space-time classification:

- *Steady uniform flow*, in which the depth is constant, both with time and space. This constitutes the fundamental type of flow in an open channel.

- *Steady non-uniform flow*, in which the depth varies with distance, but not with time. The flow may be either (a) *gradually varied flow* or (b) *rapidly varied.*

- *Unsteady flow*, in which the depth varies with both time and distance (unsteady uniform flow is very rare). This type of flow is considered to be the most complex type.

2.2.2 Classification based on Dimensionless Numbers

Open channel flow can also be classified on the basis of dimensionless numbers which are obtained by the following forces acting on the fluid (water).

- *Inertial force* = $\rho_w V_w a$
- *Gravity force* = ωV_w
- *Viscous force* = $\tau A = \mu \frac{\partial u}{\partial y} A$

where ρ_w is the density of water, V_w is the volume, a is acceleration, ω is the specific weight, τ is the shear stress, μ is the dynamic viscosity of water, u is the flow velocity and A is the area. Apart from these forces, other forces such as surface tension, elastic forces and pressure forces also act on the fluid. Surface tension forces may be ignored in open channel flows as the radius of curvature at the interface is often large enough to ensure surface tension force is negligible. Equally, the elastic force can also be ignored since the Mach number is less than 0.3, and the pressure distribution is generally hydrostatic. Therefore, the state of the open channel flow is governed by two independent dimensionless parameters, which describe the effects of viscosity and gravity relative to the inertial forces of the flow. Based on these forces, two dimensionless similarity numbers can be defined as:

- *Froude number* (F_r) = inertial forces/gravitational forces = $u_c / \sqrt{g l_c}$

- *Reynolds number* (Re) = inertial forces/viscous forces = $u_c l_c / \upsilon$

where, u_c and l_c are characteristic velocity and length scale, respectively, g is the acceleration due to gravity and υ is the kinematic viscosity. Depending on the magnitude of the Froude number, the flow can then be classified as *subcritical*, *critical*, or *supercritical*.

Subcritical flow, Fr< 1

- disturbances travel upstream and downstream
- upstream water levels are affected by downstream control

Supercritical flow, Fr > 1

- disturbances travel downstream
- upstream water levels are unaffected by downstream control

Critical flows do not exist naturally as they are unstable and if a flow passes through Fr = 1, a hydraulic jump will occur. Furthermore, depending upon the magnitude of the Reynolds number (Re), the flow can either be *laminar* or *turbulent*, a pictorial representation of which is shown in Figure 2.1.

For pipe flows, $\mathrm{Re} = \rho DV / \mu$;

for l*aminar* pipe flow $\mathrm{Re} < 2000$, and

for *turbulent* pipe flow $\mathrm{Re} > 2000$.

The transitional flow (zone) lies between these ranges. These results can be applied to open channel flow if a suitable form of the Reynolds number can be found. This can be achieved by replacing the diameter (for pipes) by an equivalent characteristic length for channels which is known as hydraulic radius (R_h). The characteristic length-scale for a channel of width w and depth h is given by, $R_h = hw / P$, where P is the wetted perimeter. Hence, the Reynolds number for channels is given by

$$\mathrm{Re}_{(channel)} = \rho R_h V / \mu$$

For a pipe flowing full, $R_h = D/4$, so the Reynolds number (for channels) becomes

$$\mathrm{Re}_{(channel)} = \mathrm{Re}_{(pipe)} / 4,$$

and thus for laminar channel flow, $Re < 500$ and for turbulent channel flow, $Re > 1000$. In practice, the upper limit of Re is not so well defined for channels as it is for pipes, and is normally taken to be 2000. If the conduit boundary is rough, the transition to fully turbulent flow can occur at even lower Reynolds numbers. Alternatively, laminar conditions can persist to higher Reynolds numbers if the conduit is smooth and inlet conditions are carefully designed.

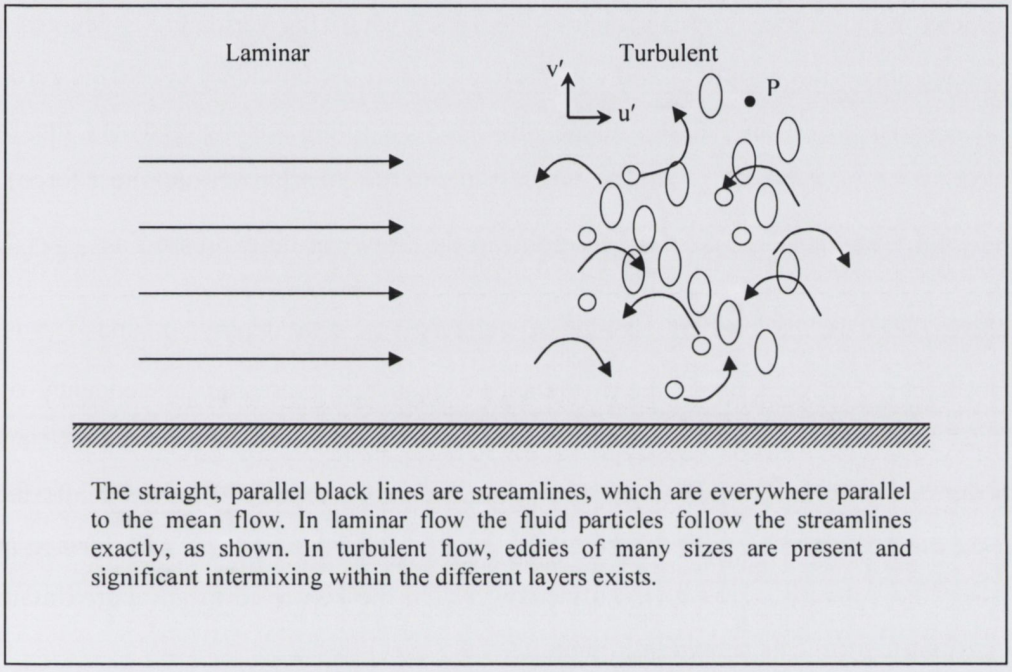

Figure 2.1: Laminar and Turbulent Flow

For most surface water systems the characteristic length scale is the catchment-scale and as this scale is typically large (1 km to 100's km), most surface water systems are turbulent. In contrast, the characteristic length scale for groundwater systems is the pore scale, which is typically quite small (<1mm) (MIT OCW, 2004), and hence, groundwater flow is nearly always laminar. The type of flow discussed in this thesis, in open channels, is classified as unsteady, non-uniform, sub-critical and turbulent.

2.2.2.1 Mean Velocity Profile in Laminar and Turbulent flow

When a fluid flows past a solid boundary or a wall, it attains the velocity of the wall due to the *viscosity of the fluid*, μ. This is called the '*no-slip*' condition, in which the fluid velocity acquires (has no slip relative to) the boundary velocity. This results in

the boundary layer formation in the mean velocity profile in which the velocity of fluid is zero at the wall (if wall is stationary) and increases to free stream velocity (u_∞) at the top surface. However, the mean velocity profile is different in laminar and turbulent flows due to dissimilar flow characteristics. The mean velocity profile for laminar and turbulent flow is shown in Figure 2.2 where the vertical axis denotes the distance above the boundary and the fluid velocity at the boundary (y = 0) is zero. It can also be observed that the mean velocity varies between the bed and the free stream over the vertical coordinate which is due to the shearing action (shear force) of the fluid. The shear stress, τ, at any point in the flow can be expressed as $\tau = C_k \frac{\partial u}{\partial y}$ where $\partial u/\partial y$ is the rate of change of velocity (u) with depth (y), and C_k is a coefficient. The velocity gradient is a shear because it expresses the tendency of a fluid to be "pulled apart" (sheared) by a differential force, with μ acting as a resistance to the shear. The drag, due to friction at the channel boundary and the air interface, causes the water to slow at the bed and, to a lesser extent, at the water surface and hence, the velocity increases rapidly from zero at the bed to form an approximately logarithmic profile as shown in Figure 2.2.

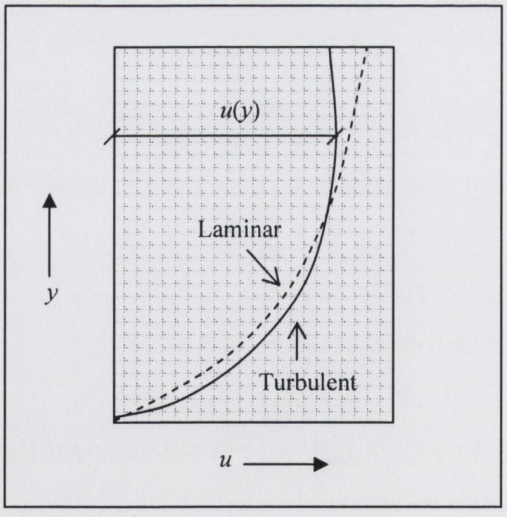

Figure 2.2: A Typical Mean Velocity Profile in Laminar and Turbulent flow (MIT OCW, 2004)

The rate of increase of velocity with distance from the bed also depends on the amount of mixing within the flow. In laminar flow, mixing is molecular and by

viscous forces (coefficient $C_k = \mu$, which is dynamic viscosity). Whereas, in turbulent flow, significant mixing occurs, due to the eddying motions, resulting in momentum exchange over long distances (coefficient C_k is comprised of the molecular viscosity, μ or $_m\mu$ and the turbulent eddy viscosity, μ_t (Boussinesq, 1877)). The molecular viscosity is negligible in comparison to the eddy viscosity; therefore high momentum fluid is transferred from near the water surface down towards the bed, resulting in a more even distribution of velocity with depth and a steeper near-bed velocity gradient. However, in natural open channels the maximum velocity can extend below the water surface due to the presence of secondary flows (discussed later).

2.3 Characteristics of Turbulent Flow

For turbulent flow, the velocity includes both a mean and a turbulent component and as the turbulent motions associated with the eddies are approximately random (Figure 2.1), they can be characterized using statistical concepts. In theory the velocity is continuous and the mean can be evaluated through integration. Thus, in a statistically steady flow, any flow variable (say velocity u) can be written as the sum of a time averaged value and a fluctuation about that value:

$$u(x_i,t) = \bar{u}(x_i) + u'(x_i,t) \tag{2.1}$$

where,

$$\bar{u}(x_i) = \lim_{T\to\infty} \frac{1}{T} \int_0^T u(x_i,t)dt \tag{2.2}$$

Here t is the time and T is the averaging interval. This interval must be large compared to the typical time scale of the fluctuations; thus, we are interested in the limit of $T \to \infty$, see Figure 2.3. If T is large enough, $\bar{u}$ does not depend on the time at which the averaging is started. Again, if the flow is unsteady, time averaging cannot be used and it must be replaced by ensemble average:

$$\bar{u}(x_i,t) = \lim_{N\to\infty} = \frac{1}{N} \sum_{n=1}^{N} u_{(n)}(x_i,t) \tag{2.3}$$

where N is the number of repeated identical experiments which must be large enough to eliminate the effects of the fluctuations. The information regarding the fluctuating part of the flow can be obtained from the root-mean-square (rms) of the fluctuations (Versteeg and Malalasekera, 1995):

$$u_{rms} = \sqrt{\overline{(u')^2}} = \left[\frac{1}{\Delta t} \int_0^{\Delta t} (u')^2 \, dt \right]^{1/2} \tag{2.4}$$

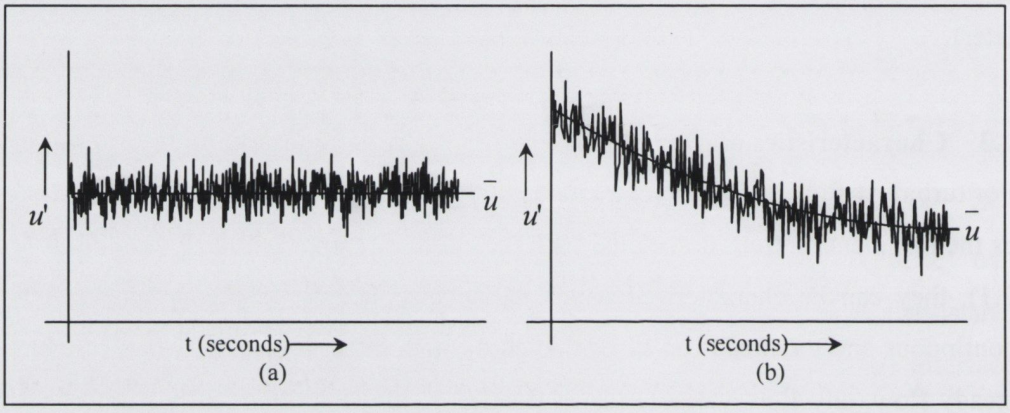

Figure 2.3: (a) Time averaging for steady flow, (b) Ensemble averaging for an unsteady flow (Ferziger and Peric, 1999)

In addition, the turbulent kinetic energy (per unit mass) associated with the turbulence is defined as,

$$k = \frac{1}{2}\left(\overline{u'^2} + \overline{v'^2} + \overline{w'^2}\right) \tag{2.5}$$

Where, u', v' and w' are the instantaneous downstream, cross-stream and vertical velocity fluctuations respectively. A larger u_{rms} indicates a higher level turbulence in the flow.

The turbulence intensity T_i is linked to the kinetic energy and mean flow velocity as follows:

$$T_i = \frac{\left(\frac{2}{3}k\right)^{1/2}}{\bar{u}} \tag{2.6}$$

The effect of turbulence on the governing flow equations is discussed in detail in Section 2.7.2.2.

2.4 Curved Open Channel

Open channels can be linearly (straight) or non-linearly (curved) aligned. The occurrence of curves in natural rivers and streams are ubiquitous and their presence is often unavoidable in the design of man-made open channels. Difficulties in flow analysis and design of these types of channels arise because of the complexity of the flow around a curved path. The streamlines of the flow are not only curvilinear but also interwoven, resulting in spiral currents. Furthermore, the centrifugal force acting on the flow around a bend produces a unique feature known as *superelevation* - a rise in the water surface at the outer bank with an accompanying lowering at the inner bank. Also, the velocity distribution in the channel sections in the bend is very irregular.

2.4.1 Spiral Flow

Spiral flow refers to movement of water particles along a helical path in the general direction of the flow. Thus, in addition to the main velocity component normal to the channel cross-section, there are transverse velocity components on the cross-section. These transverse components will create so-called *secondary flow* in the plane of the cross-section. Spiral flow in curved channels was first observed by Thomson (1876). The secondary flow phenomenon is mainly due to (1) friction on the channel walls, which causes higher velocity near the centre of the channel than near the walls; (2) centrifugal force, which deflects the particles of water from straight-line motion; and (3) a vertical velocity distribution which exists in the approach channel and thus initiates spiral motion in the flow. The centrifugal force is responsible also for the superelevation in the flow surface. It is generally known that, looking downstream, a channel curve to the right causes a counterclockwise spiral, whereas a channel curve to the left causes a clockwise spiral. In order to delineate the magnitude and effect of the spiral flow in different curves under varying conditions of flow, Shukry (1950) has used a term known as *strength of a spiral flow*. This term is defined as the percentage ratio of the mean kinetic energy of the lateral motion to the total kinetic of flow at a given cross-section. The strength S_{xy} of the spiral flow at any given section is

$$S_{xy} = \frac{v_{xy}^2}{v^2} 100 \tag{2.7}$$

where v_{xy} is the mean-velocity vector projected on the xy plane (perpendicular to the main flow direction) and v is the mean velocity in the section. Thus, for a flow with all the streamlines parallel to the axis of the channel, $S_{xy} = 0$. These cross flow velocity vectors (caused due to the curvature within the channel) are also known as '*Prandtl secondary flow of the first kind*' (Prandtl, 1952). These cross flows have pronounced effect in natural river courses where secondary flows at bends result in the sand, gravel, etc. carried along by the current at the bottom of the river, being removed from the outer side of the bend and piled up at the inner, so that the river is deepened at the outer side of the bend and made shallower at the inner. The combination of this effect with the erosion on the outer side by the particularly rapid flow there causes the bend to become more and more pronounced. Hence, where they can, rivers always follow a winding course known as "meandering". Thus, prediction of secondary flow is considered to be a foremost issue in solving river engineering problems (Hicks, *et al.*, 1990, Naot, *et al.*, 1993, Ye and McCorquodale, 1998, Blanckaert, 2003). Several studies have been performed to understand the behaviour and to develop new methods for the determination of secondary flows in curved open channels. The studies are categorized into two main approaches *analytical* and *computational*, review of which follows.

2.4.1.1 Analytical Approach

As the description of secondary flows in the previous section suggests, the primary flow direction must be known beforehand in order to determine the plane in which the secondary flow exists. In artificial or man-made channels where the channel shape is often prismatic, the primary flow is in the direction parallel to the channel walls and subsequently the direction of secondary flow can be easily found in the plane normal to that direction. However, this is not the case with natural channels where irregular cross-sectional shapes and variable bed forms are present and the prediction becomes a little more cumbersome. Studies done by Rozovskii (1957), Bathurst *et al.* (1977, 1979) recommended analytical benchmark methods to determine secondary flows based on velocity measurements along various vertical lines (or segments) across any cross-section and these measurements were gathered using intrusive instruments like velocity meters. Rozovskii (1957) determined the secondary circulation for the whole

cross-section by defining the primary flow direction for each vertical segment within the plane normal to the primary flow on the basis of zero depth-averaged secondary velocity. Hence, the method is called the zero net secondary discharge. Figure 2.4 shows the primary and secondary flow direction with respect to the reference cartesian coordinate system x and y. Angles α and β are the angles made by the resultant velocity and primary flow with the axial direction respectively. The resultant magnitude and the direction of the velocity is given by:

$$u_r = \sqrt{(u_x)^2 + (u_y)^2} \tag{2.8}$$

$$\alpha = \tan^{-1}\left(\frac{u_y}{u_x}\right) \tag{2.9}$$

where, u_x and u_y are velocity flow components in x and y directions respectively.
Now, the mean primary flow and secondary velocity at every location in each vertical segment is found by resolving components in respective directions

$$u_p = u_r \cos(\alpha - \beta) \tag{2.10}$$

$$u_s = u_r \sin(\alpha - \beta) \tag{2.11}$$

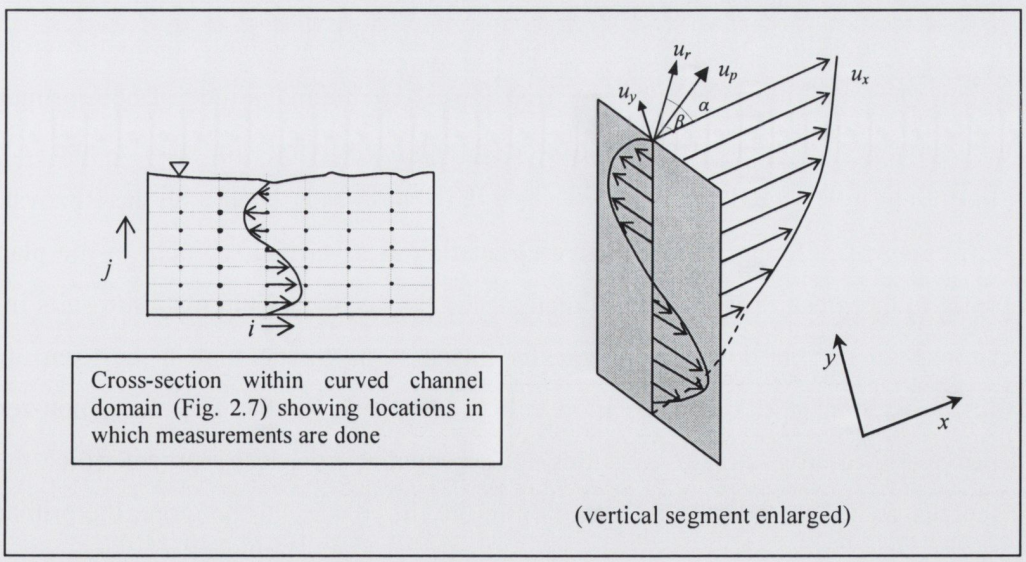

Figure 2.4: Analytical approach (primary and secondary flow direction)

Eqns. 2.10 and 2.11 can be expanded as

$$u_p = u_x \cos\beta + u_y \sin\beta \tag{2.12}$$

$$u_s = u_y \cos\beta - u_x \sin\beta \tag{2.13}$$

as

$$u_x = u_r \cos\alpha \tag{2.14}$$

and

$$u_y = u_r \sin\alpha \tag{2.15}$$

The Eqns. 2.8 to 2.15 (procedure for determining primary and secondary components) are applicable for individual locations and thus for the segment, the individual velocity values are added together. The unknown value of angle β can be found using the Rozovskii (1957) definition in which all the secondary currents in one direction are considered equal to the secondary currents in the opposite direction at each vertical segment. Therefore, equation 2.13 should be equal to zero if integrated over the whole of the segment and rearranging the same, we get:

$$\beta = \tan^{-1}\left(\frac{\sum_{j}^{m} u_{y_j}}{\sum_{j}^{m} u_{x_j}}\right) \tag{2.16}$$

where j denotes the number of locations (within each segment) along the cross-section. Once the direction is known from Eqn. 2.16, the magnitude of both primary and secondary components can also be found by solving Eqns. 2.12 and 2.13 respectively. Unfortunately, there are a few drawbacks associated with the Rozovskii (1957) way of defining the secondary circulation at a vertical segment in the plane normal to the mean primary flow direction. Firstly, secondary circulation results in a net cross-stream and downstream transfer of mass and momentum in the form of a helix rather than a closed circulation cell (Lane *et al.*, 2000). Therefore, non-zero depth-averaged cross-stream velocities are expected at a vertical segment which thus disagrees with the fundamental definition in the first place. Furthermore, the primary and secondary velocities are calculated with reference to a local plane associated with each vertical section. The orientation of these planes varies between verticals and is different to the orientation of the cross-section in which the velocity data were measured. Therefore, two dimensional plots depicting the calculated primary and secondary velocities do not represent the flow in the plane of the cross-section. Such

plots are a composite picture of velocity components assembled from multiple planes. In spite of this insufficiency, this method can be applied to a limited number of vertical sections (Bathurst *et al.*, 1977, 1979) and as such it does not require data collection across a complete cross-section. A similar technique for determining secondary circulation by Bathurst *et al.* (1977) based on that of Rozovskii (1957) was developed and is called the zero net cross-stream discharge method. Instead of assuming zero depth-averaged secondary velocity for a vertical, it is assumed that there are zero depth-averaged secondary velocities for the entire cross-section and thus, equation 2.16 changes to:

$$\beta = \tan^{-1}\left(\frac{\sum_{i}^{n}\sum_{j}^{m} u_{y_{ij}}}{\sum_{i}^{n}\sum_{j}^{m} u_{x_{ij}}}\right) \tag{2.17}$$

where i denotes number of segments in a cross-section. The primary and secondary components of the measured velocity data are calculated at each point in the cross-section based on this angle. Unlike the Rozovskii definition, the zero net cross discharge (ZNCD) definition enables non-zero depth-averaged cross-stream velocities at individual verticals, however, the orientation of the parallel planes of secondary flow at each vertical are still different from the orientation of the cross-section in which the flow velocities were measured. Hence, similar to the Rozovskii definition, the primary and secondary velocities do not represent the flow in the plane of the cross-section. Recently Corney *et al.* (2006) compared experimental results on meandering fluvial and submarine channels with the analytical model based on the velocity defect law. Their model, however, failed to interpret and understand secondary flow process in channel flows where vertical profiles vary from the typical open-channel logarithmic profile and thus have limited application. These studies failed to provide any suitable way for interpreting secondary (helical) flow phenomena and the need of more robust methods becomes imperative. In addition, the identification of coherent secondary flow structures has been hampered by only collecting velocities in two-dimensions, from which vertical velocities must be inferred. Numerical modelling eliminates the problems associated with section orientation, enabling the evaluation of downstream evolving flow structures, through

enhanced representation of the three-dimensional velocity field (see references in computational approach).

2.4.1.2 Computational Approach

With the advent of high performance computing, researchers worldwide are able to simulate open channel flows with sufficient ease and more importantly with more accuracy as compared to analytical methods. Computational studies done by Hicks, *et al.*, (1990), Naot, *et al.*, (1993), Ye and McCorquodale, (1998), Blanckaert, (2003), Rameshwaran and Naden (2004a, b) were able to simulate secondary flows successfully in curved open channels. They highlighted the importance of secondary flows in river engineering problems as engineering solutions are increasingly required to retain natural channel features and to maintain a balance between economic, environmental, ecological and amenity issues. In past decades, two-dimensional (2-D) (Bathurst, *et al.*, 1979; Rameshwaran and Shiono, 2002, 2003) and three-dimensional (3-D) computational fluid dynamic (CFD) methods (Nicholas, 2001; Ma, *et al.*, 2002) have been used in river engineering in order to improve understanding of turbulent flow behaviour in open channel flows. In 2-D CFD methods, the depth-averaged continuity and Navier-Stokes equations are solved with either a zero equation turbulence model (the constant eddy viscosity or mixing length model) or a depth averaged form of the two equation turbulence model, to predict the depth-averaged velocity and bed shear stress. However, 2-D methods are unable to simulate all the flow features in the channel and hence there is a need for 3-D analysis in which the 3-D Reynolds-Averaged Navier Stokes (RANS) equations are solved using an appropriate model for turbulence closure. The most common turbulence models are the linear and nonlinear k-ε models (Lin and Shiono, 1995; Jia *et al.*, 2001), the algebraic stress model (Naot, *et al.*, 1993) the Reynolds stress transport model (Cokljat *et al.*, 1995) and large eddy simulation (Booij, 2003). Rameshwaran and Shiono (2002, 2003) in their studies on two stage channels found that two dimensional depth-averaged equations are unable to predict all the features of the channel and a 3-D approach may therefore be necessary for good predictions of the flow fields. Ye and McCorquodale (1998) did numerical investigations on the experiments done by Hicks, *et al.* (1990) on sloped bank curved channel using a

modified k-ε turbulence model and found that the agreement between both results was generally good. Recently Blanckaert (2003) performed experimental studies on a 120° curved developed bed topography open channel using a non-intrusive acoustic Doppler velocity profiler (ADVP) and found out that, besides the classical helical motion (center-region cell), a weaker counter rotating cell (outer-bank cell) is also present in the corner formed by the outer bank cell and the water surface. Patel and Gill (2005, 2006) did CFD investigations on curved open channels using FLUENT®. They also applied Volume of Fluid (VOF) model on experiments conducted by Blanckaert (2003) and simulated outer bank cell successfully using Reynolds stress model (Patel and Gill, 2006).

This thesis intends to present results on secondary flows and velocity redistribution in curved channels for different degrees of bend 15°, 30° and 45° and at different flow rates 4, 5, 6, 8, 10 and 15l/s (or corresponding depth/curvature ratio from 0.038 to 0.096) using the CFD software FLUENT®. As such a comparison has never been reported and it will also help to simulate the effects of these parameters on secondary flows in detail. Concurrently, such analysis will also enable modelling of the effects of secondary flows on individual particle fates using the Discrete Phase Model.

2.5 Sediment Transport in Open Channels

2.5.1 Definition

Sediment transport is the general term used for the transport of material (e.g. silt, sand, gravel, boulders) in rivers and streams. The transported material is called the '*sediment load*' which comprises of the '*bed load*' and the '*suspended load*'. The bed load characterizes grains rolling or sliding along the bed while the suspended load refers to grains maintained in suspension by turbulence. The distinction is, however, sometimes arbitrary when both loads are of the same material (Chanson, 1999). Sediment transport is a process of some significance as it governs or influences many situations that are of importance to mankind. Silt deposition reduces the capacity of reservoirs, interferes with harbour operation and blocks or modifies the path of watercourses. Equally, erosion or scour may undermine structures. In rivers and on

coastlines, sediment movements form a part of the long term pattern of geological processes. In the wastewater industry, the grit travels within the classifiers and conveying channels and grit channels can be significant in relation to the grit removal from wastewater as a part of preliminary treatment process. However, grit particle concentration in industrial/domestic waste water is relatively small (see Section 2.6.1) compared to sediment flows in rivers and estuaries and the interaction within various grit particles is usually neglected in the former (Stovin and Saul, 1996, 1998, 2000; Faram and Harwood, 2003; Jayanti and Narayanan, 2004; Egarr, *et al.*, 2004).

2.5.1.1 Physical Properties of Sediments

Sediment particles are distinguished between two categories: cohesive material (silt, clay) and non-cohesive (sand, gravel). In this thesis, only non-cohesive materials are considered. The density of quartz and clay minerals is typically: $\rho_p = 2650 kg/m^3$. Most natural sediments have densities similar to that of quartz. The relative or (specific density) of a sediment particle equals: $s = \frac{\rho_p}{\rho}$; where ρ is the fluid density. Thus, for a quartz particle in water, $s = 2.65$ and the typical density of natural sand is considered to be close to $2650 kg/m^3$. However, in the present study the exact density for each individual particle size was measured in order to provide a precise input to the computational model (see Section 3.3.2). The grit particle sizes are distinguished on the basis of their sieve diameter (where, sieve diameter is the size of particle that passes through a square mesh sieve of given size but not through the next smallest size: e.g. $1180\mu m < d_s < 2000\mu m$). The results from which enables a particle size distribution (PSD) of the grit sample to be produced (see Section 3.3.2).

2.5.2 Sediment Dynamics: Forces acting on a Particle

For an open channel carrying discrete sediment particles, the forces acting on each sediment particle (Chanson, 1999) are:

- the gravity force, $F_g = \rho_p g V_p$
- the buoyancy force, $F_b = \rho g V_p$

- the drag force, $F_d = {C_d \rho A_p v^2}/{2}$
- the lift force, $F_l = {C_l \rho A_p v^2}/{2}$;
- the friction force, $F_f = \mu_f N$

where V_p is the volume of the particle, A_p is a characteristic particle cross-section area, C_d and C_l are the drag and lift coefficients respectively, and v is a characteristic velocity, μ_f is coefficient of friction and N is normal reaction force. The gravity force and the buoyancy force both act in the vertical direction while the drag force acts in the flow direction and the lift force in the direction perpendicular to the flow direction as shown in Figure 2.5.

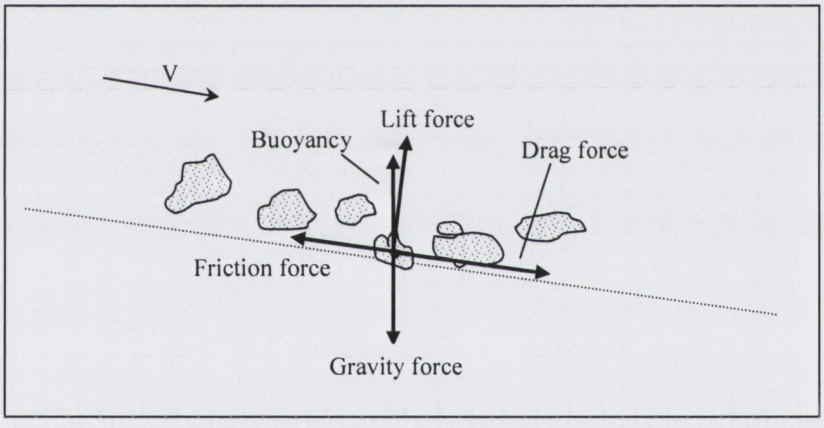

Figure 2.5: Forces acting on a Sediment Particle

Other forces: There also exist forces called the virtual mass forces which are the force required to accelerate the fluid surrounding the particle, the force in a rotating frame of reference, and the force due to a temperature gradient (Fluent, 2005). These respective forces are neglected in the present study as the density of fluid is not greater than the density of grit particle, there is no rotating reference frame and no temperature gradient in the flow. In addition, the lift force is neglected as it i s recommended for only sub-micron particle range (Li and Ahmadi, 1992; Fluent, 2005). The prediction of the discrete (grit) phase particle trajectory in the present

thesis is obtained by the force balance equation based on Fluent (2005) and is discussed in mathematical formulation in Section 2.7.5.

2.5.3 The Threshold of Movement

The term 'threshold of sediment motion' describes the flow conditions and boundary conditions for which the transport of sediment starts to occur. The threshold of sediment motion cannot be defined with an exact (absolute) precision but most experimental observations (Schoklitsch, 1914; Shields, 1936 - see Graf, 1971; Rijn, 1984a) have been based on critical shear stress and have provided reasonably accurate and consistent results.

2.5.3.1 Dimensional analysis

The relevant parameters for the analysis of sediment transport threshold are: the bed shear stress τ_0, the sediment density ρ_s, the grain diameter d_s, the gravity acceleration g and the fluid viscosity μ:

$$f_1(\tau_0, \rho, \rho_s, \mu, g, d_s) = 0, \tag{2.18a}$$

In dimensionless terms, it yields:

$$f_2\left(\frac{\tau_0}{\rho g d_s}; \frac{\rho_s}{\rho}; \frac{d_s\sqrt{\rho\tau_0}}{\mu}\right) = 0 \tag{2.18b}$$

In uniform equilibrium flow down an open channel, the shear velocity u_*, equals:

$$v_* = \sqrt{g\frac{D_h}{4}\sin\theta} \tag{2.19a}$$

where, D_h is the hydraulic diameter and θ is the bed slope. So, the mean boundary shear stress equals:

$$\tau_0 = \rho g\frac{D_h}{4}\sin\theta \tag{2.19b}$$

For a wide rectangular channel, it yields:

$$v_* \approx \sqrt{gd\sin\theta} \tag{2.20a}$$

$$\tau_0 = \rho g d\sin\theta \tag{2.20b}$$

Critical Shear Stress: Particle movement occurs when the movement of the destabilizing forces (i.e. drag, lift, buoyancy), with respect to the point of contact, becomes larger than the stabilizing moment of the weight force. Experimental observations (Shields, 1936) highlighted the importance of the stability parameter τ_* (which may be derived from dimensional analysis) defined as:

$$\tau_* = \frac{\tau_0}{\rho(s-1)gd_s} \tag{2.21}$$

The stability parameter τ_* is commonly called the *Shields parameter* and is a dimensionless parameter and sometimes also denoted as θ. A critical value of the stability parameter may be defined at the inception of the motion: i.e. $\tau_* = (\tau_*)_c$. Shields (1936) showed that $(\tau_*)_c$ (commonly known as the critical Shields parameter) is primarily a function of the shear Reynolds number, $v_* d_s / \upsilon$. The Bed load motion occurs for:

$$\tau_* > (\tau_*)_c \tag{2.22}$$

In summary, the initiation of bed load transport occurs when the bed shear stress τ_0 is larger than a critical value:

$$(\tau_0)_c = \rho(s-1)gd_s(\tau_*)_c \tag{2.23}$$

Further increase of bed shear stress results in the inception of a suspended load. Several researchers (Bagnold, 1966; Rijn, 1984b; Raudkivi, 1990; and Julien, 1995) proposed criteria for the onset of suspension. The criteria for the particle to be in suspension is generally based on the value of $\frac{v_*}{v_s}$. In a first approximation, suspended sediment load occurs for:

$$\frac{v_*}{v_s} > 0.2 \text{ to } 2 \tag{2.24}$$

where, v_s is terminal settling velocity. Bagnold (1966) proposed the criteria as:

$$\frac{v_*}{v_s} > 1 \tag{2.25}$$

while according Rijn (1984b), the critical value is 0.4. Raudkivi (1990) and Julien (1995) suggested the critical value is 0.5 and 0.2 respectively.

2.5.4 Numerical Modelling in Rivers and other Environmental Flows

The usage of numerical sediment concentration models for the prediction of sediment transport in natural rivers and Discrete Phase Model (DPM) in other environmental flows (if the concentration of particles is less than 10% by volume) is becoming common place which allows sophisticated descriptions of the turbulent flow field. In river flow analysis, numerical models incorporating the interaction between sediment particles and sediment concentration equations are solved for each grit particle size coupled with governing fluid flow equations. This type of method is computationally intensive and requires a tremendous amount of computer space especially for solving sediment laden flow for more than one particle size.

2.5.4.1 River Morphology

The associated development linked with the sediment transport phenomena is river morphology as it determines the evolution of river beds, estuaries and coastlines. In natural rivers, secondary flows initiate sediment transport in a transverse plane (where erosion occurs on the outside and deposition on inside of the bend) resulting in the meandering of channels (Figure 2.6).

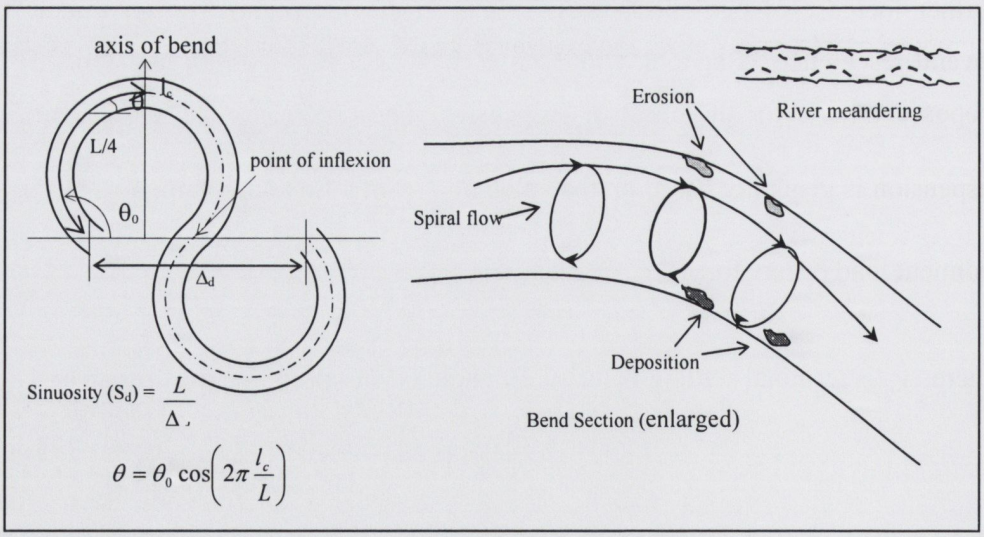

Figure 2.6: Secondary Flow – River Meandering

The mechanism of sediment transport in such rivers is more complicated than that in an engineered straight channel because the flow is usually turbulent, the geometry is irregular and can vary with time. Many investigations have attempted to predict the

composition of bed material and model armoring effects in a channel bend. Several analytical solutions have been introduced e.g. Bridge (1976); Odgaard (1982); Ikeda *et al.* (1987), most of which are based on the force balance between the pull of upslope secondary flow and the downslope component of gravity. Each size of sediment shifts its locus to find a stable position where these forces are in balance as it moves around the bend. However, the analytical models are restricted to steady flow and normally only an equilibrium state is considered. Therefore, the results of these models become questionable if the bed topography is to be computed at a specified time prior to when the equilibrium condition is reached. In order to overcome the limitations of the analytical models, several numerical models have been developed. One dimensional models include those developed by Han and He (1987), Park and Jain (1987) and Bhallamudi and Chaudhry (1991). However, most of the 1D models need to choose sediment transport functions which themselves are not certain to give good performance (Vanoni, 1984). Olsen and Kalkwijk (1987) presented a two-dimensional model to predict grain sorting and bed topography in channel bends. Sun *et al.* (2001) developed a computer model for meandering channels in which a theory for the multiple size bed-load sediment transport and sorting in the meander bends is utilized. General-purpose software models for flow and sediment transport in the two-dimensional domain have also been developed recently, e.g. CCHE2D (NCCHE, University of Mississippi) and SED2D-EMS (Environmental Modelling Systems, Inc.). In the CCHE2D model, a bed material sorting procedure is considered in which the bed material above the non-erodible layer is divided into several layers and the bed material gradation is estimated based on the local flow condition and bed deformation (Wu, 2001). SED2D-EMS is a model for the transport of cohesive or a representative grain size of non-cohesive sediments and their deposition, erosion and formation of bed deposits. Recently Kassem and Chaudhry (2005) upgraded their 2D numerical model by including the effects of bed armoring with non-uniform sediments and to investigate its effects on the bed topography of channel bends with unsteady flow, finding good agreement between measured and computational results. Their results also showed that the bed armoring reduces scour and deposition in channel bends. The computed magnitude and location of the maximum scour excluding the armoring effect differ from those simulated including bed armoring.

Several 3D models for water flow and sediment transport have also been published where the models consider a single, effective grain size for each simulation. This means that a separate model run is required for each size during each simulation and also that, in such models, the armoring effect is not included. Wang and Adeff (1986) developed an unsteady 3D model for these processes based on a finite element method. Rijn (1987) established a combined model in which the sediment transport is calculated with a 3D approach and the flow with a depth-averaged approach in combination with the assumption of a vertical logarithmic velocity profile, which is valid only for gradually varied flow. Demuren and Rodi (1986) used the κ-ε turbulence model (see Section 2.7.3.1) in 3D simulations of the flow and transport of a neutral tracer in meandering channels, and Demuren (1989) extended this work to calculate suspended sediment transport. Later, Demuren (1991) also included a simple model for bed-load transport and performed calculations of the flow and sediment transport in the 180° laboratory channel bend studied experimentally by Odgaard and Bergs (1988). Wu *et al.* (2000) proposed a 3D model for flow and sediment transport in which models for calculating the water level and for treating rough beds are added in order to make the code more suitable for open channel flow situations. Studies done on 3D models suggested that 1D and 2D simulations usually neglect the influence of secondary flows and their effect can only be accounted realistically with a 3D model. However, 3D simulations on sediment transport are still not being used ubiquitously because it requires tremendous computational time and space.

2.5.4.2 Miscellaneous Environmental Flows

As discussed earlier, if the concentration of particles in the flow is less than 10% by volume as in municipal wastewater, storm-water or the chemical process industry, the method for solving the concentration equation for each particle size can be overlooked without compromising accuracy. In this scenario the Discrete Phase Model (DPM) approach (Stovin and Saul, 1996, 1998, 2000; Faram and Harwood, 2003; Jayanti and Narayanan, 2004; Egarr, *et al.*, 2004; Fluent, 2005) can be used in which the discrete particle trajectories (or fates) are obtained by solving governing fluid flow equations and particle force balance equation. As the name would suggest, each particle is treated as an individual and interaction between various particles is not modeled.

Stovin and Saul (1996) were one of the few researchers who have used the DPM method (available in CFD software Fluent (2005)) to obtain a statistical distribution of sediment destinations in their studies on combined sewer overflows (CSOs). Their subsequent studies highlighted the importance of appropriate specification of DPM boundary conditions in the computational model like '*trap*', '*reflect*' or '*escape*' (i.e. (a) to understand the physical process involved and (b) to assign these boundary conditions to their respective boundary zones (see Section 4.3 for the explanation of these boundary conditions). Based on their studies, they concluded that their results were highly sensitive to the particle injection location, but less sensitive to either the particle size or the density. Faram and Harwood (2003) and Jayanti and Narayanan (2004) in their studies also demonstrated the ability of DPM to provide reliable outputs for industrial applications like sediment interceptors and sedimentation tanks respectively. Studies done by Egarr *et al.* (2004) recommended that the effect of shape factors should be included in the DPM approach. Thus, considering the extent of accuracy to which DPM is able to deal with various industrial problems and the nature of current work, a three dimensional DPM approach has been used in the present study to model grit particle movement across a grit removal channel. The detailed mathematical formulation of DPM is presented later in Section 2.7.5.

2.6 Open Channel as a Grit Removal Device

Grit separation is part of the preliminary treatment of sewage entering a treatment plant. This process removes large inert particles and prevents abrasion of mechanical equipment such as pumps, or blockage of conduits and digestion tanks. Two problems which are still being faced by engineers are, (1) large fluctuations in the rate of incoming sewage flow, and (2) the need to have selective grit separation. The process should be designed such that the settling particles do not include organic material which should be treated by other processes downstream. A review on grit characteristics found in typical municipal wastewater and a performance assessment of grit removal devices which are being used worldwide, is presented below.

2.6.1 Nature of Grit: Characteristics, Sources and Loading Rate

Grit present in wastewater (both sanitary and combined) flows is normally defined as inorganic particles with a specific gravity of 2.65. However, grit removed by wastewater treatment processes is considered to be a mixture of both organic and inorganic substances with a specific gravity ranging from 1.3 to about 2.7 (Metcalf and Eddy, 1991; Marais and Haandel, 1996). The organic matter can contain putrescible and non-putrescible components. The non-putrescible portion typically is ash, cinders, and plastic. Egg shells, seeds, coffee grounds, vegetables (i.e., peas and corn), and fruit rinds make up the bulk of the putrescible portion (Hides and Griffiths, 1997).

2.6.1.1 Selective Grit Removal

The most serious problem grit can cause is premature wear and tear on pumps and mechanical equipment through abrasion (Metcalf and Eddy, 1991). Additionally, grit accumulation in pipes and aeration basins can increase losses and reduce hydraulic capacity. Hence, removal of grit from the wastewater becomes a central issue in designing any wastewater treatment unit. However, it should also be noted that not all grit particles cause problems at the wastewater treatment plant. According to Metcalf and Eddy (1991), Rupke (1994) and USEPA (2003), the majority of problems are caused by those grit particles which are larger than 200μm (0.2mm) in diameter. Fine grit particles, sub 100μm (0.1mm), may be present in small quantities and generally don't tend to be as abrasive. Studies (Hides, 1999) have indicated that it may even be beneficial to the downstream settlement processes to have a small amount of grit present to act as a nucleus to improve the settleability of lighter organics and flocs. Studies made by Gardner and Deamer (1996) also concluded that the removal of 'grits' down to 75μm (0.075mm) is not only unnecessary (as they do not damage pumps) but also aids in sludge handleability. Sawicki (2004) on his studies on aerated grit chambers acknowledged the classical concept of Imhoff and Imhoff (1979) that a properly functioning aerated grit chamber should remove 100% of coarse sand fraction ($d>200\mu m$) and 65-75% of the medium sand fraction ($100\mu m<d<200\mu m$). Moreover, the organic matter content in the removed grit should not exceed 10% (percentage by weight). Faram *et al.* (2004) and Egarr *et al.* (2004) also specified that hydrodynamic vortex separators (HDVs) can be designed to remove particle size

down to 150μm diameter. It should also be noted that most grit specifications are approximately for 95% removal down to 150μm particles (U.S.) and 200μm particles (U.K.). Also that performance of grit removal devices also depends on influent grit loading. Hence, on the basis of the above studies, the present study analyzes grit particles from size varying from 63μm to 2000μm and aims to achieve 95% removal efficiency of grit particles down to 150μm using a curved grit channel.

2.6.1.2 Grit Loading

The majority of grit enters the collection system from surface water runoff from streets and paved areas, although significant volumes of grit may also enter the system from construction activity, infiltration and industrial discharges. In the United States (Hides, 1999), the largest source is perceived as deriving from wash-off from winter gritting of roads and highways. These phenomena can also be seen in the northern United States and Canada where grit loadings tend to be highest in late winter and early spring. Intense spring rains generate first flush wash-off from winter gritting of roads mobilizing accumulated grit and carrying it into the collection systems. Finally wind blown sand from beaches onto roads can produce shock loading for treatment plants serving coastal areas. Thus, grit characteristics for a particular treatment plant are determined by factors as: *the type of collection systems, the physical condition, the grade of the pipe, routine maintenance practice, presence of construction, industrial process and washwaters and geographical location* (Hides, 1999). These factors are responsible for the hydraulic loading, grit loading, average and peak daily flow at any typical wastewater treatment plant. Studies made by Hides and Griffiths, (1997) on the quantifying the nature of the grit shows that the grit loading can vary from a minimum value of 0.6 mg/l to a maximum of 80 mg/l. In their studies, grit samples from five different treatment plants in New England were collected and analyzed for moisture and organic content. In addition, grain size distribution and hydrometer analysis were performed. Based on their findings they concluded that as flow increases, the relative size of grit increases because the flow traveling at higher velocities can entrain larger particles. The average grain size distribution indicated that about 20% of the sample was composed of particles finer than 75μm and the majority of the grit particles lie between 100 and 2000μm. Steel and Mcgee (1979),

Marais and Haandel (1996) indicated that 80 to 250kgs of inorganic solids is to be expected per 1000m^3 of raw sewage in a sewerage system with a separate system for storm water. Marais and Haandel (1996) also indicated that this ratio may be well outside the range for special cases like combined systems. Similar loading rates were found by Gravette, *et al.* (2000) in their study on King County's West Point Treatment Plant (WPTP), Seattle. They found that the average influent grit concentration to the aerated grit chamber for the two storms was 11.3mg/l. Some studies in semi urban areas (SUAs) in southern India found that grit concentrations were in the range of 30-150mg/l in a municipal wastewater (Sundaravadivel *et al.*, 2000). However, Rupke (1994) observed comparatively higher loading rate of 180mg/l during his studies on Grit King® (Hydro International Plc.) and Eutek Tea-Cup™ (Eutek Systems) grit removal systems at Main Treatment Plant (MTP), Toronto indicating that the loading rate varies quite significantly at different places. In addition to the grit loading, the average influent flow rate also varies significantly across a treatment plant. At WPTP (Seattle), the average annual influent flow during 1998-1999 was approximately 124mgd and the peak flow was 440mgd, a flow which occurred 7 times during that period. The mean flow can obviously differ significantly depending on the size of the wastewater catchment. USEPA (2003) studies have also indicated that there are no obvious trends associated with design flow rate and the quantity of grit removal through a plant making the correlation between both nearly impossible.

2.6.2 Grit Removal Devices

A traditional grit removal facility typically comprises of a primary grit removal system to remove grit particles from the waste stream and a secondary device to dewater the grit. Based on the literature (see following sub-sections), the grit removal devices can be categorized into Detritus Tanks, Aerated Grit Chambers, Vortex Grit Chambers and Grit Channels.

2.6.2.1 Detritus Tanks

Detritus tanks (see Figure 2.7) are one of the oldest types of grit removal system (Metcalf and Eddy, 1991). The detritus tank is essentially a short period sedimentation

tank having a detention time of less than one minute. Flow within the detritus tank follows a circular flow path and the grit that settles out is moved across the flat base by mechanical scrappers. The major disadvantage of a detritus tank is that, along with the grit, they tend to remove large settleable organics (USEPA, 2003). There are still a number of detritus units in operation; however they are rarely designed into new facilities. Detritus tanks are still in use in parts of southern India with reed-beds for a combined wastewater treatment system for populations of 25,000 to 75,000 (Sundaravadivel *et al.*, 2000). However, the performance of detritus tanks which are in use in SUAs in India is not reported. Several technical reports as Beder (1993), MEDEP (2002), USEPA (2003) also acknowledge the fact that the detritus tanks were used in former times but fail to provide any quantitative or qualitative data on their on-site performance.

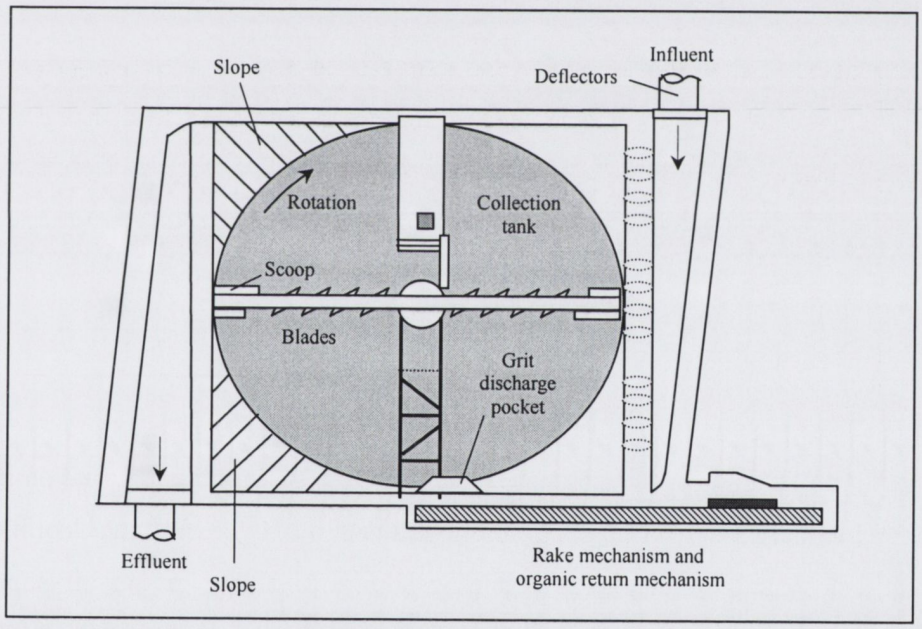

Figure 2.7: Detritus Tank

2.6.2.2 Aerated Grit Chambers

An aerated grit chamber (AGC) is illustrated in Figure 2.8 (Metcalf and Eddy, 1991). It is a settling tank equipped with an aeration system in which air bubbles are introduced along one side of the chamber, usually near its bottom to induce a transverse circulation, which combines with the longitudinal motion of the wastewater

and forms a characteristic spiral flow. As the introduction of air induces a spiraling or rolling motion within the channel, changing the airflow can subsequently regulate removal efficiency.

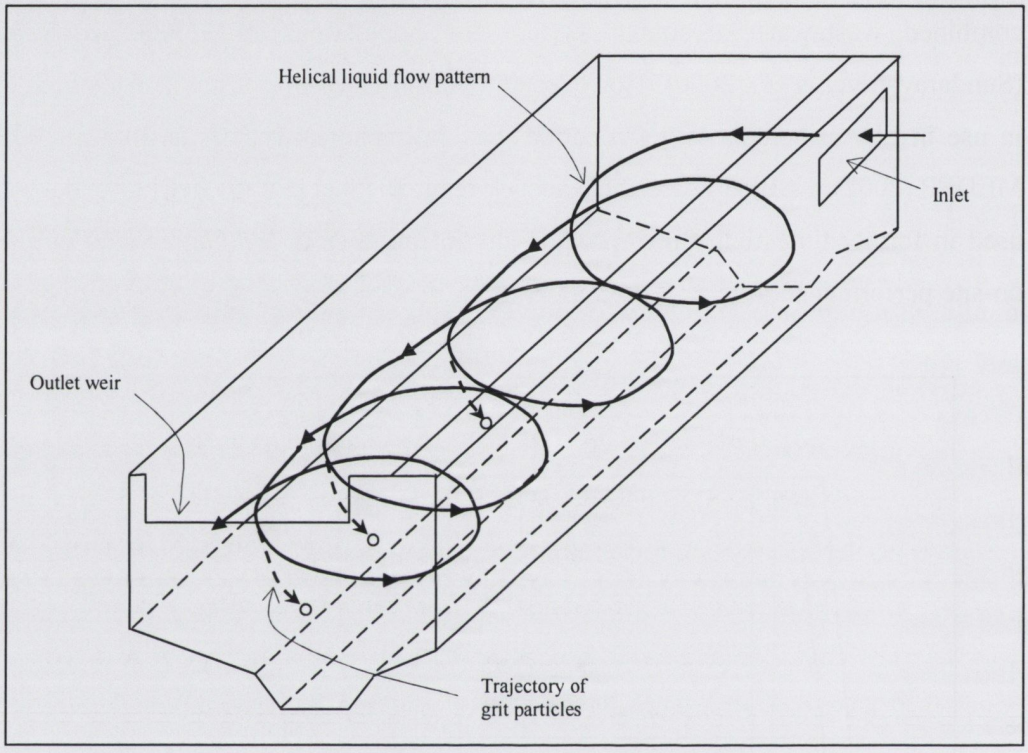

Figure 2.8: Aerated Grit Chamber

The grit removal and organic content is therefore less susceptible to variation in flow rates. Aerated grit chambers are commonly designed for larger treatment facilities and normally designed to remove grit particles down to 200μm at an air supply of $0.18m^3/min.m$ to $0.46m^3/min.m$ with 2-5 minute detention periods at the peak hourly rate of flow. (For example, for a peak flow rate of $1.38m^3/s$ and detention period of 3minutes, two AGCs are employed each having the total volume $124.2m^3$ for dimensions-width=3.6m, depth=3m, and length=11.5m, the efficiency is 100% removal of 200μm at an air supply rate of $0.3m^3/min.m$). The surface loading rates for all the grit removal devices are shown in Table 2.3. It should also be noted that the size of the grit particles removed with an aerated grit chamber tends to be relatively coarser as the air has a tendency to resuspend finer grit and sand. Some on-site performance assessment of AGCs at WPTP, Seattle (Gravette *et al.*, 2000) indicated that the grit chamber was more efficient at removing larger grit than the smaller grit as

expected. They found 79.1% of 300μm, 75.4% of 212μm and 64.9% of 150μm grits were removed at storm events ranging from 260-285mgd and 300-400mgd at an airflow rate of 0.55m^3/min.m. A performance certification report (DPW, LA, 1998) found that the performance of AGCs to capture grit is not significantly affected if the air supply is reduced from 0.7m^3/min.m to 0.4m^3/min.m. The advantages of AGCs include pre-aeration, potential for use for chemical mixing and flocculation, while disadvantages include high capital and operational cost to run the aeration systems. Some of the design information for AGCs is shown in Table 2.1.

Table 2.1: Design information for AGCs

Item	Range	Typical
Detention time at peak flow rate (min)	2 - 5	3
Depth (m)	2.1 - 4.9	
Length (m)	7.6 - 19.8	
Width (m)	2.4 - 7	
Width-depth ratio	1:1 - 5:1	1.5:1
Length-width ratio	3:1 - 5:1	4:1
Air Supply (m^3/min.m of length)	0.18 - 0.5	

2.6.2.3 Vortex Grit Chambers

As the name suggests, vortex grit chambers (VGCs) rely on an induced vortex motion to separate the grit from the water. In VGCs, gravity effects are also important and often dominant over centrifugal forces. The retention time for a typical vortex chamber is around 30 seconds. The vortex separators generally fall into three categories based on energy levels or headloss across the device.

(i) *The "low" energy vortex separator* - It is often referred to as the Pista® (Smith & Loveless Inc.) type grit removal system which is a low headloss device with losses typically less than 2.5cm (see Table 2.3 for surface loading rates). A typical Pista® unit is shown in Figure 2.9 (Metcalf and Eddy, 1991). In this device, a turning paddle is used to induce rotary motion inside a cylindrical chamber, thereby maintaining a constant velocity irrespective of the inflow rate. Pista® systems are widely used on medium and large scale facilities. A straight channel is required upstream of the unit to establish uniform laminar flow conditions prior to the inlet. Pista® systems are

designed to remove 65% of particles greater than or equal to 150μm (Smith and Loveless Inc.).

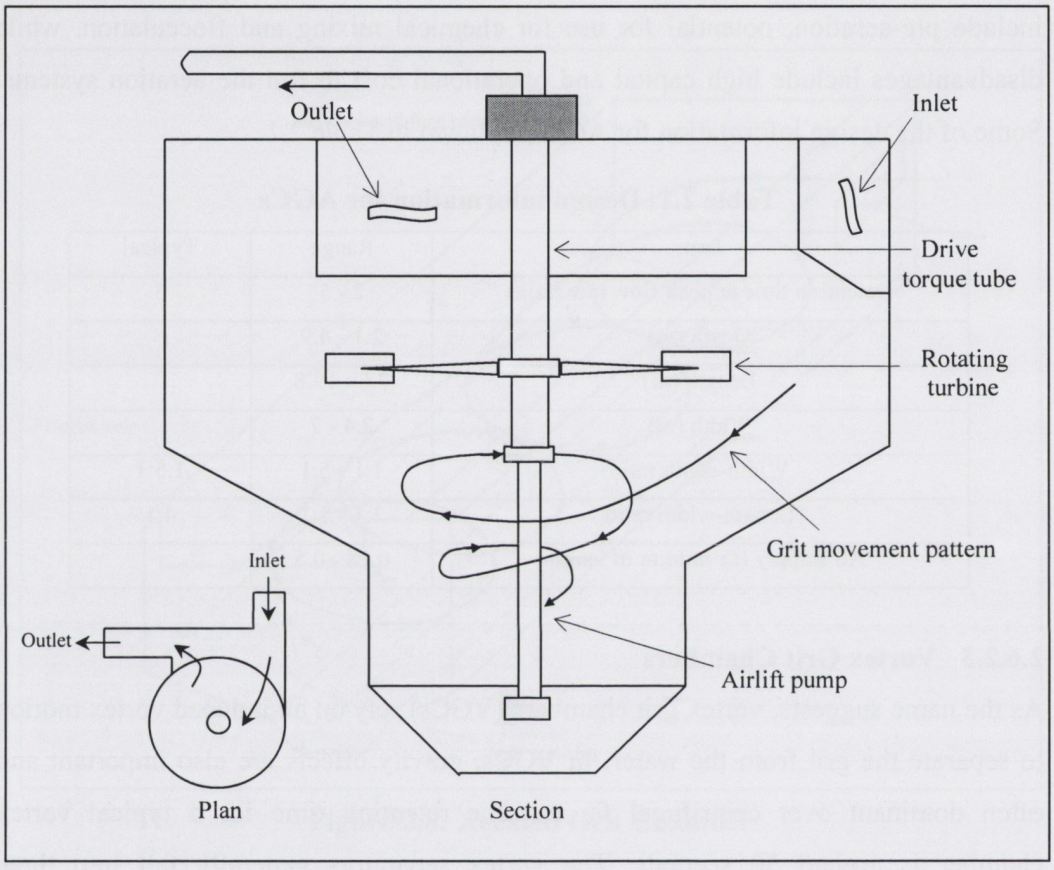

Figure 2.9: Low Energy Vortex Separator (Pista® Unit)

(ii) *A "medium" energy vortex separator* - This is famously known as The Grit King® (Hydro International Plc.) dynamic separator. The Grit King® (shown in Figure 2.10) has no moving parts and uses a tangential feed to induce rotary motion within a circular chamber. The rotary flow patterns are stabilized by flow modifying members within the vessel. Headlosses are typically less than 30cm and the device is able to maintain high removal efficiencies over a wide range of flow rates. Medium energy vortex separators have been applied to both pumped and gravity flow applications. Grit removal efficiencies are typically 95% of particles down to 200μm (Hydro International Plc.). Pilot scale studies at MTP, Toronto conducted on the Grit King® (0.9m unit) with a 300mm screw clarifier by Rupke (1994) found that the efficiency of Grit King® was around 87% for 100μm diameter particles at flow rates of 4.2 to

23.1l/s. The Grit King® assessed in the studies of Rupke (1994) was considered to be efficient as it was rated for removal of 95% of particles larger than 100μm at a flow rate of 8.8l/s and has relatively lesser surface loading rates compared to other devices (see Table 2.3).

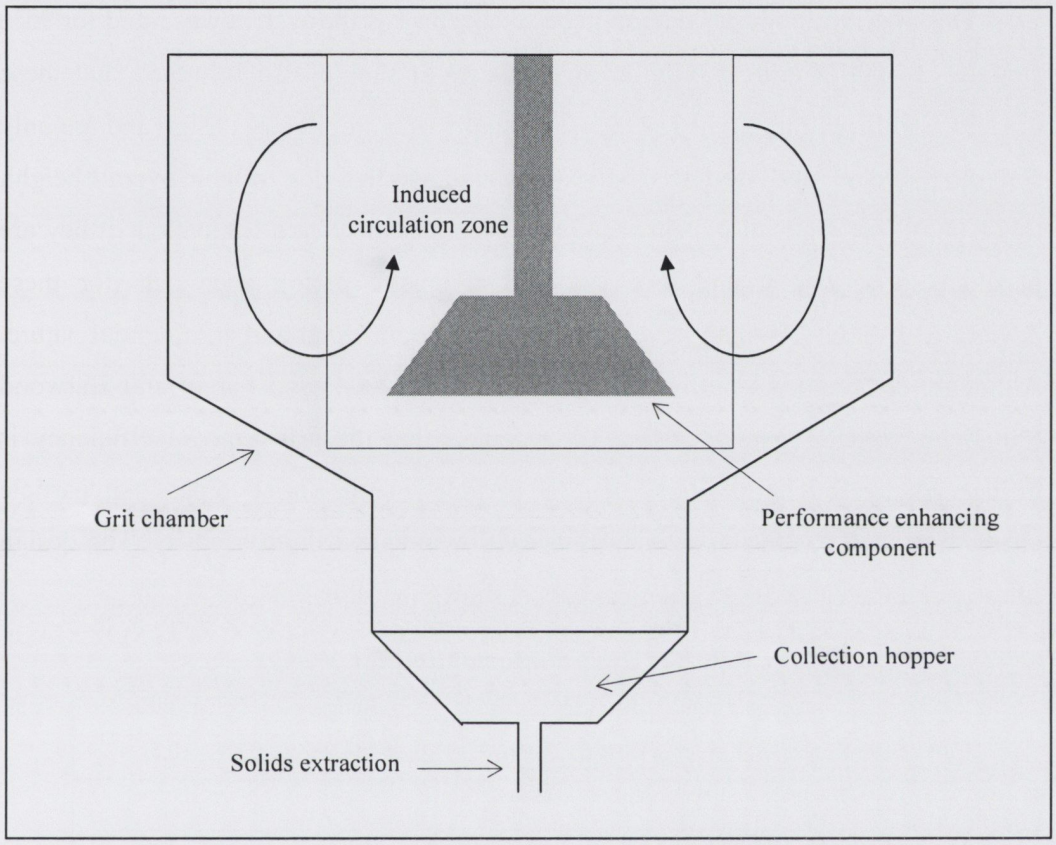

Figure 2.10: Medium Energy Vortex Separator (Grit King®)

(iii) *The "high" energy vortex separator* - also known as Teacup™ (Eutek Systems) separators. These high energy vortex separators have no moving parts and rely on a tangential feed to generate a 'free' vortex within a circular chamber. The headloss across high energy vortex separators are significantly higher than the vortex separators discussed earlier, typically in the 1-3m range. The removal efficiency of the high energy vortex separators is similar to the medium energy units (Eutek Systems). However, the performance of the high energy devices is susceptible to variations in inlet pressure and flow rates. Removal efficiencies can reduce dramatically as the flow rate decreases. Therefore, this type of device is most suited to constant flow pumped applications. Pilot scale studies at MTP, Toronto conducted on

a Teacup™ (trailer mounted-1.22m) by Rupke (1994) found that the efficiencies of around 70% for the removal of 150μm particles at flow rates of 30 to 60l/s (see table 2.3). This observation is considered to be satisfactory as the system was rated for 95% capture of 100μm grit at 35l/s on raw sewage. It should also be noted that these devices are difficult to modify as they are usually of a proprietary design and are only suitable for relatively low flow applications and also that due to their overall height, this type of grit removal system requires a deep basement or a lift station if they are installed above the ground level. Additional on-site performance data for these devices is difficult to acquire due to their highly commercial and confidential nature. Although, some studies performed by Egarr *et al.* (2004) and Faram and Harwood (2003) on vortex separators using CFD depicts that the grit removal efficiency is influenced by initial position of the particle in the inlet pipe, the particle characteristics (i.e. density, size and shape), flow rate and fluid viscosity. The design information for vortex-type grit chambers is shown in Table 2.2.

Table 2.2: Design information for VGCs

Item	Range	Typical
Detention time at average flow rate (min)		0.5
Diameter – upper chamber (m) (Main chamber)	1.2 - 7.3	
Diameter – lower chamber (m) (Grit collection hopper)	0.9 - 1.8	
Height (m)	2.7 - 4.8	
Removal rates (%) 0.3mm		95+
Removal rates (%) 0.24mm		85+
Removal rates (%) 0.15mm		65+

Table 2.3: Surface Loading Rate for Different Types of Grit Chambers

Grit Removal Device	Surface Loading Rate ($m^3/m^2.s$)	Retention Time (mins)	Particle Size
Aerated Grit Chamber	$33.3*10^{-3}$	1-3	95% removal of 200μm
Vortex Grit Chamber (Pista® Unit)	$5*10^{-3}$ to $50*10^{-3}$	1	95% removal of 300μm
Vortex Grit Chamber (Grit King®)	$6.6*10^{-3}$ to $36.3*10^{-3}$	0.5	95% removal of 200μm
Vortex Grit Chamber (Teacup™)	$25.7*10^{-3}$ to $51.4*10^{-3}$	1	95% removal of 100μm

2.6.2.4 Grit Channels

Grit channels or constant velocity channels rely on differential settling velocity between inorganic and organic fractions to separate grit from the influent flow stream. A grit channel (Figure 2.11) primarily consists of an open channel (with sufficient length at the upstream) and a sump at the base of the channel to collect grit which is intermittently pumped out to secondary clarifiers. The side walls are kept at a slope to accommodate for the variable flow rates which aids in maintaining constant velocity in the channel. Some of the features of constant velocity grit channels include:

- Settling - horizontal flow
- Uniform velocity at 0.25 - 0.35m/s
- Ideal parabolic shape or approximation (cross-section)
- Width:depth ratio 1:1
- Length $\geq$ 18 x max. depth

For an effective grit removal of size 200μm, flow velocities within the grit removal devices should be maintained at or close to 0.3m/s (Marais and Haandel, 1996; Brenner and Diskin, 1991; and Hides, 1999). But as cited by Metcalf and Eddy (1991) and Hides (1999), most wastewater treatment plants peak flows are often 3-4 times greater than the average daily flow levels and these variations lead to inconsistent removal efficiencies. Thus, a need of robust system/design of a grit channel is required to ensure maximum removal efficiency of grit particles larger than 0.15mm even at variable flow rates. One way to mute the variable flow rates is to employ weirs, Parshall flumes or outlet flow controls with the open channels. Very few studies seemed to have been carried out on grit channels in which an open channel was coupled with Parshall flume in order to keep the velocity in the main channel constant. Marais and Haandel (1996) in their studies presented detailed theoretical investigations and design guidelines for grit channels, although the performance of their designed grit channels is still to be validated either physically or computationally. NWW Engineering (1995) did some investigations on a curved channel in which the grit is collected at the inside of the bend due to the formation of secondary flows in the curved channel and are removed with the help of a sump located at the inside of the bend. Their investigations revealed that on an average 80% of particles greater than 300μm were removed using the bendy channel for the

average flow velocity of 0.35-0.5m/s. which is relatively less, though comparable, to the other devices tried at the same sites at the same flow rates.

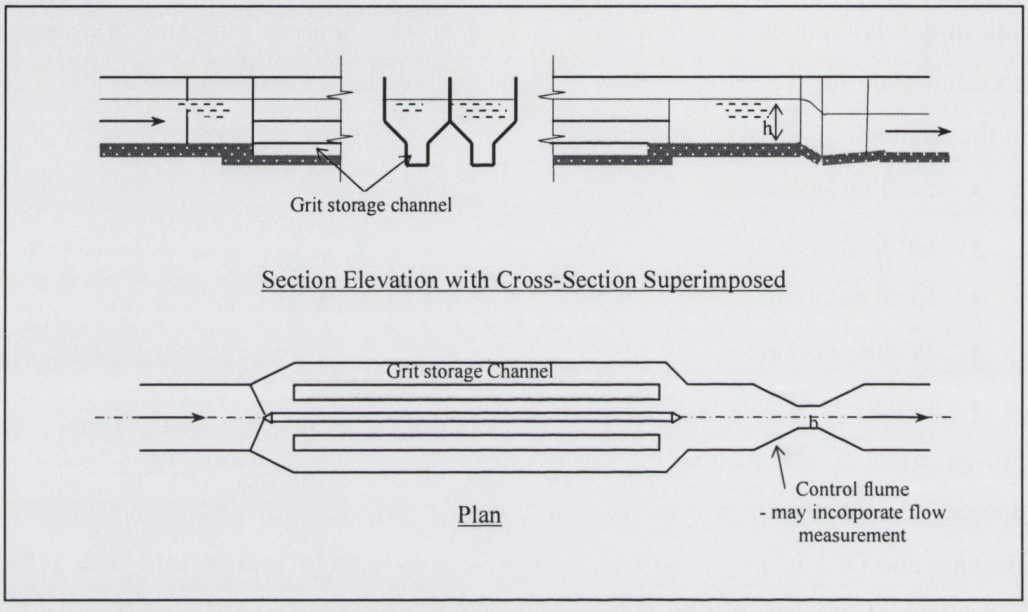

Figure 2.11: A Typical Constant Velocity Channel Arrangement

However, the studies failed to quantify the performance of grit channels at different bend angles, flow rates and radius of curvature which can prove to be critical parameters in their design and subsequent performance. Also, it seems that compared to other grit removal devices, this system has not been widely implemented due to lack of site performance data and their sensitivity to different flow rates compared to constant velocity channels, for example. In addition, in spite of high designed grit removal efficiency claimed by other grit removal devices, they do not perform consistently in the field as suggested by some of the literature discovered above. Also often, consultants/contractors prefer to implement pre-engineered/proprietary systems which come ready built rather than design and construct their own system which could mean taking a risk. This could be a major reason for the underutilization of public or textbook designs of any system. Thus, this thesis intends to present a detailed experimental and computational analysis of grit channels for the different geometrical and dynamical parameters which affect the grit removal efficiency. The advantages associated with the grit channels, which would encourage their future use include:

- No moving parts and hence small maintenance and operation costs.
- Lower capital costs compared to aeration systems.
- Minimum energy requirements except grit removal pumps and associated secondary clarifiers.
- Head loss in the grit channel is very small. For example, the level of the discharge of the sewage in the primary tank or biological reactor could be at the same level as the flume base.

2.7 Computational Modelling: Theory

This section deals with a general introduction of computational fluid dynamics, structure of a typical commercial CFD software, mathematical formulation of governing equations of fluid flow and turbulence modelling. Methods used for the simulation of the free surface and movement of grit particles are also discussed.

2.7.1 Computational Fluid Dynamics

Computational Fluid Dynamics or CFD is the analysis of systems involving fluid flow, heat transfer and associated phenomena such as chemical reactions by means of computer based simulation. This is accomplished by solving governing fluid flow equations (partial differential equations for conservation of mass, momentum and energy) that represent the physical system and conceptual modelling assumptions (or turbulence modelling). The computer model implements the mathematical model and includes the code and the data input into the code, such as geometry data, initial and boundary conditions. It should also be remembered that the principal mathematical concepts useful for determining the success of any CFD code are convergence, consistency and stability (Versteeg and Malalasekera, 1995). Convergence is the property of a numerical method to produce a solution which approaches the exact solution as the grid spacing, control volume size or element size is reduced to zero. Consistent numerical schemes produce systems of algebraic equations which can be demonstrated to be equivalent to the original governing equations as the grid spacing tends to zero. Stability is associated with damping or errors as the numerical method proceeds. If a technique is not stable, then even the round-off errors in the initial data can cause wild oscillations or divergence. In broader terms, it can be said the

credibility of any numerical simulation is achieved through verification and validation, where validation is 'solving the correct governing equations while verification is 'solving the governing equations correctly' (Roache, 1994).

2.7.1.1 Structure of a CFD Code

A general purpose commercial CFD package FLUENT® (2005) was used for this research which incorporates three main stages during the modelling procedure: (i) *a pre-processor*, (ii) *a solver* and (iii) *a post-processor*.

(i) *Pre-processor*: Pre-processing consists of the input of a flow problem to a CFD program into a form suitable for use by the solver. The primary steps involved during the pre-processing stage are as follows:

- Preparation of geometry under consideration or the computational domain.
- Grid generation - the sub-division of the domain into number of non-overlapping control volumes (cells).
- Selection of physical and chemical phenomenon that need to be modelled.
- Specification of the boundary conditions.

Once the boundary conditions are specified, the grid nodes in the whole of the flow domain is initialised and the iterations required to solve the governing fluid flow equations can get underway.

(ii) *Solver*: The numerical method that forms the basis of the solver performs the following steps:

- Approximation of the unknown flow variables by means of simple functions.
- Discretization by substitution of the approximations into the governing flow equations and subsequent mathematical manipulations.
- Solution of the algebraic equations

Discretization is the process of converting a continuous problem into one considered at only a finite number of points. The finite-volume method uses a control volume (CV) approach to derive the discretized equations. A grid is generated that divides the domain into discrete CVs. The governing equations are then integrated over a CV to yield a discretized equation at a nodal point within the CV or cell. The discretized equations at each nodal point produce a system of linear algebraic equations which are

solved using a matrix solution method (the tri-diagonal matrix algorithm (TDMA)) to obtain the distribution of the variable at the nodal points. Other iterative methods like Jacobi and Gauss-Seidel can although easy to implement (Patankar, 1980; Versteeg and Malalasekera ,1995), but they can be slow in convergence when the system of equations is large and hence they are not considered suitable for general purpose CFD packages (Versteeg and Malalasekera, 1995).

(iii) *Post-processor*: Post-processing includes the geometry and grid display, representation of flow field results in form of contours, vectors and particle tracking.

Section 2.7.2 is based on Patankar (1980), Versteeg and Malalasekera (1995) and Ferziger and Peric (1999).

2.7.2 Mathematical Formulation

The governing equations of fluid flow are based on mathematical statements of the conservation laws of physics: mass conservation and Newton's second law (i.e. the rate of change of momentum equals the sum of the forces on a fluid particle). The flow equations are developed by systematically accounting for changes in the mass and momentum due to flow across its boundaries and, where necessary, due to the action of sources inside the element.

2.7.2.1 Governing Equations of Fluid Flow

The unsteady, three-dimensional mass conservation or continuity equation at a point in a compressible fluid is given by:

$$\frac{\partial \rho}{\partial t} + div(\rho \mathbf{u}) = 0 \tag{2.26}$$

where, ρ is the density of the fluid and $\mathbf{u}$ is the velocity vector. For an incompressible fluid, the density ρ is constant, and Eqn. 2.26 becomes:

$$div\mathbf{u} = \frac{\partial u_i}{\partial x_i} = 0 \tag{2.27}$$

The unsteady, three dimensional momentum conservation equations are given by:

$$\rho \frac{Du_j}{Dt} = -\frac{\partial p}{\partial x_j} + \frac{\partial \tau_{ij}}{\partial x_j} + S_{Mj} \tag{2.28}$$

where,

$$\frac{Du_j}{Dt} = \frac{\partial u_j}{\partial t} + \frac{dx}{dt}\frac{\partial u_j}{\partial x} + \frac{dy}{dt}\frac{\partial u_j}{\partial y} + \frac{dz}{dt}\frac{\partial u_j}{\partial z} \tag{2.29}$$

$u_{j(j=x,y,z)} = u, v, \& w$ are the components of the velocity of the fluid element in a cartesian coordinate system, τ_{ij} is the tensor of all surface stresses and S_{Mj} is the source term of j-momentum per unit volume per unit time. The term on the LHS of Eqn. 2.28 corresponds to the rate of increase of momentum per unit volume of a fluid particle. On the RHS of Eqn. (2.28), the sum of the first two terms corresponds to the total force on the fluid element due to surface stresses and the last term describes the overall effect of external body forces, i.e. the rate of increase of momentum due to sources. For example, the body force due to gravity would be modeled by $S_{Mx} = 0$, $S_{My} = 0$ and $S_{Mz} = -\rho g$ for x, y and z directions respectively (z being in the vertical direction). The governing equations still contain unknowns: the viscous stress components τ_{ij} and the useful form of the governing equations are obtained by introducing a suitable model for the viscous stresses τ_{ij}. In a Newtonian fluid the viscous stresses are proportional to the rates of deformation and hence, according to the Newton's law of viscosity, τ_{ij} is given by:

$$\tau_{ij} = \mu\left(\frac{\partial u_i}{\partial x_j} + \frac{\partial u_j}{\partial x_i}\right) - \frac{2}{3}\mu\frac{\partial u_k}{\partial x_k}\delta_{ij} \tag{2.30}$$

where, δ_{ij} is the Kronecker δ function and its value is 1 if $i = j$, and its zero otherwise. The repeated suffix notation represents the summation over all $k(k = 1,2,3)$ whilst μ is the laminar viscosity. Liquids are assumed incompressible and as already discussed earlier in the section, the mass conservation equation. (Eqn. 4.1) becomes $div\mathbf{u} = 0$, and thus Eqn. 2.30 takes the form

$$\tau_{ij} = \mu\left(\frac{\partial u_i}{\partial x_j} + \frac{\partial u_j}{\partial x_i}\right) \tag{2.31}$$

Substituting the value for τ_{ij} in the momentum equations (Eqn. 2.28), we get

$$\rho\frac{Du_j}{Dt} = -\frac{\partial p}{\partial x_j} + \frac{\partial}{\partial x_i}\left(\mu\frac{\partial u_j}{\partial x_i}\right) + S_{Mj} \tag{2.32}$$

Eqn. 2.32 is famously known as Navier-Stokes equations of fluid flow.

2.7.2.2 Effect of Turbulence and its Modelling

In a turbulent flow, an instantaneous component of the flow variable can be decomposed into its mean component and fluctuating component as:

$$\phi(x_i,t) = \bar{\phi}(x_i,t) + \phi'(x_i,t) \tag{2.33a}$$

Similarly the velocity variables (u, v and w) and pressure (p) can be represented as:-

$$\begin{aligned} u_i &= \overline{u_i} + u_i' \\ p &= \overline{p} + p' \end{aligned} \tag{2.33b}$$

Substituting Eqn. 2.33 into Eqns. 2.27 & 2.32, the averaged continuity and momentum equations without body forces for incompressible flows can be written in cartesian coordinates as:

$$\frac{\partial\left(\rho\overline{u_i}\right)}{\partial x_i} = 0 \tag{2.34}$$

$$\frac{\partial\left(\rho\overline{u_i}\right)}{\partial t} + \frac{\partial}{\partial x_j}\left(\rho\overline{u}_i\overline{u}_j + \rho\overline{u'_i u'_j}\right) = -\frac{\partial\overline{p}}{\partial x_i} + \frac{\partial\overline{\tau}_{ij}}{\partial x_j} \tag{2.35}$$

where the $\overline{\tau}_{ij}$ are the mean viscous stress tensor components given by:

$$\overline{\tau}_{ij} = \mu\left(\frac{\partial\overline{u}_i}{\partial x_j} + \frac{\partial\overline{u}_j}{\partial x_i}\right) \tag{2.36}$$

The conservation equations (Eqn. 2.35) are known as Reynolds Averaged Navier Stokes equations (RANS) which contain terms such as $\rho\overline{u'_i u'_j}$, called the Reynolds stresses. The presence of these Reynolds stresses in the conservation equations makes the situation in which unknowns are more than the number of equations requiring turbulent models to solve these equations.

2.7.2.3 The Eddy-Viscosity Hypothesis

Boussinesq (1877) recommended that the stress-strain relationship for a Newtonian fluid in laminar motion could similarly be applied to time-averaged turbulent flows. The Boussinesq hypothesis, linearly relates the Reynolds stresses with the mean strain rate and can be written in the form

$$-\rho\overline{u'_i u'_j} = \mu_t\left(\frac{\partial\overline{u_i}}{\partial x_j} + \frac{\partial\overline{u_j}}{\partial x_i}\right) - \frac{2}{3}\rho\delta_{ij}k \tag{2.37}$$

where, k is the turbulent kinetic energy.

Boussinesq introduced the concept of "eddy viscosity" μ_t to account for the turbulent momentum transfer. Eddy viscosity, unlike molecular viscosity, is a property of a flow and not a property of the fluid and hence varies for different types of flow. Prandtl (1925) suggested a method, based on dimensional analysis to determine the eddy viscosity known as Prandtl's mixing-length model. The model is based on the fact that as the eddy viscosity is property of the turbulent flow, it can thus be determined from the velocity and length scales of the turbulence (v_t and l_t, respectively). It is a zero equation model as turbulent length and velocity scales can be prescribed algebraically and doesn't require any additional model equations. However, this model is incapable of predicting flows with separation and recirculation (Versteeg and Malalasekera, 1995).

2.7.3 Turbulence Models

Two types of turbulence model were implemented in the thesis and are reviewed below:

2.7.3.1 The κ-ε Turbulence Model

The standard κ-ε model (Launder and Spalding, 1974) has two model equations, one for κ (the turbulent kinetic energy) and the other for ε (turbulent energy dissipation rate). The κ and ε are used to define the velocity scale v_t and length scale l_t as follows:-

$$v_t = k^{1/2}; \qquad l_t = \frac{k^{3/2}}{\varepsilon} \tag{2.38}$$

The dynamic viscosity is given by:

$$\mu_t = C\rho v_t l_t \tag{2.39}$$

Now, substituting the values for v_t and l_t, we get:

$$\mu_t = \rho C_\mu \frac{k^2}{\varepsilon}; \tag{2.40}$$

where, C_μ is a dimensionless viscosity constant.

The κ-ε model is the most widely used and validated turbulence model. It has achieved notable successes in calculating a wide variety of industrial flows which include flow inside buildings and pollutant dispersion in the atmosphere and in lakes (Rodi, 1980). In spite of the numerous successes, the κ-ε model has problems in simulating swirling flows and flows with large, rapid, extra strains (e.g. highly curved boundary layers and diverging passages) since it does not contain a description of the subtle effects of streamline curvature on turbulence. Secondary flows in long non-circular ducts, which are driven by anisotropic normal stresses, can also not be predicted owing to the assumption of isotropic turbulence within the κ-ε model. It should be noted that modifications made on standard κ-ε for simulating flows in curved ducts by Launder *et al.* (1977) yielded satisfactory results. The *realizable* κ-ε model has also shown substantial improvements over the standard κ-ε model in validation studies of separated flows and flows exhibiting complex secondary flow features (Shih *et. al.*, 1995). However, studies done by Blanckaert (2003) indicated that the linear κ-ε model has restricted capabilities in simulating secondary flows in curved open channels with developed bed topography.

2.7.3.2 Reynolds Stress Model (RSM)

The Reynolds stress model was also used as an alternative with κ-ε model in the present study. It is well known as a second-order or second-moment closure model. The modelling strategy for RSM originates from work reported in Launder *et al.* (1975). The modelling equations include six additional equations (one for each Reynolds stress τ_{ij}) and hence are computationally very intensive. RSM is considered to be a relatively complex type of model with the potential to describe all the mean flow and turbulent properties without case-by-case adjustment. However, the RSM is not well validated as the κ-ε model and their usage mainly depends on the type of CFD problem under consideration. Some studies made by Cokljat and Younis (1995) using RSM on open channel flows found good agreement with experimental results and very recently Kang and Choi (2006) also successfully predicted the mean and turbulent features of an open channel flow using RSM.

2.7.4 Free Surface Treatment

The evolution of the free surface boundary is not known *a priori* and needs to be simulated as part of the solution. The numerical solution of flow problems involving free surfaces requires:

(i) a method to numerically depict the location and shape of the boundary;

(ii) an algorithm for determining the time evolution of the boundary; and

(iii) a scheme to impose the desired surface boundary conditions on the surrounding computational mesh.

FLUENT® employs the Volume of Fluid (VOF) method to simulate the air-water interaction at the free surface. The VOF method developed by Hirt *et al.* (1981) is a type of interface-capturing method which relies on the fact that two or more fluids/phases are not interpenetrating and for each additional phase, a new variable - the volume fraction of the phase in the computational cell - is introduced. The time evolution of the elevation of the free surface is governed by the solution of a continuity equation for the volume fraction in the form (Fluent, 2005):

$$\frac{\partial \alpha_q}{\partial t} + \vec{u}.\nabla \alpha_q = 0 \tag{2.41}$$

where, α_q is the volume fraction and $\nabla = (\frac{\partial}{\partial x} + \frac{\partial}{\partial y} + \frac{\partial}{\partial z})$.

The volume fraction equation is not solved for the primary phase, but is based on the constraint that the volume fraction of all phases in each cell must sum to unity:

$$\left(\sum_{q=1}^{n} \alpha_q = 1 \right) \tag{2.42}$$

A single momentum equation is solved throughout the domain, and the resulting velocity field is shared among the phases. The momentum equation depends on the volume fractions of all the phases through the fluid properties, which are determined by the presence of the component phases in each control volume, e.g.,

$$\rho = \alpha_q \rho_q + (1 - \alpha_q)\rho_p \tag{2.43}$$

$$\mu = \alpha_q \mu_q + (1 - \alpha_q)\mu_p \tag{2.44}$$

where, subscripts p (air) and q (water) denote the primary and secondary phases respectively for the open channel flow modelling in this research. For an unsteady fluid flow, the cells currently filled with air provide the space for the water when the water level rises. Thus, this method allows free movement of the water at the interface.

2.7.5 Discrete Phase Model (DPM)

The movement of grit particles within the domain is done using a discrete phase model (DPM) approach. In this model, once the fluid flow field is established by solving the governing fluid flow equations, discrete phase (particles) are injected into the stream and their position is simulated by solving the force balance equation on the particle. The force balance equation is based on Newton's second law where all the forces acting on the particle equal the product of mass and acceleration of the particle. Hence, in addition to solving transport equations for the continuous phase, FLUENT® also simulates a discrete second phase in a Lagrangian frame of reference. This second phase consists of particles (which may be taken to represent grit, droplets or bubbles) dispersed in the continuous phase. FLUENT® predicts the trajectory of a discrete phase particle (or droplet or bubble) by integrating the (force balance/mass) on the particle, which is written in a Lagrangian reference frame.

This force balance equates the particle inertia with the forces acting on the particle, and can be written (for the x direction in Cartesian coordinates) as:

$$\frac{du_p}{dt} = F_D\left(u - u_p\right) + \frac{g_x\left(\rho_p - \rho\right)}{\rho_p} + F_x \tag{2.45}$$

where, F_x is an additional acceleration (force/unit particle mass) term, $F_D\left(u - u_p\right)$ is the drag force per unit particle mass given by:

$$F_D = \frac{18\mu}{\rho_p d_p^2}\frac{C_D \mathrm{Re}_l}{24} \tag{2.46}$$

and Re_l is the relative Reynolds number, defined as

$$\mathrm{Re}_l = \frac{\rho d_p \left|u_p - u\right|}{\mu} \tag{2.47}$$

Here, u is the fluid phase velocity, u_p is the particle velocity, μ is the molecular viscosity of the fluid, ρ is the fluid density, ρ_p is the density of the particle, C_D is the drag coefficient and d_p is the particle diameter. Frictional force is taken care by the *reflection* boundary condition discussed later in Section 4.3. Similarly, force balance equations can be solved in y and z directions respectively.

Other forces: Eqn. 2.45 incorporates additional forces (F_x) in the particle force balance that can be important under special circumstances. The first of these is the 'virtual mass' force, the force required to accelerate the fluid surrounding the particle, and is important when $\rho > \rho_p$. In the present study, this force is neglected as the density of the grit is greater than the density of fluid (water), its density being approximately 2.65 times the density of the latter. Similarly other forces such as forces due to temperature gradient and forces due to rotating frame of references are not significant in the present study and again are not taken into account.

A detailed methodology of the discretization of flow domain, numerical method, interpolation/discretisation schemes, boundary conditions employed, analysis of results and procedure of the overall computational modelling employed is discussed in Chapter 4 (Computational Modelling: Methodology).

3. EXPERIMENTAL METHODS AND RESULTS

This chapter discusses the methodology adopted in the physical modelling. The primary aim of the physical modelling is to establish benchmark experimental results of the system at different particle sizes and under varying flow rates in order to calibrate the computational model. The analysis of experimental results for different flow rates are then discussed in detail thereafter.

3.1 Physical Modelling in Fluid Mechanics

Like other physical sciences, fluid mechanics also has a sound and extensive mathematical basis. It is usually possible to formulate the differential equations of the various flow variables (like velocity, pressure or temperature) in such a way that a complete solution can be determined mathematically when the precise conditions are defined at the boundaries. Unfortunately, it is not always feasible to solve the governing flow equations without the support of experimental data in order to calibrate the computational model and it becomes even more difficult in the present study where very few experimental studies on grit removal from wastewater have been done using grit channels. Additionally, experimental fluid mechanics is considered to be a very useful technique not only as a method of solving flow problems, but also as a source of providing information for the improvement of theoretical analysis. It should be remembered that even when mathematical analysis cannot solve the problem, it may help to indicate which features of the flow are important. According to Bradshaw (1970) "*the experimenter's most useful tool is mathematics, and if he neglects to use it he is making just as big mistake as the theorist who takes no interest in experimental work*". Thus, both experimental procedure and mathematical modelling complement each other in solving fluid flow problems.

3.2 Theory of Similitude: Scale Considerations of the Grit Channel

In order to perform physical experiments in a laboratory, a prototype with large physical dimensions must be reduced in scale and despite the reduction (in scale), the model must behave in a similar manner to the prototype which it intends to emulate. Scaling laws for hydraulic physical models are derived from the concept of theory of similitude, which requires that the ratios of certain parameters between the prototype and model must conform to set mathematical conditions and like any typical hydraulics problem, similitude was achieved through dimensional analysis in the present study as well, whereby it was believed that the flow conditions in a physical model were similar to those in the prototype if the *geometric*, *kinematic* and *dynamic* similarities are obeyed.

A physical model to a reduced scale of the curved grit channel will be constructed in the laboratory in order to perform experimental investigations. A preliminary full-scale model has already been built by NWW Engineering (1995) installed at Fleetwood wastewater treatment plant. The required similitude properties between the model and the prototype are discussed below.

3.2.1 Geometric Similarity

Geometric similarity requires that the prototype to model ratios of all corresponding linear dimensions should be constant. The width of the channel was kept 130mm taking into consideration the range of velocities (~0.55m/s to 1m/s) allowed in the grit channel for efficient grit removal and available laboratory space. An approach length of 2000mm was kept before the bend which is more than 12 times the width of the channel in order to comply with the geometric similarity of the model and the prototype. Such a length was provided in order to allow settlement of the grit particles to the channel bottom before the bend as suggested by NWW Engineering (1995). However in practice this length can be made as long as possible depending upon the site conditions. The radius of curvature to width ratio of 12 and the angle of bend of 30° was also maintained as recommended by NWW Engineering (1995). The design guidelines were experimented with (Figure 3.1) in order to maintain the similarity hypothesis and to attain benchmark experimental data of

grit removal efficiency of the curved grit channel at different flow rates for the calibration of the computational model. It should be noted that NWW Engineering (1995) failed to publish the results of their work on channels in terms of grit removal efficiency at different angle of bend, sump configurations and radius of curvature in any quantifiable detail.

3.2.2 Kinematic Similarity

Kinematic similarity requires that the prototype to model ratios of length with respect to time (i.e. velocity) should be constant and thus, the flow velocity was kept the same in the model as in the prototype ranging from approximately 0.55m/s to 1m/s to avoid any kinematic dissimilarity. The settling velocities of various particles were also the same since grit particles of similar sizes (63μm to 2000μm) found in typical wastewater treatment plant were used during the experiments.

3.2.3 Dynamic Similarity

Dynamic similarity requires that the prototype to model ratios of all forces acting on the system should be constant and equal. In the majority of hydraulic models the dominant forces acting on the system are inertial, gravity, viscous and surface tension, which results in three dimensionless dynamic similitude numbers; Froude number, Reynolds number and Weber number (also see Section 2.2.2). Surface tension effects in open channel flows are seldom significant in comparison to the inertial forces in the prototype (Dingman, 1984) and therefore the Weber criterion may be neglected in most open channels and river flows. In the scaling of the prototypes in open channels, it is often impossible to satisfy the Froude and Reynolds scaling criteria simultaneously especially if the same fluid is used in both the prototype and the model because the Froude similarity requires $v_s = \sqrt{l_s}$; whereas Reynolds similarity requires $v_s = 1/l_s$, where, v_s is the prototype to model velocity ratio and l_s is the prototype to model length ratio. This obviously creates a difficult situation if trying to obey both the similarities simultaneously. So, to maintain the similarity between both prototype and the model, the

most significant force ratio is satisfied and thus open channel models are normally scaled with Froude similitude, since relaxation of the flow Reynolds number allows more flexibility in the model scaling (Peakall *et al.*, 1996). In Froude scale models, the Froude number is kept in the same *range* in the model and the prototype (Yalin, 1971). The flows under investigation are defined as subcritical, which requires the Froude number to remain below unity. To minimize the effect of viscosity in the model, and hence potential viscous scale effects, the Reynolds numbers are kept within the range of turbulent flow, where the viscous forces become independent of Reynolds number (Chanson, 1999), i.e. the flow regime is subcritical turbulent, requiring:

$$F_r = \frac{\bar{u}}{\sqrt{gR_h}} < 1, \qquad R_e = \frac{\bar{u}R_h}{\upsilon} > 12500 \tag{3.1}$$

where, $\bar{u}$ is the average velocity, υ is the kinematic viscosity, and R_h is the hydraulic radius. In addition, all the forces (drag, lift and buoyancy, etc.) acting on the particle would be equal as in a prototype as similar sizes of particles are used. It should also be noted that the removal efficiencies obtained on the site can be more than the efficiency obtained in the laboratory conditions as all the dynamic parameters are the same but geometrical parameters such as approach length are reduced. This discrepancy between full-scale and scale model was also obtained by NWW Engineering (1995) in some of their comparison studies between model and prototype.

3.3 Details of Physical Model

Experiments were conducted on a 30° curved open channel bend made of Perspex with a radius of curvature of 1560mm and a channel width of 130mm. The detailed layout along with the sump details of the curved channel is shown in Figure 3.1. The sump was strategically placed right after the end of the bend open at the inner half side of the channel bend (see Figure 3.1) to collect grit where it gets accumulated due to the secondary currents induced by the bend. Water was fed to the channel through a pump (Calpeda pump: max. 16.6l/s @ 6m head) connected to a water tank and water level

within the feeder tank was also kept constant in order to diminish minor variations which may occur due to change in water level.

3.3.1 Basis of Design

As open channel flow enters a bend, a secondary current, as shown in Figure 3.2 is generated causing a spiral flow within the channel (see Section 2.4.1) and due to this flow pattern the suspended grit is swept across the channel floor to the inside of the bend.

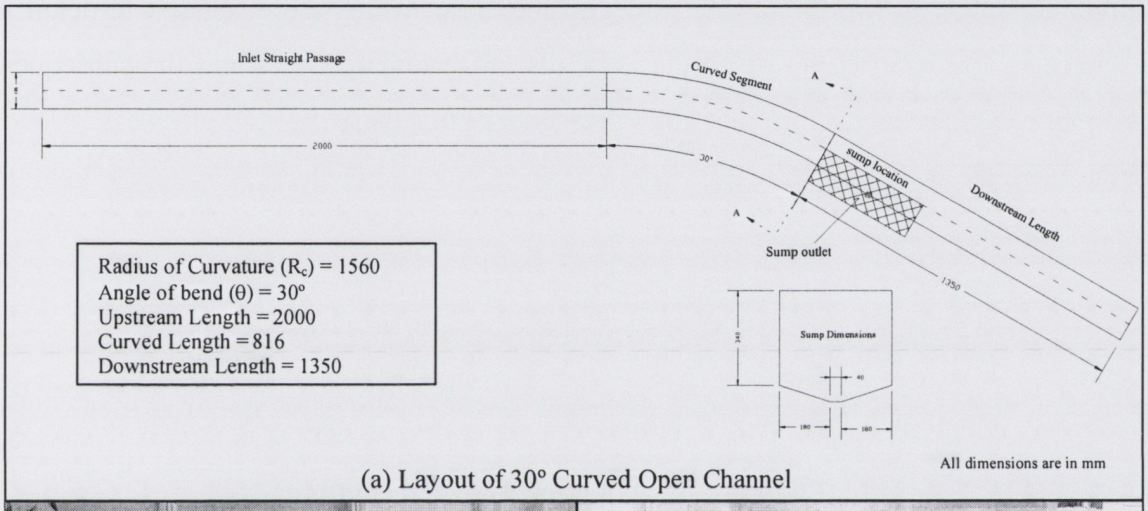

(a) Layout of 30° Curved Open Channel

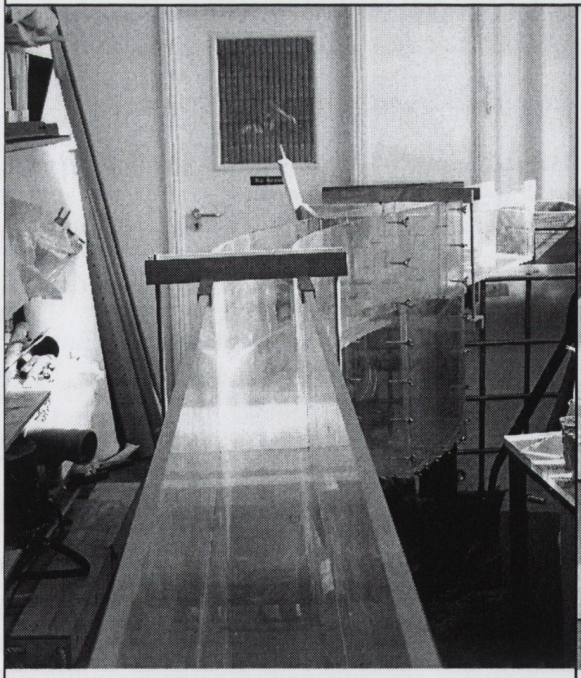

(b) View from Upstream

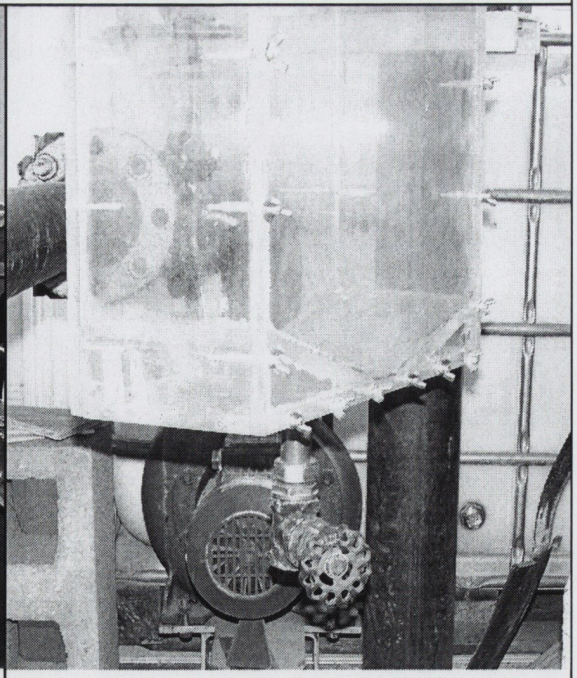

(c) Sump Details

Figure 3.1: Schematic Diagram of 30° Curved Open Channel

The angle of bend in the grit channel is kept such that the spiral upflow velocity on the inside of the bend is less than the settling velocity of the grit. Thus, as the flow takes the bend, the grit accumulates and rolls to the bottom inside corner of the channel from where it is removed via a port into a hopper, for subsequent pumped or mechanical removal. However, the strength of secondary flow depends upon many factors such as flow rate, velocity, width and radius of curvature, etc. which are discussed in detail in Chapter 5. The relationship of all these factors on secondary flows and the subsequent grit removal efficiency is the main aim of research of this thesis.

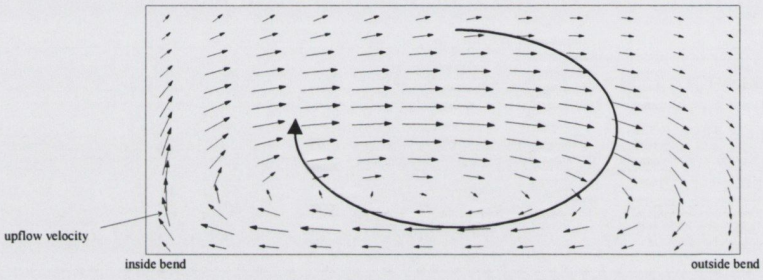

Figure 3.2: Secondary Flow Circulation
(Section A-A in Figure 3.1)

Some preliminary studies done by NWW Engineering (1995) suggested that the "*bendy channel*" is designed according to the maximum and minimum flow rates. They considered the main channel velocity to be a critical variable whereby a range of between 0.5m/s - 1m/s was desired suitable for both removal of the grit and to keep the grit moving within the channel. The width of the grit channels in the wastewater plant was based on the maximum velocity whilst the number of channels was determined by the minimum velocity. A depth to width ratio of about 1.1 at maximum flow was suggested so that the flow area varies with the flow rate and thus reduces the velocity variation which may then remain in the required range. Based on these investigations experiments have been carried out on a 30° bend and the grit removal efficiency was evaluated for three different discharges as presented in the next section. The bottom of the sump was kept at a slope to facilitate efficient removal of the grit once the experiment was complete.

3.3.2 Characteristics of Grit Particles

The objective of the physical experiments was to establish benchmark results of grit particle removal efficiency for different grit particle sizes under varying flow conditions. Experiments were carried out on three different flow rates: 4l/s (0.48m/s), 5l/s (0.51m/s) and 6l/s (0.54m/s). Natural sand was selected as a solid phase (grit) due to its particle size distribution and density resembling grit found in any typical municipal wastewater treatment plant. The density of natural sand is generally considered to be around 2650kg/m^3, although the specific gravity (particle density) for each category of particle size used in the experiments was measured (see Appendix A.3 for detail results) using specific gravity test (BS:1377, 1990) in order to provide precise input details for the computational model. The variation of measured particle density with size is shown in Figure 3.3. The settling velocity for each grit particle size is also shown in the secondary axis in the same figure which was calculated using Stokes' law as:

$$3\pi\mu v_s d_p = \frac{\pi}{6} d_p^3 \rho_p g - \frac{\pi}{6} d_p^3 \rho g \tag{3.2}$$

$\therefore$

$$v_s = \frac{d_p^2}{18\mu}(\rho_p - \rho)g \tag{3.3}$$

where, μ is the dynamic viscosity of the fluid (N-s/m^2), v_s is the settling velocity (m/s), d_p is the (grit) particle diameter (m), ρ_p is the particle density (kg/m^3) and ρ is the density of fluid (kg/m^3).

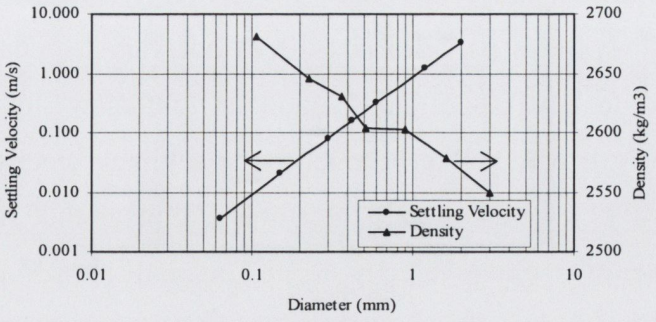

Figure 3.3: Variation of Particle Density with Settling Velocity and Particle Diameter

The grit sample was sieved into fractions of 0-63μm, 63-150μm, 150-300μm, 300-425μm, 425-600μm, 600-1180μm, 1180-2000μm and 2000-4000μm the normal diameter categories used for analysis of grit removal devices in treatment plants (Annen, 1972; Rupke, 1994). The grit particles collected on sieve size 63μm is considered to be in 63-150μm fraction and so on. It should be noted that the settling velocity (as it is calculated in stead of being measured) of various particles is plotted for lower range diameter values of 63μm, 150μm, 300μm, 425μm, 600μm, 1180μm and 2000μm respectively and the density is plotted for mid range values of 106μm, 225μm, 363μm, 513μm, 890μm, 1590μm and 3000μm respectively. During the computational modelling, density values are rounded-off on the higher side for various grit particle size (for example, for the particle range of 63-150μm, density measured is 2549kg/m^3 and as the CFD simulations were carried out using single particle size, density for 63μm is adopted as 2549kg/m^3. The detailed nature of grit and loading rates is already discussed in Section 2.6.1. It can be seen from the graph that the density decreases with an increase in the particle size which can be due to the two reasons. The first reason can be due to the definition of the particle density itself, i.e. the average mass per unit volume of the solid particle, where the volume could include any sealed voids within the solid particles. The second reason is that natural sand consists of particles which may originate from several different materials like anhydrite, quartz, peat, gypsum, etc. each of which may have weathered to typical sizes with slightly different material densities (Head, 1997). However, the measured density for various particles sizes does not vary to a large extent ranging between 2681kg/m^3 for the 63-150μm fraction to 2549kg/m^3 for the 2000-4000μm diameter fraction of grit particles respectively. The settling velocity however changes quite significantly with increases of up to three orders of magnitude from finer to coarser particles. The value of settling velocity for 63μm and 150μm particles is around 0.0036m/s and 0.02m/s respectively, making the particles of size (<=150μm) very difficult to remove during grit separation process (Metcalf and Eddy, 1991; Marais and Haandel, 1996). It should also be noted that the settling velocity of particles were calculated for a single size rather than range (for eg. 63μm instead of 63-149μm) and it

was based on the assumption that they are perfectly spherical in shape and in any typical grit sample, different shapes of particles might occur like angular, etc. and hence, the effect of shape factors for various particles is also taken into account in the computational model and is discussed later in chapter 5. Particle size distributions (PSDs) obtained for the various grit samples used during the experimental investigations are also shown in Figure 3.4 which indicates that the ranges of 0-63μm and 600-1180μm particles are lowest in terms of mass fraction. The distribution of the various mass fractions remained more or less consistent throughout the whole set of observations, except for small variations.

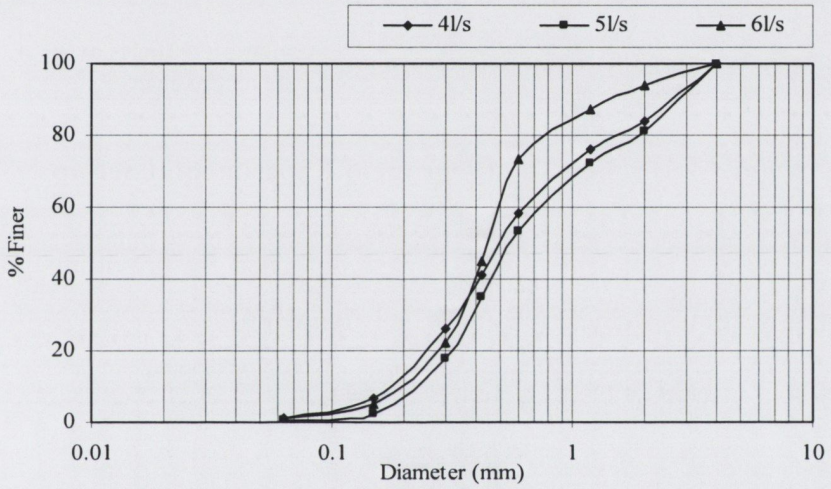

Figure 3.4: A Typical Particle Size Distribution

3.3.3 Experimental Procedure

A schematic layout of the experimental set up is shown in Figure 3.5. It can be easily observed from the figure that the test run was in the form of closed loop as the flow from the outlet was recycled back to the inlet tank. It should be noted that before allowing the grit into the channel, steady state flow conditions were allowed to establish within the system which was verified by measuring the flow rate using an electromagnetic flow meter (Xytec 7300, Buhler Montec) attached to the pipe which was feeding the channel through the (constant head) tank. This took approximately 5 minutes from the time the pump was switched on. The inlet tank was filled with small aggregates (20-40mm) in order to dissipate energy and to reduce the effect of turbulence at the channel inlet.

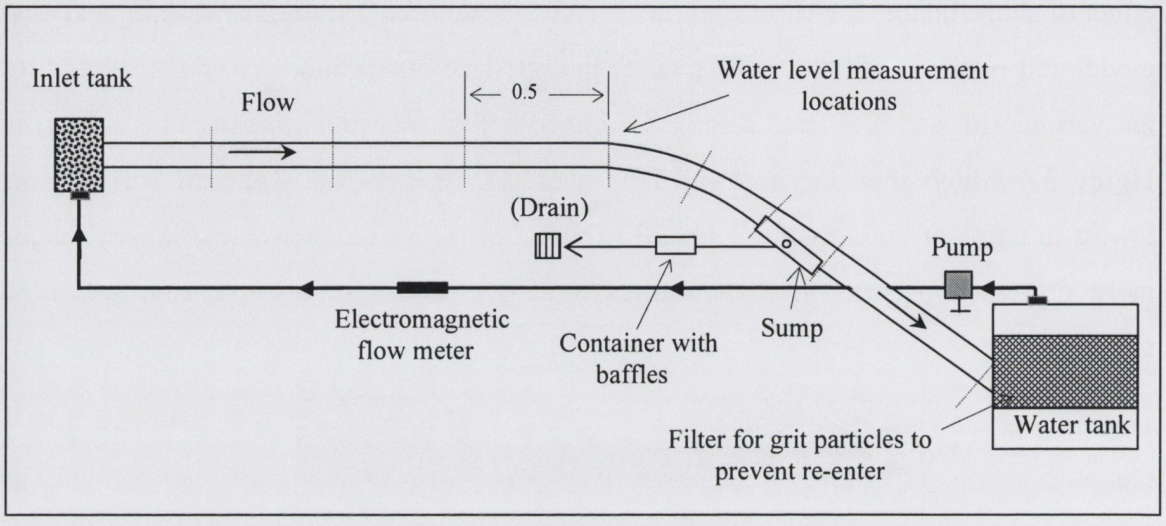

Figure 3.5: Schematic Diagram of Experimental Set-up

The flow towards the channel inlet was also smoothened by providing gradual curve towards the cross-section with a supple material (Figure 3.6).

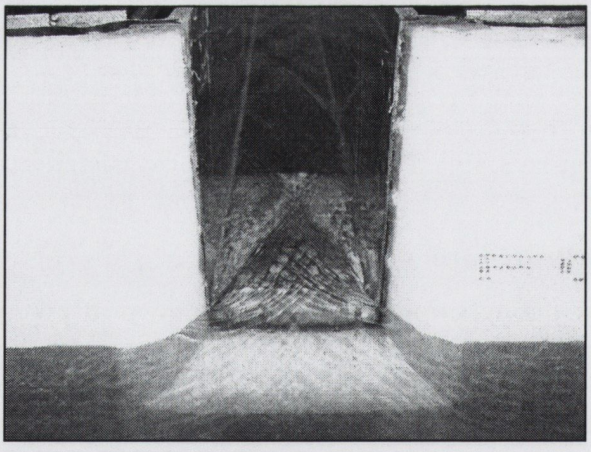

Figure 3.6: View from Upstream of the Channel Inlet

The water level measured at inside and outside bend at various locations for 4l/s (0.48m/s) is shown in Figure 3.7. It can be observed that the water level increases gradually from the inlet to the bend and then again falls towards the outlet. Once the flow moves round the bend, the water level at the outer bend tends to increase due to centrifugal forces. Each grit sample was washed and dried in the oven for 24 hours at 100°C before sieving so as to avoid dirt and foreign particles entering into the system.

The grit sample was (manually) added gradually and uniformly from the inlet of the channel in such a manner that the concentration of the solid phase was kept less than 10% by volume to imitate real flow conditions. This was ensured by recording the duration of time the known quantity of grit was added for each set of observation. The movement of grit particles was also investigated by means of digital camera, although they were not conclusive and some of the (instantaneous) pictures are shown in Appendix B. Once the experiment was over, the grit was collected from the sump and same drying and sieving procedure was carried out again to measure the collected PSD which allowed the final assessment of the particle removal efficiency to be made for each trial.

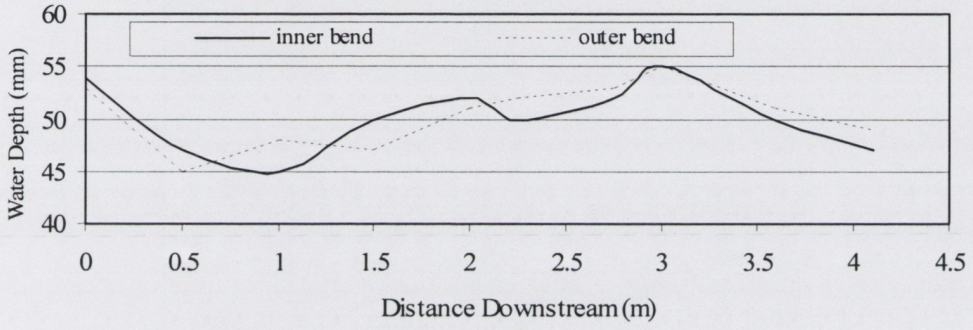

Figure 3.7: Measured Water Level at 4l/s

As stated earlier, the sump was placed at the inside of the bend in order to collect grit and a certain amount of flow is allowed from the outlet (of the sump) to allow extraction of grit from the sump. This process of allowing flow from the sump is also being employed in real situations for removal of grit from the sump (NWW Engineering, 1995). The performance of the grit channel was also assessed with the sump-open case. For the experiments conducted where the constant flow was leaving the sump the known flow rate was discharged from the sump into a funnel from its outlet which fed a plastic container with baffle plates (See Figure 3.8). Again, before inserting grit into the channel, steady state conditions were allowed to establish both within the main channel (measured by Xytec 7300, electromagnetic flow meter) and also from the sump outlet (measured by bucket and stop watch). The flow from the plastic container was then allowed to pass through 63μm or (63-150μm range) sieve before discharging to drain in order to avoid any escape of finer size particles. Introduction of baffle plates within the plastic container

clarifier aided in attaining error free results for sump-open trials. Preliminary trials were also carried out on the final clarifier (container) which proved that no particles <63μm were present in the flow and if there were any then they would be captured by the baffles and the sieve placed before the drain. Once the experiment was over, all the particles were allowed to settle down for approximately 15-20 minutes within the container and then finally collected into the baking tray and dried for PSD analysis.

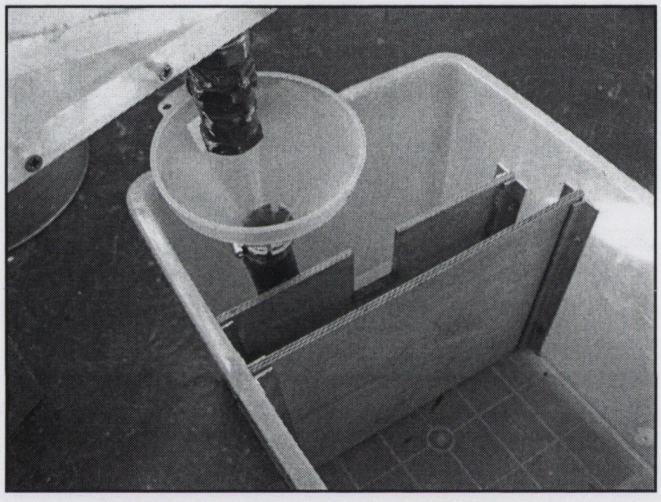

Figure 3.8: Outlet Arrangement for Sump-Open Case (Container with Baffles)

The experimental set-up is already shown in Figure 3.5 and the filter at the outlet of the main channel ensured that the particles (which were not captured by the sump) were not re-circulated into the main flow. Each set of experiments was repeated at least four times to minimize the effect of human error and random variations caused by sieve analysis.

3.4 Analysis of Results - Grit Removal Efficiency

3.4.1 Sump with no Flow

The grit removal efficiency of the curved grit channel with a closed sump at three different flow rates is shown in Figure 3.9. It should be noted that the efficiency results are plotted for all the ranges of the particles discussed in Section 3.3.2. The detailed experimental data for all the individual trials conducted are also shown in tabular form in

Appendix A.1. It should be noted that each set of experiments was repeated multiple times with the arithmetic mean value plotted on the graphs with their respective standard errors for the three different flow rates of 4l/s, 5l/s and 6l/s and all the trials were carried out with the composite grade. It can be seen that the maximum error range for most of the cases is not more than $\pm 5\%$ indicating the repeatability of the experimental procedure. The highest errors involved during experiments observed were for 150-300μm particles and the variation of standard error across the different particle sizes was observed to be quite random which can also be seen from graphs for the flow rates examined later. It should also be kept in mind that even minor fluctuations in the average flow could easily affect the removal efficiency for any particular grit size. These sort of variations for a single flow rate during multiple runs were also found by NWW Engineering (1995). The main outcome from these preliminary experiments is that the overall effiency to remove the grit particles decreases with the increase in flow rate. The effect of flow rate is relatively more on the particles of sizes (<=300μm) than for the coarser particles where the efficiency remains almost constantly at 100%.

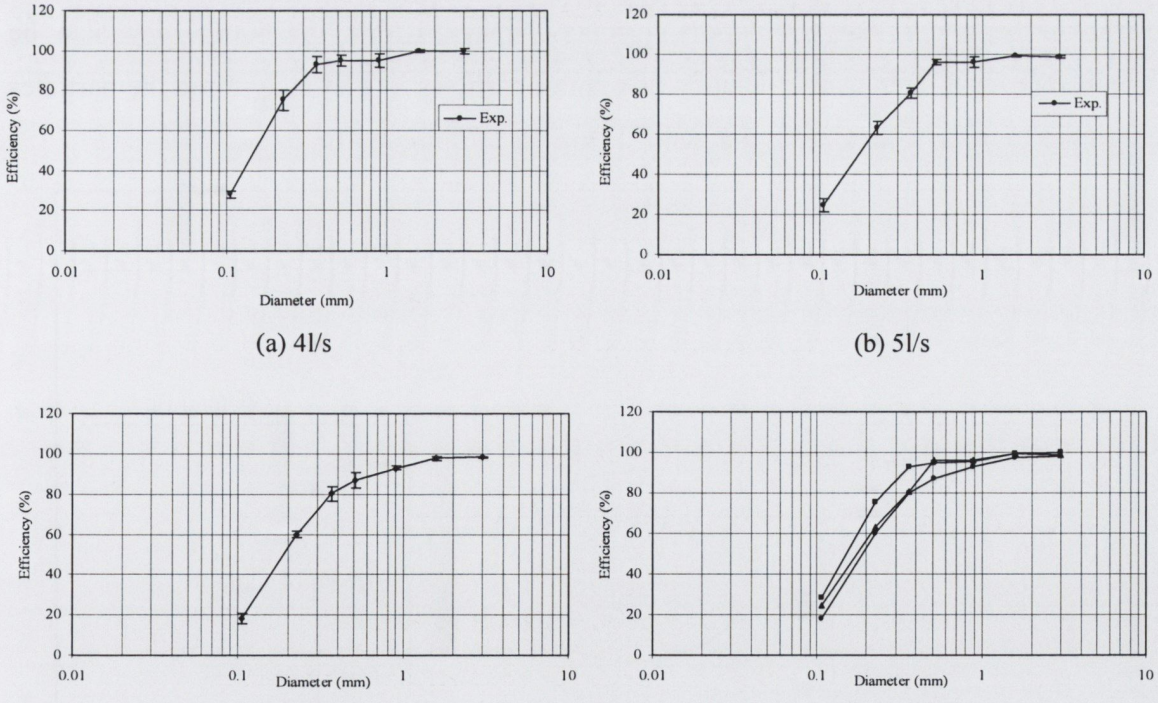

(a) 4l/s (b) 5l/s

(c) 6l/s (d) Combined

Figure 3.9: Variation of grit removal efficiency for a closed sump at flow rate (a) 4l/s, (b) 5l/s, (c) 6l/s, (d) Combined result

It should be noted however, that in no case the average value of 100% removal efficiency was recorded for any set of discharges for any particle size. The efficiency for the 63-150μm particle size varies from around 28% for 4l/s to 18% for 6l/s. This can be compared to the efficiency for the 2000-4000μm particle size which varies from 99.91% to 98.34% for 4l/s and 6l/s respectivley, indicating that smaller or lighter particles are more affected by the flow rate than the coarser or heavier particles. It should also be noted that there was no deposition within the main channel and all the grit particles were able to pass though the channel at all flow rates including 4l/s (0.48m/s). The graphs also suggest that the particle sizes between 63μm and 300μm are most sensitive to the flow rate for the curved grit channel. The variation within the particle range also seems to follow an almost similar trend for each set of flow rates with the least efficiency for the smallest particles and highest efficiency for the largest particles. Grit of size >300μm is not affected by the increase in the flow rate and their efficiency remains almost constant. It should be noted that circulation currents induced within the sump may also be responsible for the reduced efficiency of smaller particles as they may force the particles out of the sump to re-enter into the main stream (see Figure 3.10).

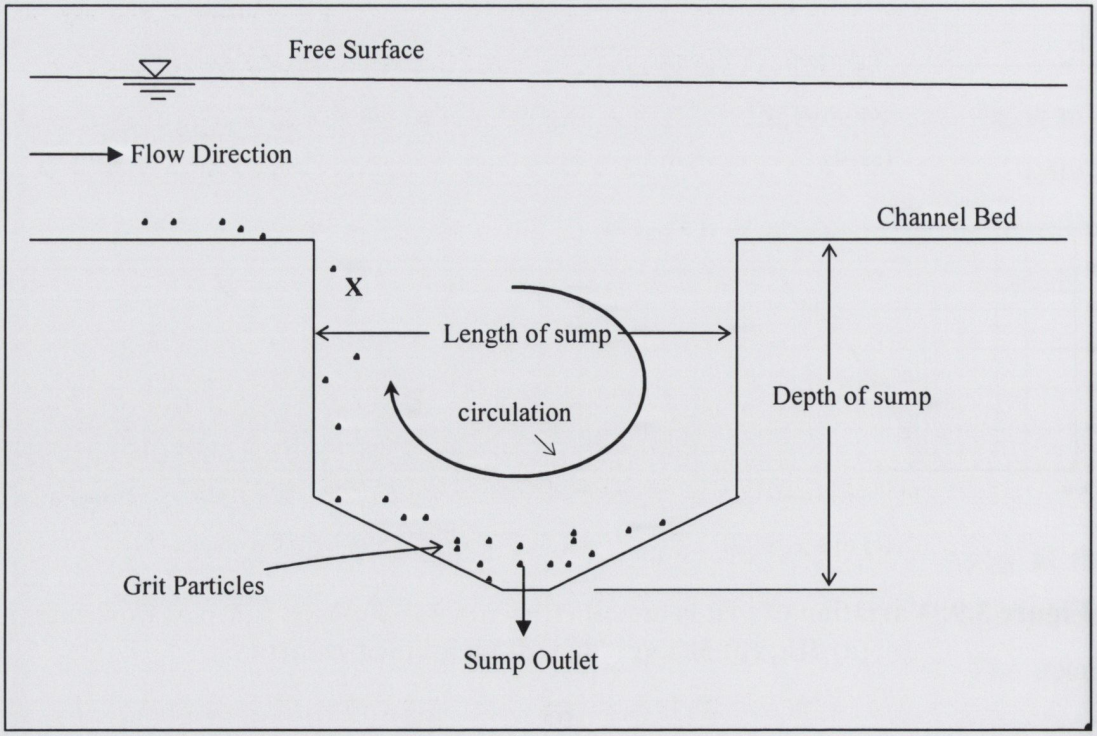

Figure 3.10: Outline - Grit Channel with Sump

This shows that the water in the main channel dragging over the quiescent sump, will generate a sump circulation as shown which is opposing the gravitational force acting on the particle within the sump (point X).

3.4.2 Sump with Flow

Allowing the flow out of the sump was thought to aid in increasing the grit removal efficiency as it will interfere with the circulation (within the sump) causing to reduce magnitude of the circulation and hence its effect on the grit particles. It would also be essential for the operation of a full-scale plant as the accummulated grit will have to be removed for disposals continuously. This was achieved by allowing a known quantity of water out of the sump of 0.1l/s to 0.45l/s for two different flow rates of 4l/s and 6l/s in the main channel. The overall particle removal efficiency graphs for different flow rates out of the sump are shown in Figure 3.11(a-g). Figure 3.11(a-d) represents removal efficiency for 4l/s and Figure 3.11(e-g) represents removal efficiency for 6l/s respectively again with their standard error values shown. Again, the efficiency obtained for different grit particles is shown in Appendix A.2 in tabular form. The graphs are shown for both individual cases with their respective standard errors and combined with the various flow rates out of the sump. It can be easily seen from the graphs that as the flow rate out of the sump increases, the removal efficiency increases for all the particle sizes especially those $\leq 300\mu m$. This confirms that the finer particle size range is relatively more sensitive than their coarser counterparts to the circulation currents within the sump, proving that they can be forced back out of the sump into the main flow due to the action of the current. It can also observed at a flow of 4l/s, that the effect of the flow rate out of the sump on removal efficiencies for particle sizes of 63-150μm and 150-300μm is more pronounced than at a flow rate of 6l/s: the removal efficiency increases from around 28% to 48% for 63μm compared to the same increases from around 75% to 95% for 150-300μm when the sump is kept closed and for flow rates of 0.45l/s from the sump respectively. However, it should be realized that the more flow allowed out of the sump the larger the downstream clarifier (and return of the water) needs to be.

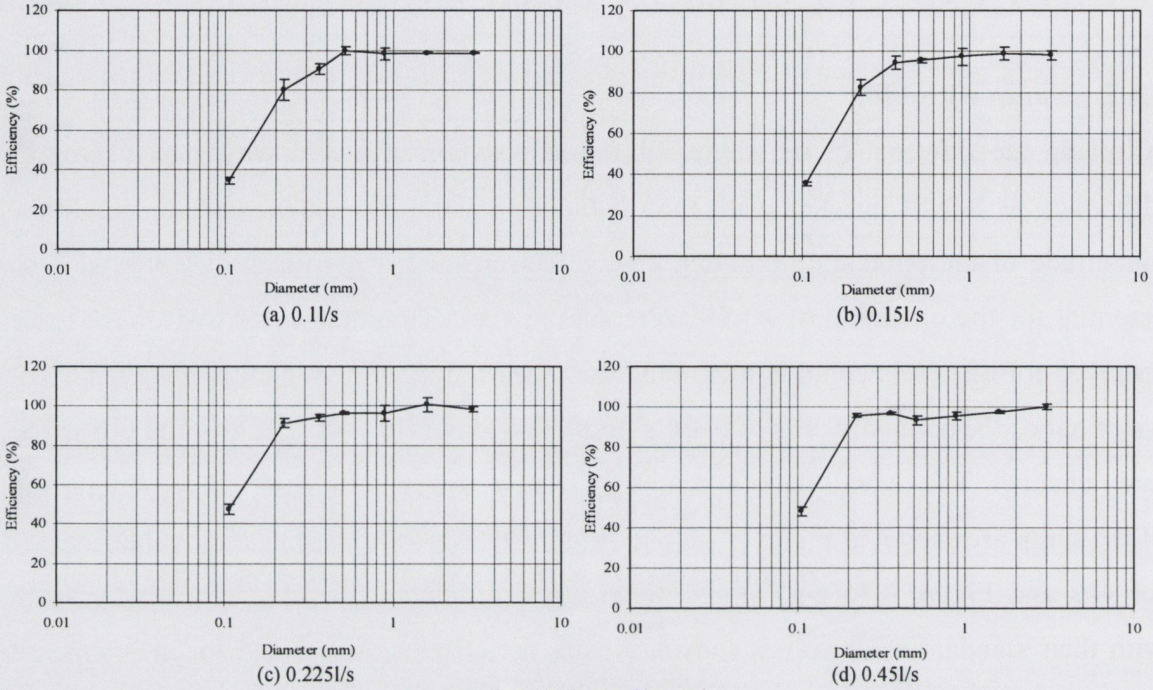

(a) 0.1l/s (b) 0.15l/s

(c) 0.225l/s (d) 0.45l/s

(a-d): 4l/s (Main Channel

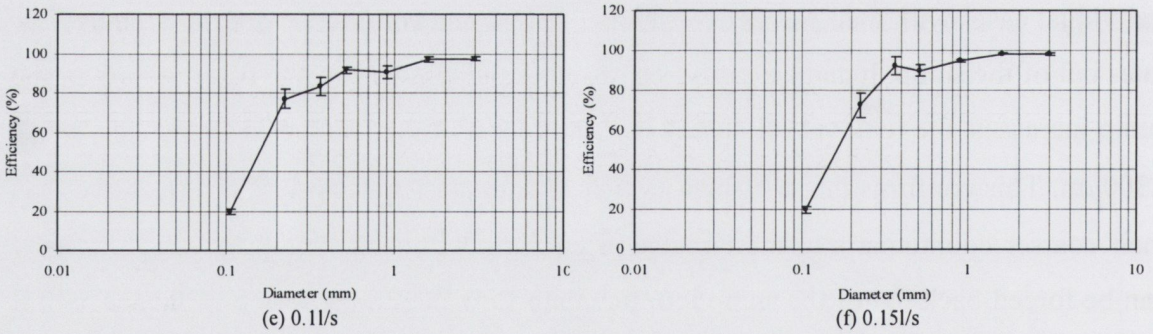

(e) 0.1l/s (f) 0.15l/s

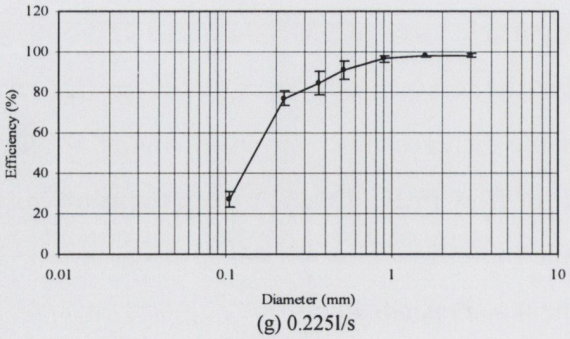

(g) 0.225l/s

(e-g): 6l/s (Main Channel)

Figure 3.11: Variation of grit removal efficiencies for channel flow at 4l/s and sump flow rate of: (a) 0.1l/s, (b) 0.15l/s, (c) 0.225l/s (d) 0.45l/s, 6l/s - (e) 0.1l/s, (f) 0.15l/s, (g) 0.225l/s

Hence, a balance is required in terms of economy of construction, operation and maintenance and so consideration needs to be given to how much flow should be allowed from the sump outlet, otherwise the handling problem of the effluent/wastewater becomes an additional issue to account for. In contrast, the effect of the sump outlet flow rate on removal efficiency for 6l/s for smaller particles of size ≤300μm does not appear to be significant. The reason could be that at higher disharges, a significant percentage of particles are not able to enter the sump in the first place and manage to escape out to the outlet of the main channel directly owing to the higher flow velocity within the main channel. It has already been shown that at the flow rate of 4l/s, the circulation within the sump is not a significant factor for the removal efficiency of larger particles, a trend which is also observed for discharge of 6l/s. The combined plots for 4l/s and 6l/s for different sump flow rates are also shown in Figure 3.12 (a, b). Hence, it can be concluded that the removal efficiency of the grit particles is dependent on both flow rate in the main channel and the induced curculation zone within the sump to a certain extent. Thus, based on the initial physical modelling results it can be concluded that the critical factors on which removal efficiency of different grit particles for a particular channel geometry depends are angle of bend, radius of curvature and width, particle size, flow rate or velocity in the main channel and circulation within the sump which is a function of the main channel flow rate.

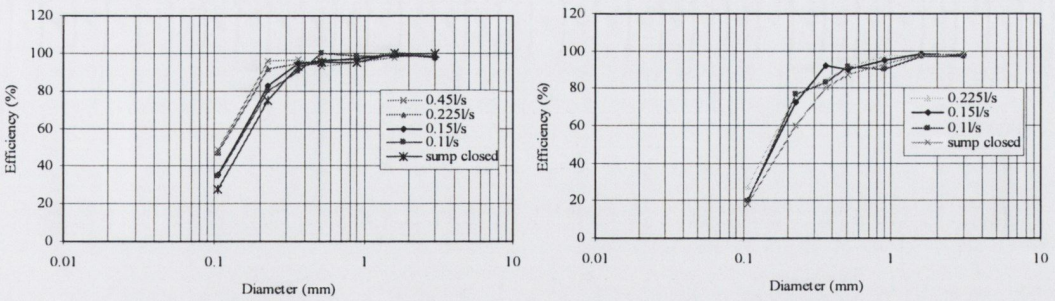

(a) Combined: 4l/s (b) Combined: 6l/s

Figure 3.12: Variation of grit removal efficiencies at different sump flow rates at channel flow rates of (a) 4l/s, (b) 6l/s

It was not possible to conduct all the experiments physically on different bend angles and radii of curvature due to time and financial constraints and thus based on these

investigations, a computational model was calibrated using the single geometry case and then further investigations or parametric investigations were carried out by modifying the computational model.

4. COMPUTATIONAL MODELLING: METHODOLOGY

This chapter discusses the methodology adopted in modelling curved grit channel flow using Computational Fluid Dynamics. The grid characteristics, boundary conditions, numerical method and interpolation schemes employed are presented in detail. Methods used for the post-processing of results and tracking final destinations/fates of grit particles within the channel domain are also discussed.

4.1 Overview of Computational Modelling: Theory

Chapter 2 provided the theory on mathematical formulation of governing equations of fluid flow, turbulence modelling and modelling technique for tracking free surface and discrete phase. This chapter continues the theme from Section 2.7 whereby the general methodology adopted during the computational modelling is developed here.

4.2 Construction of Flow Domain

The geometry of the curved open channel was created in *Gambit* (ver. 2.2.30), which is an inbuilt preprocessor in FLUENT® (Fluent, 2005). Figure 4.1 shows the isometric view of the channel generated in the software.

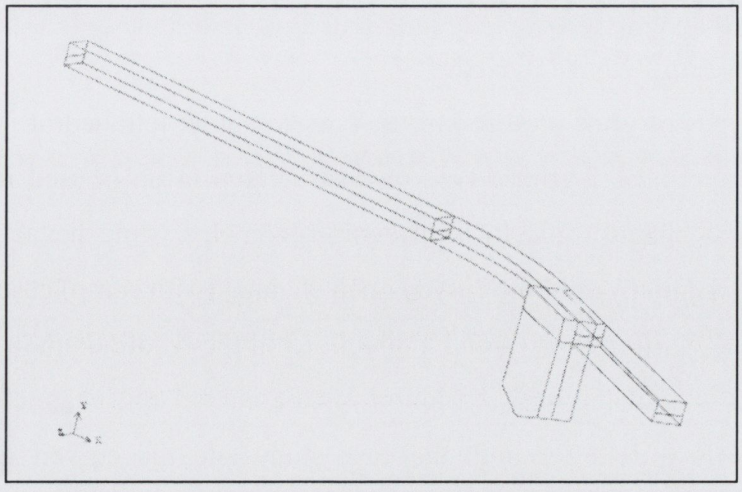

Figure 4.1: Layout of Generated Curved Open Channel Flow Domain (Gambit)

A bottom-up approach was used to generate the flow domain due to its irregular geometry in which first vertices are created and then from all the vertices, lines are joined and from these lines, planes and eventually the volumes are formed. As discussed in the Section 3.3, the flow domain consists of a 30° bend and a radius of curvature of 1560mm with the sump attached at the inside of the bend for the collection of the grit.

4.2.1 Domain Discretization

After describing the flow or solution domain, it was divided into number of non-overlapping control (finite) volumes using a computational grid. Boundary-fitted non-orthogonal grids were used to calculate the flows which are used by most of the commercial codes such as FLUENT®. Grid resolution is also an important feature while generating any computational grid and special considerations should be taken into account while selecting the grid size as a coarse grid consisting of a relatively small number of cells may not resolve all the characteristics of the flow, leading to inaccurate results. Also, resolving a very fine grid can take significant time in computations. However, it is also necessary to compare results for different grid resolutions to systematically evaluate the accuracy (Freitas, 1993) and demonstrate grid independent or grid-convergent results.

4.2.2 Grid Type and Characteristics

Two different types of grids are used in the present study: tetrahedral grid or t-grid and hexahedron (Figure 4.2). T-grid, a type of unstructured mesh is used in the case study (discussed in next chapter) due to its irregular geometry while hexahedron, a type of structured mesh is employed in the curved open channel (with sump) case. The spacing of the grids was kept uniform in x, y and z directions in the whole domain for all the cases analyzed. The details of the grid resolution for the curved grit channel are provided in Table 4.1. The flow field for both the case study and the curved grit channel was compared with different grid resolutions which enabled a reasonably good comparison to be made of different grids from the results. All the properties of the cells such as grid

skewness ratio or cell shape, and aspect ratio are well within their respective allowable limits in the flow domain as mentioned in Fluent (2005).

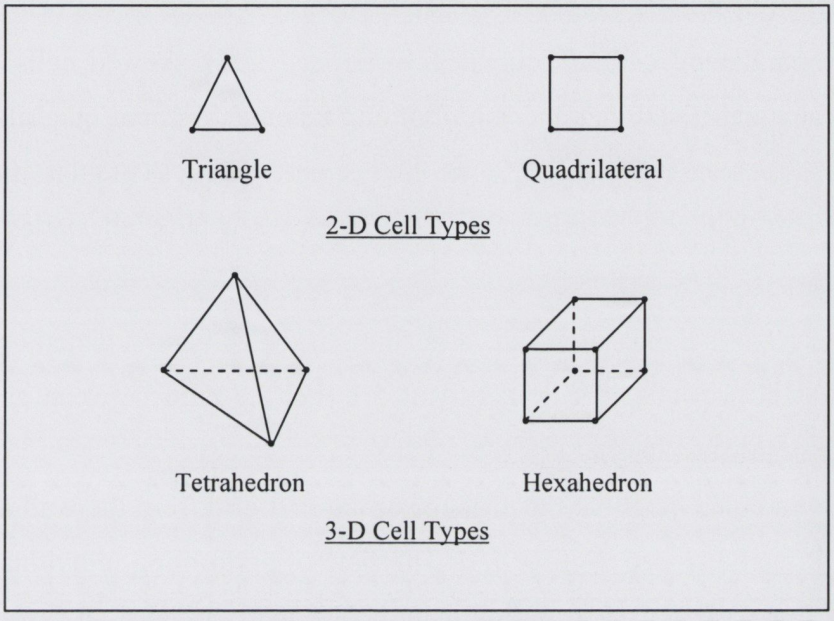

Figure 4.2: Cell Types

All the definitions of various cell properties and their allowable limits are presented below:

(i) Smoothness

Truncation error is the difference between the partial derivatives in the governing equations and their discrete approximations. Rapid changes in cell volume between adjacent cells translate into larger truncation errors. FLUENT® provides the capability to improve the smoothness by refining the mesh based on the change in cell volume or the gradient of the cell volume.

(ii) Cell Shape

The shape of the cell (including its *skewness* and *aspect ratio*) also has a significant impact on the accuracy of the numerical solution.

- *Skewness* is defined as the difference between the shape of the cell and the shape of an equilateral cell of equivalent volume. Highly skewed cells can decrease accuracy and destabilize the solution. For example, optimal quadrilateral meshes will have vertex angles close to 90 degrees, while triangular meshes should preferably have angles of close to 60 degrees and have all angles less than 90 degrees.
- *Aspect ratio* is a measure of the stretching of the cell and a general rule of thumb is to avoid aspect ratios in excess of 5:1 (i.e. the ratio between any of the two dimensions of the cell).

It should also be noted here that the distance of the first grid from the wall also complied with the wall functions (see Section 4.3). The time of performing individual simulations (~1500 iterations) varied from approximately two to four days on an *Intel Pentium* processor having 2.99 GHz of processing speed and 2 Gb Ram. As can be seen in Table 4.1, the number of cells for the G_{T1} type of cell (fine grid) was significantly higher (approx. 3 million) than the other cell types.

Table 4.1: Grid Spacing Details (Curved Grit Channel)

Grid Name	Spacing (mm)			Total No. of cells
	X	*Y*	*Z*	
G_{T1}	3	3	3	2924947
G_{T2}	4	4	4	1210110
G_{T3}	5	5	5	631408

This enabled an evaluation to be made that the results do not vary much when the grid was refined to approximately 4 times of the coarsest grid (G_{T3}). The case files with grid spacing type (G_{T1}) took a considerable number of days (>4) to finish the simulations under the convergence criteria of 0.0001 and thus, after comparing the experimental data with all the three grid types and confirming that the results obtained were grid independent, subsequent parametric investigations were done with 5mm spacing of the grid. Finer spacing in the longitudinal direction also ensured that the curvature within the

flow domain is properly approximated and all the flow features are properly simulated in detail not only in transverse directions but also in longitudinal directions. Figure 4.3 also confirms the extent of the grid uniformity in all the three directions within the flow domain.

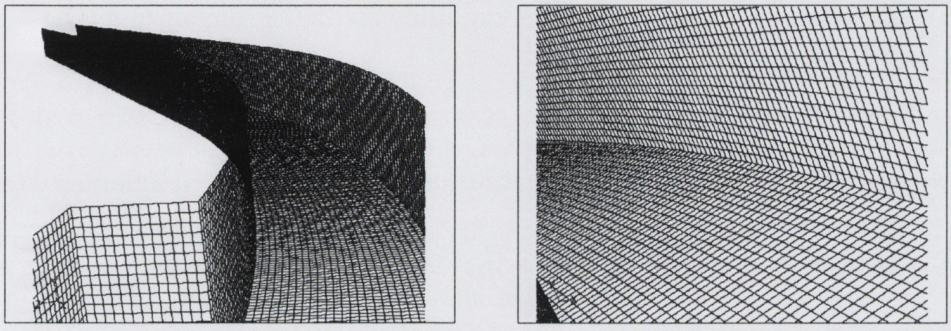

(a) View from downstream (b) Enlarged view (spacing 5mm)

Figure 4.3: Grid Resolution: Spacing (G_{T3})

4.3 Boundary Conditions

The boundary conditions employed for the flow domain are as follows:

(i) Inlet

A new boundary condition 'Open Channel' (available in FLUENT® (2005)) is defined at the inlet. Two separate inlets are defined for air and water with the same group ID (see Figure 4.4.). Mass flow rates are defined for both phases depending upon the velocity and the inlet area. The depth of the flow is known in advance from the experimental results which help in defining the free surface level before starting the simulations. The flow domain is initialized with the volume fraction of secondary phase (i.e. water) equal to 1 up to the free surface level. This procedure also helps in the rapid convergence of the problem. The volume fraction secondary phase (water) is also defined at this location as VF=1.

(ii) Outlet

The pressure outlet boundary condition is applied at the outlet. The pressure is kept at atmospheric pressure (i.e. gauge pressure = 0). Here also two separate outlets are kept for both the phases based on initial measured conditions with the same group ID.

(iii) Top Surface

The top of the water surface (above which is air) is initially kept at symmetry (a defined boundary condition). In this type of boundary condition, all the normal gradients ($\partial/\partial z=0$) and the normal components are zero. Once the solution stabilizes, the top surface boundary condition is changed to ambient pressure conditions to represent the real flow conditions more accurately.

(iv) Wall

The bottom and side surfaces are defined as *Wall* or no slip boundary condition. In this, study, the standard wall function has been employed (Launder and Spalding, 1974), which may be expressed as follows:

$$\frac{u_p u^*}{\tau_w / \rho} = \frac{1}{\kappa} \ln\left(E \frac{\rho u^* y_p}{\mu} \right) - \Delta B \tag{4.1}$$

Replacing $\frac{u_p u^*}{\tau_w / \rho}$ by U^* and $\frac{\rho u^* y_p}{\mu}$ by y^*, we get

$$U^* = \frac{1}{k} \ln(E y^*) - \Delta B \tag{4.2}$$

where,

$$u^* = C_\mu^{1/4} \kappa_p^{1/2} \tag{4.3}$$

$$\Delta B = \frac{1}{\kappa} \ln f_r \tag{4.4}$$

here, f_r is the roughness function that quantifies the shift of the intercept due to roughness effects, u_p is the mean velocity at point P, k_p is the turbulent kinetic energy at point p, τ_w is wall shear stress, μ is molecular viscosity, y_p is the distance from the wall, E ~ 9.79 is empirical constant and κ~0.4 is Von Karman's constant. ΔB depends on

the roughness of the material. The logarithmic law for the mean velocity is generally valid for $30 < y^* < 300$. In Fluent, the log-law is employed when $y^* > 11.225$. When the mesh is such that $y^* < 11.225$ at the wall-adjacent cells, Fluent applies the laminar stress-strain relationship that can be written as:

$$U^* = y^* \tag{4.5}$$

It should be noted here that there is no universal function valid for all types of roughness. For a sand-grain roughness (and other similar types of elements), however, ΔB has been found to be well-correlated with the non dimensional roughness height, $K_s^+ = \rho K_s u^* / u$, where K_s is the physical roughness height. Analysis of experimental data show that the roughness function is not a single function of K_s^+, but takes different forms depending upon on the K_s^+ value (Cebeci and Bradshaw, 1977). It has been observed (4.6a)

that there are three distinct regimes: (4.6b)

- Hydrodynamically smooth $(K_s^+ \leq 2.25)$ (4.6c)
- Transitional $(2.25 < K_s^+ \leq 90)$
- Fully rough $(K_s^+ \geq 90)$

In FLUENT®, the whole roughness regime is also subdivided into the three regimes, and the formulas proposed by Cebeci and Bradshaw (1977) are adopted to compute ΔB for each regime.

For the hydrodynamically smooth regime $(K_s^+ \leq 2.25)$:

$$\Delta B = 0 \tag{4.7}$$

For the transitional regime $(2.25 < K_s^+ \leq 90)$:

$$\Delta B = \frac{1}{k}\ln\left[\frac{k_s^+ - 2.25}{87.75} + C_s K_s^+\right] \times \sin\left\{0.4258\left(\ln K_s^+ - 0.811\right)\right\} \tag{4.8}$$

where C_s is a roughness constant, and depends on the type of the roughness.

In the fully rough regime $(K_s^+ \geq 90)$:

$$\Delta B = \frac{1}{k}\ln(1 + C_s K_s^+) \tag{4.9}$$

It should also be noted here that a fine grid resolution near the wall has been avoided by using the wall function which resulted in a significant reduction of the computational time.

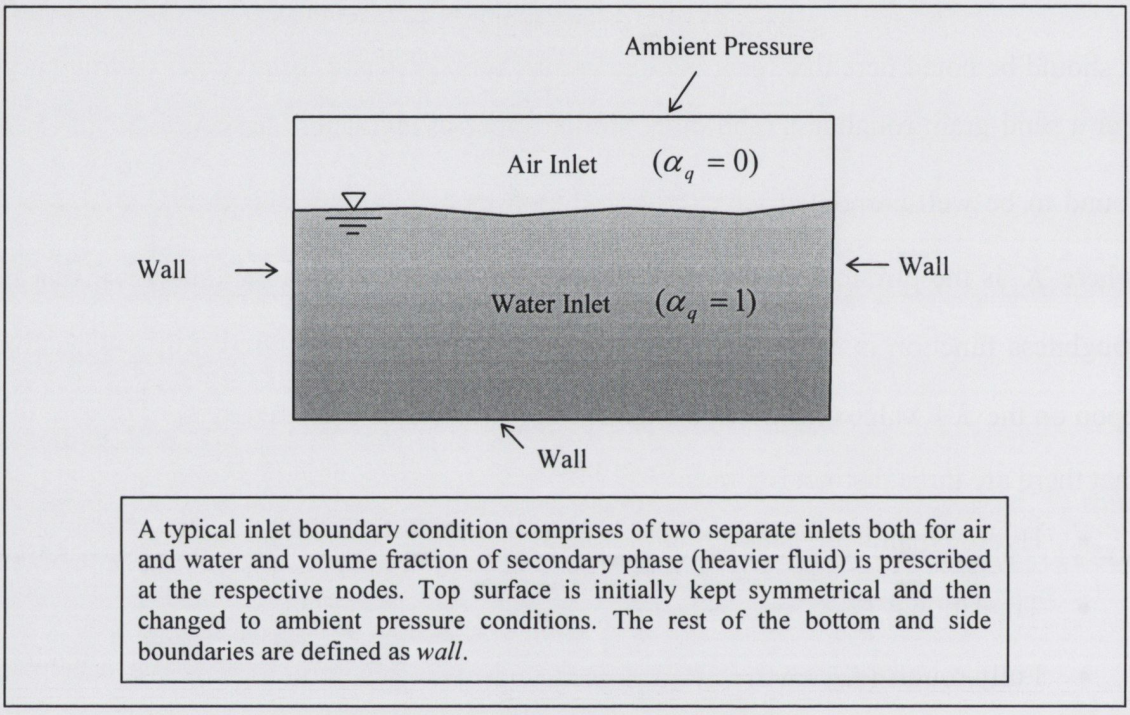

Figure 4.4: Boundary Conditions

(v) Discrete Phase Boundary Treatment

When a particle strikes a boundary face, several possibilities may arise like reflection, entrapment, and escape depending upon the type of problem being investigated and thus the following boundary conditions were employed while modelling discrete phase particles:

- Reflection - when a particle hits the wall or it's being reflected back into the domain. However, a limit can be set as to how long a particle can remain in the domain so its does not continue for an infinite time. All the walls in the curved grit channel were defined '*reflect*' boundary condition including sump wall. Here the friction due to the wall is taken care of by providing a coefficient of restitution (COF) for a grit particle hitting the Perspex wall. However, the collision was

treated as a perfect elastic collision and the computational results for different COF are given in Chapter 5.

- Trap - when a particle hits any boundary zone and if it's required that calculations should be terminated for that particle then the fate of the particle is reported as '*trapped*'. This boundary condition was not used in the present case.
- Interior - means that the particle will pass through the internal boundary. This option is available only for internal boundary zones.
- Escape - reports the particle as having '*escaped*' when it encounters the boundary in question and trajectory calculations are terminated. The main outlet of the channel was prescribed with '*escape*' boundary condition.

It should also be noted that, the density of different particle sizes were measured (Chapter 3) and accordingly different particles were created in the solver, each assigned a particular diameter and corresponding density value. The discrete phase was treated as a non-reactive or inert particle. The particles are injected from the inlet of the flow domain and are reported using a user defined function (UDF) as they hit a particular boundary such as outlet, wall or any interior zone. The UDF used to track the fates of various grit particles is discussed below:

This UDF was used to track the fates of various grit particles during CFD simulations. The particles were separated from each other based on their particle 'id', 'diameter' and their 'time of birth'. This was done because the particles were introduced in the domain at different time steps and as such each particle has a unique id and diameter but different time of birth so such UDF will help to analyze the particles in more detail.

```
/*********************************************************************
  UDF for specifying a DPM particles birth time
*********************************************************************/

# include "udf.h"


DEFINE_DPM_OUTPUT (pos, header, fp, p, t, plane)
{
 if (header)
```

```
  {
        fprintf(fp,"X, Y, Z, U, V, W, time of birth, time, diameter, particle id\n");
  }
 else
  {
   fprintf(fp,"%10.6g, %10.6g, %10.6g, %10.6g, %10.6g, %10.6g, %10.6g, %10.6g,
%10.6g, %d \n", p->state.pos[0], p->state.pos[1], p->state.pos[2], p->state.V[0], p-
>state.V[1], p->state.V[2], p->time_of_birth, p->state.time, p->state.diam, p->part_id);
  }
}
```

4.4 The Numerical Method

FLUENT® employs the Finite Volume (FV) method to solve the governing flow equations. It uses the integral form of the conservation equations as its starting point. The solution domain is subdivided into a finite number of contiguous control volumes (CVs), and the conservation equations are applied to each CV. At the centroid of each CV lies a computational node at which the variable values are calculated. Interpolation is used to express variable values at the CV surface in terms of nodal (CV-centre) values. The resultant linear algebraic equation system is solved using an iterative solver (TDMA) to provide updated values of the dependent variables at a central nodal point of each grid cell. The FV method can accommodate any type of grid, so it is suitable even for complex geometries. The grid defines only the control volume boundaries and need not be related to a coordinate system. The CV approach is based on the physical laws, rather than on the continuum physics (Roache, 1998). Thus an asset of the finite volume technique is the clear physical interpretation behind the discretized equation which constitutes a flux balance in a CV.

4.4.1 Interpolation Schemes

The algebraic form of the governing equations is obtained by approximating the partial derivative terms using interpolation or discretization schemes. This process often leads to discretization errors and even diffusion in the solver if not properly dealt with. Truncation or discretization errors are a consequence of algebraically approximating the partial derivatives in the governing equations in a discrete form. The fundamental finite-

difference approximations for partial derivatives are derived from partial Taylor series expansions. The truncation error is the result of neglecting the higher order or truncated terms. For a grid spacing Δx, the forward or backward difference approximation is first-order accurate, the central difference approximation is second-order accurate and the MUSCL (Monotone Upstream-Centred Schemes for Conservation Laws) scheme approximation is third-order accurate (Fluent 2005). Since the truncation terms in a finite difference method are of the order of Δx^n, the truncation error can be reduced by decreasing the grid spacing Δx. Thus, grid refinement can improve the accuracy of the solution to a large extent. Additionally, the order of the discretisation schemes can be used as a measure of their efficiency, since the power n of Δx determines the rate at which the error tends to zero as the grid is refined; for a refined grid the errors reduce more rapidly in a second-order accurate differencing scheme compared to a first-order accurate scheme (Versteeg and Malalasekera, 1995). In this study, the iterations were started with the first order interpolation (discretization) scheme, and then after few iterations (the initial number of iterations varied from case to case and hence no certain value can be defined here), the interpolation scheme was switched to higher (third) order so as to avoid any initial instabilities in the solution and simultaneously to obtain higher order accurate results (see Figure 4.6 later).

4.4.2 Calculation of the Flow Field

The flow field in the whole domain is obtained by calculating the velocity and the pressure field components from the governing equations for each control volume. The velocity field is calculated by solving the continuity and momentum equations. As these equations are coupled with each other, severe difficulties arise during their discretized formulation into linear algebraic equations. The major issue in calculating the velocity field is determining the pressure gradient, which forms a major part of the source term in a momentum equation, as there is no other equation for pressure. Patankar and Spalding (1972) introduced the SIMPLE (Semi-Implicit Method for Pressure-Linked Equations) method for the calculation of pressure on a staggered grid arrangement. This pressure-velocity coupling method enabled pressure to be introduced into the continuity equation

and bridge the velocity-pressure link enabling the pressure field calculation as part of the solution process. In the SIMPLE algorithm the discretized continuity equation is used to obtain an intermediate pressure correction equation. The SIMPLE algorithm uses these relationships between velocity and pressure corrections to satisfy mass continuity and to obtain, through iteration, the correct pressure field (Patankar, 1980). However, an additional pressure interpolation scheme is required since FLUENT® uses a collocated grid arrangement, whereby the pressure and velocity are both stored at the cell centres. The body-force-weighted scheme is employed in the present simulations as it is recommended for problems involving large body forces such as gravity, swirl or cariolis. (Fluent, 2005). This scheme computes the face pressure by assuming that the normal gradient of the difference between the pressure and body forces is constant. This works well if the body forces are known a priori in the momentum equations. This scheme enables a "staggered" grid to be generated such that the CV surrounds the face enabling the pressure on the face to be calculated.

4.4.3 The Segregated Solver

Fluent uses the segregated solver (solution algorithm) for solving the transport equations. In this approach, the governing equations are solved sequentially (i.e., segregated from one another). Because the governing equations are non-linear (and coupled), several iterations of the solution loop are required before a converged solution is obtained. Each iteration consists of the steps illustrated in Figure 4.5 and are discussed below.

(i) The fluid properties are updated based on the current solution. (If the calculation has just begun, the fluid properties will be updated based on the initialized solution.)

(ii) The u, v and w, and momentum equations are each solved in turn using current values for pressure and face mass fluxes, in order to update the velocity field.

(iii) Since the velocities obtained in Step 2 may not satisfy the continuity equation locally, a pressure correction is derived from the continuity equation and the linearized momentum equations. This pressure correction equation is then solved to

obtain the necessary corrections to the pressure and velocity fields and the face mass fluxes such that continuity is satisfied.

(iv) Wherever required, equations for scalars such as turbulence, energy, species, and radiation are solved using the previously updated values of the other variables.

(v) If inter-phase coupling is required, the source terms in the appropriate continuous phase equations may be updated with a discrete phase trajectory calculation.

(vi) A check for convergence (see Section 4.4.5) of the equation set is made.

These steps are continued until the convergence criteria are met.

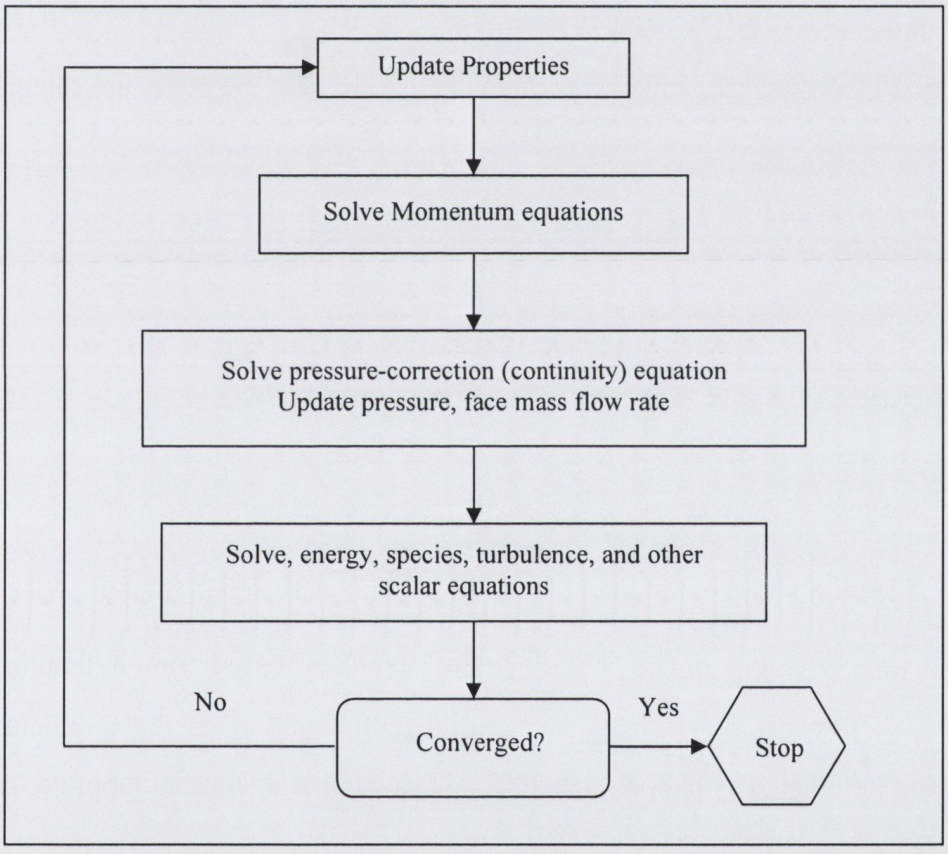

Figure 4.5: Outline of Segregated Solution Method (FLUENT®, 2005)

4.4.4 Initialization of Flow Domain

Before starting the simulations, the entire flow domain is initialized using appropriate fluid flow variable values and turbulent parameters. This practice also enabled

augmentation of convergence during the iteration process. The velocity, the volume fraction of the water phase and turbulence parameters are assigned to each node before starting the iterations. For the volume fraction, the following steps are incorporated:

(i) Initialize the entire domain by setting the volume fraction of the secondary phase to 0, and providing the inlet velocity.

(ii) Patch the domain using a volume fraction value of the secondary phase to 1, up to the *Free Surface Level* specified at the inlet.

(iii) Patch the inlet velocity again in the full domain.

In addition, the turbulence parameters which are initialized at the nodes are calculated as:

$$I \equiv \frac{u'}{u_{avg}} = 0.16(\mathrm{Re}_{DH})^{-1/8} \tag{4.10}$$

$$l = 0.07L \tag{4.11}$$

$$k = \frac{3}{2}(u_{avg} I)^2 \tag{4.12}$$

$$\varepsilon = C_{\mu}^{3/4} \frac{k^{3/4}}{l} \tag{4.13}$$

where, I is the turbulence intensity, u' is the turbulent fluctuation component, u_{avg} is average inlet velocity, Re_{DH} is Reynolds number based on hydraulic radius (characteristic dimension), l is the turbulent length scale, k is the turbulent kinetic energy, ε is turbulent dissipation rate and C_{μ} is an empirical constant (approx. 0.09).

4.4.5 Convergence Criterion

The convergence of the solver depends upon many factors such as grid size, interpolation schemes, and under-relaxation factors. Once the grid size and interpolation schemes are selected, convergence can be further accelerated by modifying the under-relaxation factors (URF). URFs are required in the iterative process to control the change of any flow variable, ϕ as the systems are nonlinear basically reducing the change of ϕ produced during each iteration. In other words, the new value of the variable ϕ within a

cell depends upon the old value ϕ_{old}, the computed change in ϕ, $\Delta\phi$ and the under relaxation factor α_r as follows:

$$\phi = \phi_{old} + \alpha_r \Delta\phi \tag{4.14}$$

The under relaxation factors used during the simulations are presented in Table 4.2. It should be also noted that the URFs shown in the table are the final UDFs and the reduction (or rate of decrease) in the respective URF values during the iteration process should be gradual (~0.05 to 0.1) for all the flow variables in order to ascertain the stability of the solver. The convergence of the solution is decided by the magnitude of the residuals after each iteration and clearly, if the residual decreases with successive iterations, the solution is considered to be converging. The residual criteria selected for this study was 10^{-4} for all of the flow variables (i.e. the summation of all the residuals for any flow variable should be less than 10^{-4}) which is desirable for complex flow problems (Patankar, 1980; Stern, *et al.*, 1999; Fluent, 2005). However, special attention is required in the assessment of the residual levels, especially if the computational domain is initialized with a reasonably good estimation of all the flow parameters (like velocity, turbulent kinetic energy, dissipation rate and volume fraction (if VOF model is used)). The residuals may not decrease by three orders of magnitude when the initial guess is close to the real or actual solution. On the other hand, if the initial guess is not close enough to the real solution, a three-order reduction in the residual does not certify the convergence. Therefore, it should be appreciated that residual levels depend not only on the absolute number (in terms of the magnitude), but also on the rate at which the iterative system converges. Thus, the present criteria of 10^{-4} for all the flow variables, ascertained that all the factors discussed above are taken into account during the simulations. Other factors with which the residual levels are judged are mass flow imbalance between inlet and outlet and monitoring of the water surface evolution of the flow domain. The monitoring of the same also ascertained the convergence of the solution.

Table 4.2: Under Relaxation Factors

Equation (Variable)	URF (Default)	URF (Employed)
Pressure	0.3	0.05
Momentum	0.7	0.1
Volume Fraction	0.2	0.02
Turbulent Kinetic Energy	0.8	0.2
Turbulent Dissipation Rate	0.8	0.2
Reynolds Stress	0.5	0.3

4.5 Outline of Modelling Procedure

The steps involved during computational modelling are briefly revisited in Figure 4.6. All the individual steps shown have already been discussed in the chapter and the figure gives an indication of how the modelling procedure has been divided into three main stages which are pre-processing, solver and post-processing. A few modifications during the solving process were made such as changing discretization schemes and URFs which proved quite effective in terms of stability of the iterative scheme. As Figure 4.6 depicts, the flow field is solved initially before injecting the discrete particles into the domain. Once the particles are injected, their fate (i.e. hitting any particular boundary zone in the domain) is recorded using a UDF already discussed earlier in this chapter and the analysis of results of the flow field and DPM are carried out thereafter.

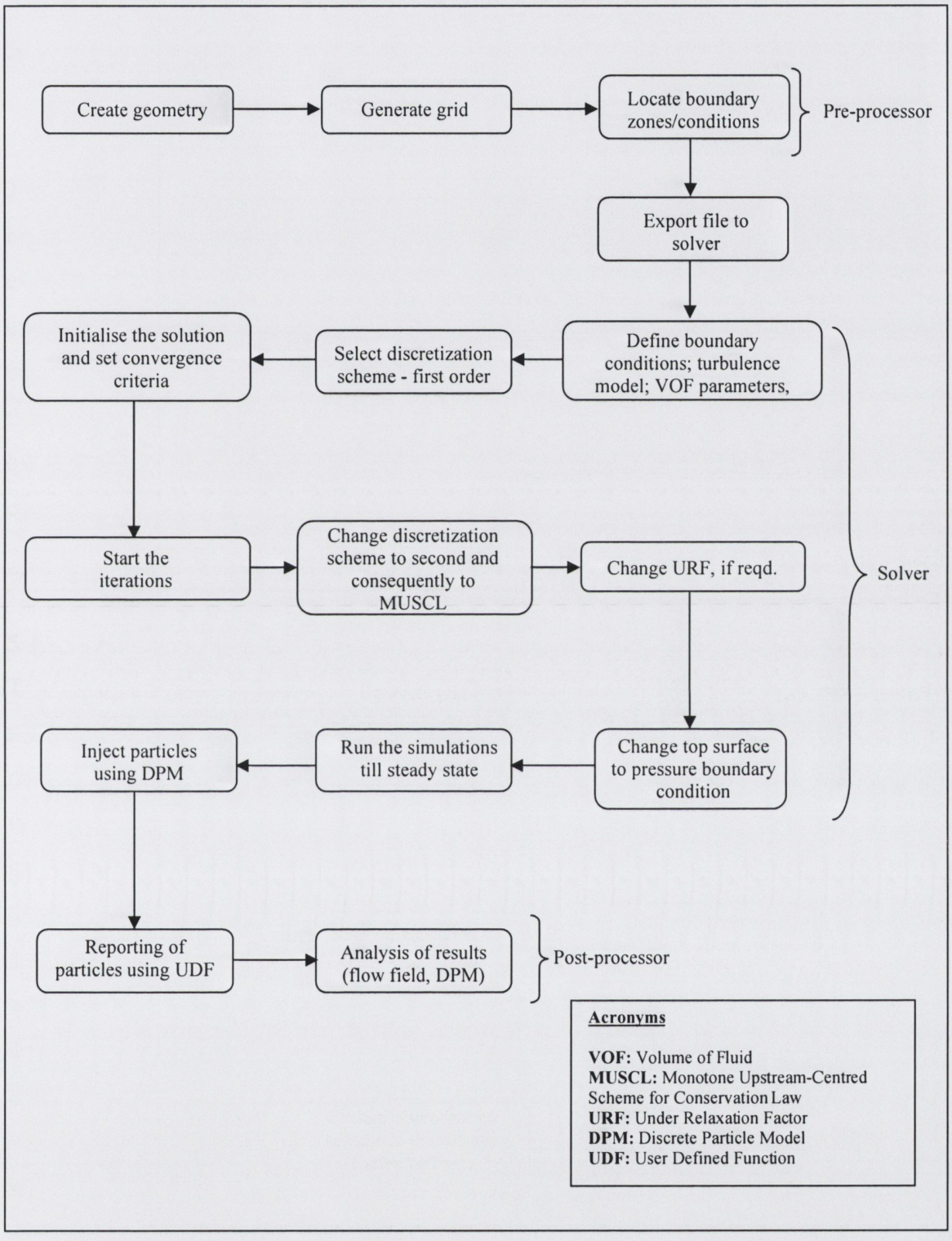

Figure 4.6: Flow Chart - Steps involved during Computational Modelling

5. CFD SIMULATIONS OF CURVED OPEN CHANNELS

The objective of this chapter is to present the detailed computational results which have been obtained using CFD. A validation of the computational model using the experimental data of a case study from literature is presented. This is followed by calibration of the computational model of the bend used in this study (Chapter 3) with the experimental data using DPM from which an analysis of the grit removal efficiency of the curved grit channel is made. Thereafter, detailed parametric investigations are done on the curved grit channel in which the effect of bend angle, flow rate and radius of curvature on secondary flows and grit removal efficiency is examined.

5.1 Case Study

The purpose of carrying out flow analysis of the case study was to find out whether secondary flows can be simulated using FLUENT® (a general purpose CFD software) or not. In the case study, an actual velocity measurement of the secondary flow phenomenon was obtained using an Acoustic Doppler Velocity Profiler (ADVP). Such an experimental investigation using ADVP was not possible for the curved grit channel studied in this thesis. This comparison with the experimental data also aids in the development of a methodology to model secondary currents using FLUENT® in curved channels which will be incorporated in the model for the curved grit channel.

CFD analysis was carried out on the 120° curved open channel experiment conducted by Blanckaert (2003). Figure 5.1 shows the geometrical layout and the cross-sectional details where the experimental data were taken. The hydraulic parameters for the fluid flow within the curved channel are also shown in Table 5.1. The test case was selected to model the real flow conditions which included variable bed topography (as found in nature) and, particularly due to its high resolution, experimental data of the velocity field which enables the computational model to be validated in detail. As stated earlier, the

modelling procedure adopted for the case study will also aid in developing a methodology which will be incorporated to model the curved grit channel flow, which is the main objective of this thesis.

Table 5.1: Hydraulic Parameters

Radius of Curvature	Depth of flow	Channel width
2m	0.114m	0.4m
Mean Velocity (u)	Discharge	Reynolds Number
0.38m/s	17l/s	67260

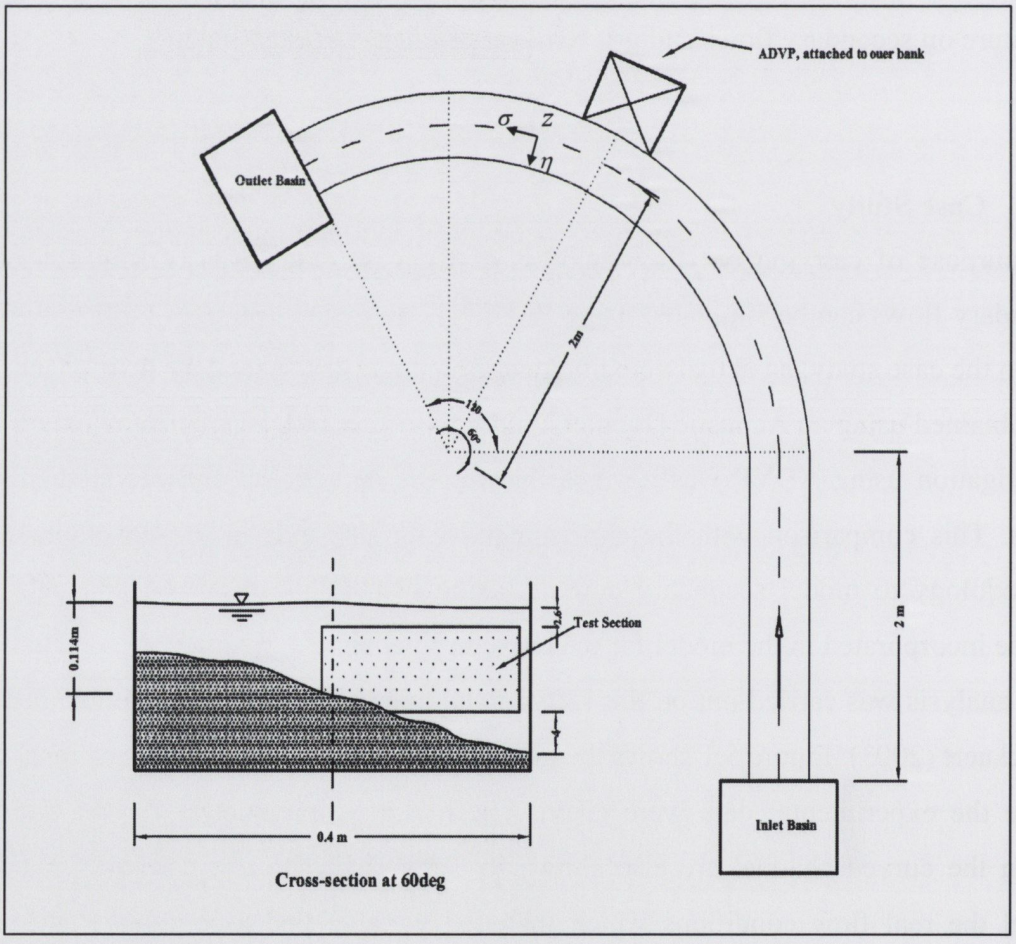

Figure 5.1: Geometrical Layout of the Channel

The experimental data were obtained at the outer half of the 60° section using the ADVP. The computations were performed on an adaptive grid using FLUENT® (2005). The

governing flow equations, as discussed in Chapter 4, are solved with the RSM turbulence model to simulate the fluid flow field. It should also be noted that the bottom of the cross-section was approximated in the CFD model as a straight slope (plane slope) and the (bottom) surface was assigned roughness height equal to ~1mm. It should be noted here that the unsteady solver is used only to get the steady flow results, and was not intended to obtain time-dependent solutions. Time derivative terms are discretized using the first order accurate backward implicit scheme. Convection terms are discretized using the third order Monotone upstream-centered schemes for conservation laws (MUSCL) scheme, while diffusion terms are discretized using the second order accurate central differencing scheme. However, before switching to higher order schemes, the iterations were started with the single order upwind scheme for stability (of the solver) purposes (Fluent, 2005). The pressure-velocity coupling is achieved using the SIMPLE algorithm which is discussed in Patankar (1980). As mentioned earlier, the VOF method has been employed to simulate the air-water interaction at the free surface. The VOF method, which was developed by Hirt *et al.* (1981), is a type of interface-capturing method which relies on the fact that two or more fluids/phases are not interpenetrating and for each additional phase, a new variable - the volume fraction of the phase in the computational cell - is introduced (see Section 2.7.4). This is the methodology adopted with all the subsequent simulations done on the curved grit channel. Numerical grids were constructed with the *Gambit* preprocessor available in the CFD package FLUENT®. The flow domain was divided into a number of non-overlapping unstructured (T-grid) meshes. The analysis was performed on two different meshes, whereby the total number of grid cells was 1,144,662 (G_{C1}) and 773053 (G_{C2}) respectively after grid adaptation. It should be noted here that the grid resolution of the case study is different than the grid characteristics discussed in Chapter 4 which are for the curved grit channel. All the boundary conditions are employed as already mentioned in Section 4.3. However, depending upon the hydraulic parameters, the initial conditions of the flow variables such as mass flow rate and turbulence parameters (κ & ε) will change and are calculated by the relations mentioned in Section 4.4.4. The initial simulations took a considerable amount of time (6-8weeks) to finish as such study of secondary flows using FLUENT® was never

been performed earlier and thus various factors were varied (such as the time step, discretization scheme, grid resolution, turbulence models, etc.) to evaluate their effects on the solution of the flow field. Initially, simulations were started with a very small time step of 0.001 seconds and then increased gradually to 0.1 seconds for the final solutions. Again, this was done to maintain stability in the solver. A comparison between the simulated normalized depth-averaged values for velocity and discharge and measured ones are presented in Figure 5.2 (a, b) for both of the grid resolutions. The figure also aids in understanding the flow behaviour in detail through the investigated outer half section. The value for normalized depth-averaged velocity (v_s) and normalized discharge (Q_{sn}) is calculated as:

$$v_{sn} = \frac{1}{h}\int_{z_b}^{z_t} v_s dz; \qquad v_s = v_{sn}/u \tag{5.1}$$

$$Q_{sn} = v_{sn} Bh/Q \tag{5.2}$$

where 'v_{sn}' is depth-averaged velocity, 'B' is width, 'h' is local depth of flow, subscript 't' and 'b' denotes free surface and bottom of the channel. It can be seen that the flow remained concentrated over the deeper part of the section and the majority of the discharge flows through the investigated half-section owing to the presence of secondary flows.

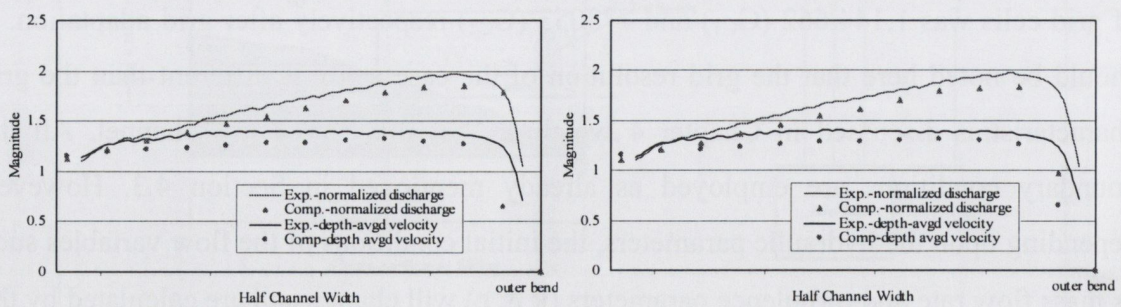

(a) G_{C1} (b) G_{C2}

Figure 5.2: Comparison between Experimental and Simulated Normalized Depth-Averaged Velocity (v_s) and Discharge (Q_{sn}) for two different Grid Resolutions (a) G_{C1}, (b) G_{C2}

However, the depth-averaged values of the downstream velocity remain almost constant throughout the outer half-section and reduce to zero near the side wall due to the presence of the boundary layer. Comparison between both the plots in Figure 5.2 also confirms that the simulated results are grid independent and minimal difference is found between the two different grid resolutions. It should be noted that the computational model under predicts the normalized values for velocity and discharge to some extent. However, the main features of the flow are very well simulated and overall a good agreement is found between both the experimental measurements and simulated results.

5.1.1 Secondary Flow Vectors and Longitudinal Velocity Contours

The comparison between the experimental and computational results for velocity vectors and contours is now presented. As discussed earlier, the simulated results are compared at the outer half of the 60° section. It should be noted that before switching to the RSM turbulence model, the solution is obtained with k-ε turbulence model. This process helps in better convergence and stability of the solution and will also enable a comparison to be made between the velocity field for both the turbulence models in detail. The measured cross-flow velocity vectors are shown in Figure 5.3(a) and the cross-flow velocity vectors (or secondary flows) simulated by k-ε model are shown in Figure 5.3(b) which is calculated as: $\sqrt{(v_\eta^2 + v_z^2)}$; where, v_η is the transverse component and v_z is the vertical component at the 60° section. The scale of the vectors is shown along with the figure. It should be noted that all the plots in Figures 5.3 and 5.4 are shown for the half channel width. It can be seen that the k-ε turbulence model is unable to simulate the outer bank cell but is able to generate the centre region circulation cell (secondary flow). This can be due to the fact that the k-ε turbulence model is based on the assumption of isotropic turbulence. The reproduction of the main circulation cell by the k-ε model also agrees well with the previous studies made by Rameshwaran *et al.* (2004a, b) and Ye and McCorquodale (1998). Figure 5.3(c) shows the cross-flow vectors simulated by the RSM turbulence model where it can be observed that the outer bank cell has been successfully captured and the main flow features are very well simulated. Contrary to the center-

region cell, the outer-bank cell has not always been observed either in previous experiments or computational studies on flows in channel bends. One of the reasons that it is not well documented may be because, in most previous investigations, the measuring experimental grid was too coarse and the accuracy was too low to measure these small velocities of the order of ~0.01m/s.

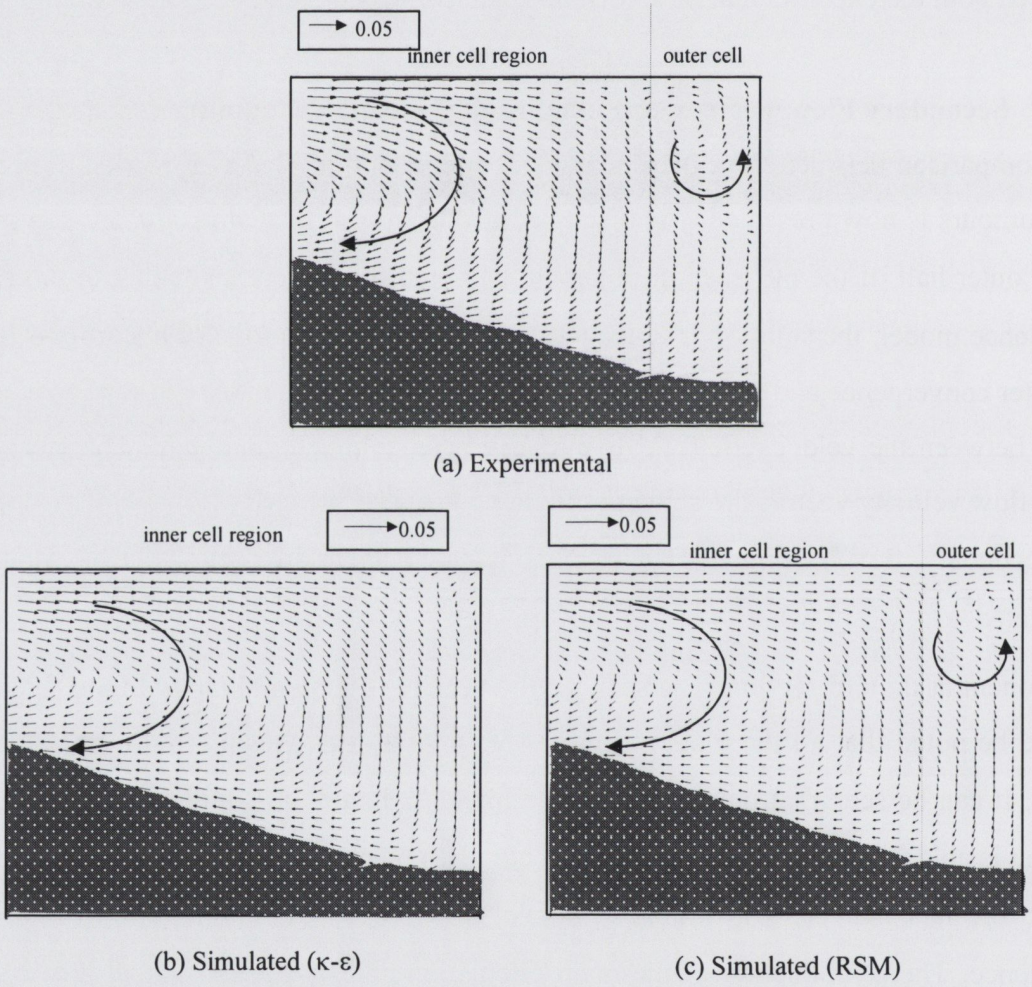

Figure 5.3: Secondary Flow Vectors for (a) Experimental, (b) Simulated κ-ε model and (c) Simulated RSM model

Furthermore, the outer-bank cell has an intermittent behavior and is thus difficult to visualize experimentally. However, the CFD results shown here are any particular instant and that instant was considered to be reached in steady state. It is only after time-averaging the measured data over long periods that it becomes discernible (Blanckaert,

2003). This outer bank cell acts as a protection to the outer bank as it keeps the maximum velocity contours away from the outer bank. The comparison of experimental results with computational ones also shows that the cross flow velocity vectors are a little under-predicted by the computational model; although all the flow features are reasonably well predicted indicating the suitability of the CFD software FLUENT® to simulate similar types of curved open channel flow domains. The comparison between predicted and measured longitudinal velocity contours is shown in Figure 5.4. The experimental contour plot shows that the maximum value is around 0.55 where the same value is 0.44 for the predicted plots by the computational model. The figure shows that the variation of the longitudinal contours is not symmetric and is shifted towards the outer bank owing to the presence of secondary flows. The location of the maximum velocity contour is also of interest and is found well below the free surface. The horizontal position of the maximum velocity contour is found at the intersection of both the circulation cells which agrees well with the experimental data. The longitudinal contour value decreases to zero near the wall due to boundary layer formation.

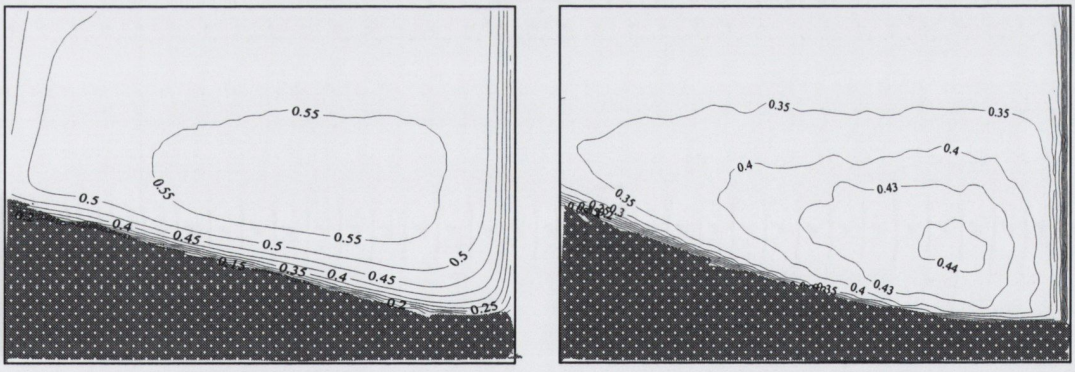

(a) Experimental (b) Simulated -RSM

Figure 5.4: Longitudinal Velocity Contours: (a) Experimental and (b) Simulated-RSM

Hence, based on the investigations it can be concluded that the case study has identified the approach to model secondary flows in curved channels and so the same methodology will be employed for the simulation of the '*curved grit channel*' using FLUENT®. The free surface was also successfully captured by the computational model and the water

level was observed to be higher at the outer bend compared to the inner bend. However, there exists a little discrepancy between the experimental and computational predictions due to high resolution at the air-water interface. The computational model was over predicting the water surface by approximately ~2mm at the 60° section (see Appendix B).

5.2 Curved Grit Channel: Analysis of Results

5.2.1 Secondary Flow Vectors and Longitudinal Velocity Contours

A computational model of the curved grit channel (Figures 3.1 and 4.1) was generated in order to simulate the flow field and movement of grit particles within the curved channel domain. The details of the computational model have already been discussed in the previous chapter and so are not repeated here. Figure 5.5 shows the simulated secondary flows and longitudinal velocity contours for the different grid resolutions (G_{T1} (finest grid), G_{T2}, and G_{T3}) for the flow rate of 4l/s.

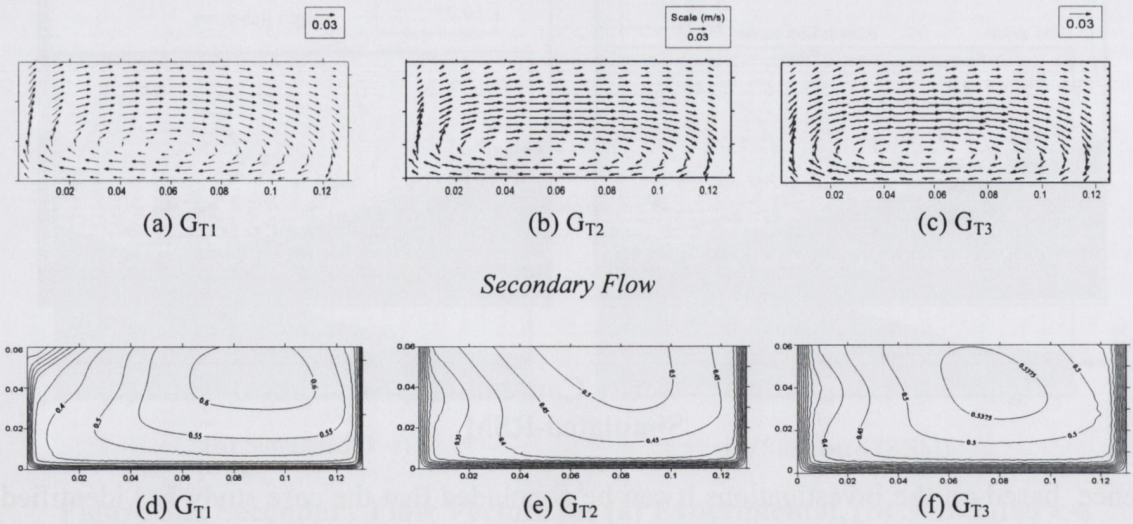

Figure 5.5: (a-c) Secondary Flows and (d-e) Longitudinal Velocity Contours for different grid resolution

It can be observed that the prediction of secondary flow vectors and velocity contours by all the three grid resolutions is almost similar. However, small variations exist between

the secondary flow vectors (see scale) for all the three different grid resolutions but these can be considered negligible. The same phenomenon can be seen for longitudinal plots where the velocity contours are skewed towards the outer bank owing to the presence of secondary flows. The maximum velocity contour varies from approximately 0.6m/s to 0.5m/s for all the three different grid resolutions and is present at almost the same distance from the outer wall (for all the three grid resolutions), indicating that the results are approximately grid independent. The free surface measurements were also verified using VOF model and the results are shown in Figure 5.6.

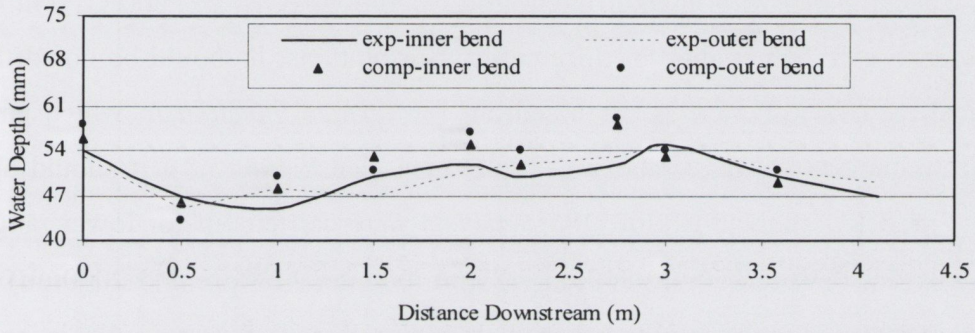

Figure 5.6: Comparison of Free Surface (Water level) with VOF Model (G_{T1})

It can be easily observed from Figure 5.6 that the main features of free surface evaluation within the curved grit channel is very well simulated where the water level rises at the outer bend. However, there exists a little discrepancy between the computational predictions and the experiments measurements and the computational over predicts the water level by approximately 10% throughout the channel. This can be due coarse grid size at the air-water interface and also because of discretization scheme for VOF model equation (FLUENT®, 2005). The water level for different angle of bend simulated with VOF model is also shown in Appendix B.

5.2.2 Sump with no Flow - Calibration of the CFD Model

Once, the flow field was simulated, the grit particles of known physical properties (diameter and particle density) are injected from the inlet of the channel into the domain in

order to learn their fates as to whether they are being captured by the sump or they escape directly to the main outlet of the channel. The grit removal efficiency (η) is calculated as:

$$\eta\ (\%) = \frac{\text{Total no. of particles retained within the system} * 100}{\text{Total no. of particles introduced}} \quad (5.3)$$

The calibration of the computational model was carried out at three different flow rates of 4l/s, 5l/s and 6l/s. The grit removal efficiency for 4l/s (or an average velocity of ~0.48m/s) is compared with three different grid resolutions (G_{T1}, G_{T2} and G_{T3}) in Figure 5.7 in order to establish results for different grid resolutions. It should be noted that all the particle removal efficiencies discussed are for *surface injection* in which particles were injected uniformly across the water inlet area (see Figure 5.8). It should also be noted that the CFD simulations for DPM analysis were carried out for lower range grit particles sizes of (63μm, 150μm, 300μm, 425μm, 600μm, 1180μm and 2000μm) rather than the whole range of particles between the respective sizes. However, in order to ascertain the accuracy of the CFD model, mid-range diameter values (106μm, 225μm, 363μm, 513μm, 890μm, 1590μm, 3000μm) were also simulated and are compared with experimental results in Figure 5.7(b). The experimental results are also shown for mid-range values of diameter through out the thesis. Figure 5.7 (a, b) indicates that the predictions do not vary significantly with different grid resolutions and also that the computational model is able to simulate the significant feature of the discrete particles very well whereby the grit removal efficiency of the grit channel increases with the increase in the diameter of the particle, as shown by the experimental results. Figure 5.7(a) also indicates that the computational model over predicts the removal efficiency for the particles <363μm to some extent. It was also confirmed that the mid-range diameter values analysis agrees well with the lower range diameter analysis and henceforth all the analysis and discussion will be shown for the lower range diameter values of 63μm, 150μm, 300μm, 425μm, 600μm, 1180μm and 2000μm. Figure 5.7(c) represents the relationship between different grid resolutions for the particle size of 63μm, 150μm and 300μm which indicates a good relationship between all the three grid resolutions. The relationships for the three grid resolutions are also shown along with the

figure. A straight line of slope =1 indicates a good relationship between the predictions of different gird resolutions. Figure 5.7 (c) indicates that the slope obtained for different grid resolutions were respectively 1.02, 1.02 and 1.04 for G_{T1}-G_{T2}, G_{T2}-G_{T3} andG_{T1}-G_{T3} respectively reconfirming that the results are almost grid independent and thus an efficiency prediction for different grid resolution does not change significantly.

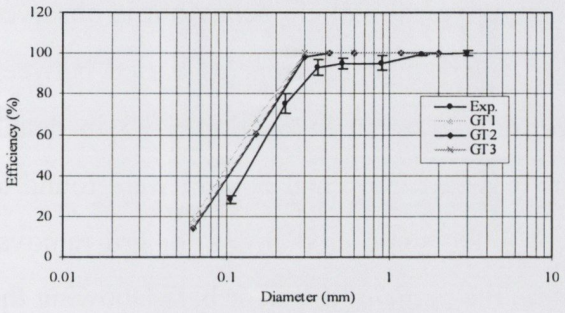

(a) Different Grid Resolution

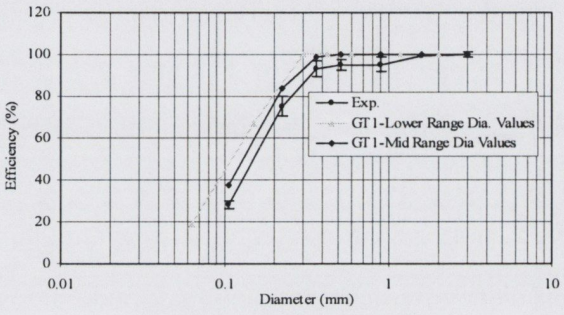

(b) Mid-range Dia. analysis

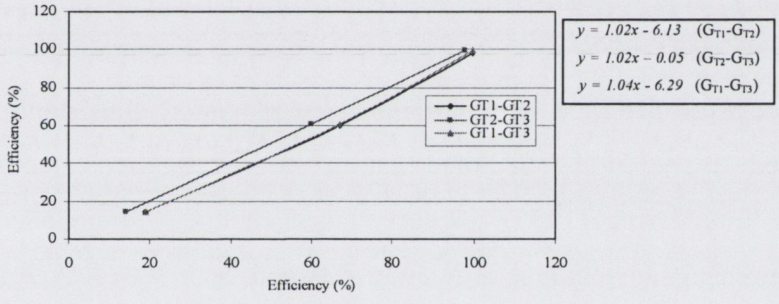

(c) Grid Independence

Figure 5.7: Grit Removal Efficiency, (a) Comparison of Computational predictions with Experimental Results for different Grid Resolution, (b) Mid-range diameter analysis, (c) Grid Independence

The difference between experimental and computational results may be due to the fact that the grit removal efficiency attained (especially for larger particles) for sizes ≥300μm during experiments should have been approximately 100% in the first place, but due to experimental errors, their removal efficiencies are measured as less than that and thus, the difference between the both is observed. This difference between the experimental and computational model may also be due to random variations such as minor flow fluctuations within the channel which are not controllable during the experiments.

However, for smaller particles of size ≤150μm, the difference is relatively higher than their larger counterparts. This over prediction by the computational model for these smaller particles remained consistent throughout during the comparison study in the curved grit channel. It should also be noted that, a typical particle behaviour is observed for the particle sizes of 1180μm and 2000μm where their efficiencies varied between 99.7% to 100%[1] - this behaviour will be considered again in Section 5.3.3 in detail. However, grit removal efficiency for particles of size 425μm and 600μm were found to be exactly 100%. The comparison also indicates that some predictions for grit removal efficiency by the computational model lie within the range of the error bars (showing the repeatability of the experiments) and the extent of accuracy with which the computational model was able to predict the behaviour of grit particles in the curved grit channel. It should be noted that the trend at which the computational model predicts the grit removal efficiency for different grit particle sizes remained consistent for all the flow rates analyzed. It should also be noted that on-site investigations (see Appendix A.5) done by NWW Engineering (1995) on curved grit channels found a considerable amount of differences in the removal efficiency between each set of experiments, confirming the difficulties in assessing the actual removal efficiency of such grit processes.

Before obtaining the final results of grit removal efficiencies (as in Figure 5.7), various parameters (like particle density, time step, friction considerations, injection location and shape factors) were also varied in order understand the effect of each parameter in detail and are discussed below. It should also be noted that particle tracking was done with flow coupling option available in FLUENT® (2005).

5.2.2.1 Effect of Particle Injection Location

The sensitivity of the discrete phase model (DPM) against the location of particle injection has also been verified as it could potentially affect the particle fates considerably, as pointed out by Stovin and Saul (1996). The effect of injection location becomes even more important in the present study of curved grit channel as the particles

[1] See Section 5.3.3 for details

injected from the bottom will hit the base sooner than their top counterparts and have more probability of being captured by the sump. However, the amount of particles accumulated by the sump will also depend on the inlet length of the channel (before the bend). The effect of the length of the inlet section will be revisited later in Section 5.6. Figure 5.8(a, b) shows the different locations from which particles were injected during the simulations. Figure 5.8(a) represents '*point*' and '*line*' injections and Figure 5.8(b) represents '*surface injection*' for which the particles were injected uniformly across the inlet cross-section.

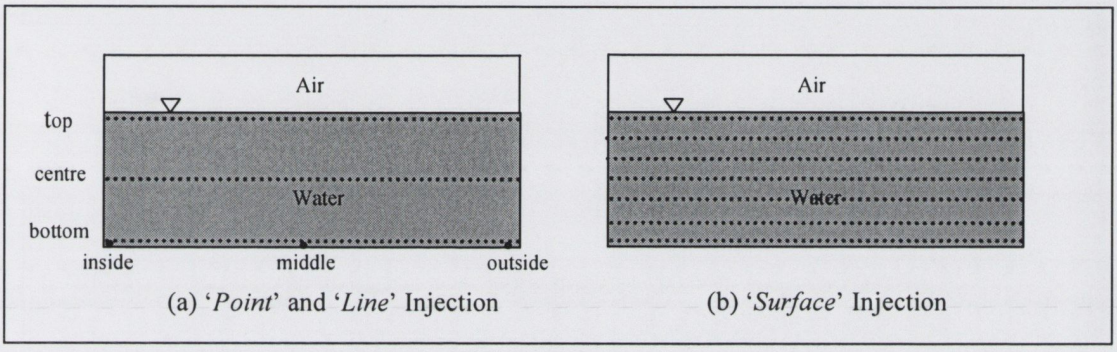

Figure 5.8: Particle Injection Location (a) *Point & Line*, (b) *Surface*

The sensitivity of the DPM to the particle injection location was established by injecting particles at different horizontal segments which were named as top, centre and bottom (depending upon their vertical locations) and as inside, middle and outside (depending upon their individual horizontal locations). Apart from the location of the particles, various other authors (Stovin and Saul, 1996, 1998, 2000; Faram and Harwood, 2003) have also suggested that a large number of particles are required to be injected in order to avoid any effect of random variations and also to obtain representative particle fates. Thus, on the basis of previous studies and considering the nature of the present study, a minimum of 5000 particles were injected for each set of simulations. In the case of '*line*' injections, a group of 50 particles were injected 100 times for each horizontal strip and for the '*point*' injection, a single particle was injected (5000 times) from the bottom of the inlet (see Figure 5.8) in order to establish a detailed comparison between different

locations. Figure 5.9 shows the variation of grit removal efficiency at various locations for different grid resolutions for a flow rate of 4l/s.

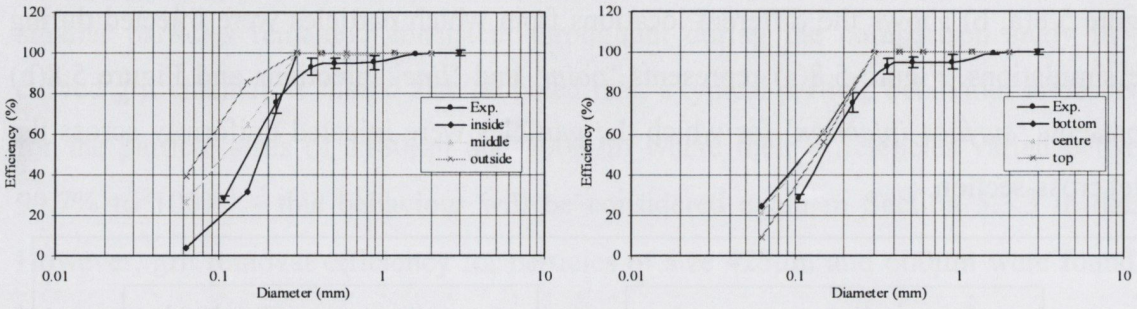

(a) Point Injection (b) Line Injection

(a, b) Grid-G_{T1}

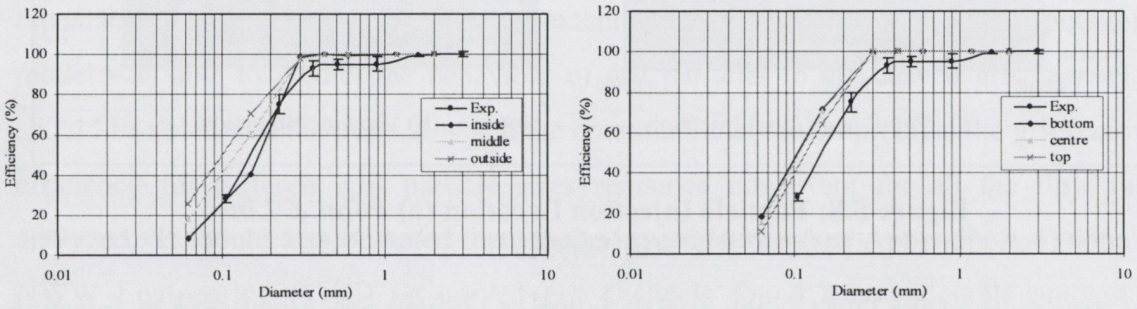

(c) Point Injection (d) Line Injection

(c, d) Grid-G_{T2}

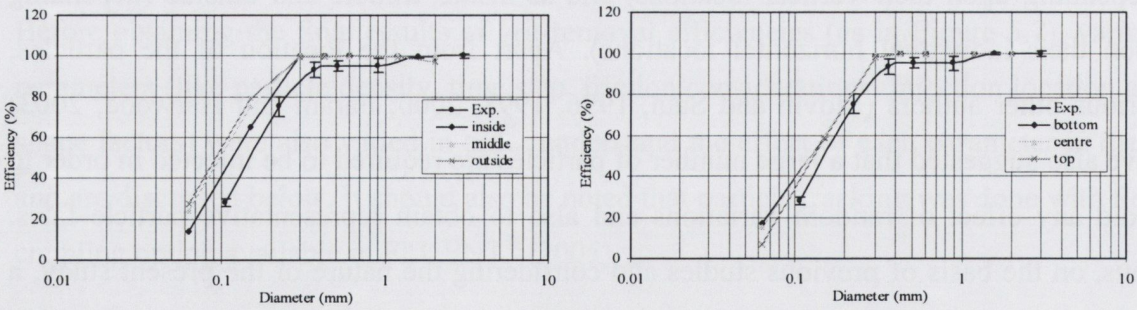

(e) Point Injection (f) Line Injection

(e, f) Grid-G_{T3}

Figure 5.9: (a-e) Grit Removal Efficiency – Particle Injection Location

It can be easily seen that for the '*line*' injection, particles which were injected from the bottom of the inlet demonstrate a comparatively better grit removal efficiency especially for particles (≤300μm) than the particles injected at the centre and top indicating that the grit removal efficiency can be a function of the injection location in a computational

model. Again, the results obtained for grit removal efficiencies for various injection locations are grid independent. An interesting phenomenon is observed for the analysis with '*point*' (Figure 5.8a) injection where the particles (of size ≤300μm) which were being injected from the inside of the bend have the lowest grit removal efficiency compared to their corresponding outside and centrally located ones. This may be due to the fact that these particles are already present at the inside of the bend and as soon as they reach the bend they have more probability of getting lifted by the uplift velocity of the secondary flow than the particles which are being injected from other locations (the middle or outside) and are thus not captured by the sump. This phenomenon is clearly seen in Figures 5.11 & 5.12 where the particles injected from the inside, strike the 30° plane at relatively higher vertical distances (shallower depths). This was done using DPM analysis (DPM output files) in which particles hitting any particular plane are recorded with respect to their *x*, *y* and *z* co-ordinates.

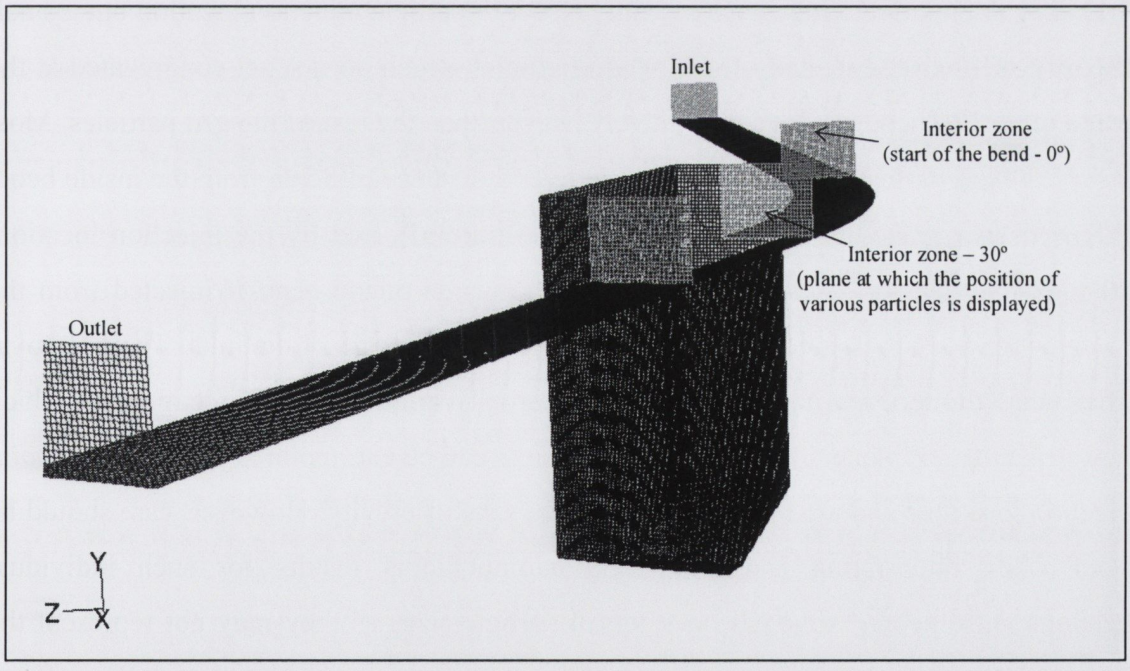

Figure 5.10: Curved Grit Channel Domain showing the plane at 30° Section

Figures 5.11 (a-e) and 5.12 (a. b) represent the scatter plot which shows the locations at which different particles strike the 30° plane which is situated just before the sump. It

should be noted that the vertical scale for the various particle sizes has been adjusted accordingly in order to visualize the behaviour of particles in detail and for better comparison between the different particles. The different locations (Figure 5.11a-e) at which the individual particle strike the 30° section plane (shown in Figure 5.10) for the same individual injection location indicates that each individual particle behaves differently in the flow domain due to the randomness of turbulence in the flow field. It can be seen from Figure 5.11(a-c) that the particles (especially ≤300μm particles) are highly sensitive towards their injection location. If these particles are injected from the inside (of the cross-section at the inlet) they get lifted more often reducing their corresponding removal efficiencies as they would not be able to enter into the sump. The locations at which larger particles (>300μm) strike the 30° plane and their removal efficiency are relatively independent with respect to particle injection location but a small disparity still exists especially for 2000μm particles which do not get congregated at the inside of the 30° bend as they are relatively heavier than the rest of the grit particles. Most of the 2000μm particles remain well spread over a distance of 8cms from the inside bend. The particles of size 300μm to 600μm are also little affected by the injection location, although they tend to gather increasingly at the inside of the bend if injected from the inside of the inlet compared to when injected from the outside of the inlet. Their removal efficiencies though, are not affected by their small variations in the locations at which they strike the 30° plane. The *line* injection results can be extrapolated from various *point* injection locations and are not discussed for the sake of brevity. However, care should be taken while interpreting and comparing computational results for such individual locations with the experimental ones for all particle sizes as they may not represent the actual grit particle phenomenon (behaviour) within the curved grit channel. The effects due to different particle locations have been avoided in this computational modelling study by injecting particles uniformly across the inlet area (Figure 5.8b) so that removal efficiencies obtained for the different particle sizes are only due to variations in the flow field. All the subsequent analysis presented for the grit particles was carried out with the surface injection, a methodology adopted for the ranges of flow rates and other parametric investigations.

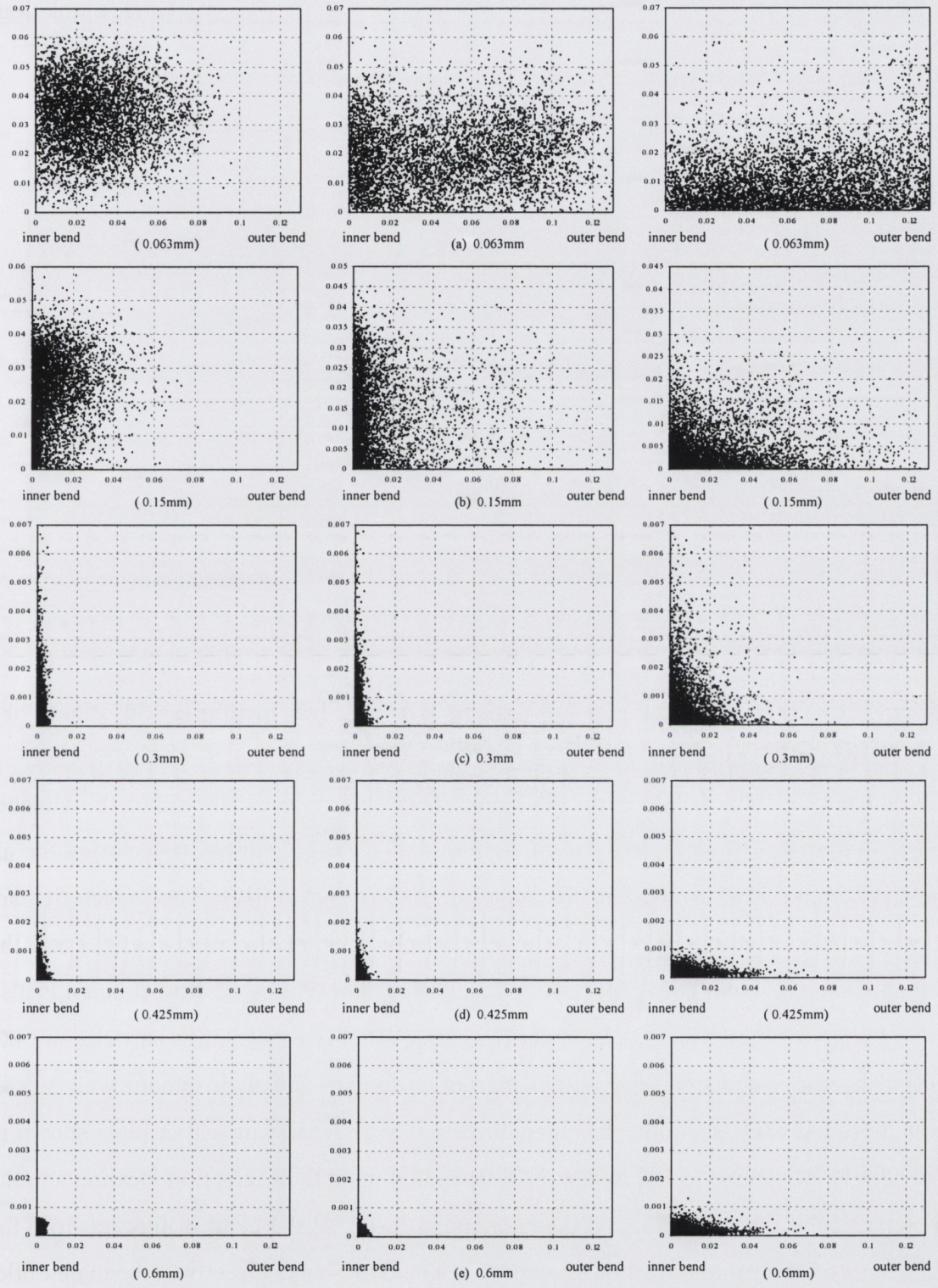

(i) Inside (ii) Centre (iii) Outside

Figure 5.11 (a-e): Scatter Plot for Various Particle Sizes hitting the 30° Plane for particles (0.063mm – 0.6mm)

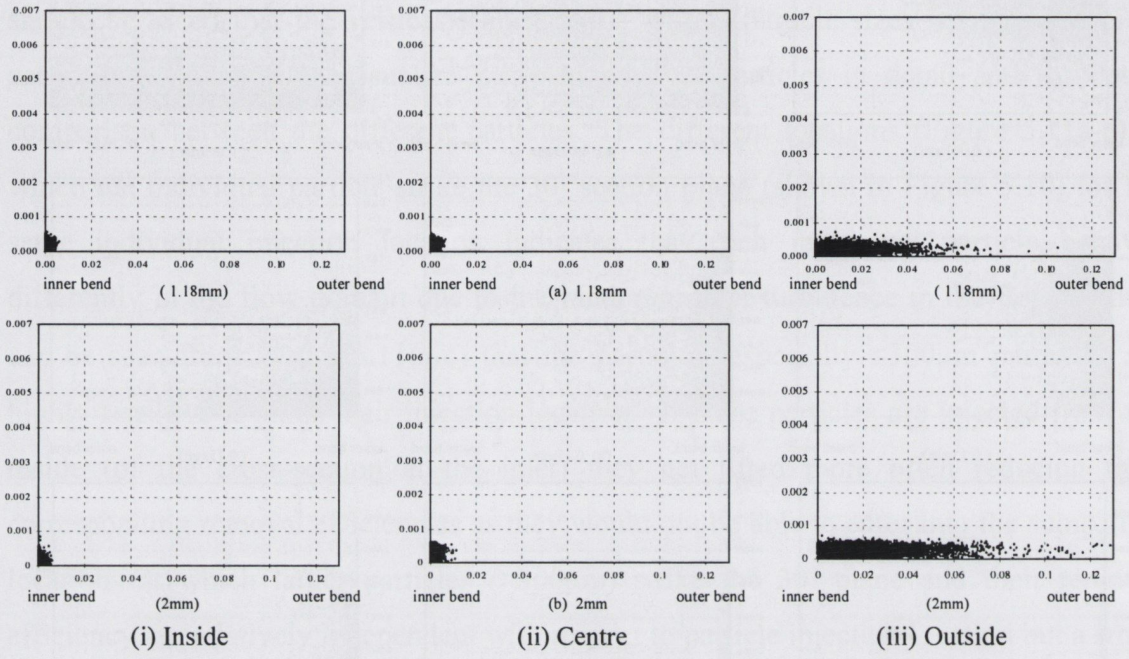

Figure 5.12 (a, b): Scatter Plot for Various Particle Sizes hitting the 30° Plane for Particles 1.18mm and 2mm

The analysis can also be done on the basis of particle trajectories within the channel domain. Figures 5.13 (a-f) & 5.14 shows the plan view of particle trajectories for all diameters from 63μm to 2000μm for angle of bend of 30° at 4l//s. The trajectories are shown for line injection where 100 particles of each diameter size were injected into the flow domain. The bend portion, outlet and sump location within the flow domain is also shown along with the trajectories. It can be easily observed that 63μm particles are not effected by the secondary flow within the curve domain and they remain well spread through out the cross-section. This phenomenon is also evident in scatter plots shown in Appendix B. They tend to follow the path depending upon their injection location and the geometry of the flow domain, and thus remaining inside of the bend if injected from the inside otherwise outside. Most of these particles tend to escape directly to the main outlet of the channel as clearly seen in Figure 5.13(a). Particles of size 150μm tend to accumulate increasingly at the inside as they pass through the bend as shown in Figure 5.13(b). It should be noted that all the particle trajectories are plotted with respect to their residence time in the channel.

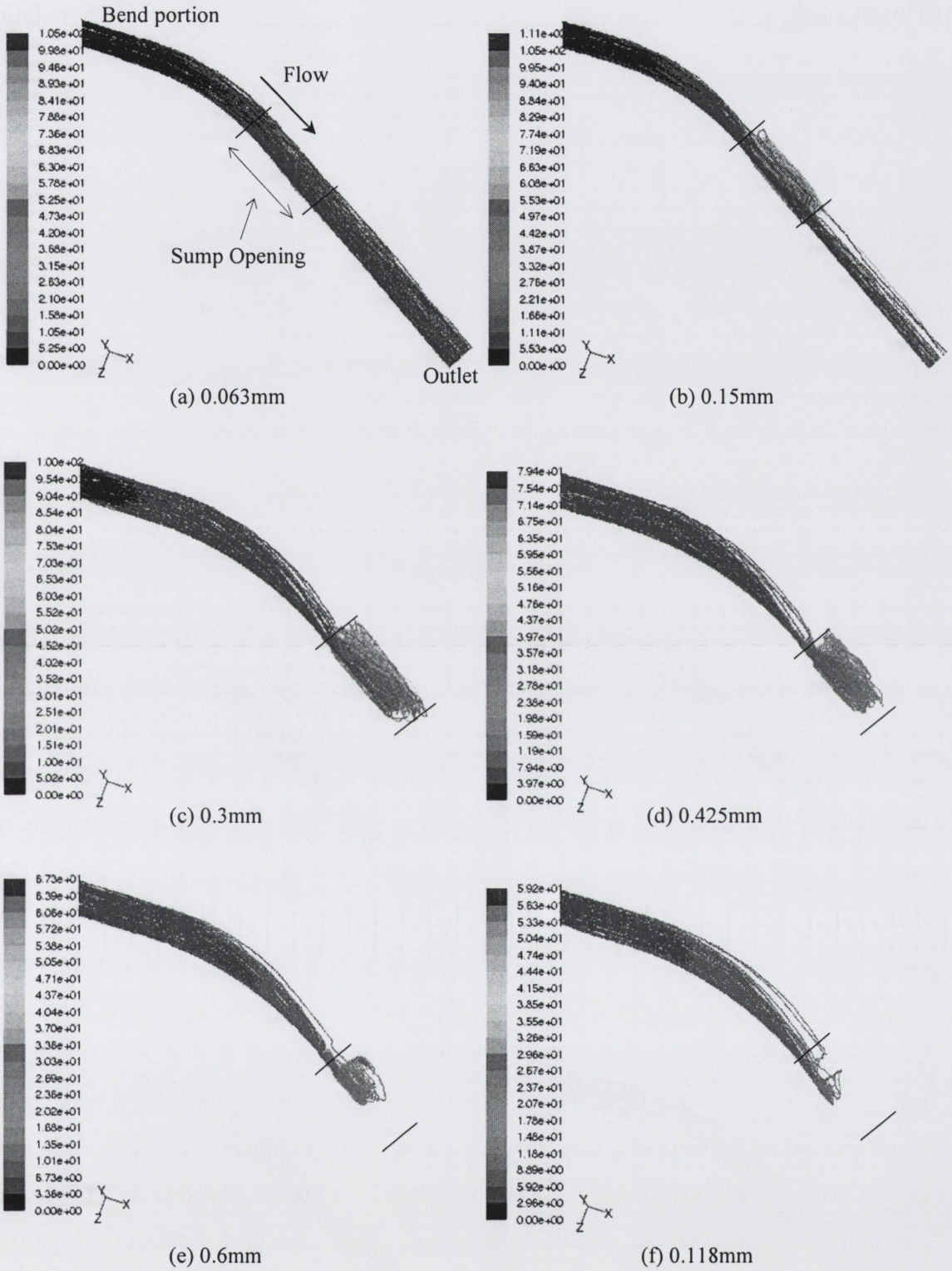

Figure 5.13: Trajectory of Particles at 4l/s within 30° angle of bend (a) 0.063mm, (b) 0.15mm, (c) 0.3mm, (d) 0.425mm, (e) 0.6mm, (f) 1.18mm

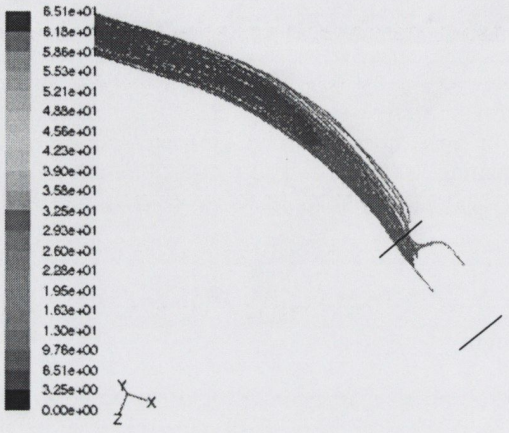

2mm

Figure 5.14: Trajectory of Particles within the 30° angle of bend (2mm)

Their trajectory behaviour is more or less similar to the particle sizes of 300μm, 425μm and 600μm where they strike at the inside half of the bend as they reach the sump making their removal relatively easier. An interesting phenomenon can be observed for particles of size 1180μm and 2000μm where not all the particles are accumulated at the inside of the bend as they reach the sump (or end of the bend) and some particles remain well spread through out the cross-section as evident from their trajectory plots (Figure 5.13f & 5.14). This can be due to their heavier nature and some particles are not being swept away by the secondary flows. Again the scatter plots shown in Appendix B for various configurations confirm the behaviour of various particles. Figures 5.13(c-f) & 5.14 shows that there are no particle tracks after the sump for particle size of 300μm-2000μm. This can be due to the fact that these particles remain within the inside half of the bend as they reach the end of the bend and hence they are able to enter the sump thus preventing their escape. Therefore, there are no particle tracks seen in Figures 5.13(c-f) & 5.14. Overall, the trajectories of various particles depend on their injection location but particles ≥300μm are able to accumulate at the inside half of the bend as they reach the sump and are captured by the sump.

5.2.2.2 Effect of Shape Factor

The efficiency of the particles for the flow rate of 4l/s has also been verified against different shape factors of 0.25, 0.5 and 0.75 where the shape factor (ϕ) is defined as:

$$\phi = \frac{s}{S} \tag{5.3}$$

where, 's' is the surface area of a sphere having the same volume as the particle and 'S' is the actual surface area of the particle. According to the definition, the higher the value of the shape factor the closer the particle is to a spherical shape i.e. a shape factor of 1 indicates a perfect spherical particle. A shape factor of 0.25 indicates a flat particle having maximum surface area for a particular volume. The variation of efficiencies achieved for different shape factors simulated with the grid resolution G_{T3} (coarsest grid size) is shown in Figure 5.15. The modelled results show that the grit removal efficiency for various particles increases with an increase in shape factor due to the drag laws being obeyed (i.e. less drag on typical spherical particles).

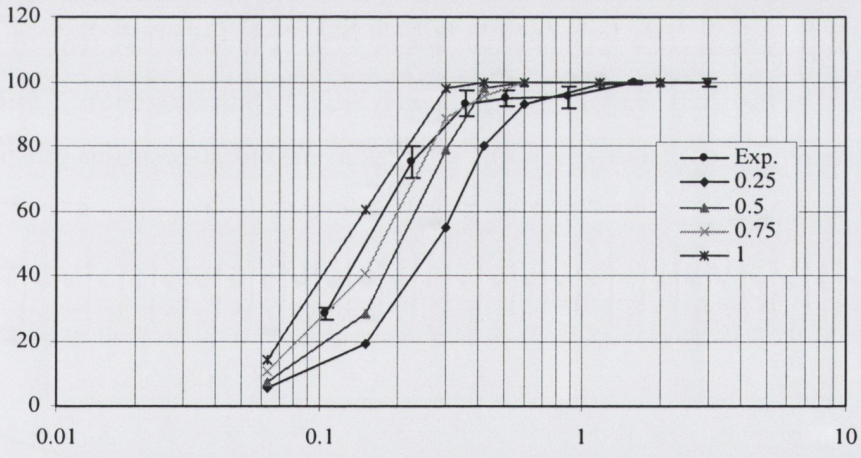

Figure 5.15: Grit Removal Efficiency for different Shape Factors

Figure 5.15 shows that the computational predictions for particles 150μm are between shape factors of 0.75 to 1 and also that analysis in this thesis was done for perfectly spherical particles. Thus, on the basis of analysis of injection location and shape factors, all the subsequent analysis of grit removal efficiency was made with surface injection and spherical particles with grid resolution of G_{T3} to avoid the effects due to injection location

and shape factors in the computational model. It should be noted that during the experiments the grit particles might have different shape factors and Figure 5.15 also suggests that the experimental sand may be approximately between shape factors of 0.75 and 1.

5.2.2.3 Friction Force Considerations - Particle Behaviour near the Wall

When a grit particle hits the (Perspex) wall, the particle is reflected back based on the coefficient of restitution (COR) between the particle and the Perspex. Hence, by including the phenomenon of collision of the particle at the wall, this friction force is taken into account by the '*reflect*' boundary condition (see Chapter 4). Three different COF of 0.25, 0.5 and 0.75 – default is 1) were investigated in order to observe their effects on grit removal efficiencies for different particle sizes. It was found that the results did not vary much for different CORs and that the grit removal efficiencies remained almost constant for all the particle sizes (see Figure 5.16). This phenomenon also indicates that the final fate of the particle is relatively independent of COR. Thus, for all simulations elastic collision (i.e. COR was taken as 1) between the grit particle and Perspex was assumed.

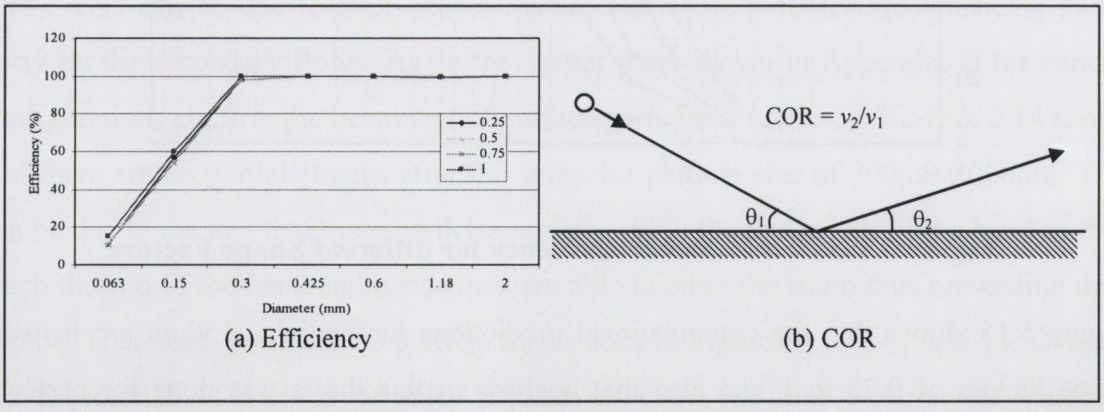

(a) Efficiency (b) COR

Figure 5.16: (a) Grit Removal Efficiency at Different COR, (b) definition of COR

5.2.3 Effect of Flow Rate

Figure 5.17 (a ,b) compares computational predictions with experimental results for flow rates of 5l/s (~0.51m/s) and 6l/s (~0.545m/s). It can be observed that the computational model predicts the same behaviour as found in the experimental investigations where the efficiency decreases with an increase in the flow rate or average flow velocity. However, the computational model again under predicts the efficiency for particles of size 63μm and 150μm and over predicts the efficiency for the rest of the particles reconfirming that the computational model predicts with the same trend at different flow rates analyzed. After comparing the grit removal efficiency for three different flow rates, the investigations were also performed with the flow rates of 8l/s, 10l/s and 15l/ and their computational predictions are shown in Figure 5.17c. The computational results also indicate that the particle efficiency decreases with an increase in the flow rate (or average flow velocity).

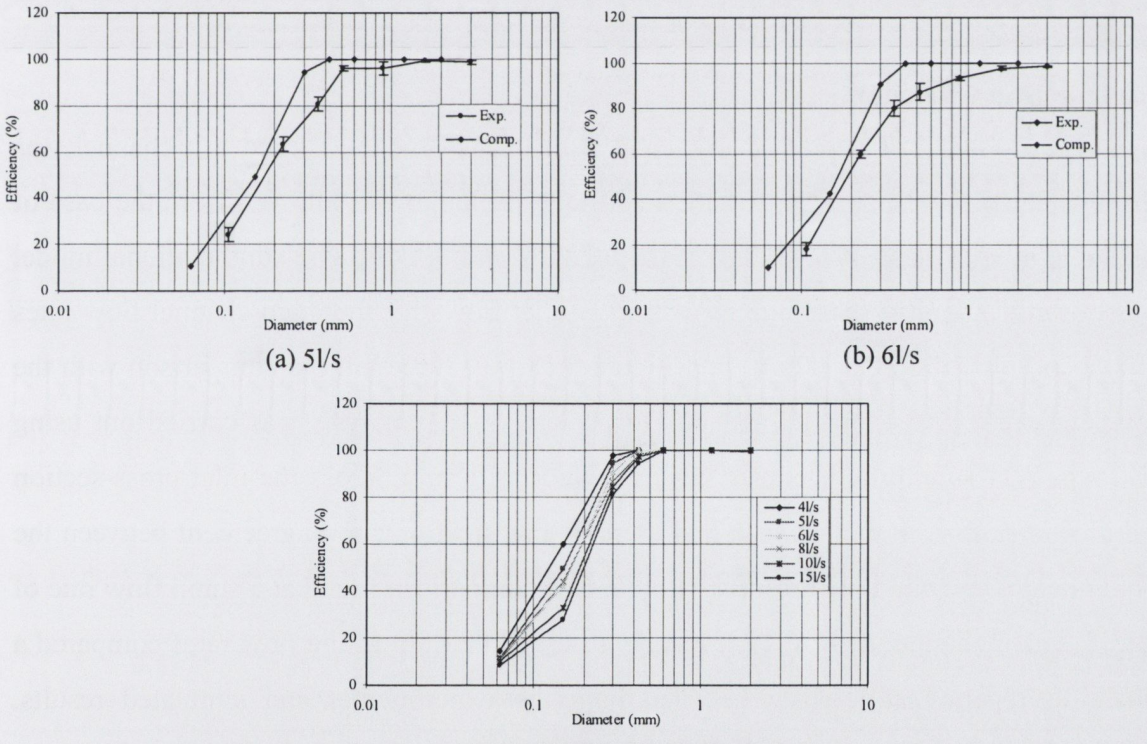

(a) 5l/s

(b) 6l/s

(c) Combined - Computational

Figure 5.17: Comparison of Grit Removal Efficiency at channel flow rates of (a) 5l/s, (b) 6l/s, (c) Combined (4l/s-15l/s)

The average flow velocity simulated for various flow rates is also shown in Table 5.2 which indicates that the velocity increases with an increase in the flow rate even though the rate of increase of velocity is small compared to the flow rate (as it is a type of gravity driven flow). Table 5.2 indicated that the average velocity within the curved grit channel varies from 0.48m/s for the flow rate of 4l/s to a high of 0.74m/s for the flow rate of 15l/s. It can also be confirmed from Figure 5.17c that any marginal increase in the average flow velocity affects the efficiency of the grit removal device considerably, especially for particles in the size range of 63μm to 300μm.

Table 5.2: Flow Rates and Corresponding Average Flow Velocities (Simulated)

Flow Rate (l/s)	4	5	6	8	10	15
Velocity (m/s)	0.48	0.51	0.54	0.59	0.65	0.74

5.2.4 Sump with Flow

As already stated in Chapter 3, grit removal efficiency for the curved grit channel was also evaluated for the scenario where a constant discharge was allowed from the base of the sump at fixed rate of 0.11l/s, 0.15l/s, 0.225l/s and 0.45l/s. The computational model was calibrated against these ranges of sump outlet flows for the main channel flow rates of 4l/s and 6l/s. Figure 5.18(a-d) and Figure 5.18(e-g) represent the comparison with the computational model for 4l/s and 6l/s respectively. The analysis was carried out using grid type (GT3) and the particles were injected uniformly across the inlet cross-section (*surface injection*). It can be seen that there is a reasonably good agreement between the experimental and simulated results with the best comparison found at a sump flow rate of 0.15l/s (main channel flow 6l/s). It can be observed that for all the flow rates compared a small discrepancy still exists between both the experimental and simulated results. However, a significant feature can be seen whereby the removal efficiency increases (especially for particles ≤300μm) with an increase in the flow rate out of the sump as found in the experimental physical modelling and that the trend of the prediction by the computational model remains consistent. Another interesting conclusion that can be drawn from both the experimental and computational results is that particles of 63μm size

are largely not affected by the sump discharge and their grit removal efficiency remains almost constant for various sump flow rates.

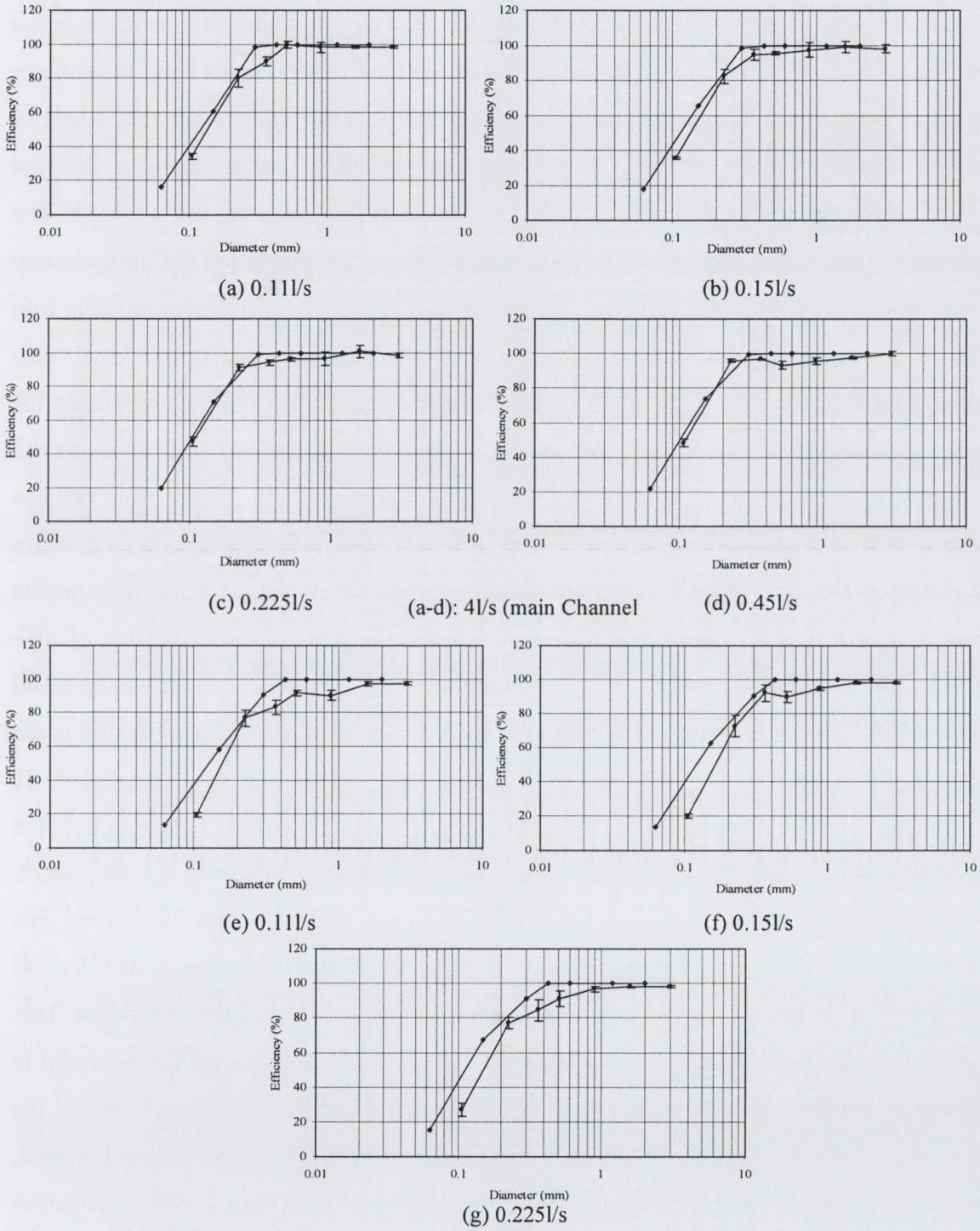

(a) 0.11l/s (b) 0.15l/s

(c) 0.225l/s (a-d): 4l/s (main Channel (d) 0.45l/s

(e) 0.11l/s (f) 0.15l/s

(g) 0.225l/s

(e-g): 6l/s (main Channel

Figure 5.18: Comparison of Efficiency for Various Sump-Flow Rates, (a-d) 4l/s, (e-g) 6l/s

This can be due to the fact that these particles may not have entered into the sump in the first place and would have directly escaped into the main outlet of the grit channel. An analysis of the particle hitting any particular plane also confirms the same, whereby approximately only 28% of injected particles from the inlet enter the sump in the first place and so can obviously get removed from the main flow into the sump outlets. The remaining particles escape directly along the main channel outlet for the closed sump case for 4l/s. It should also be noted that percentage of the 63μm particles entering into the sump for 4l/s typically varied from 30-38% for all the flow rates out of the sump which signifies that the sump outlets have very little effect on grit removal efficiency for this particular grit particle size. However, if the prediction of removal efficiencies by the computational model of particle size of 150μm is considered, it increases from 60% to around 74% for 4l/s and from approximately 58% to around 64% for 6l/s with an increase in the sump flow rate from 0.11l/s to 0.45l/s signifying the impact of sump flow outlets rates. The DPM analysis also confirms that approximately 85% of particles of size 150μm are able to enter into the sump for the closed sump case compared to increased value of 90-95% for the sump flow rates of 0.11l/s to 0.45l/s. For the flow rate of 6l/s the same value drops down to around 80% for the sump closed case and only increases marginally with the increase in the flow rate out of the sump. All these analysis with the DPM model also ascertained that the flow rate in the main channel and the circulation zone within the sump are critical factors for the case analyzed of a 30° curved grit channel. It can also be seen from Figure 5.18 that for sump flow rates of 0.11l/s and 0.15l/s, the increase in the removal efficiency for various particles is not significant. This indicates that allowing flow from this particular geometrical configuration of sump is obviously not a robust means of reducing the magnitude of the circulation zone as the desired increase in removal efficiency for various particles can not be attained. Hence, further methods have been investigated in the following section such as the introduction of baffle plates within the sump as an additional/alternative method of counteracting the circulation. Figure 5.19 shows the effect of allowing a high sump outlet flow rate of 0.45l/s on the strength of the circulation zone within the sump.

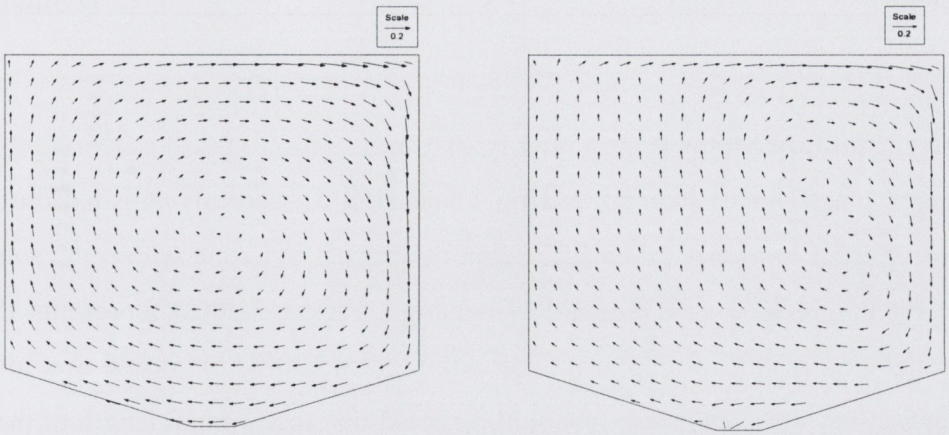

(a) Sump Closed

(b) Sump Outlet – 0.45l/s

Figure 5.19: Velocity Vectors of Circulation zone in Sump with (a) no flow, (b) outlet flow of 0.45l/s

The figure depicts that there is a decrease (though not significant) in the magnitude of the circulation zone due to the sump outlet flow of 0.45l/s which equates to an increase in the removal efficiency for 150μm size particles from 60% to around 74% for the flow rate of 4l/s in the main channel. However, further increase in the flow rate out of the sump would not recommended in practice as the handling of the wastewater at this primary treatment stage can become an issue such as operation of the classifier and return of the supplement flow. Hence, in the present study, the maximum flow rate out of the sump was restricted to 0.45l/s which is around 10% of the main flow in the grit channel.

5.3 Parametric Investigations

A detailed parametric investigation is now presented in which the dependency of grit removal efficiencies for various particles has been analyzed for two different sump shapes, various baffle configurations, different sump opening positions, angle of the bend, flow rates, widths of the channel and radii of curvature. The effect of angle of bend on the magnitude of secondary flows and redistribution of axial velocity contours within the main curved grit channel is also discussed.

5.3.1 Effect of Sump Shape

Two different sump shapes (named as Hop 1 and Hop 2) were investigated during the simulations in order to observe their effects on the circulation zone within the sump and thus subsequent effect on grit removal efficiency. Figure 5.20(a) represents the grit removal efficiency results from the model and Figure 5.20(b, c) shows two modified sump shapes which were analyzed. It should be noted that the original length of the sump was kept in both the changed shapes of the sump. The figure also includes the representation of the circulation zone for both the cases analyzed. It can be seen that the magnitude of the circulation zone has reduced as compared to Figure 5.19(a) although the decrease in the magnitude is again not significant. It should be noted that even with the reduction in the magnitude of circulation within the sump, the efficiency does not change significantly. This indicates that a considerable reduction in the magnitude of circulation zone is required in order to obtain an increased grit removal efficiency.

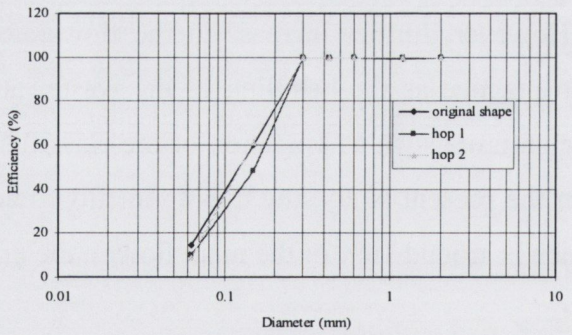

(a) Grit Removal Efficiency

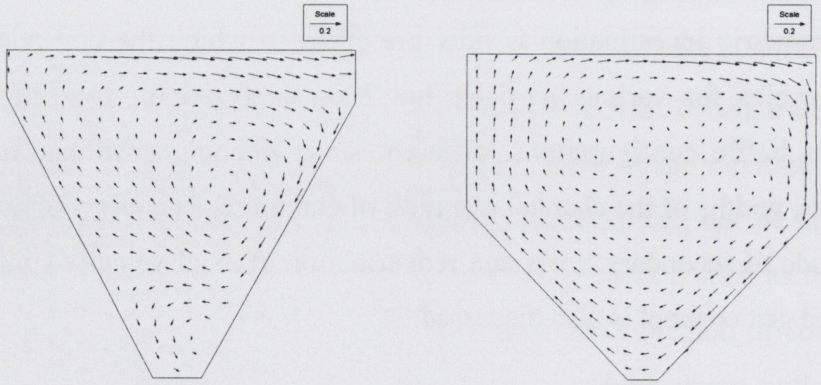

(b) Hop 1 (c) Hop 2

Figure 5.20: (a) Grit Removal Efficiency for two different sump shapes compared with Original Shape, (b) Circulation Zone Hop 1, (c) Circulation Zone Hop 2

The DPM analysis also confirmed that only around 70% of the particles of 150μm size were entering into the sumps for both shapes. If we consider the flow characteristic of the circulation zone itself, its main feature from Figure 5.19a is still preserved where a main rotating flow in a clockwise direction is found within the sump. The almost same phenomenon is observed for both the sump shapes confirming that there is very little change in the flow behaviour within the sump even after modifying their respective shapes (as in Hop 1 or Hop 2). A small variation can be observed between Hop 1 and Hop 2, where a small circulation zone of relatively low strength is formed in both the cases. However, these small variations in circulation zone would have little or no effect on the grit removal efficiency. Considering the outcomes of this analysis (i.e. no considerable changes in the performance of the sump), all the subsequent parametric investigations were performed with the original shape of the sump as shown in Figure 5.19(a).

5.3.2 Effect of Baffles and Sump Outlet Location

5.3.2.1 Sump with no Flow

Baffle plates at various locations along the sump length were introduced in order to observe their effect on the grit removal efficiency at the flow rate of 4l/s. Figure 5.21(a) shows the locations of three different baffle plates (baf 1, baf 2 and baf 3), sump outlet locations (O1, O2 and O3) and an inclined orientation of baffle plate at 45° (baf4) for the flow rate of 4l/s. Vertical baffles were placed at a distance of every quarter of the length of the sump. Different configurations were tried in order to find the optimum positioning and orientation of the baffles plates. The removal efficiency was also found for a reduced length of the baffle plate at similar three different locations (baf1, baf2 and baf3) as shown in Figure 5.21(a). Figure 5.21(b-d) represents the grit removal efficiency for the various baffle configurations obtained using the computational model. In addition, the length of the baffle was also varied in which the depth of the baffle was halved.

Figure 5.21(b-d) clearly depicts that the introduction of baffle plates within the bottom sump improves the grit removal efficiency for the particle size 150μm from around 60% to 95% for all individual baffles and also for all different configurations (i.e. 1-2, 1-3, 2-3 or 1-2-3). However, the inclined baffle shows a relatively worse grit removal efficiency than the vertical baffle plate no. 1.

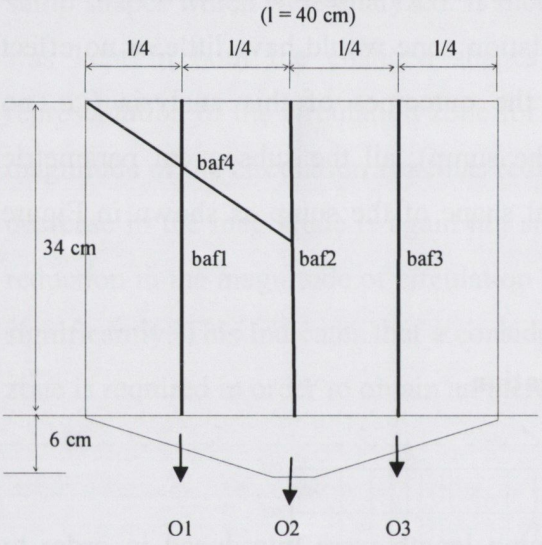

(a) Baffle Plate Locations

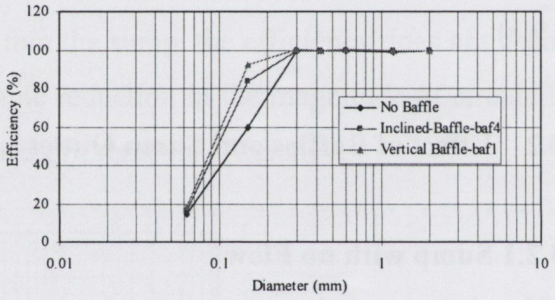

(b) Baffle (1 & 4)

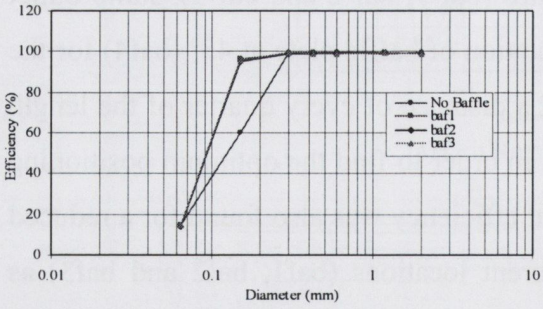

(c) Vertical Baffles – Reduced Length (1, 2 & 3)

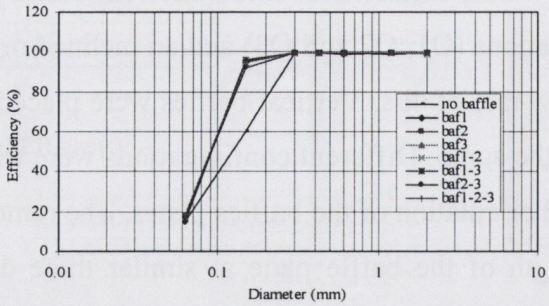

(d) Vertical Baffles – Full Length (1,2 & 3)

Figure 5.21: (a) Baffle Plate Locations, (b-d) Computational prediction of grit removal efficiencies for different Baffle Plates Configurations

It should also be noted that baffle no. 1 is found to be relatively more efficient in removing particles than the other corresponding vertical baffles 2 and 3, although this difference is marginal and can be ignored. The computational analysis on the sump also

indicates that the chambered sump (where all the three baffles 1, 2 & 3 can be incorporated simultaneously) can be used to reduce the effect of circulation zone on grit particles within the sump. An interesting outcome from this analysis is obtained, showing that the efficiency for various grit particles remains almost constant for all the different baffle configurations no matter whether they are used individually or in any combinations of the three baffles. The same conclusion can be drawn for the reduced length of the baffles where the efficiency again remains constant for the three different baffles analyzed individually. The removal efficiency for 63μm particles by the sump does remain constant for all the cases analyzed and they are not affected considerably even after introduction of baffles indicating that the majority of organic matter would not be removed and hence no additional design considerations are required for 63μm particles. This phenomenon also indicates that the handling of the wastewater from the sump outlet would not be a major problem at the primary grit removal stage with the introduction of baffles. The circulation flow plots in Figure 5.22(a-f) also show that the magnitude of the circulation zone reduces after the introduction of the baffle plates but does not vary much for various baffle plate configurations, as expected perhaps from the grit removal efficiencies results. Figure 5.22(a-d) shows the circulation zone simulated for individual baffle plates 1, 2 & 3 and the combination of the three (1-2-3) and Figure 5.22(e & f) shows the simulated circulation zone for a reduced length of baffle no. 1 and for the angled baffle 4 respectively. It can be observed from Figure 5.22(a-c) from the individual baffle (1, 2 & 3) analysis, that two circulation zones of almost equal strength are formed one on each side of the baffle plates. The strength of the circulation zone for each case does not differ much and hence equal grit removal efficiencies were obtained for these cases. Figure 5.22(d) indicates that four circulation zones of relatively lesser strength than those found for individual cases are formed between the baffle plates. The magnitude of the circulation zone is relatively less because of the increased wall effects caused by the baffle plates. However, as already discussed, the reduction of the magnitude of the circulation zone for the chambered sump does not result in any further increase in grit removal efficiency, and as the grit removal efficiency has already reached a high of 95%,

minor variations for 150μm particles can still exist due to turbulence in the main curved grit channel.

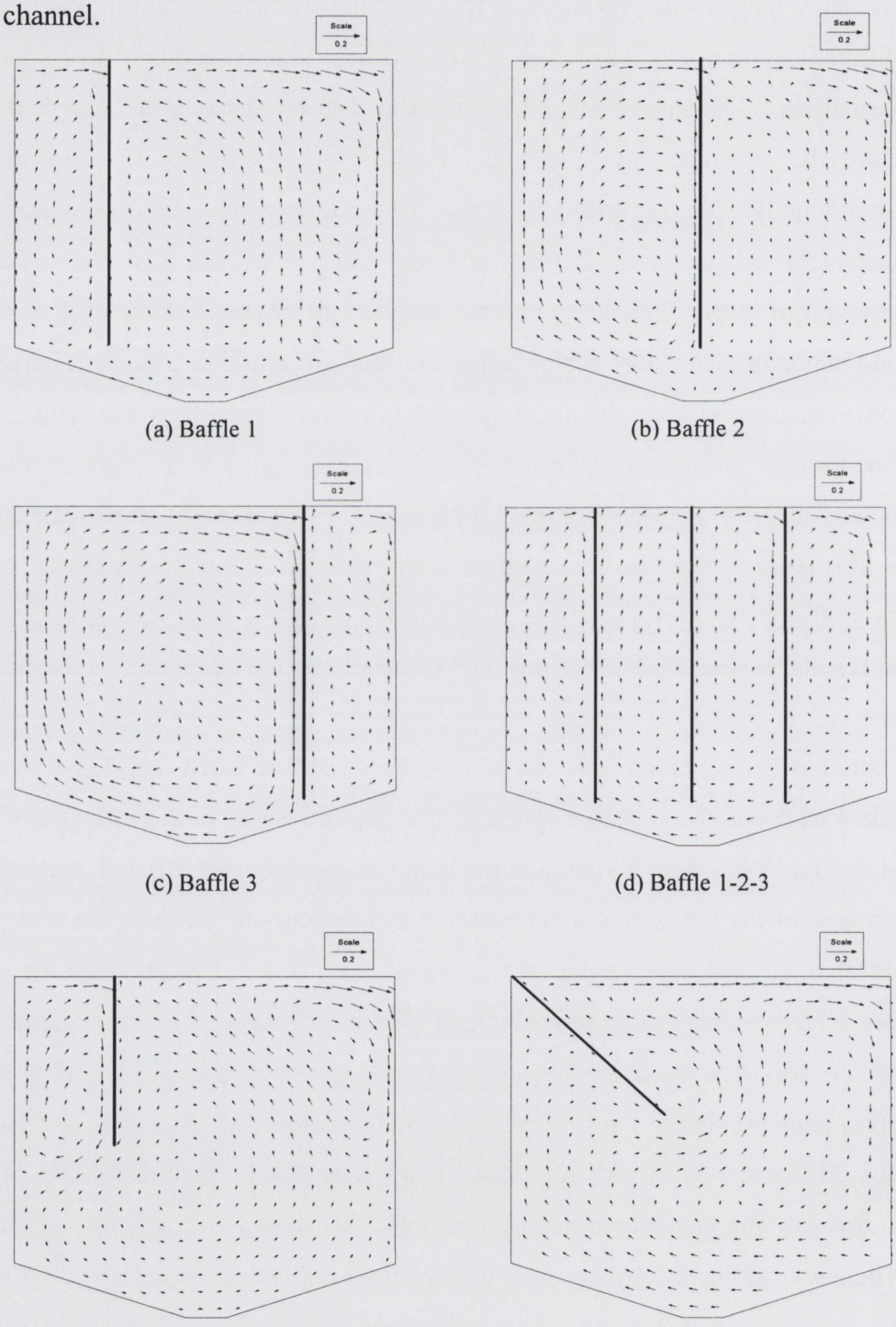

(a) Baffle 1

(b) Baffle 2

(c) Baffle 3

(d) Baffle 1-2-3

(e) Baffle 1 – Reduced Length

(f) Baffle 4 (Inclined)

Figure 5.22(a-f): Simulated Circulation Zone for Various Baffle Configurations

Figure 5.22(e) represents the circulation zone for the reduced length of baffle no. 1 and again a similar range of magnitude of circulation zone is observed. A small (though of relatively equal strength) circulation zone is found which is comparable to the circulation zone in Figure 5.22(a). A similar type of outcome was found for the inclined baffle analysis which is shown in Figure 5.22(f). In this case the efficiency for the 150μm particles was found to be reduced to some extent and this can be attributed to the fact that relatively higher flow velocities at the interface of the sump and main channel were found which may be responsible for short circuiting of the particles directly into the main channel outlet. The DPM analysis also demonstrated this fact where relatively fewer particles (~90%) than the other cases were entering into the sump in the first place. The effect of baffle plates can also be visually seen on particle tracks within the sump. Figures 5.23(a-d) and 5.24(a-c) show the particle tracks for various diameter sizes ranging from 63μm to 2000μm at 4l/s for no baffle, baffle1 and bafle1-2-3 cases. It should be noted that all the particle trajectories are plotted with respect to their residence time in the channel. It can be easily seen that particles of sizes 63μm and 150μm circulate within the sump due to the induced circulation zone and some of these particles tend to escape out again into the main flow making their removal efficiency smaller. This can be due to their smaller settling velocity as compared to the magnitude of the circulation zone. As discussed earlier, with the introduction of baffle plates, the magnitude of circulation zone decreases and their effect can also be seen in the trajectory plots where they confined themselves between various baffle plates as shown in Figures 5.23 & 5.24. This phenomenon is observed for all particles sizes. The DPM analysis also confirmed that the removal efficiency of 150μm increases from 60% to approximately 90% at 4l/s for sump closed case. It should be noted that trajectory plots are plotted assuming steady state tracking conditions as it is not possible to do the same in unsteady conditions in FLUENT®. It can also be observed that as the particles of size ≥300μm enter into the sump they tend to remain within the sump because their settling velocity is higher compared to induced circulation zone. These heavier particles tend to settle at the bottom of the sump and there remains no circulation loops for these particles especially for baffle cases as shown in Figures 5.23(c, d) and Figures 5.24(a-c).

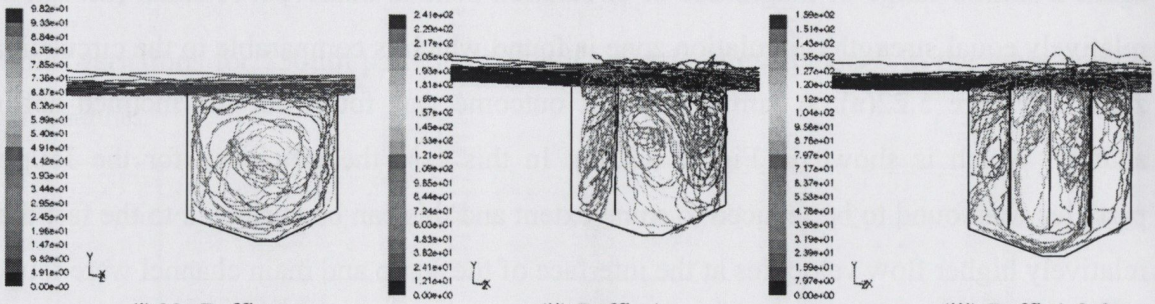

(i) No Baffles (ii) Baffle 1 (iii) Baffle1-2-3

(a) 0.063mm

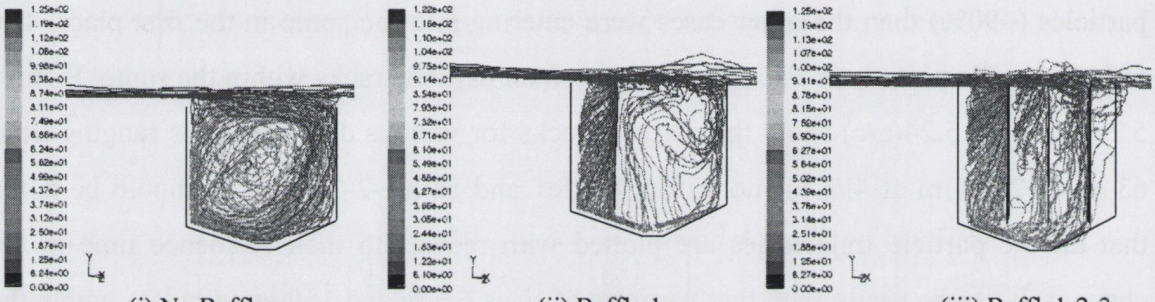

(i) No Baffles (ii) Baffle 1 (iii) Baffle1-2-3

(b) 0.15mm

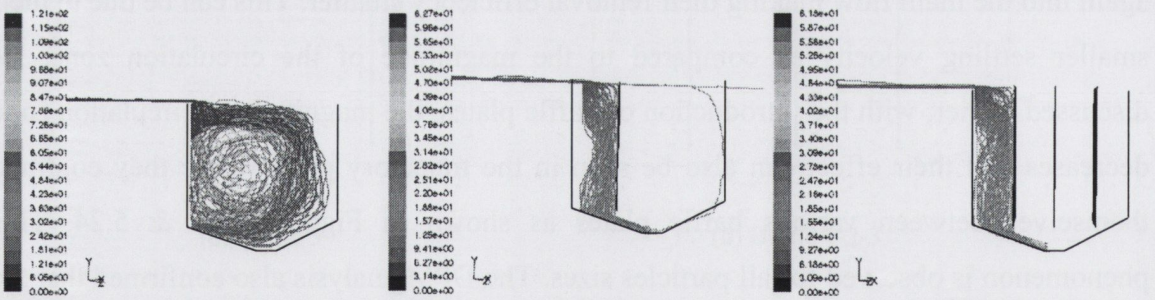

(i) No Baffles (ii) Baffle 1 (iii) Baffle1-2-3

(c) 0.3mm

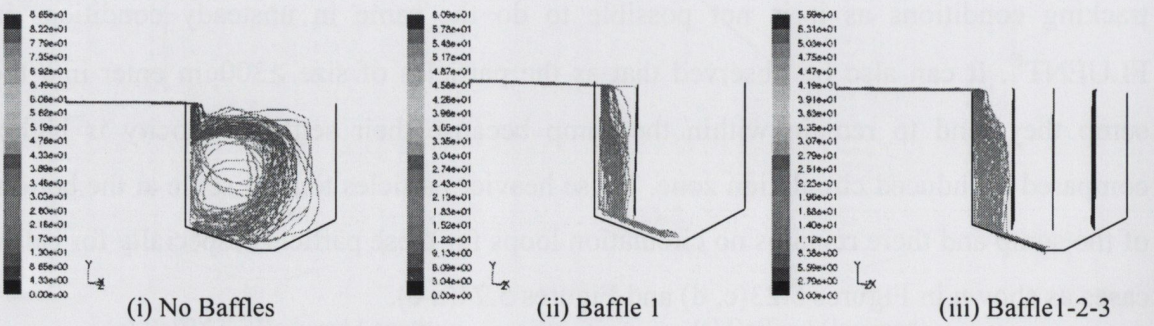

(i) No Baffles (ii) Baffle 1 (iii) Baffle1-2-3

(d) 0.425mm

Figure 5.23: Trajectory of Particles at 4l/s within sump for different baffle configurations (a) 0.063mm, (b) 0.15mm, (c) 0.3mm, (d) 0.425mm

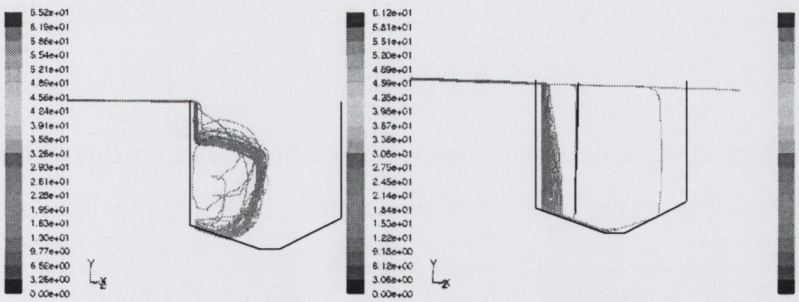

(i) No Baffles (ii) Baffle 1 (iii) Baffle1-2-3

(a) 0.6mm

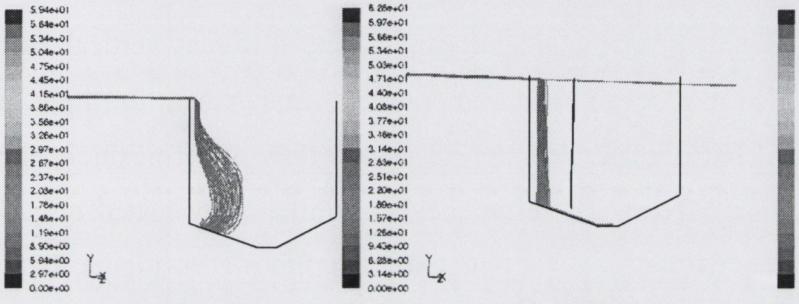

(i) No Baffles (ii) Baffle 1 (iii) Baffle1-2-3

(b) 1.18mm

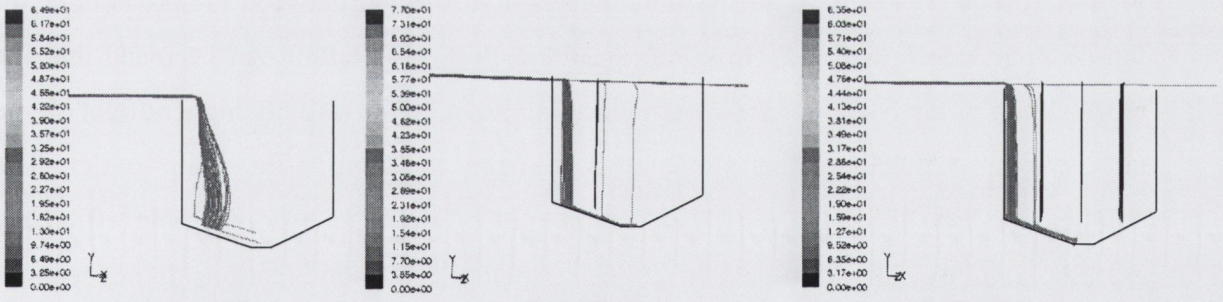

(i) No Baffles (ii) Baffle 1 (iii) Baffle1-2-3

(c) 2mm

Figure 5.24: Trajectory of Particles at 4l/s within sump for different baffle configurations (a) 0.6mm, (b) 1.18mm, (c) 2mm

It should also be noted that no particle tracks for 300μm-2000μm are visible after the sump which was also observed earlier in the Section 5.2.2.1. The behaviour of particles within the sump changes significantly depending upon the baffle configurations. Although this phenomenon does not effect the grit removal efficiency of these particle

sizes. The particle size 300μm-600μm forms a close loop within the sump for without baffle case and they tend to settle down directly at the bottom of the sump for baffle cases. However, the trajectories of particles >1180μm are not effected by the baffles and they tend to follow almost straight downward path even for no baffle case.

5.3.2.2 Sump with Flow

Various configurations of three different outlet locations and different vertical baffle plate positions were also tried in order to obtain an optimum arrangement for these two parameters. The locations of baffle plates and the respective flow outlet positions have already been shown in Figure 5.21(a). The efficiency was initially evaluated only for three different outlet positions without the introduction of baffle plates. Figure 5.25(a) shows the grit removal efficiency for various outlet locations (O1, O2 & O3) and for combined arrangements of: baffle no. 1 - outlet 1, baffle no. 2 - outlet 2 and baffle no. 3 - outlet 3. It can be seen that no significant change was found between the predictions for the different configurations. However, an interesting observation can be made that the introduction of the baffles alone within the sump has a comparatively higher affect on the grit removal efficiency than allowing flow from the non-baffle sump outlet. The combined effect of baffle plates and sump outlets has also a comparable efficiency corresponding to using baffle plates alone and their various combinations do not seem to affect the grit removal efficiency to any considerable extent. The extent at which the strength of the circulation zone is reduced for a sump flow outlet rate of 0.45l/s (see Figure 5.19b) and introduction of baffle plates respectively (see Figure 5.22(a-f)) also demonstrate the fact that the magnitude reduces considerably after the introduction of baffle plates alone compared to allowing flows as high as 0.45l/s. It should also be remembered (as discussed before) that that there is always a restriction of amount of flow allowed from the sump which is a major factor in the design of such grit removal devices. Different combinations with baffle no. 1 and three different outlets were also modelled but again no significant differences were found (Figure 5.25(a, b)) between all the configurations indicating that any combination could be incorporated in the design.

However, the positioning of baffle at position 1 and either of outlets 1 or 2 is recommended.

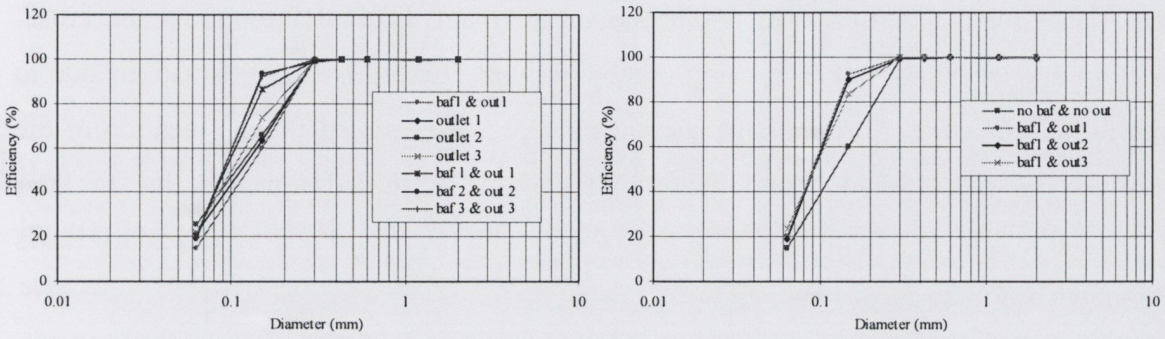

(a) (b)

Figure 5.25(a, b): Grit Removal Efficiency for Various Baffle Plates and Outlets Configurations

5.3.3 Effect of Width of Sump-Opening at the base of the Curved Grit Channel

Three different sump openings (quarter, half and full) at the base (floor) of the grit channel were investigated in order to see their effect on grit removal efficiency. This modification was investigated using the DPM particle analysis (particles hitting the 30° plane) for the surface injection which indicated that not all the larger size particles (especially 1180μm and 2000μm) were being gathered by the secondary flow (towards the inside of the bend) and they tended to remain well spread over a distance of more than half the channel width. As a result, 100% efficiency for particles of size 1180μm and 2000μm was not recorded by the computational model. This phenomenon makes analyzing the affect of sump opening at the base an even more interesting parameter to be verified. The percentage (0 to 0.03% for the particles of size 1180μm and 2000μm) appears to very small compared to the nature of any typical municipal wastewater. However, an increased accumulation of the particles over time can hamper the performance of the components downstream. Figure 5.26 shows the scatter plot of various particles sizes hitting the 30° plane for 4l/s. It can be noted that particles of all the different sizes from 63μm to 2000μm were concentrated on the inside of the 30° bend owing to the formation of secondary flow, with the effect being more prominent on particles of sizes 150μm to 600μm. However, the effect of secondary flow is not that

prominent for the particle size 63μm and they remain diffused throughout the cross-section due to their small size, being relatively more affected by the fluctuations due to the flow turbulence. An important phenomenon can be observed for the location of the particles of size 150μm where they are found to be shifted upwards due to their comparable settling velocity value of (~0.02m/s) with the magnitude of secondary flows as shown in Figure 5.26.

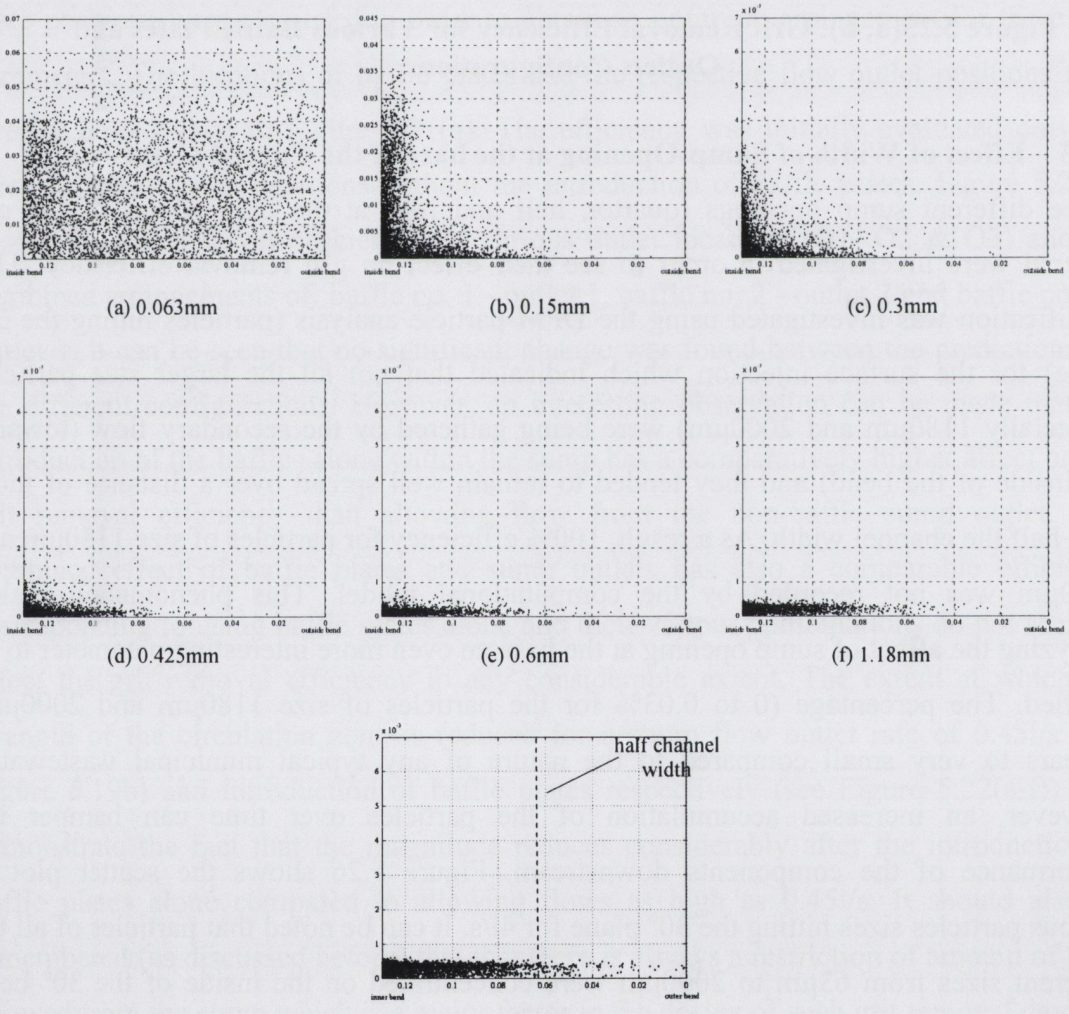

(a) 0.063mm (b) 0.15mm (c) 0.3mm

(d) 0.425mm (e) 0.6mm (f) 1.18mm

(g) 2mm

Figure 5.26: Scatter Plot for Various Particle Sizes hitting the 30° Plane

Due to this phenomenon, this particle size could be considered a critical factor in the optimum design of the angle of bend in curved grit channels. If the location of particles of size 300μm to 600μm is visualized, it can be easily seen that they behave more or less in a similar pattern having been concentrated well inside the bend and having very low vertical co-ordinate distances. The maximum co-ordinate being 0.007m also indicates that they remain very close to the bottom wall enabling them to be removed more easily by the sump. The particles of size 1180μm and 2000μm were also found to be affected by secondary flows but few of those particles (~0.5%) are beyond the distance of half channel width, as can be seen from the Figure 5.26(g). This may be due to the relatively smaller magnitude of secondary flows and their heavier weight. The analysis for different angles of 15° and 45° (see Section 5.3.4 and scatter plots in Appendix B) also indicated that their locations are affected by the magnitude of secondary flows where they were relatively closer to the inside bend for 45° than the 15° and 30° cases, as discussed later in the chapter. Thus, the scatter plot for the 1180μm and 2000μm particle sizes indicates that analysis of different sump openings at the base of the channel would be interesting. Figure 5.27(b) shows the grit removal efficiency for three different sump openings (Figure 5.27a) which indicates that the grit removal efficiency for 1180μm and 2000μm was found to be 100% for a fully open sump and less than 100% for the other two cases analyzed. The effect of the sump opening is easily seen for the quarter open case where the efficiency for 2000μm particle size reduces to ~98% indicating that the opening can also be one of the critical parameters in the design of curved grit channel. However, the pattern of efficiency for half and fully opened almost remained constant - except for the fact that for 2000μm size particles, the efficiency was not exactly 100% for the half-open case. An interesting behaviour is found for the quarter open case where the efficiency increases for 63μm and 150μm particles from 14% and 60% to around 29% and 79% respectively. This is due the fact that the interface between sump water and the channel bottom has more wall effects and, as a result, the circulation zone within the sump does not interfere with the main flow as much as for the case for half-open or fully-open cases. Hence, a relatively larger number of the particles are able to enter into the sump. The DPM analysis also found similar outcomes where only 57% and 2.4% of particles of size

63μm and 150μm were evading the sump for the quarter-open cases which increased to 74% and 35% for the fully-open case. Thus, a balance is required between removal for all the grit particle sizes. On this basis the fully-open sump at the base of the curved grit channel was used for all the cases discussed in the next sections.

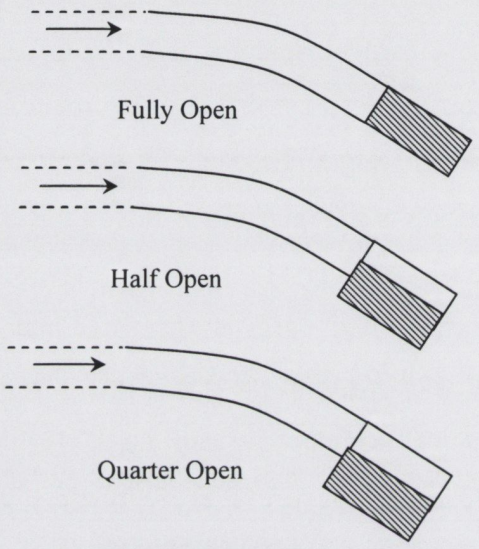

(a) Sump-Openings

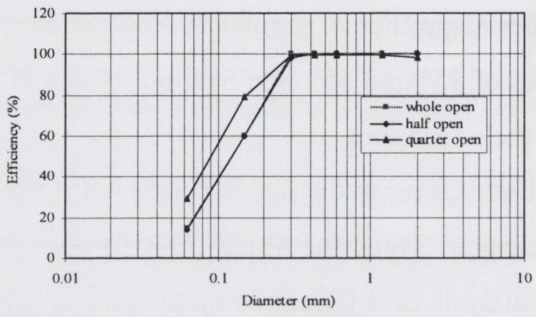

(b) Efficiency

Figure 5.27: Grit Removal Efficiencies for Different Sump-Openings (a) Sump-Openings, (b) Efficiency

5.3.4 Effect of Angles of Bend

As already stated, three different bend angles were investigated at six different flow rates of 4l/s, 5l/s, 6l/s, 8l/s, 10l/s and 15l/s. The corresponding average velocities were found to in the range of 0.48m/s to 0.74m/s (Table 5.2). Such analysis enables a comparison to be made of the behaviour of the secondary flows for the different configurations and consequently their effect on movement of grit particles within the bend of curved grit channel. Figures 5.28 and 5.29 show the secondary flows for bend angles of 15°, 30° and 45° for 4l/s, 5l/s, & 6l/s and for 8l/s, 10l/s & 15l/s respectively or corresponding depth/curvature ratio from 0.038 to 0.096. It should be noted that all the plots for the velocity vector and contours are presented as viewed from the downstream side: i.e. the outer bend lies on right side of the figure. The magnitude of secondary flows can be judged using the scale on each plot and it can be observed that the magnitude of

secondary flow increases with the increase of the bend angle for a particular flow rate. However, the rate of increase of magnitude for secondary flow from 15° to 30° is relatively higher than from 30° to 45°. This trend was observed for all ranges of flow rates from 4l/s to 15l/s. If the pattern of the secondary flow is analyzed while keeping the angle of bend constant, it can also be observed that the magnitude of the secondary flows increase with the increase in the flow rate (or average flow velocity).

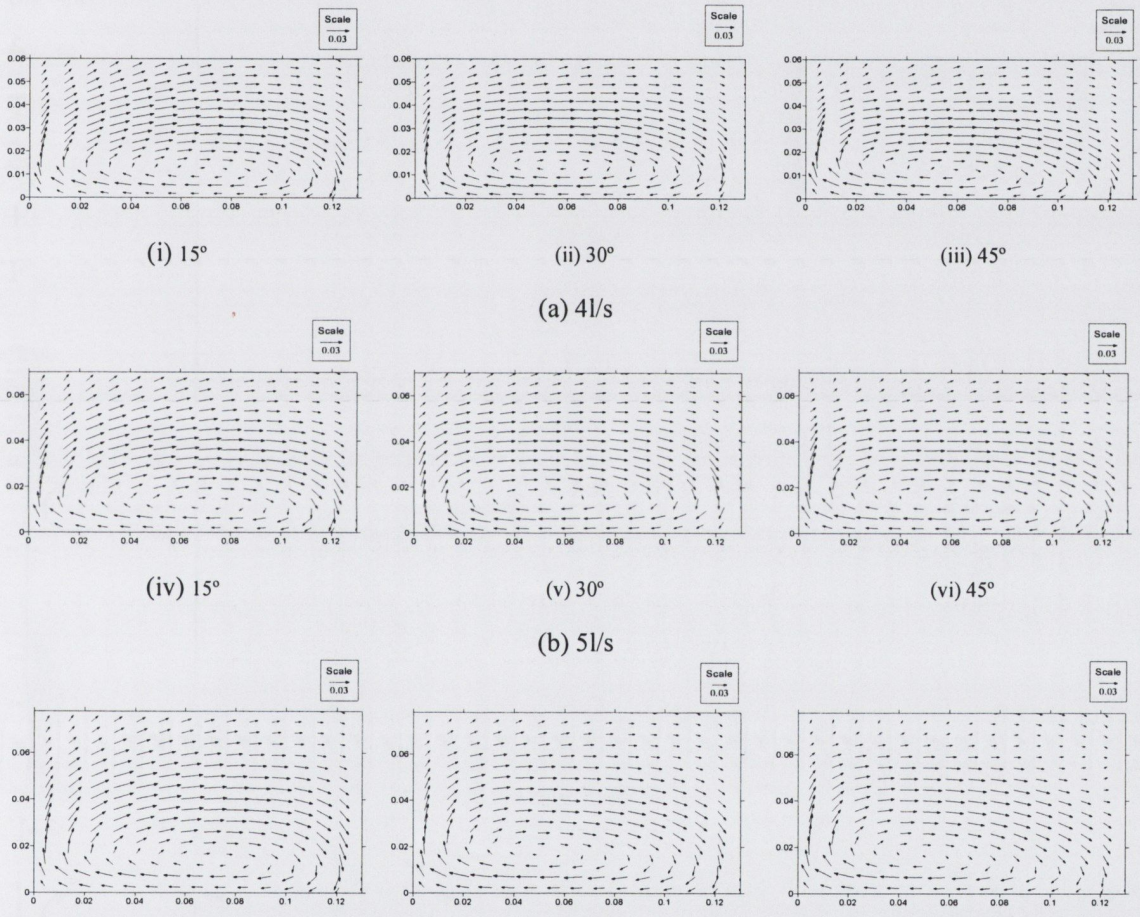

(i) 15° (ii) 30° (iii) 45°

(a) 4l/s

(iv) 15° (v) 30° (vi) 45°

(b) 5l/s

(vii) 15° (viii) 30° (ix) 45°

(c) 6l/s

Figure 5.28: Cross-Flow Velocity Vectors for different Angle of Bend at (a) 4l/s, (b) 5l/s, and (c) 6l/s

The maximum magnitude of secondary flow was found to be around 0.06m/s for 45° at 15l/s. It should be noted that the secondary flow does not increase greater than 10% of

the main flow velocity for any of the cases analyzed. The range at which the secondary flow varied for all the cases was approximately 0.03m/s to 0.06 m/s which appears small compared to the mean flow velocity, but it has significant affect on redistribution of longitudinal velocity contours as seen from the plots of velocity contours in Figures 5.30 and 5.31 for the various ranges of flow rates analyzed.

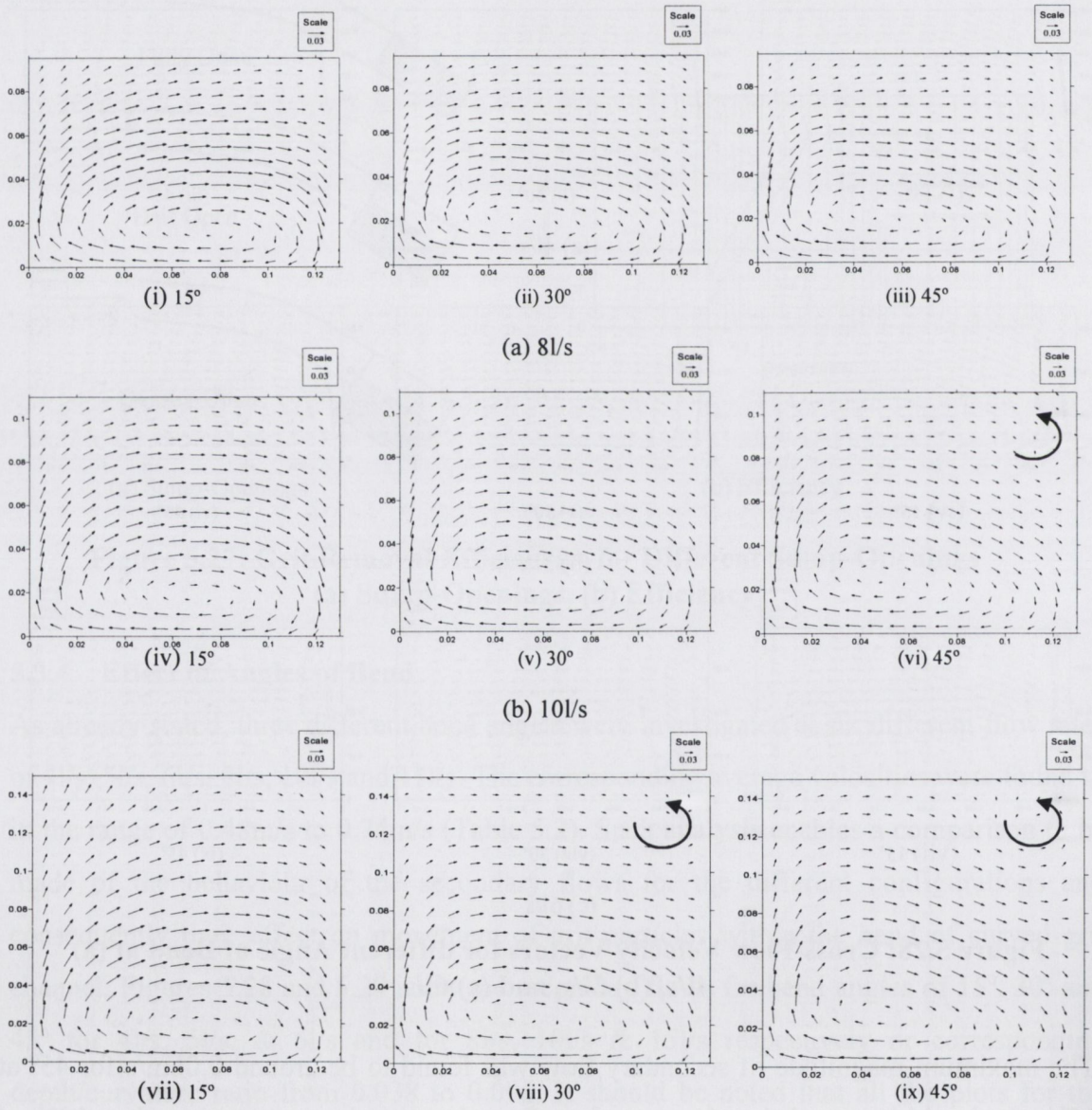

Figure 5.29: Cross-Flow Velocity Vectors for different Angle of Bend at (a) 8l/s, (b) 10l/s, and (c) 15l/s

An interesting phenomenon for the cross-flow velocity vectors is observed for the combination of 15l/s with 30° and 45° where an outer bank cell of a relatively smaller magnitude (compared to the main circulation cell) is found at the intersection of the outer bank and the free surface. The similar pattern of two circulation cells consisting of one main and one outer was also was also observed by Blanckaert (2003). This outer cell formed at the outer bank of the curved grit channel is believed to have a protective effect on the outer bank as it is able to keep the maximum longitudinal velocity contour away from the outer bank, hence preventing scour at the outer bank, as discussed in Chapter 2. This phenomenon can be crucial while analyzing flow behaviour in natural rivers and estuaries. The distribution of longitudinal velocity contours across the cross-section for 15°, 30° and 45° bends for 4l/s, 5l/s and 6l/s and for 8l/s, 10l/s and 15l/s is shown in Figures 5.30 and 5.31 respectively.

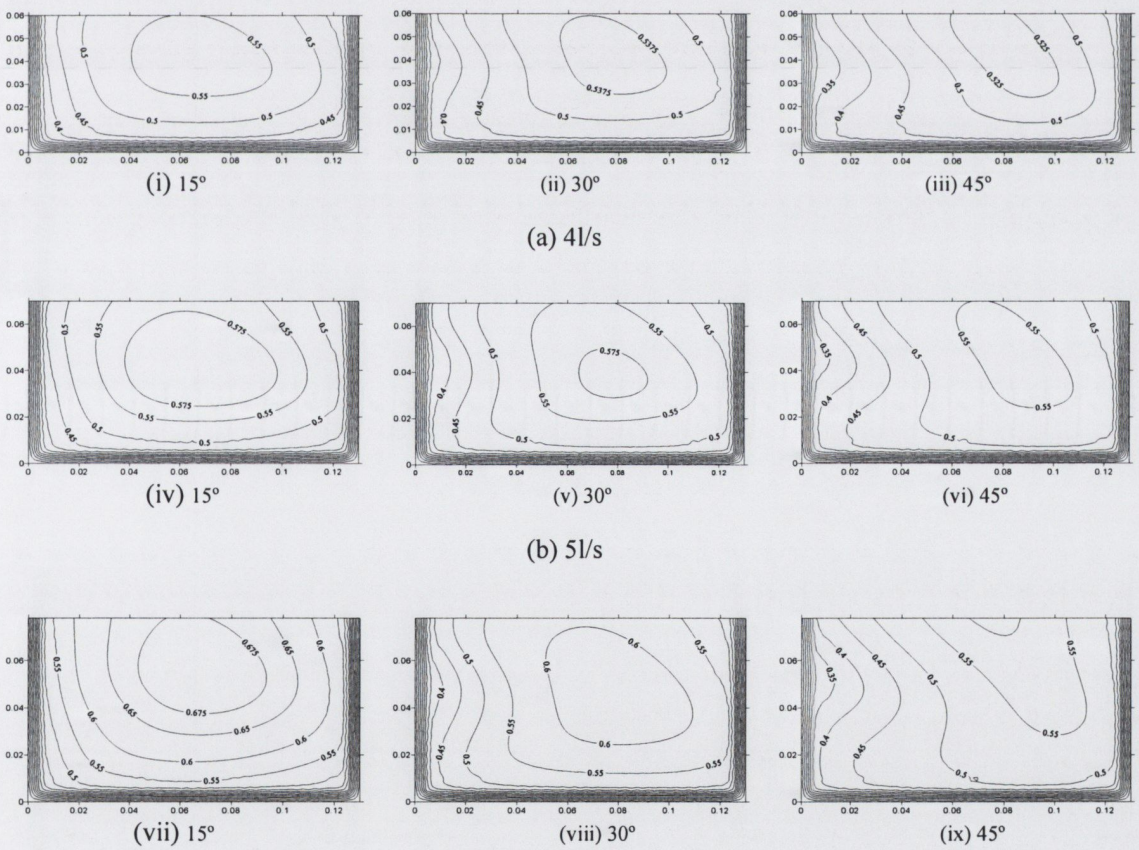

(i) 15° (ii) 30° (iii) 45°

(a) 4l/s

(iv) 15° (v) 30° (vi) 45°

(b) 5l/s

(vii) 15° (viii) 30° (ix) 45°

(c) 6l/s

Figure 5.30: Longitudinal Velocity Contours for different Angle of Bend at (a) 4l/s, (b) 5l/s, and (c) 6/s

It can be easily observed that the distribution of longitudinal velocity contours along the cross-section for 15°, 30° or 45° is not symmetric and is shifted towards the outer bank owing to the formation of secondary flows. However, the effect of secondary flow for 15° for all the flow rates on the redistribution of longitudinal velocity contours is not prominent due to their smaller magnitude (~0.03m/s).

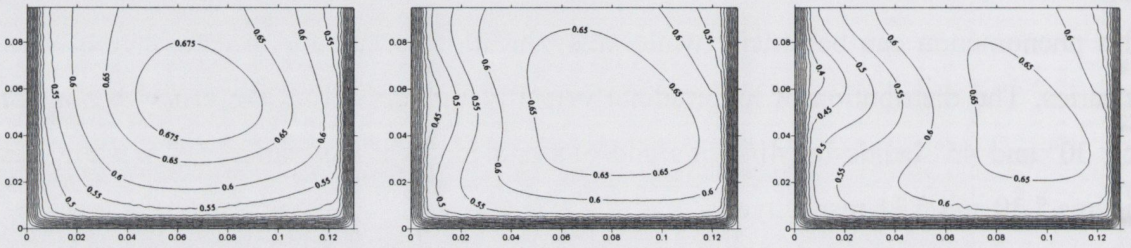

(i) 15° (ii) 30° (iii) 45°

(a) 8l/s

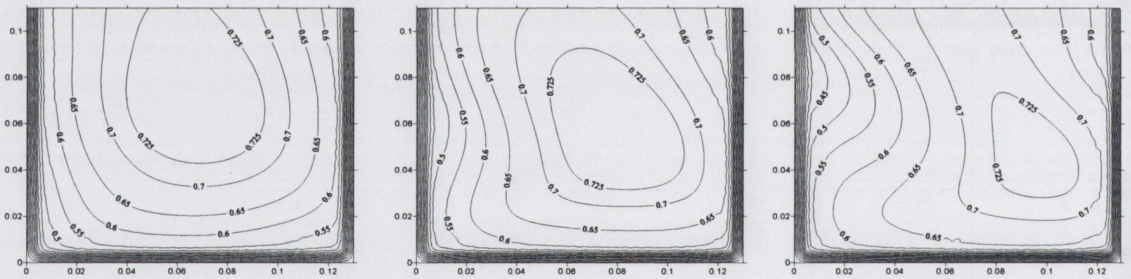

(iv) 15° (v) 30° (vi) 45°

(b) 10l/s

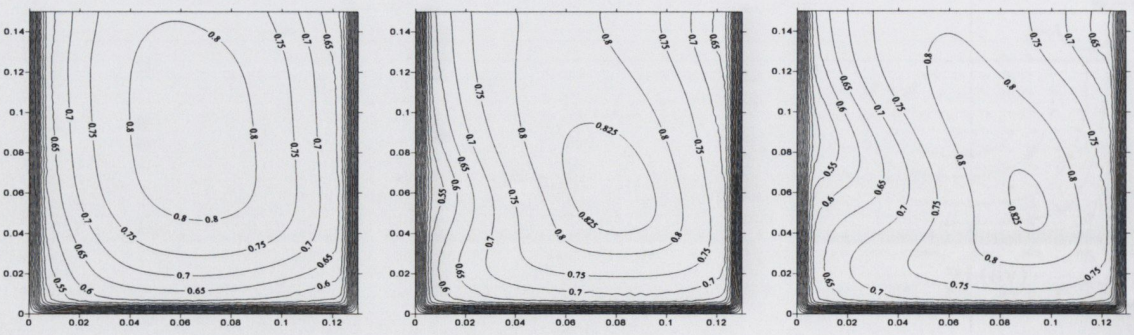

(vii) 15° (viii) 30° (ix) 45°

(c) 15l/s

Figure 5.31: Longitudinal Velocity Contours for different Angle of Bend at (a) 8l/s, (b) 10l/s, and (c) 15l/s

Equally, the distribution of longitudinal velocity contours for 15° is similar to any typical straight channel flow. A common feature exists in all the plots for the velocity contours where the maximum velocity contours lie well below the free surface, attributed to the presence of secondary flows. The asymmetric behaviour of the longitudinal behaviour of the velocity contours is considered to be due to both the angle of bend and the different flow rates as the secondary flow also varied for both the parameters to a certain extent. The contours also appear to be increasingly skewed outwards with an increase in the angle of bend (or secondary flows) and this trend was observed for all the ranges of flow rates analyzed. The corresponding maximum values of velocity contours for various flow rates was found to vary from approximately 0.55m/s to 0.82m/s for flow rates of 4l/s and 15l/s respectively. The grit removal efficiency at six different flow rates for bend angles of 15°, 30° and 45° is shown in Figure 5.32. It can be easily observed that the grit removal efficiency decreases with the increase in the bend angle, behaviour which can be understood in more detail by DPM analysis in Table 5.3.

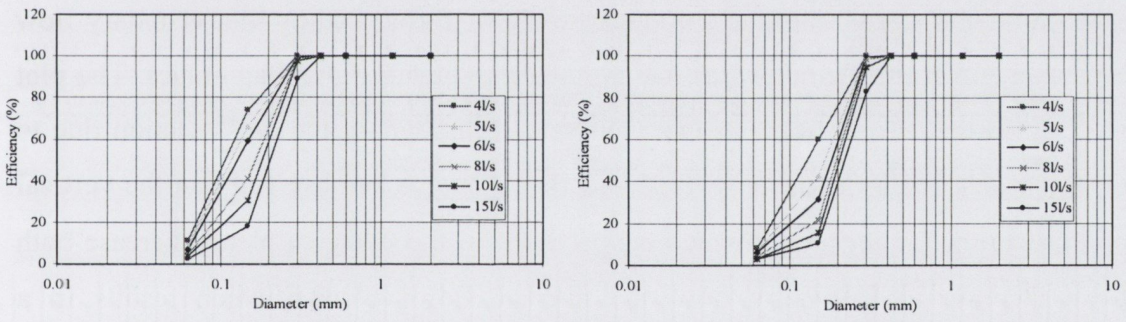

(a) 15° (b) 30°

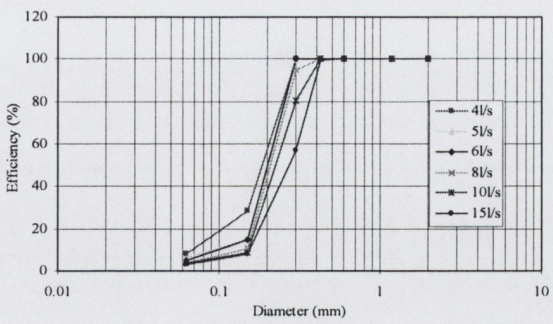

(c) 45°

Figure 5.32: Grit Removal Efficiency at Different Angles of Bend (a) 15°, (b) 30° and (c) 45°

As can be seen from Figure 5.32, the grit removal efficiency decreases (especially for particles ≤ 300μm) with an increase in the angle of bend for all the different flow rates showing the maximum efficiency for the 15° bend and the minimum for 45° at 4l/s. This behaviour of grit removal efficiency can be attributed to increasing magnitude of the secondary flows as angle of bend increases. The scatter plots of particles hitting the θ degree (15°, 30° or 45°) for all the various configurations are provided in Appendix B. It can be observed that the secondary flows were able to sweep the particles at the bottom inside of the curved grit channel but the particles were getting resuspended again at the plane due to the uplift velocity of secondary flows, making the removal of grit from the main flow very difficult. The scatter plots in the Appendix B for the various configurations represent that with the increase in the angle of bend, more and more particles are swept to the inside of the bend. The scatter plot for the 45° bend reconfirms that the particle sizes of 150μm and 300μm are highly influenced by the secondary flow at the inside and are shifted upwards due to higher secondary flow magnitudes. The plot for 15° shows that the particles remain well spread throughout the cross-section due to obvious reasons. From the plots in Appendix B, it can also be observed that the vertical co-ordinate in the scatter plot at which the particles hit the θ degree plane, increase both with an increase in secondary flow and average flow velocity which results in a significant decrease in the grit removal efficiency for the particles in the range ≤300μm. The pattern of scatter plot for particles of size >300μm does not seem to change for different configurations indicating that they are not affected either by secondary flows or average flow velocity, with their efficiency remaining at 100% for all the cases analyzed. This shows the robustness of curved grit channels for removal of larger particles. A significant effect of secondary flow can be seen for 45°, where the larger particles are swept well inside of the bend which was not the case with 15° or 30°. Table 5.3 also gives an indication of the extent of the effect caused by secondary flows. Using DPM analysis, a detailed number of particles hitting the sump plane (which is at the interface between sump and the main channel – an interior zone in FLUENT®) are presented along with the particles escaping from the sump and the actual grit removal efficiency. The particles escaping from the sump (after entering into the sump) indicates the effect of the

circulation zone (already discussed in Section 5.3.2) within the sump which allows some of the particles out of the sump into the main flow enabling them to escape to the main channel outlet. However, the number of particles entering into the sump provides a more quantitative depiction of the extent at which the particles are affected by increasing the angle of bend of any curved grit channel. Table 5.3 indicates that the percentage of particles (of size 150μm) which were entering into the sump reduces from approximately 95% to 35% for 4l/s (comparing θ = 15° to 45°) and from 31% to 14% for 15l/s highlighting the combined affect of average flow rate and secondary flow. The same behaviour was also found for different ranges of flow rates for the particle size of (≤ 300μm).

Table 5.3: Details of Particles entering into the Sump for Different Angles of Bend

Percentage of injected particles entering sump: θ = 15°						
Dia. (mm)	Q (l/s)					
	4	5	6	8	10	15
0.063	31.72	22.78	20.24	14.40	12.48	8.14
0.15	95.03	87.48	80.35	61.80	49.78	31.20
0.3	99.99	99.99	99.93	99.90	99.75	92.67
Percentage of injected particles entering sump: θ = 30°						
Dia. (mm)	Q (l/s)					
	4	5	6	8	10	15
0.063	26.03	19.85	19.12	14.17	11.88	8.14
0.15	71.30	54.24	43.32	34.63	27.20	31.20
0.3	100.00	100.00	100.00	99.17	96.03	92.67
Percentage of injected particles entering sump: θ = 45°						
Dia. (mm)	Q (l/s)					
	4	5	6	8	10	15
0.063	22.67	18.20	15.20	12.45	11.63	8.13
0.15	34.71	18.34	19.20	15.97	15.11	13.87
0.3	100.00	100.00	100.00	95.06	81.86	68.60

Overall, the CFD analysis of the effect of the bend angle suggests that with an increase in the angle of bend, the grit removal efficiency tends to decrease. It also concludes that the grit removal efficiencies of various particles are dependent on their vertical position rather than their horizontal position as they strike the θ° (15°, 30° or 45°) plane. The particles are able increasingly to congregate on the inside of the bend with an increase in

the angle of bend, but they tend to resuspend again due to the higher uplift velocity (see scatter plots in Appendix B). In other words, the higher the angle of bend, the higher the uplift velocity at the inside of the bend which tends to nullify the effect of the sweeping action of the secondary flows on grit particles and hence reduce grit removal by the curved grit channel. Further parametric investigations on the effect of channel width and radius of curvature are presented below which will enable the variation in the phenomenon of secondary flow (for these parameters) to be understood and secondly it will also provide a more realistic scenario of the curved grit channel as a potential grit removal device.

5.3.5 Effect of Channel Width

The effect of grit removal efficiency for two different widths of 0.19m and 0.25m was analyzed at the same average flow velocity of around 0.48m/s. The efficiency was evaluated at the same flow velocity as it has already been established that the efficiency reduces with the increase in the average flow velocity. Hence, the average flow velocity was kept the same for two different widths to analyze the effect of width only. It was observed that significant secondary flows were present of the order of 0.03m/s for the new cases and these secondary flows cause the particles to behave in a similar pattern as in the earlier case analyzed with 0.13m width (see Appendix B for scatter plots). Figure 5.33(a, b, c & d) shows the simulated secondary flows, longitudinal velocity contours and the grit removal efficiencies respectively for the width of 0.13m, 0.19m and 0.25m. It can be observed that the magnitude of the secondary flow increases with the increase in the width of the channel and the rate of increase is significantly higher from 0.13m to 0.19m than from 0.19m to 0.25m. The reason for the relative increase in the grit removal efficiency for the 150μm size particles can be attributed to the decrease in the flow depth for the cases of 0.19m and 0.25m. The decrease in the depth is because of the fact that as a grit channel is gravity driven flow and thus every flow velocity will have a unique depth corresponding to a slope and a width of any channel. Hence, due to the decrease in the depth, the flow particles will remain relatively less spread along the vertical depth. This phenomenon was also successfully simulated by the computational model which can

also be seen in the scatter plot in Appendix B allowing more particles (~95%) to enter into the sump. However, care should be taken while analyzing flow and particle behaviour for different flow rates as the depth-width ratio can also change with the variations in the flow rate as has already been discussed for the 0.13m width scenario.

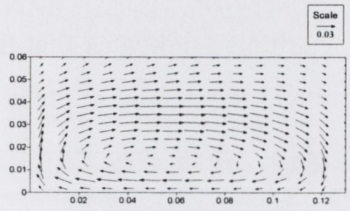

(i) Cross-flow Vector

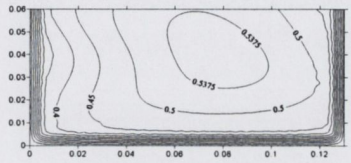

(ii) Velocity Contour

(a) Width: 0.13m

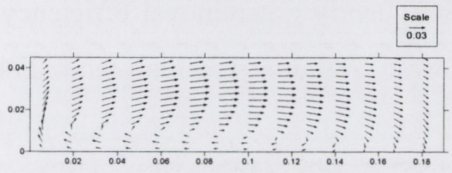

(i) Cross-flow Vector

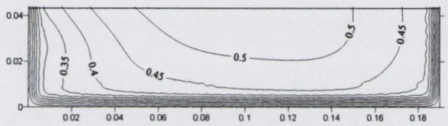

(ii) Velocity Contour

(b) Width: 0.19m

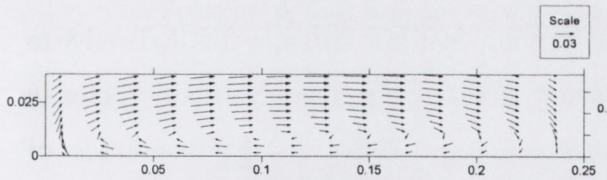

(i) Cross-flow Vector

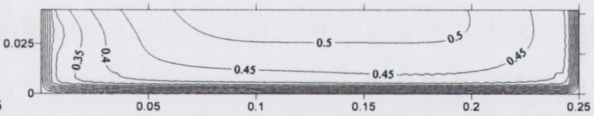

(ii) Velocity Contour

(c) Width: 0.25m

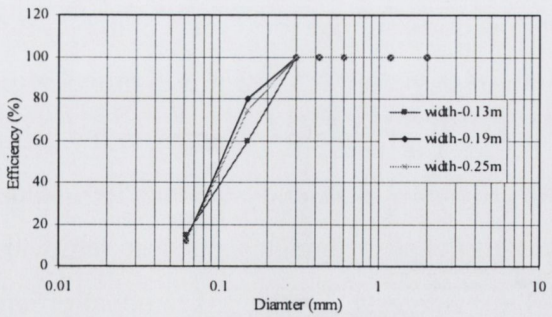

(d) Grit Removal Efficiency

Figure 5.33: Cross-Flow Velocity Vectors and Longitudinal Velocity Contours, (a) 0.13m, (b) 0.19m, (c) 0.25m, (d) Grit Removal Efficiency

Such investigations also ascertained that the width of the grit channel is not so critical in the design provided that the mean velocity remains between 0.5m/s to 1m/s which can be varied according to the number of channels with respect to the incoming flow rates at any wastewater treatment plant. CFD analysis on channel width also indicates that the width can be varied on-site depending upon the influent flow rate to the treatment plant.

5.3.6 Effect of Radius of Curvature

Three different radii of curvature were investigated for the standard 30° bend in order to establish their effect on secondary flows and subsequently grit removal efficiency. The three different radii of curvature investigated were 780mm, 1560mm and 2340mm making the radius of curvature to width ratio (R_c/B) of 6, 12, 18 and ∞ respectively for the channel width of 130mm and the angle of bend of 30°. Figure 5.34(a-d) shows secondary flows for all the four cases of R_c/B ratios analyzed. The secondary flow plots suggest that a decrease in the R_c/B ratio, leads to an increase in the magnitude of secondary flow. The increase is approximately doubled from 0.01m/s for R_c/B =18 to 0.04m/s for R_c/B = 6 indicating that the radius of curvature can also be a major factor in secondary flows and consequently in river morphology. However, the magnitude of secondary flow does not seem to change significantly from R_c/B = 12 to R_c/B = 6. The same behaviour can also be seen in axial velocity contour plots (Figure 5.34b) where the pattern of velocity contours is quite similar for R_c/B = 6 and R_c/B = 12. The grit removal efficiency for different radii of curvature is shown in Figure 5.34(e). A similar secondary flow trend for R_c/B = 6 and R_c/B =12 is also reflected in the grit removal efficiency for 150μm particles where the efficiency is around 54% and 59% respectively. This indicates that the secondary flow significantly regulates the grit removal efficiency to a large extent. Overall, Figure 5.34(e) suggests that the grit removal efficiency increases with an increase in the R_c/B ratio. Hence, grit removal efficiency for an infinite radius of curvature (or a straight channel with no bend) was also evaluated which indicates that the formation of excess secondary flows (i.e. greater than the settling velocity of particles ≤300μm) can be detrimental to the grit removal efficiency for the particles of size ≤300μm in the design of the grit channels to some extent.

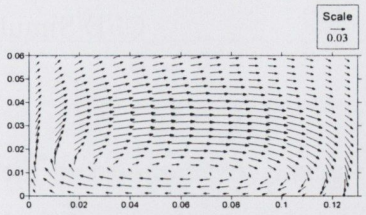

(i) Velocity Vector

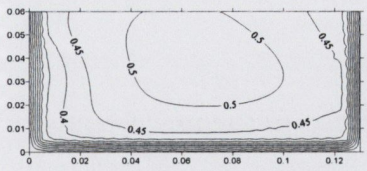

(ii) Velocity Contour

(a) $R_c/B=6$

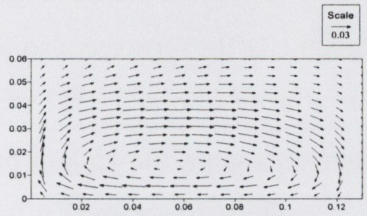

(i) Velocity Vector

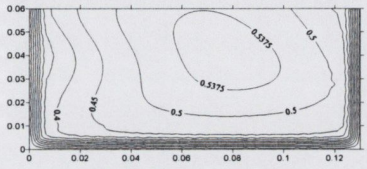

(ii) Velocity Contour

(b) $R_c/B=12$

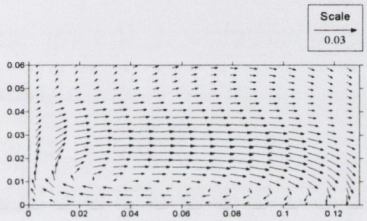

(i) Velocity Vector

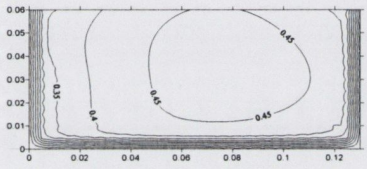

(ii) Velocity Contour

(c) $R_c/B=18$

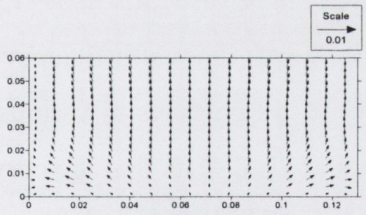

(i) Velocity Vector

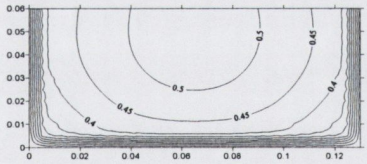

(ii) Velocity Contour

(d) $R_c/B=\infty$

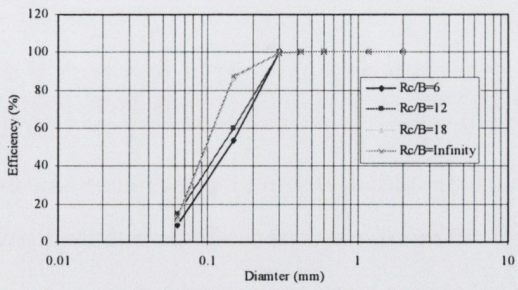

(e) Grit Removal Efficiency

Figure 5.34: (a) Cross-Flow Velocity Vectors and Longitudinal Velocity Contours (a) $R_c/B=6$, (b) $R_c/B=12$, (c) $R_c/B=18$, (d) $R_c/B=\infty$, (e) Grit Removal Efficiency

However, the grit removal efficiency for $R_c/B=18$ was found to be almost in the same range as in a straight grit channel for all the particle sizes indicating that a mild curvature of not more than 30° should be provided in conditions where curves or bends are unavoidable. CFD investigations on a straight open channel ($R_c/B=\infty$) were also carried out at the same geometrical and dynamical parameters as a result of outcomes from radii of curvature from which it was found that the maximum efficiency for 150μm particle was around 90% for 4l/s. It was also observed that the magnitude of secondary flows is very small (see scale in Figure 5.34d) and the distribution of longitudinal velocity contours is also symmetric. The scatter plots of various particles at 4l/s for straight channel flow is also shown in Appendix B. The CFD analysis on the effect of radius of curvature (R_c) again indicates that with the decrease in R_c, the grit removal efficiency tends to decrease which is attributed to the behaviour of secondary flow. Thus, based on all investigations, a mild curvature is required to attain the maximum efficiency which is almost equivalent to a straight grit channel (for example angle of bend of θ =15° and $R_c/B=18$ is almost equal to a straight channel) in terms of grit removal efficiency. This analysis presents a realistic scenario of the behaviour of the grit particles of various sizes ranging from 63μm to 2000μm in the curved grit channel and suggests that the curvature within the channel promotes the accumulation of grit on the inside of the bend but that it is the vertical position rather than horizontal position of grit which decides their respective removal efficiencies. Some studies on the position of the sump were also analyzed and it was found that the original design in which the sump was placed right after the bend is the optimum position for maximum grit removal. Overall, the CFD analysis of various geometrical and dynamical parameters on curved grit channels has also highlighted the significance of presence of secondary flows in natural rivers and certain man-made open channels where curves and bends in their alignment are often unavoidable in the design.

5.4 Suggested Analytical Model for Secondary Flow Prediction

An attempt has been made to develop a mathematical relation between the angle of bend (θ), radius of curvature to width ratio (Rc/B) and the average velocity with the simulated

average magnitude of secondary flow. The CFD simulations on curved open channel has shown that the secondary flow tends to increase with the decrease in the radius of curvature and the same tends to increase with the increase in the angle of bend. However, it should be noted that the rate of increase of secondary flow is comparatively more from 15° to 30° than 30° to 45°. This pattern is almost consistent with all ranges of flow rates (or average velocity analyzed) as shown in Table 5.4.

Table 5.4: Comparison between Simulated and Model Values of Secondary Flow

Rc/B=12				
Angle	Average Velocity (m/s)	Simulated - CFD (m/s)	Model (m/s)	Difference (%)
15deg	0.48	0.028	0.029	1.9
	0.51	0.032	0.030	5.2
	0.54	0.036	0.032	10.6
	0.59	0.035	0.035	1.0
	0.65	0.039	0.040	1.4
	0.74	0.044	0.047	6.5
30deg	0.48	0.034	0.030	11.6
	0.51	0.037	0.032	13.8
	0.54	0.036	0.034	6.3
	0.59	0.042	0.037	12.1
	0.65	0.045	0.041	8.7
	0.74	0.054	0.048	10.3
45deg	0.48	0.038	0.036	6.3
	0.51	0.034	0.037	10.0
	0.54	0.035	0.039	12.1
	0.59	0.042	0.042	1.1
	0.65	0.043	0.047	8.4
	0.74	0.059	0.054	8.6
Rc/B=6				
30deg	0.48	0.051	0.059	15.7
Rc/B=18				
30deg	0.48	0.019	0.021	10.5

Based on this analysis, a relation between secondary flow and the various dynamical and geometrical parameters is proposed:

$$S_{xy} = \left(\frac{\theta}{1+\theta}\right)^{a} + \left(\frac{u_{avg}^{b} - u_{avg}^{c} + u_{avg}^{d}}{R_c/B}\right) \tag{5.4}$$

where, S_{xy} is the strength of the secondary current, θ is the angle of bend in radians, u_{avg} is the average velocity (m/s), R_c is the radius of curvature (m), B is the width of the channel (m) and a, b, c & d are constants given by a = 6, b = 1.2, c = 2.9, d = 4.2. It can be seen that the predicted values are compared well with simulated ones and the main feature of the variation of the secondary flow for various geometrical and dynamical parameters are very well captured by the model. However, some inconsistencies exist with the magnitude of the secondary currents and the maximum difference is found for radius of curvature to width ratio of 6 and 18 respectively. It should also be noted that this mathematical relationship is only an indication of the strength of secondary flow and does not give additional information regarding formation of outer bank cell, observed at higher flow rates. Overall, this model provides a detailed behaviour of the secondary flow for the parameters investigated in this thesis. Based on the study, there are few limitations observed for this model which are as follows:

(i) Valid for only narrow channels (B/D<5).

(ii) Unable to predict outer bank cell scenario.

(iii) Requires verification for higher angles of bend (θ>60°). However, the model predicts the secondary flow of the case study reasonably well where the model value is approximately 0.054m/s compared to experimental value of around 0.055m/s.

(iv) Not valid for radius of curvature: $R_c=\infty$.

These limitations of the analytical model are due to various factors such as turbulent flow, variable bottom topography of the channel and shape of the channel cross-section. Studies done by Hicks, *et al.*, (1990), Ye and McCorquodale, (1998) and Rameshwaran and Naden (2004a, b) also indicated that the secondary flow does not increase indefinitely as they move across a curved channel and approaches a maximum value around 90°. This model though remains valid for the present study for the angles of bend of 0° to 45°, however, additional data is required both experimentally and computationally to validate this model for all scenarios of angle of bend, flow rates and radius of curvature and also to make modifications, if required.

5.5 Overall Analysis: Effect of Uplift Velocity and Variation of Grit Removal Efficiency with Settling Velocity to Average Velocity Ratio

In order to better understand the effect of uplift (base) velocity or the vertical velocity component of secondary flow on behaviour of the particles, the settling velocity of 150μm is compared with the base velocity. Figure 5.35(a-f) shows the vertical component of the velocity at three different horizontal lines at heights of 5mm, 15mm and 30mm from the base respectively at θ° plane for different configurations at 4l/s. It should be noted that some plots in Figure 5.35(a-f) are plotted at different vertical scale in order to better understand the variation of vertical velocity for different configurations. The settling velocity of 150μm particle (~0.02m/s) is shown in Figure 5.35(a). It can be observed from the Figure 5.35(a-f) that the uplift velocity tends to increase from 5mm to 15mm height but then it again tends to decrease upwards till 30mm. The vertical velocity plots at three lines at different vertical depths also enable to understand the variation of the uplift velocity at the same in more detail which is not obvious from the secondary flow discussed earlier in the chapter. The vertical velocity component is maximum for $R_c/B=6$ (~0.042m/s) which agrees well with the cross-flow velocity vector (secondary flow) plots. However, the uplift velocity for $R_c/B=18$ and $R_c/B=\infty$ is very small making their grit removal efficiency maximum as the particle tends to remain near the base of the channel. Furthermore, the velocity for straight channel is also very small (~0.0025m/s) as there is no curvature in the alignment and the secondary flow formed in this type of channel is known as '*Prandtl secondary flow of the second kind*' (Prandtl, 1952). The Figure 5.35(a-d) also indicates that the uplift velocity at various heights remain close to or greater than 0.02m/s making removal of 150μm particle size a difficult process by curved grit channel. The assessment of grit removal efficiency for different angles of bend and flow rates (or average flow velocity) is also done in terms of settling velocity to average velocity ratio (v_s/U_{avg}). The parameter (v_s/U_{avg}) was selected on the basis of studies done by Harwood and Saul (1999) on combined sewer overflow chambers. Figure 5.36(a-f) shows the variation of grit removal efficiency for different settling velocity to velocity ratios. Figure 5.36(a-c) shows the variation of efficiency for a particle diameter

and different angle of bend whereas Figure 5.36(d-f) shows the variation of efficiency for different flow rates and angle of bend.

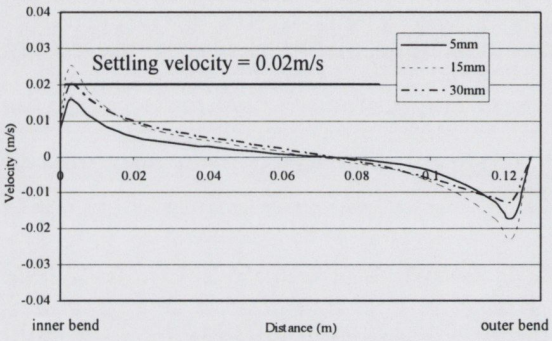

(a) $R_c/B=12$, $\theta=15°$

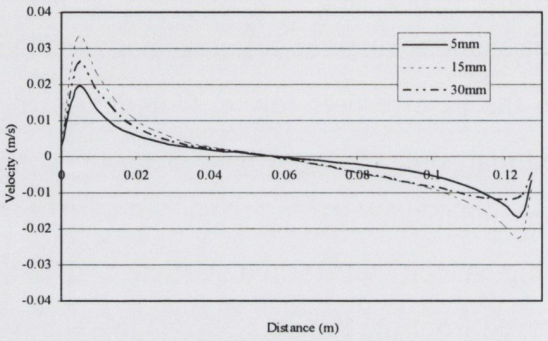

(b) $R_c/B=12$, $\theta=30°$

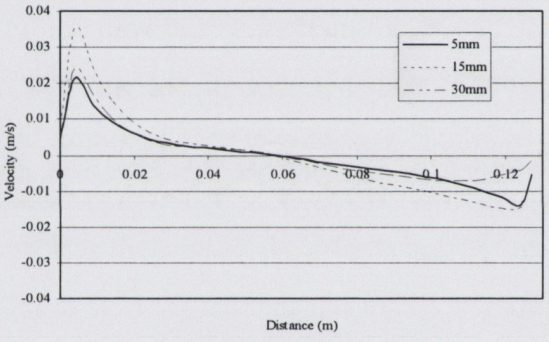

(c) $R_c/B=12$, $\theta=45°$

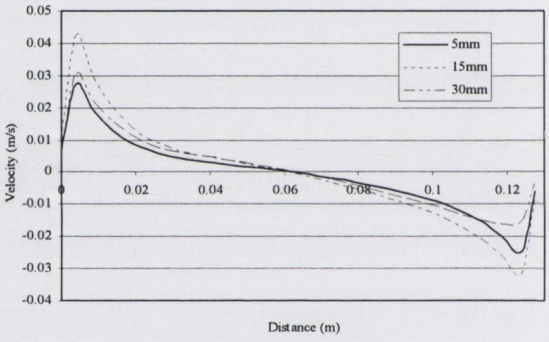

(d) $R_c/B=6$, $\theta=30°$

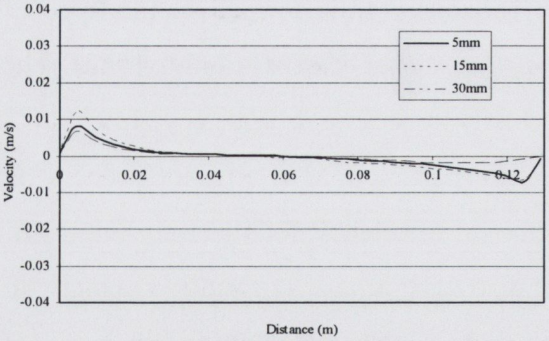

(e) $R_c/B=18$, $\theta=30°$

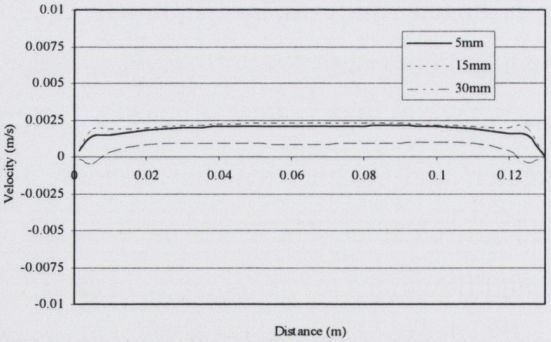

(f) $R_c/B=\infty$ (Straight Channel)

Figure 5.35: Uplift Velocity for different Configurations at different Heights (a) $R_c/B=12$, $\theta=15°$, (b) $R_c/B=12$, $\theta=30°$, (c) $R_c/B=12$, $\theta=45°$, (d) $R_c/B=6$, $\theta=30°$, (e) $R_c/B=18$, $\theta=30°$, (f) $R_c/B=\infty$ (Straight Channel)

It should be noted that the analysis for a specific particle range of only 0-300μm is performed here as the grit removal efficiency of the higher diameter particle ranges (>300μm) were observed to be 100% (see Figure 5.32). It can be seen that the grit

removal efficiency decreases with the increase in the angle of bend for all range of average flow velocities (or settling velocity to average flow velocity ratios). This phenomenon is consistent for all the particle sizes which can be seen in Figure 5.36(a-c).

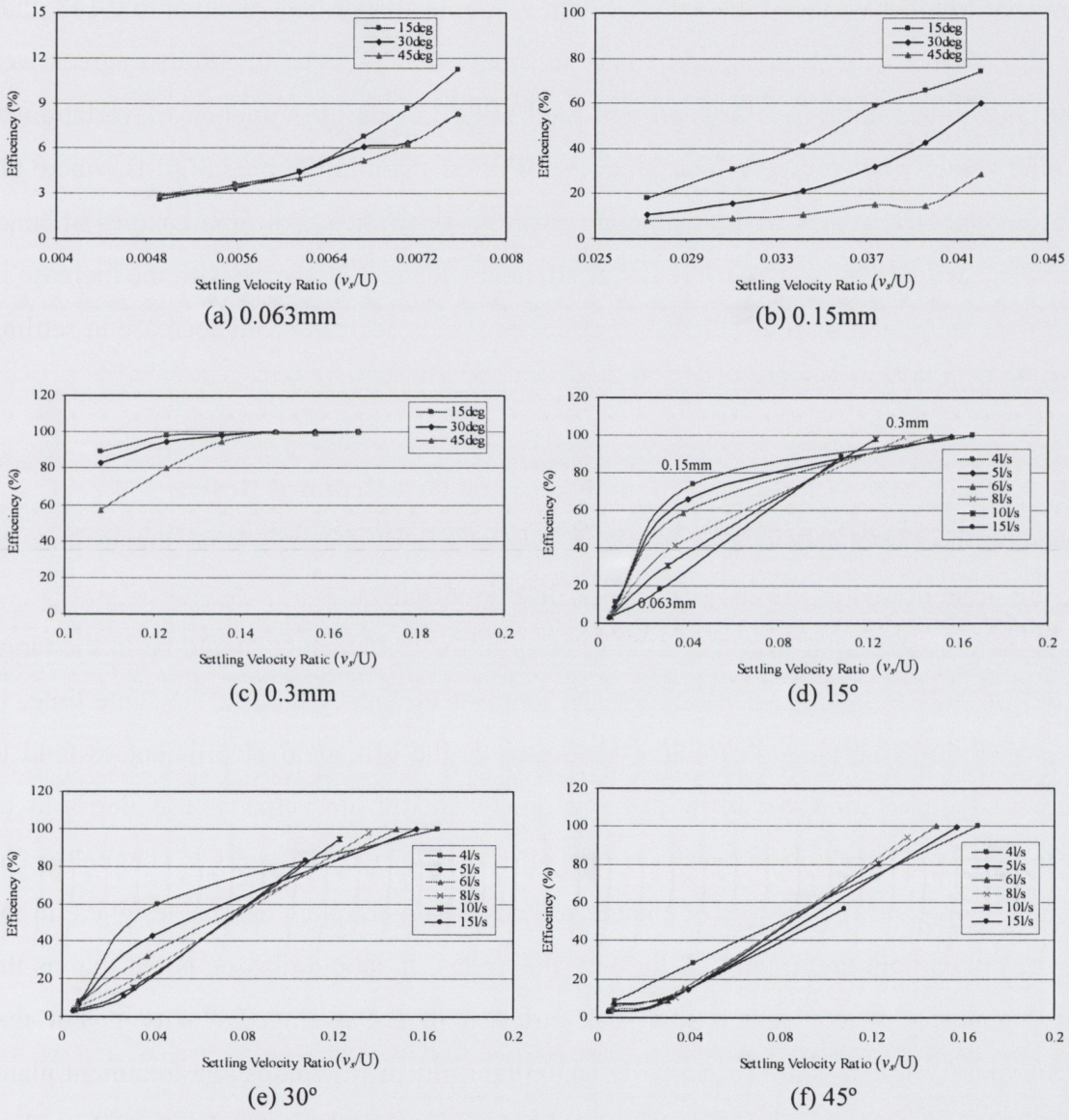

Figure 5.36: Variation of Grit Removal Efficiency with Settling Velocity Ratio (v_s/U) for different configurations, (a-c) Particle Size, (a) 0.063mm, (b) 0.15mm, (c) 0.3mm, (d-f) Angles of bend, (d) 15°, (e) 30°, (f) 45°

In addition to this pattern of grit removal efficiency variation, a significant occurrence is also found that the grit removal efficiency is approximately 100% at the velocity ratio

(v_s/U_{avg}) of 0.148. This ratio is independent of the flow rate, angle of bend or the particle diameter. In other words, if the value of ratio v_s/U_{avg} is greater than or equal to 0.148, than the 100% grit removal efficiency would be achieved. The value 0.148 also agrees well with the studies done by Harwood and Saul (1999). This phenomenon of variation of settling velocity to average velocity ratio is reflected again in Figure 5.36(d-f), where the grit removal efficiencies are plotted against various flow rates at different angles of bend. It can be easily seen that the grit removal efficiency tends to decrease with the increase in the flow rate (average flow velocity) or efficiency tends decrease with decrease in settling velocity to flow velocity ratio.

5.6 Recommendations for Design of full-scale Grit Removal Device

Based on the parametric investigations on the curved grit channel, some suggestions for the full-scale design of the grit channel are discussed below.

As already discussed in Chapter 3, the velocity in the grit channel should be in the range of 0.5 to 1m/s to attain the maximum grit removal efficiency and, at the same time, to keep all the grit particles in motion. However, as the grit removal efficiencies tend to decrease with an increase in the average flow velocity, the velocity also needs to be controlled by flow regulators such as Parshall flumes or weirs (as in CV channels). The channel width and the number of channels in any treatment plant can be designed on the basis of maximum and minimum influent flow rates. It should also be noted that as the grit channel is open channel flow, the variation of the average velocity is not that sensitive to different widths at variable incoming influent flow rates at a treatment plant. Simultaneously, the depth-width ratio should also not exceed 1.1 for the maximum flow rate. The parametric investigations suggested that if a bend exists in a grit channel, the grit removal efficiencies for various particle sizes tends to decrease and should be avoided in the design. However, a mild curvature having an angle of bend $\leq 30^{\circ}$ could be provided if a specific site situation dictated such a design. The sump (to collect grit) should again be placed right after the bend as already discussed in Chapter 3. Baffles should be incorporated at regular intervals within the sump to improve the grit removal efficiency. The length of the sump should be such that it will allow sufficient settling

time for the lowest particle size targeted for removal during the primary treatment process. For example, for the removal of a 150μm particle at an average velocity of around 0.35m/s, the length required can be calculated as:

$$d_{sump}/v_s = l_{sump}/v \tag{5.5}$$

where, d_{sump} = depth of the sump (m), v_s = settling velocity (m/s), l_{sump} = length of the sump (m), v = flow velocity (m/s).

$\therefore l_{sump} = 0.4*0.35/0.02 = 7\text{m}$

Hence, for a sump depth of at least 0.4m, the length of the sump required for a full-scale grit channel is minimum 7m. It should be noted that in the present laboratory study, the length of the sump was kept as 0.4m in order to enable the small scale laboratory experiments to be performed. This reduced length of 0.4m was kept constant in all the parametric investigations in order to observe only the effect of other (individual) parameters such as the angle of bend, flow rate, radius of curvature and channel width. The other scaling effects such as kinematic similarity can also be assessed for Chapter 3 where it was mentioned that the inlet length to the bend should be at least 12 times the width of the channel. Additionally, in a full-scale grit channel, the inlet length to the bend would obviously be greater than the length of the channel in the laboratory model and would only aid in increasing the grit removal efficiency as it would provide additional time for the particles to settle at the channel bottom.

6. REVISED PHYSICAL MODELLING RESULTS

This chapter discusses the outcomes of revised physical modelling performed on the 30° curved grit channel following the introduction of baffles within the sump as a result of the improved efficiency predicted by the mathematical model. The results will also be used to ascertain the accuracy of the predictions by the computational model.

6.1 Experimental Procedure

The experimental procedure during the revised physical modelling on the modified 30° curved grit channel was similar to that as discussed previously in Chapter 3 and so is not repeated here for the sake of brevity. Three different baffle and sump outlet configurations with main flow of 4l/s were investigated, two with baffle 1 with and without sump flow (outlet 2) and the other one with all three baffles 1, 2 and 3 without sump flow (see Figures 5.21(a) and Figure 6.1 for locations of the different configurations).

6.2 Sump with no Flow

Figure 6.1(a, b) shows the location of the baffles on which revised physical experiments with flow rate of 4l/s were performed. Again, the detailed data in tabular form are shown in Appendix A.6. As has already been discussed in Chapter 5, the introduction of the baffle within the sump, significantly reduces the magnitude of the circulation zone which results in particles of especially size 150-300μm being removed more efficiently. It was also found computationally that, the grit removal efficiency of 150-300μm particles could increase to as high as 95% with the introduction of baffles. Figure 6.2 shows the results of the revised experiments for three different configurations superimposed with the respective computational predictions. The grit removal efficiencies are shown along with their standard error values and it can be seen that the main trend is again established

where an increase in removal efficiencies follows on with the increase in the particle size. The range of the standard error values also tends to decrease with an increase in the particle size. Although, the grit removal efficiencies for various grit particle sizes ≥300μm was not measured during the physical experiments as exactly 100% this can again be attributed to experimental errors and minor flow variations within the main channel. However, the values were very close to 100%, as can be observed from Figure 6.2, and the behaviour of these particles for all the three cases analysed also remained consistent. As was discussed in the Chapter 5, the computational model under predicts the removal efficiencies- behaviour which was observed with this set of revised experiments as well. However, the agreement between the experimental and computational results with baffles tends to improve to some extent with the smallest difference between experimental results and computational predictions being found for the trials with baffle 1 (see Figure 6.2b). The average grit removal efficiencies observed for 150-300μm with no sump outlet was approximately 94% and 97% for baffle 1 and baffle1-2-3 respectively. However, this minor variation during physical experiments between the grit removal efficiency for 150μm particles size is considered to be random due to the experimental error as it was already established computationally that introduction of only baffle 1 tends to improve the removal efficiency to the same extent as having all three baffles. The computational prediction of grit removal efficiency for particle size 63μm remains consistent but is over predicted by the computational model.

(a) Side view (b) Front view

Figure 6.1: Baffle Plate Locations (baffle1-2-3), (a) Side view, (b) Front view

6.3 Sump with Flow

Figure 6.2(c) shows the comparison using the configuration of baffle 1 with flow rate out of the sump (outlet 2 - 0.45l/s) for the main flow of 4l/s, which can be observed be behave in a similar pattern as the trials with out of the sump. However, the standard error for particle size 63-150μm was relatively higher which has been attributed to experimental error.

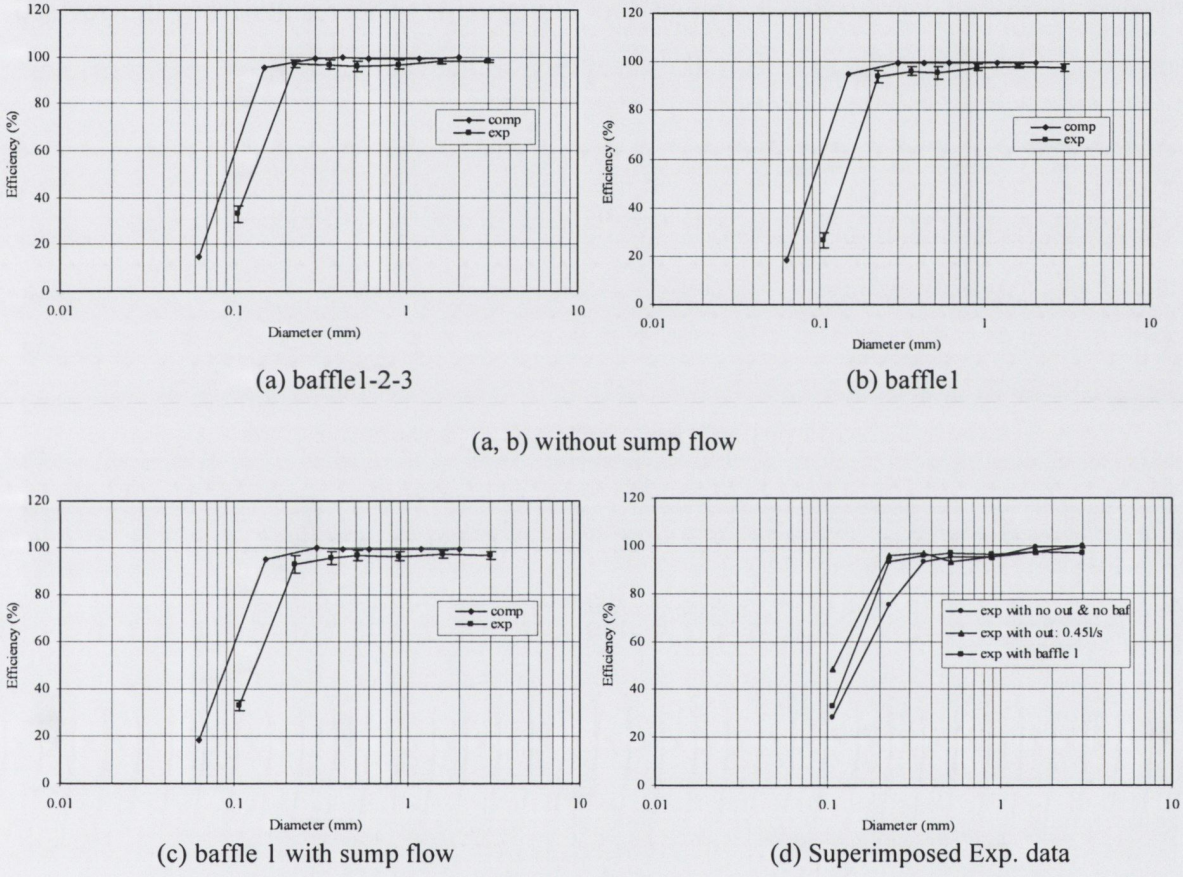

(a) baffle1-2-3

(b) baffle1

(a, b) without sump flow

(c) baffle 1 with sump flow

(d) Superimposed Exp. data

Figure 6.2: Grit Removal Efficiencies, (a) baffle1-2-3 without flow, (b) baffle 1 without flow, (c) baffle 1 with sump flow 0.45l/s, (d) Superimposed Exp. data

The DPM analysis also indicated that only <3% of particles were able to re suspend again due to significant reduction in the circulation zone within the sump as already discussed in Chapter 5. This value was approximately 11% for the case of without baffles within the sump indicating the significance of the same at 4l/s with no flow. Figure 6.2(d) shows the superimposed experimental results with previous results of no baffles and no

outlets configurations. It indicates that the introduction of baffles significantly results in the increase in the removal efficiency of 150-300μm. The salient feature of the curved grit channel is again very well simulated indicating the accuracy of the CFD model to simulate behaviour of grit particles using the discrete phase model and its potential for use in storm and wastewater treatment process systems. The results from the revised physical experiments also reconfirm the capability of the CFD model.

7. CONCLUSIONS AND RECOMMENDATIONS FOR FUTURE WORK

An evaluation of grit removal efficiency on a curved grit channel for different geometrical and dynamical parameters was car ried out in detail both physically and computationally. A case study was also modelled in order to verify the ability of CFD software FLUENT® to simulate secondary flows. The methodology adopted in modelling secondary flows in the case study was then employed in the simulation of curved grit channel flow. Once the computational model of the curved grit channel was calibrated, parametric investigations were undertaken in order to establish their effects on the secondary flows and subsequent grit removal efficiency. The physical experiments were then performed again on the modified curved grit channel (which involved adding baffles into the sump) in order to ascertain the accuracy of the CFD model to simulate the behaviour of grit particles within the curved grit channel. A good agreement was observed between the results of physical modelling and the computational predictions.

7.1 Conclusions

The case study was initially used in order to establish a methodology to simulate secondary flows in curved open channels; following which the physical model of a curved grit removal channel was constructed and experiments were carried out to provide benchmark data for the successful calibration of the computational model. The main conclusions of this study are as follows:

7.1.1 Secondary Flows

- A reasonably good comparison was found between the experimental and computational results using the highly instrumented case study and the main flow features were very well simulated. However, a limitation of the computational

model was an under prediction in the longitudinal velocity contours and cross flow velocity vectors to some extent. For the case study, in addition to the main circulation cell, an outer bank cell was also found at the investigated 60° cross-section at the intersection of the outer bank and the free surface for a depth/curvature ratio of 0.055 and a curvature/width ratio of 5.

- CFD studies on the 30° curved grit channel indicate that, on average, the magnitude of secondary flows varies approximately from 0.03m/s to 0.06m/s with the increase in the average channel flow velocity from 0.48m/s to 0.74m/s (flow rates of 4l/s to 15l/s).
- Three different radii of curvature were investigated on the 30° curved grit channel and CFD studies on the same indicate that with a decrease in the radius of curvature, the magnitude of the secondary flow increases. This increase is quadrupled from approximately 0.01m/s for $R_c/B=18$ to 0.04m/s for $R_c/B=6$. The magnitude of the secondary flow also tends to increase with an increase in the bend angle, although the rate of increase in secondary flow magnitude for a bend of 15° to 30° was relatively higher than from 30° to 45° - a trend that was observed to be almost consistent for all ranges of flow rates from 4l/s to 15l/s.
- Due to the presence of the secondary flows, the distribution of longitudinal velocity contours was not symmetric and tends to become increasingly skewed towards the outer bank with an increase in the magnitude of secondary flows. In addition to the main circulation cell, an outer bank cell was also found in the curved grit channel for a depth/curvature (H/R_c) ratio of 0.096 at the flow rate of 15l/s. The outer bank cell seems to form at relatively higher values of H/R_c. However, further parametric studies may be helpful (radii of curvature, width, flow rate, etc.) in order to understand this mechanism in more detail with respect to the conditions that lead to the generation of the outer bank cell.
- The revised physical modelling results have also ascertained the accuracy of the predictions of the calibrated CFD model of curved grit channel.

- Secondary flows in straight open channels are very small compared to curved open channels and the particles tend to remain near the bottom wall enabling their removal relatively easier by the sump.
- An analytical model has also been suggested in which magnitude of secondary flow is predicted by a relationship consisting of angle of bend, average velocity and radius of curvature to width ratio.

7.1.2 Grit Removal Efficiencies – DPM Analysis

- Particle densities of various particle sizes from 63μm to 2000μm were measured during the physical modelling and the same densities were provided as an input to the computational model to improve precision. Grit removal efficiencies were also evaluated for the 30° curved grit channel for three different sump openings and it has been concluded that the optimum grit removal was attained using a fully open sump across the base of the channel as the all heavier particles (≥1180μm) does not seem to accumulate at the inside of the bend due to secondary flow.
- Grit removal efficiencies tend to increase with an increase in particle size at the same flow rate and they tend to decrease with the increase in the main channel flow rate (or the average flow velocity). Again, removal efficiencies tend to decrease with an increase in the angle of bend for the same flow rate, varying approximately from 75% to 30% for bend angles of 15° and 45° respectively for 150μm particle. The analysis with different radii of curvature for 4l/s indicates that with an increase in the radius of curvature, the grit removal efficiencies tend to increase for any particle size. This phenomenon can again be attributed to the induced secondary flows where they tend to decrease with increased curvature. This leads to the conclusion that the uplift velocity at the inside of the bend should be less than the settling velocity of the critical particle size in consideration (150μm in present case) to achieve maximum grit removal efficiencies.
- The extent of grit removal is decided by the location of the particles hitting any θ° (15°, 30° or 45°) vertical plane (just preceding the sump). It is the particles vertical

location rather than their respective horizontal location when they strike at any θ plane which remains the critical issue in deciding the grit removal efficiency for the different particle sizes. Introduction of baffles within the sump improved the grit removal efficiency for the 150μm particle size significantly from approximately 60% to 90%.

- It is also concluded that the settling velocity to average velocity ratio of 0.148 or higher results in 100% removal of grit particles irrespective of the flow rate, angle of bend or particle diameter.
- Baffle plates should be positioned within the sump at regular intervals in order to reduce the effect of an induced circulation zone within the sump and thus increase the overall grit removal efficiency.
- Overall, the CFD analysis of the curved grit channel for various geometrical and dynamical parameters indicated that the grit removal efficiency for various grit particle sizes tends to decrease with the increase in the curvature in the alignment. Hence, a bend in the design of grit channels should be avoided as uplift velocity of secondary flow tends to lift particles again as they reach the inside of the bend.

7.2 Potential of Curved Grit Channel as a Grit Removal Device

This study suggests that with the increase in the angle of bend or decrease in the radius of curvature of the curve grit channel, the magnitude of secondary flow tends to increase (or the magnitude of the uplift velocity tends to increase) which results in the re-suspension of grit particles (especially 150μm) at the inside of the bend. This phenomenon leads to a relatively fewer number of particles entering into the sump compared to a straight grit channel where no significant secondary flows are formed (due to absence of curvature in the alignment) and hence a reduced grit removal efficiency for a curved grit channel. Overall, it is recommended to avoid any curvature in alignment in the design of grit channels as they will promote the development of secondary flows. However, it is suggested the incorporation of baffle plates within the sump will reduce the effect of an induced circulation zone on the grit particles once they enter in the sump.

7.3 Limitations of the Study

The aim of the study was to simulate the flow behaviour and movement of grit particles within the curved grit channel using a commercial CFD package. The development of an in-house code and algorithm were out of the project's scope. Hence, it became very difficult to provide robust reasons for under prediction by the computational model for fluid flow and DPM results in terms of the inbuilt turbulence models, discretization schemes, drag laws and the numerical grid. The comparison of the computational results with the high resolution experimental data of the case study (Blanckaert, 2003) indicated that the predictions using the CFD software FLUENT® were under predicted with respect to the experimental data to some extent; the discrepancies also existed for the prediction of grit particle behaviour in the curved grit channel. These discrepancies could also be attributed to the magnitude of the secondary flows in the curved grit channels and circulation zone within the sump which was not verified with their experimental results due to unavailability of high resolution experimental techniques. The variation of drag laws for various types of particles with respect to size and shape was also not analyzed experimentally and would have otherwise enabled the interaction of these grit particles with the flow to be understood more clearly. Thus, a further detailed study would be required in order to improve the computational predictions and gain a better understanding of the physics of the flow. This can be achieved firstly, by performing three dimensional experimental studies using high resolution experimental techniques (to understand multi-phase flows better) followed by computational validation. This will enable fully the processes associated with multi-phase flows to be more clearly understood, particularly those in the wastewater treatment industry. Such analysis will also aid in providing more precise reasons (in terms of the assumptions associated with the turbulence models, drag laws and numerical schemes) for the discrepancies between the experimental and computational studies, if any.

7.4 Recommendations for Future Work

- It has been observed that the DPM model was able to simulate all the main features of the grit particle movement within the curved grit channel satisfactorily. However,

the comparison between the experimental and computational predictions was not totally precise and further simulations with the '*Eulerian*' or '*Mixture*' multi-phase could be attempted to improve the model to include the mechanisms for the exchange of momentum, heat, and mass between the phases (i.e. interaction between the grit particles at high concentrations). This technique would incorporate the solution of additional conservation equations of mass and momentum for each phase and would require an enormous amount of computational time and space.

- Experimental investigations with high resolution experimental techniques such as an Acoustic Doppler Velocimeter (ADV) or Laser-Doppler Anemometer/ Velocimeter (LDA/V) on curved grit channels with multi-phase flows should be carried out. This would enable the secondary flow phenomenon and actual behaviour of grit particles within flow (i.e. drag laws, velocity drift between flow and the solid phase, etc.) to be evaluated in a more detailed way. The experimental data obtained using these instruments would enable the computational model to be validated more precisely for multi-phase flows.
- A full-scale trial on a curved grit channel could also be carried out on raw sewage which particularly investigates the removal efficiency of the process under shock loading events for example, after rainstorms. The full-scale performance of the curved grit channel can also be compared with straight CV channels.
- Experiments can also be conducted in which pressure measurements at the wall can be done using pressure points at various cross-sections.
- The present work can be extended to the development of in-house code which will aid to improve the understanding of physics of the flow and numerical schemes.

REFERENCES

Annen, G. W. (1972). Efficiency of a grit chamber. Water Research Pergamon Press. vol. 6., pp. 393-394.

Bathurst, J. C., Thorne, C. R. and Hey, R. D. (1977). Direct measurement of secondary currents in river bends. Nature, vol. 269, pp. 504–506.

Bathurst, J. C., Thorne, C. R. and Hey, R. D. (1979). Secondary flow and shear stress at bends. J. of the Hyd. Div., ASCE, vol. 105, pp. 1277–1295.

Bagnold, R. A. (1966). An approach to the sediment transport problem from general physics. US Geological Survey, Professional Paper 422-I, Washington DC, USA, 37 pages.

Beder, S. (1993). From sewage farms to septic tanks: Trials and Tribulations in Sydney, Journal of the Royal Australian Historical Society, vol. 79, parts 1 and 2, pp. 72-95.

Bhallamudi, S. M. and Chaudhry, M. H. (1991). Numerical modelling of aggradation and degradation in alluvial channels. J. of Hyd. Engg., ASCE, vol. 117, no. 9, pp. 1145-1164.

Blanckaert, K. (2003). Flow and turbulence in sharp open channel bends. PhD Thesis, EPFL, Laussane.

Booij, R. (2003). Measurements and large eddy simulations of the flows in some curved flumes, J. of Turbulence, vol. 4, pp. 1-17.

Boussinesq, J. (1877). Th'eorie de l'ecoulement tourbillant. Memoires Present'es par Div'ers Savants a l'Academie Royale des Sciences de l'Institut de France 23, pp. 46-50.

Bradshaw, P. (1970). Experimental Fluid Mechanics, 2nd Edition. Pergamon Press Ltd.

Brenner, A. and Diskin, M. H. (1991). Model study of jet-circulated grit chamber. J. of Env. Engg., ASCE, vol. 117, no. 6, pp. 782-787.

Bridge, J. S. (1976). Bed topography and grain size in open channel bends. Sedimentology, Vol. 23, no. 3, pp. 407-414.

British Standard (1990). BS:1377 - Part 2.

Cebeci, T. and Bradshaw, P. (1977). Momentum transfer in boundary layers. Hemisphere Publishing Corporation, New York.

Chadwick, A. and Morfett, J. (1993). Hydraulics in civil and environmental Engineering. E & FN SPON Publishers, London.

Chanson, H. (1999). The hydraulics of open channel flow: An Introduction. Arnold Publishers, London.

Chow, V.T. (1973). Open channel hydraulics. Civil Engineering Series, McGraw-Hill International Editions.

Cokljat, D., & Younis, A. (1995). Second-order closure study of open-channel flows, J. of Hyd. Engg., ASCE, vol. 121(2), pp. 94-107.

Corney, R. K. T., Peakall, J., Parsons, D. R., Elliot, L., Amos, K. J., Best, J. L., Keevil, G. M. and Ingham, D. B. (2006). The orientation of helical flow in curved channels. Sedimentology, vol. 53, pp. 249-257.

Demuren, A. O. and Rodi, W. (1986). Calculation of flow and pollutant dispersion in meandering channels. J. Fluid Mech., vol. 172, pp. 63-92.

Demuren, A. O. (1989). Calculation of sediment transport in meandering channels. Tech. Session A, Proc., 23rd IAHR Congr., IAHR, Delft, Netherlands.

Demuren, A. O. (1991). Development of a mathematical model for sediment transport in meandering rivers. Rep. No. 693., Inst. for Hydromechanics, University of Karlsruhe, Karlsruhe, Germany.

Department of Public Works, Los Angeles (DPW, LA) (1998). Performance Certification Report. Hyperion Full Secondary Headworks and Service Facilities.

Dingman, S. L. (1984). Fluvial Hydrology, pp. 383. New York: W.H. Freeman.

Egarr, D. A., Faram, M. G., O' Doherty, T. and Syred, N. (2004). An investigation into the factors that determine the efficiency of a hydrodynamic vortex separator. NOVATECH Conference.

Environmental Modelling Systems (EMS), Inc. Software modelling, training and consulting services for water resources.

Eutek® Systems. Manufacturer of grit removal equipments, US. Website-http://www.eutek.com/.

Faram, M. G. and Harwood, R. (2003). A method for the numerical assessment of sediment interceptors. Wat. Sci. Tech., vol. 47, no. 4, pp. 167-174.

Faram, M. G., James, M. D. and Williams, C. A. (2004). Wastewater treatment using hydrodynamic vortex separators. CIWEM 2nd National Conference, Wakefield, UK, September, pp. 79-87.

Ferziger, J. H. and Peric, M. (1999). Computational methods for fluid dynamics. Second revised edition, Springer, Germany.

Fluent user manual (2006), Fluent Version 6.2., ANSYS Inc.

Freitas, C. J. (1993). Editorial policy statement on the control of numerical accuracy. J. of Fluids Engg., ASME, vol. 115, pp. 339–340.

Gardner, P. and Deamer, A. (1996). An evaluation of methods for assessing the removal efficiency of a grit separation device. Wat. Sci. Tech., vol. 33, no. 9, pp. 269-275.

Graf, W. H. (1971). Hydraulics of sediment transport. McGraw-Hill, New York, USA.

Gravette, B., Strehler, A., Finger, D., and Palepu, S. (2000). Troubleshooting a grit removal system. Presented at the 73rd Annual WEFTEC Conference and Exposition Anaheim, California.

Han, Q., and He, M. (1987). Mathematical model of reservoir sedimentation and fluvial process. J. of Sediment res., vol. 3, pp. 14-29.

Harwood, R. and Saul, A. J. (1999). The influence of CSO chamber-size on particle retention efficiency performance. Int. Conf. on Urban Storm Drainage, Sydney, Australia (8ICUSD).

Head, K. H. (1997). Manual of Soil Laboratory Testing. Vol. 1. Pentech Press, London.

Hicks, F. E., Jin, Y. C. and Steffler, P. M. (1990). Flow near sloped bank in curved channel. J. of Hyd. Engg., ASCE, vol. 116, no. 1, pp. 55-70.

Hides, S. P. and Griffiths, E. C. (1997). Grit loadings and characteristics at wastewater treatment facilities in New England. New England Water Environment Association Meeting, Boston, MA, January.

Hides, S. P. (1999). Grit removal at municipal wastewater treatment plants. Florida Water Resources Conference, Tallahassee FL, April.

Hirt, C. W. and Nichols, B.D. (1981). Volume of Fluid (VOF) method for the dynamics of free boundaries, J. of Computational Physics, vol. 39, pp. 201-225.

Hydro International Private Limited Company (HIL Plc.). Manufacturer of wastewater treatment products. Website-http://www.hydro-international.biz/index_uk.php.

Ikeda, S., Yamasaka, M. and Chiyoda, M. (1987). Bed topography and sorting in bends. J. of Hyd Engg., ASCE, vol. 113, no. 2, pp. 190-206.

Imhoff, K. and Imhoff, K. R. (1979). Taschenbuch der stadtentwasserung, R. Oldenbourg verlag, Munich.

Jayanti, S. and Narayanan, S. (2004). Computational study of particle-eddy interaction in sedimentation tanks. J. of Env. Engg., ASCE, vol. 130, no. 1, pp. 37-49.

Jia, Y., Blanckaert, K. and Wang, S. S. Y. (2001). Simulation of secondary flow in curved channels. Proc 8th Int. Symposium on Flow Modelling and Turbulence Measurements, FMTM 2001, Tokyo, Japan.

Julien, P. Y. (1995). Erosion and sedimentation. (Cambridge University Press: Cambridge, UK), 280 pages.

Kang, H. and Choi, S. (2006). Reynolds stress modelling of rectangular open-channel flow. Int. J. Numerical Methods in Fluids., vol. 51, pp. 1319-1334.

Kassem, A. and Chaudhry, M. H. (2005). Effect of bed armouring on bed topography of channel bends. J. of Hyd. Engg., ASCE, vol. 131, no. 12, pp. 1136-1140.

Lane, S. N., Bradbrook, K. F., Richards, K. S., Biron, P. M. and Roy, A. G. (2000). Secondary circulation cells in river channel confluences: Measurement artifacts of coherent flow structures. Journal of Hydrological Processes, vol. 14, pp. 2047–2071.

Launder, B. E. and Spalding, D. B. (1974). The numerical computation of turbulent flows. Comput. Methods Appl. Mech. Engg., vol. 3, pp. 269-289.

Launder, B. E., Reece, G. J. and Rodi, W. (1975). Progress in the development of Reynolds stress turbulence closure. J. of Fluid Mech., vol. 63(3), pp. 537-566.

Launder, B. E., Priddin, C. H. and Sharma, B. I. (1977). The calculation of turbulent boundary layers on spinning and curved surfaces. J. of Fluid Engg., ASME, vol. 3, pp. 231-239.

Li, A. and Ahmadi, G. (1992). Dispersion and Deposition of Spherical Particles from Point Sources in a Turbulent Channel Flow. Aerosol Science and Technology, vol. 16, pp. 209-226.

Lin, B. and Shiono, K. (1995). Numerical modelling of solute transport in compound channel flows. J. of Hyd. Res., 33, No. 6, pp. 773-788.

MIT Open Courseware - MIT OCW (2004). Lecture Notes in Transport Processes in Environment, Massachusetts Institute of Technology.

Ma, L., Ashworth, P. J., Best, J. L., Elliot, L., Ingham, D. B. and Whitcombe, L. J. (2002). Computational fluid dynamics and the physical modelling of an upland urban river. Geomorphology, Elsevier, vol. 44, pp. 375-391.

Marais, G. v. R. and Haandel, A. C. van (1996). Design of grit channels controlled by parshall flumes. Wat. Sci. tech., vol. 33, no. 3, pp. 195-210.

Maine Department of Environmental Protection (MEDEP) (2002). Tech. Rep. - Guideline for Developing Wet Weather Management Plans and Operation Practices at Publicly Owned Wastewater Treatment Facilities. Document no. DEP - LW - 0531.

Metcalf and Eddy, Inc. (1991). Wastewater Engineering – Treatment, Disposal & Reuse. Revised by Tchobanoglous, G. and Burton, F. L. McGraw-Hill, Inc.

Naot, D., Nezu, I. and Nakagawa, H. (1993). Hydrodynamic behaviour of compound rectangular open channels. J. of Hyd. Engg., ASCE, vol. 3, pp. 390-408.

National Centre for Computational Hydroscience and Engineering (NCCHE). University of Mississippi, Mississippi. Website- http://www.ncche.olemiss.edu/.

Nicholas, A.P. (2001). Computational fluid dynamics modelling of boundary roughness in gravel-bed rivers: an investigation of the effects of random variability in bed elevation, Earth Surfaces Processes and Landforms. Vol. 26, pp. 346-362,

NWW Engineering (1995). Tech. Rep. - Biddulph Bendy Channel Report.

Odgaard, A. J. (1982). Bed characteristics in alluvial channel bends. J. of Hyd. Div., ASCE, vol. 118, no. 11, pp. 1268-1281.

Odgaard, A. J. and and Bergs, M. A. (1988). Flow processes in a curved alluvial channel. Water Resources Res., vol. 24, no. 1, pp. 45-56.

Olsen, K. W. and Kalkwijk, J. P. (1987). Mathematical model of grain sorting in river bends. Proc. 23rd Congress of the Int. Association for Hyd. Res., Delft, The Netherlands, pp. 142-147.

Park, I. and Jain, S. C. (1987). Numerical simulation of degradation of alluvial channel beds. J. of Hyd Engg., ASCE, vol. 113, no. 7, pp. 845-859.

Patankar, S. V. and Spalding, D. B. (1972). A calculation procedure for heat, mass and momentum transfer in three-dimensional parabolic flows. Intl. J. of Heat and Mass Transfer, vol. 15, pp. 1787-1806.

Patankar, S. V. (1980). Numerical heat transfer and fluid flow. Hemisphere Publishing Corporation: London

Patel, T., and Gill, L. (2005). Flow Characteristics of Curved Open Channel using Computational Fluid Dynamics. ISSEC Annual Symposium, UCC, Ireland.

Patel, T., and Gill, L. (2006). Volume of Fluid Model Applied to Curved Open Channel Flows. Advances in Fluid Mechanics Conference, AFM 2006, WIT Press, Skiathos, Greece.

Peakall, J., Ashworth, P. and Best, J. (1996). Physical Modelling in Fluvial Geomorphology: Principles, Applications and Unresolved Issues, In: Rhoads, B. and Thorne, C. E. (Eds.), The Scientific Nature of Geomorphology: Proceedings of the 27th Binghamton Symposium in Geomorphology, pp. 221–253, John Wiley and Sons.

Prandtl, L. (1925). Bericht uber Untersuchungen zur ausgebildeten Turbulenz. Zeitschriftf˙ur Angewandte Mathematik und Mechanik 5, pp. 136–139.

Prandtl, L. (1952). Essentials of fluid dynamics. Blackie and Sons Ltd., London.

Rameshwaran, P., and Shiono, K. (2002). Predictions of velocity and boundary shear stress in compound meandering channels. Proceedings of River flow 2002, international Conference on Fluvial Hydraulics, Louvain-la-Neuve, Belgium, (Bousmar D. and Zech Y (eds)), 1, 223-231, September 4-6.

Rameshwaran, P., and Shiono, K. (2003). Computer modelling of two-stage meandering channel flows. Proceedings of the Institute of Civil Engineers, Water and Maritime Engineering, vol. 156, no. 4, 773-788.

Rameshwaran, P. & Naden, P. S. (2004a). Modeling turbulent flow in two-stage meandering channels, Proc. ICE, Water Management 157, pp. 159-173.

Rameshwaran, P. & Naden, P. S. (2004b). Three-dimensional modeling of free surface variation in a meandering channel, J. of Hydraulic Research, vol. 42, no.6, pp. 603-615.

Raudkivi, A. J. (1990). Loose boundary hydraulics. 3rd edn (Pergamon Press: Oxford, UK).

Rijn, van L. C. (1984a). Sediment transport, Part I: bed load transport. J. of Hyd. Engg., ASCE, vol. 110, pp. 1431-1456.

Rijn, van L. C. (1984b). Sediment transport, Part II: suspended load transport. J. of Hyd. Engg., ASCE, vol. 110, pp. 1613-1641.

Rijn, van L. C. (1987). Mathematical modelling of morphological processes in the case of suspended sediment transport. Delft Hyd. Communication, no. 382.

Roache, P. J. (1994). Perspective: A Method for uniform reporting of grid refinement studies. J. of Fluid Engineering, FED, ASME, vol. 116, pp. 405-413.

Roache, P. J. (1998). Verification of codes and calculations. AIAA 36, 696–702.

Rodi, W. (1980). Turbulence models and their applications in hydraulics – A state of the art review. IAHR, Delft, The Netherlands.

Rozovskii, I. L. (1957). Flow of water in bends of open channels, pp. 233. Kiev, U.S.S.R.: The Academy of Sciences of the Ukrainian SSR. Translation by Prushansky, Y., Israel Program for Scienific Translations, 1961. Printed in Jerusalem by Monson, S. PST Cat. No. 363.

Rupke, M. (1994). Hydrodynamic grit separation in search of improved grit capture. WEAO Conference, Windsor.

Sawicki, J. M. (2004). Aerated grit chambers hydraulic design equation. J. of Env. Engg., ASCE, vol. 130, no. 9, pp. 1050-158.

Schoklitsch, A. (1914). Uber schleppkraft und geschiebebewegung, Engelmann Leipzig.

Shields, A. (1936). Anwendung der ahnlichkeitsmechanik und turbulenzforschung auf die geschiebebewegung, Mitteil Preuss. Versuchsanst. Wassrer, Erd, Schiffsbau, Berlin, no. 26.

Shih, T. H., Liou, W. W., Shabbir, A., Yang, Z., and Zhu, J. (1995). A new κ-ε eddy-viscosity model for high Reynolds number turbulent flows - Model development and validation. Computers Fluids, vol. 24(3), pp.227-238.

Shukry, A. (1950). Flow around bends in an open flume. Transactions, ASCE, vol. 115, pp. 751-779.

Smith and Loveless (S&L), Inc. Pumping, Water and Wastewater treatment products. Website-http://www.smithandloveless.com/.

Steel, E. W. and McGee, T. J. (1979). Water supply and sewerage. McGraw Hill Eds., New York, USA.

Stern, F., Wilson, R. V., Coleman, H. and Paterson, E. G. (1999). Verification and validation of CFD simulations. Technical Report 407, Iowa Institute of Hydraulic Research, The University of Iowa, Iowa City, I.A.

Stovin, R. S. and Saul, A. J. (1996). Efficiency prediction for storage chambers using computational fluid dynamics. Wat. Sci. Tech., vol. 33, no. 9, pp. 163-170.

Stovin, R. S. and Saul, A. J. (1998). A computational fluid dynamics (CFD) particle technique approach to efficiency prediction. Wat. Sci. Tech., vol. 37, no. 1, pp. 285-293.

Stovin, R. S. and Saul, A. J. (2000). Computational fluid dynamics and design of sewage storage chambers. J. CIWEM., vol. 14, April issue, pp. 103-110.

Sun. T., Meakin, P. and Jossang, T. (2001). A computer model for meandering rivers with multiple bed load sediment sizes. Water Resources res., vol. 37, no. 8, pp. 2227-2241.

Sundaravadivel, M., Vigneswaran, S., Doeleman, J. A. (2000). Waste management in semi-urban areas of India: appropriate technological strategies to overcome financial barriers. Environ. Engg. and Policy, vol. 2, pp. 91-104.

Thomson, J. (1876). On the origin and winding of rivers in alluvial plains, with remarks on the flow around bends in pipes, Proceedings, Royal Society of London, vol. 25, pp. 5-8.

USEPA (2003). Wastewater Fact Sheet: Screening and grit removal, Office of Water, Environmental Protection Agency, United States.

Vanoni, V. A. (1984). Fifty years of sedimentation. J. of Hyd. Engg., ASCE, vol. 110, no. 8, pp. 1021-1057.

Versteeg, H. K. and Malalasekera, W. (1995). An introduction to computational fluid dynamics: The finite volume method. John Wiley & Sons, New York.

Wang, S. S. Y. and Adeff, S. E. (1986). Three dimensional modelling of river sedimentation processes. Proc. 3rd Int. Symp. on river sedimentation, University of Mississippi.

Wu, W., Rodi, W. and Wenka, T. (2000). 3D numerical modelling of flow and sediment transport in open channels. J. of Hyd. Engg., ASCE, vol. 126, no. 1, pp. 4-15.

Wu, W. (2001). CCHE2D sediment transport model. Technical Rep. No. NCCHE-TR-2001-3, National Res. Center for Comp. Hydroscience and Engg., Univ. of Mississippi.

Yalin, M. S. (1971). Theory of Hydraulic Models, pp. 266. Macmillan civil engineering hydraulics. London: Macmillan.

Ye, J. and McCorquodale, J. A. (1998). Simulation of curved open channel Flows by 3D hydrodynamic model. J. of Hyd. Engg., ASCE, 124(7), pp. 687-698.

Appendix A: Results from Physical Modelling Trials

A.1 Sump with no Flow

Table A.1: Grit Removal Efficiencies for trials at channel flow 4l/s (Sump no Flow)

Dia (mm)	Percentage Removal						Average	Standard Error
	1	2	3	4	5	6		
0.063-0.15	27.30	33.33	26.36	29.89	20.72	30.86	28.08	1.79
0.15-0.3	67.20	87.14	64.05	89.90	63.46	79.30	75.17	4.84
0.3-0.425	99.90	99.19	103.91	88.18	89.89	78.13	93.20	3.91
0.425-0.6	94.69	97.50	87.54	96.74	89.31	104.44	95.04	2.49
0.6-1.18	90.41	84.26	90.20	95.95	107.11	103.09	95.17	3.52
1.18-2	101.41	99.35	98.52	98.25	100.96	99.43	99.65	0.52
2-4	101.36	100.95	99.75	99.87	94.47	103.03	99.91	1.19

Table A.2: Grit Removal Efficiencies for trials at channel flow 5l/s (Sump no Flow)

Dia (mm)	Percentage Removal					Average	Standard Error
	1	2	3	4	5		
0.063-0.15	22.12	18.26	30.00	17.55	33.33	24.25	3.17
0.15-0.3	60.24	56.45	71.95	69.02	57.95	63.12	3.10
0.3-0.425	80.94	76.14	80.80	74.33	90.95	80.63	2.88
0.425-0.6	90.82	97.61	96.25	97.54	97.96	96.04	1.34
0.6-1.18	97.71	99.12	99.11	85.19	98.72	95.97	2.71
1.18-2	99.20	99.80	98.57	98.88	99.32	99.16	0.21
2-4	98.56	99.13	99.71	95.52	100.11	98.61	0.81

Table A.3: Grit Removal Efficiencies for trials at channel flow 6l/s (Sump no Flow)

Dia (mm)	Percentage Removal				Average	Standard Error
	1	2	3	4		
0.063-0.15	14.34	12.34	22.14	23.45	18.07	2.77
0.15-0.3	62.64	62.54	56.34	57.48	59.75	1.66
0.3-0.425	79.54	87.64	71.30	82.34	80.21	3.41
0.425-0.6	94.35	89.96	87.69	76.23	87.06	3.87
0.6-1.18	94.27	93.11	90.58	94.24	93.05	0.87
1.18-2	97.38	95.34	99.34	98.49	97.64	0.86
2-4	98.57	98.39	98.80	97.60	98.34	0.26

A.2 Sump with Flow

Table A.4: Grit Removal Efficiencies for trials at channel flow 4l/s with different flow out of the sump (Q_s)

Percentage Removal at Q_s = 0.1l/s						
Dia (mm)	**1**	**2**	**3**	**4**	**Average**	**Standard Error**
0.063-0.15	31.97	39.22	31.79	34.83	34.45	1.73
0.15-0.3	94.56	78.60	68.97	78.30	80.11	5.31
0.3-0.425	97.39	87.62	90.78	85.40	90.30	2.61
0.425-0.6	95.94	98.70	99.65	105.14	99.86	1.93
0.6-1.18	91.50	105.38	96.64	99.35	98.22	2.89
1.18-2	98.68	97.24	99.02	99.27	98.55	0.45
2-4	99.32	98.24	97.36	99.64	98.64	0.52
Percentage Removal at Q_s = 0.15l/s						
Dia (mm)	**1**	**2**	**3**	**4**	**Average**	**Standard Error**
0.063-0.15	32.96	35.62	36.40	37.25	35.56	0.93
0.15-0.3	84.45	78.24	92.14	74.08	82.23	3.93
0.3-0.425	99.87	100.79	87.83	89.78	94.57	3.36
0.425-0.6	92.89	94.25	97.68	97.21	95.51	1.16
0.6-1.18	99.20	108.33	91.59	90.50	97.41	4.13
1.18-2	99.28	106.42	100.00	91.07	99.19	3.15
2-4	95.29	98.21	104.00	94.44	97.99	2.16
Percentage Removal at Q_s = 0.225l/s						
Dia (mm)	**1**	**2**	**3**	**4**	**Average**	**Standard Error**
0.063-0.15	54.21	47.32	41.35	46.23	47.28	2.65
0.15-0.3	93.47	96.21	87.99	87.56	91.31	2.12
0.3-0.425	98.53	91.62	94.66	91.90	94.18	1.61
0.425-0.6	96.08	95.81	94.29	98.75	96.23	0.93
0.6-1.18	100.25	93.51	86.77	105.33	96.46	4.04
1.18-2	97.52	95.06	98.85	111.43	100.72	3.66
2-4	97.92	94.87	98.08	101.59	98.11	1.37
Percentage Removal at Q_s = 0.45l/s						
Dia (mm)	**1**	**2**	**3**	**4**	**Average**	**Standard Error**
0.063-0.15	49.24	52.47	49.20	42.14	48.26	2.18
0.15-0.3	98.66	95.62	94.33	94.32	95.73	1.02
0.3-0.425	97.46	94.80	96.95	97.10	96.58	0.60
0.425-0.6	86.87	95.45	93.51	97.12	93.24	2.25
0.6-1.18	90.10	99.01	97.33	95.01	95.36	1.94
1.18-2	98.19	95.35	98.26	98.28	97.52	0.72
2-4	97.54	98.67	103.67	99.89	99.94	1.33

Table A.5: Grit Removal Efficiencies for trials at channel flow 6l/s with different flow out of the sump (Q_s)

Percentage Removal at Q_s = 0.1l/s						
Dia (mm)	**1**	**2**	**3**	**4**	**Average**	**Standard Error**
0.063-0.15	17.75	17.36	22.83	19.78	19.43	1.25
0.15-0.3	67.37	90.43	75.14	74.26	76.80	4.86
0.3-0.425	88.94	71.54	81.79	90.93	83.30	4.38
0.425-0.6	94.84	89.57	94.25	87.89	91.63	1.72
0.6-1.18	96.02	87.48	95.02	82.59	90.28	3.19
1.18-2	100.00	96.96	97.86	93.20	97.00	1.42
2-4	100.00	97.55	97.12	94.59	97.32	1.11
Percentage Removal at Q_s = 0.15l/s						
Dia (mm)	**1**	**2**	**3**	**4**	**Average**	**Standard Error**
0.063-0.15	18.52	16.42	22.22	22.66	19.95	1.50
0.15-0.3	67.99	67.05	90.55	64.07	72.41	6.10
0.3-0.425	102.11	86.22	82.29	97.30	91.98	4.64
0.425-0.6	97.34	92.35	86.00	83.43	89.78	3.14
0.6-1.18	93.90	96.79	93.17	94.74	94.65	0.78
1.18-2	97.13	99.06	97.38	99.32	98.22	0.56
2-4	96.79	96.57	98.60	99.36	97.83	0.68
Percentage Removal at Q_s = 0.225l/s						
Dia (mm)	**1**	**2**	**3**	**4**	**Average**	**Standard Error**
0.063-0.15	25.91	20.79	34.18	-	26.96	3.90
0.15-0.3	83.57	75.39	71.93	-	76.97	3.45
0.3-0.425	96.21	77.57	79.42	-	84.40	5.93
0.425-0.6	82.86	92.73	97.69	-	91.09	4.36
0.6-1.18	98.98	97.59	93.55	-	96.70	1.63
1.18-2	97.99	98.49	97.48	-	97.99	0.29
2-4	98.32	99.62	96.79	-	98.25	0.82

A.3 Specific Gravity of Grit Particles

Table A.6 (a-c): Specific Gravity Test Data

(a) Particle Size: 0.063-0.15mm			
No.	Content	Sample wt. in gms	
		1	2
A	Bottle	345.3	345.3
B	Bottle + Soil	425.6	420.55
S = B-A	Soil	80.3	75.25
D	Bottle+Water	631.2	631.2
(B-A)+D	Bottle+Water+Soil	711.5	706.45
C	Botte-Water-Soil mix	681.78	678.11
W = (B-A)+D-C	Water Displaced	29.72	28.34
S/W	**Specific Gravity**	**2.702**	**2.66**

(b) Particle Size: 0.15-0.3mm			
No.	Content	Sample wt. in gms	
		1	2
A	Bottle	345.3	345.3
B	Bottle + Soil	434.85	444.09
S = B-A	Soil	89.55	98.79
D	Bottle+Water	631.2	631.2
(B-A)+D	Bottle+Water+Soil	720.75	729.99
C	Botte-Water-Soil mix	686.86	692.73
W = (B-A)+D-C	Water Displaced	33.89	37.26
S/W	**Specific Gravity**	**2.642**	**2.651**

(c) Particle Size: 0.3-0.425mm			
No.	Content	Sample wt. in gms	
		1	2
A	Bottle	345.3	345.3
B	Bottle + Soil	423.2	436.3
S = B-A	Soil	77.9	91
D	Bottle+Water	631.2	631.2
(B-A)+D	Bottle+Water+Soil	709.1	722.2
C	Botte-Water-Soil mix	679.61	687.46
W = (B-A)+D-C	Water Displaced	29.49	34.74
S/W	**Specific Gravity**	**2.642**	**2.619**

Table A.6 (d-f): Specific Gravity Test Data

(d) Particle Size: 0.425-0.6mm			
No.	Content	Sample wt. in gms	
		1	2
A	Bottle	345.3	345.3
B	Bottle + Soil	465.12	456.2
S = B-A	Soil	119.82	110.9
D	Bottle+Water	631.2	631.2
(B-A)+D	Bottle+Water+Soil	751.02	742.1
C	Botte-Water-Soil mix	705.13	699.4
W = (B-A)+D-C	Water Displaced	45.89	42.7
S/W	**Specific Gravity**	**2.611**	**2.597**

(e) Particle Size: 0.6-1.18mm			
No.	Content	Sample wt. in gms	
		1	2
A	Bottle	345.3	345.3
B	Bottle + Soil	487.99	465.33
S = B-A	Soil	142.69	120.03
D	Bottle+Water	631.2	631.2
(B-A)+D	Bottle+Water+Soil	773.89	751.23
C	Botte-Water-Soil mix	718.99	705.16
W = (B-A)+D-C	Water Displaced	54.9	46.07
S/W	**Specific Gravity**	**2.599**	**2.605**

(f) Particle Size: 1.18-2mm			
No.	Content	Sample wt. in gms	
		1	2
A	Bottle	345.3	345.3
B	Bottle + Soil	476.83	454.36
S = B-A	Soil	131.53	109.06
D	Bottle+Water	631.2	631.2
(B-A)+D	Bottle+Water+Soil	762.73	740.26
C	Botte-Water-Soil mix	711.8	697.95
W = (B-A)+D-C	Water Displaced	50.93	42.31
S/W	**Specific Gravity**	**2.582**	**2.577**

Table A.6 (g): Specific Gravity Test Data

(g) Particle Size: 2-4mm			
No.	Content	Sample wt. in gms	
		1	2
A	Bottle	345.3	345.3
B	Bottle + Soil	459.6	382.35
S = B-A	Soil	114.3	37.05
D	Bottle+Water	631.2	631.2
(B-A)+D	Bottle+Water+Soil	745.5	668.25
C	Botte-Water-Soil mix	700.9	653.64
W = (B-A)+D-C	Water Displaced	44.6	14.61
S/W	**Specific Gravity**	**2.563**	**2.536**

A.4 '*Bendy Channel*' Evaluation - BIDDULPH Wastewater Treatment Works

Table A.7: Evaluation of On-site Grit Removal Efficiencies for various particle sizes (*Bendy Channel,* NWW Engineering, 1995)

Bendy Channel		Percentage (%) removal for Particle Size (mm)						
Run No.	Flow rate (l/s)	2.4	1.2	0.6	0.3	0.15	0.09	<0.09
Run 1	20.0	67.4	39.5	32.5	41.8	15.1	90.9	16.2
Run 2	20.0	75.7	54.8	39.6	25.4	6.7	12.9	18.9
Run 3	20.0	86.6	72.7	64.0	44.2	10.6	16.4	29.9
Run 4	20.0	90.6	73.4	69.4	52.0	7.0	6.5	18.6
Run 5	20.0	64.1	66.5	69.0	64.7	19.1	16.8	32.0
Run 6	20.0	85.5	83.5	80.2	65.8	10.4	13.6	21.0
Average	**20.0**	**78.3**	**65.1**	**59.1**	**49.0**	**11.5**	**26.2**	**22.8**
Run 7	11.5	88.7	84.7	79.5	68.4	20.1	7.4	9.2
Run 8	11.5	65.2	58.4	62.3	73.7	26.5	4.1	15.5
Run 9	11.5	68.7	58.3	56.9	63.4	27.0	7.6	9.5
Run 10	11.5	65.1	61.6	50.8	55.9	31.6	8.1	11.6
Run 11	11.5	74.2	67.1	66.2	68.5	24.5	6.4	11.4
Run 12	11.5	50.0	55.4	60.2	82.3	40.5	3.3	6.3
Run 13	11.5	88.4	83.0	76.8	82.1	22.7	6.1	14.5
Run 14	11.5	58.3	79.4	83.0	80.9	11.1	9.8	9.3
Run 15	11.5	77.0	85.3	84.4	68.6	13.7	14.8	13.2
Run 16	11.5	80.9	85.9	84.5	67.7	12.8	16.0	15.5
Run 17	11.5	71.7	78.8	79.3	68.0	12.7	10.1	14.7
Run 18	11.5	70.1	76.6	79.5	73.4	30.7	10.9	19.9
Run 19	11.5	75.0	48.7	79.9	62.2	23.3	16.9	22.7
Run 20	11.5	88.3	82.6	81.1	68.7	32.9	10.7	17.9
Run 21	11.5	82.5	79.0	75.6	69.6	26.1	20.8	31.4
Run 22	11.5	84.3	70.7	63.1	56.4	24.7	10.3	22.6
Run 23	11.5	21.0	24.4	47.9	59.3	75.4	84.2	82.4
Run 24	11.5	94.2	87.2	79.4	70.6	21.9	8.0	16.5
Run 25	11.5	94.8	94.4	81.1	58.7	8.1	6.0	1.7
Run 26	11.5	82.8	71.9	77.5	69.5	22.5	5.6	11.4
Run 27	11.5	96.8	89.5	89.0	75.1	14.3	6.5	11.1
Run 28	11.5	81.3	81.5	88.6	83.2	11.6	3.2	12.0
Run 29	11.5	86.1	74.7	72.3	69.8	21.0	6.8	20.5
Run 30	11.5	78.9	67.9	61.8	40.4	12.5	76.0	23.6
Run 31	11.5	58.4	71.1	77.1	76.0	20.2	7.0	18.2
Run 32	11.5	79.6	75.8	84.9	77.2	9.9	5.4	9.6
Run 33	11.5	82.6	77.7	74.7	64.1	9.7	15.1	24.1
Run 34	11.5	58.7	51.2	42.4	42.6	51.7	84.8	83.3
Run 35	11.5	76.8	76.3	77.1	62.1	10.1	18.7	15.6
Average	**11.5**	**75.2**	**72.4**	**73.0**	**67.5**	**23.1**	**16.9**	**19.8**

The data shown in table A.7 is also plotted with respect to the trial numbers. Figure A.1 (a, b) shows the variation of grit removal efficiency against trial numbers for Q=20l/s and Q=11.5l/s. It can be easily observed that the grit removal efficiency increases with the increase in the grit particle size. However, minor variations occur within different trail number for every particle size. An interesting behaviour is also observed for Q=11.5l/s where at run 17 and 28, the grit removal efficiency for larger particles (>150μm) decreases and for smaller particles of size (≤150μm) increases. This can be due flow fluctuations within the channel and also errors involved during sieve analysis. Thus, Figure A.1 also confirms that the assessment of actual girt removal efficiency of grit removal devices including curved girt channel is a ver y difficult process.

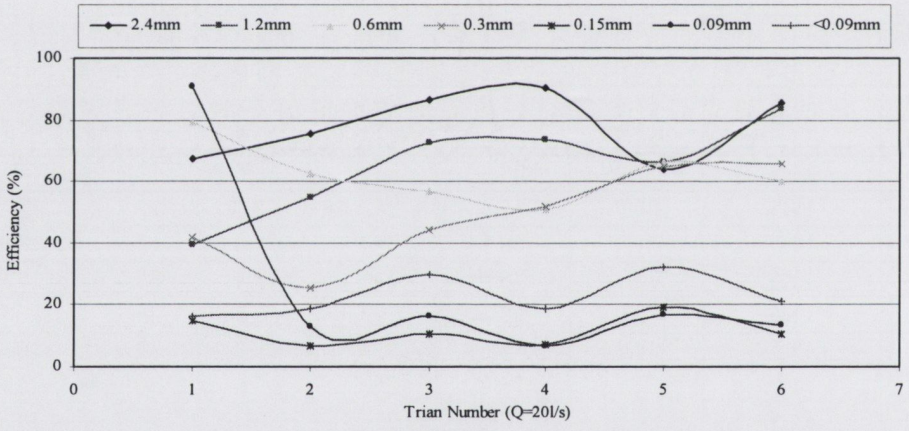

(a) 20l/s

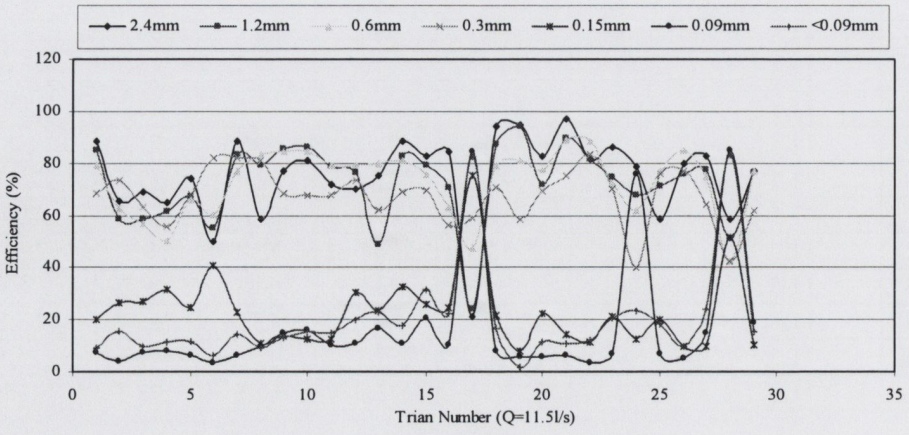

(a) 11.5l/s

Figure A.1: Grit Removal Efficiency for various Particle Sizes (a) 20l/s, (b) 11.5l/s

A.5 Revised Physical Modelling Trials Results

Table A.8: Grit Removal Efficiencies for trials at channel flow 4l/s (Baffle1-2-3, Sump no Flow)

	Percentage Removal (Baffle-1-2-3)						
Dia (mm)	1	2	3	4	Average	Std. Dev.	S.E.
0.063-0.15	42.68	29.34	34.35	26.46	33.21	7.11	3.55
0.15-0.3	92.26	99.67	99.87	96.48	97.07	3.56	1.78
0.3-0.425	98.64	91.24	97.68	99.57	96.78	3.77	1.89
0.425-0.6	90.17	99.12	97.4	97.64	96.08	4.01	2.01
0.6-1.18	97.64	98.92	98.82	91.35	96.68	3.60	1.80
1.18-2	99.86	96.2	96.48	99.92	98.12	2.05	1.03
2-4	97.24	99.16	99.83	96.47	98.18	1.58	0.79

Table A.9: Grit Removal Efficiencies for trials at channel flow 4l/s (Baffle1, Sump no Flow)

	Percentage Removal (Baffle-1)						
Dia (mm)	1	2	3	4	Average	Std. Dev.	S.E.
0.063-0.15	35.26	21.34	26.48	23.21	26.57	6.17	3.08
0.15-0.3	96.56	97.2	96.48	86.24	94.12	5.26	2.63
0.3-0.425	99.68	91.2	96.1	97.76	96.19	3.63	1.82
0.425-0.6	89.23	94.68	98.34	99.68	95.48	4.67	2.34
0.6-1.18	99.62	99.26	94.36	97.26	97.63	2.41	1.21
1.18-2	99.35	96.48	97.5	99.16	98.12	1.37	0.69
2-4	99.4	99.57	93.47	97.68	97.53	2.84	1.42

Table A.10: Grit Removal Efficiencies for trials at channel flow 4l/s (Baffle1, Sump with Flow)

	Percentage Removal (Baffle-1 and Outlet-2)						
Dia (mm)	1	2	3	4	Average	Std. Dev.	S.E.
0.063-0.15	37.68	28.64	35.24	29.46	32.76	4.41	2.20
0.15-0.3	98.37	99.14	92.46	82.17	93.04	7.83	3.92
0.3-0.425	97.64	88.23	99.76	97.42	95.76	5.13	2.57
0.425-0.6	90.81	99.93	94.67	99.87	96.80	4.42	2.21
0.6-1.18	99.83	98.6	95.46	91.37	96.32	3.78	1.89
1.18-2	99.21	92.67	97.64	99.81	97.33	3.24	1.62
2-4	98.24	99.13	91.53	97.92	96.71	3.49	1.74

Appendix B: Scatter Plot of Particles hitting θ° (15°, 30° or 45°) plane at flow rates ranging from 4l/s to 15l/s.

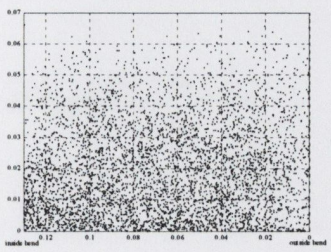

(i) 0.063 mm

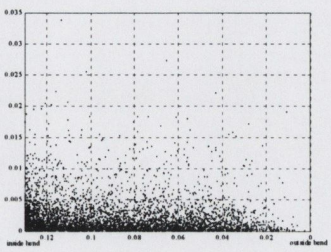

(ii) 0.15 mm

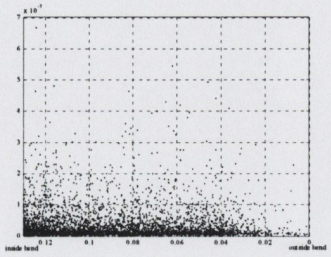

(iii) 0.3 mm

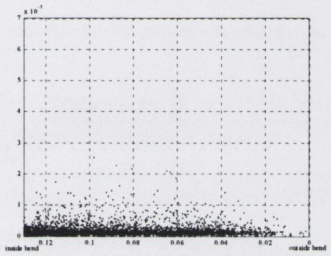

(iv) 0.425 mm

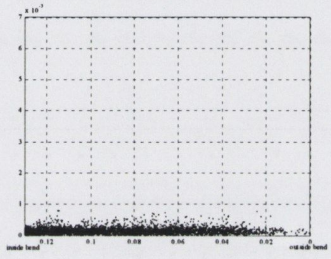

(v) 0.6 mm

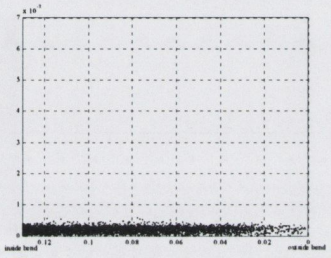

(vi) 1.18 mm

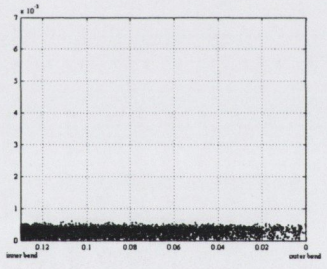

(vii) 2 mm

Figure B.1 (a): Scatter Plot of Particles hitting the plane θ = 15° at Q = 4l/s

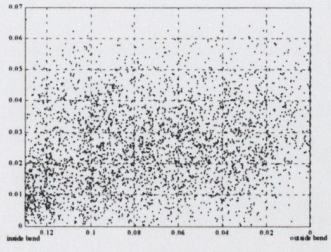

(i) 0.063 mm

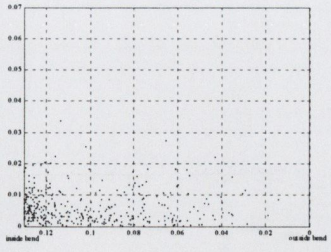

(ii) 0.15 mm

Figure B.1 (b): Remaining Particles not Entering into the Sump

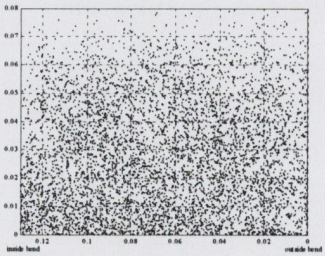

(i) 0.063 mm

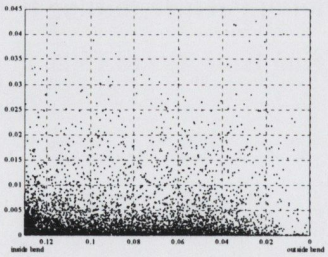

(ii) 0.15 mm

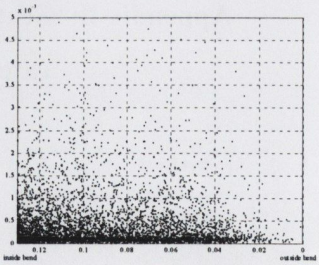

(iii) 0.3 mm

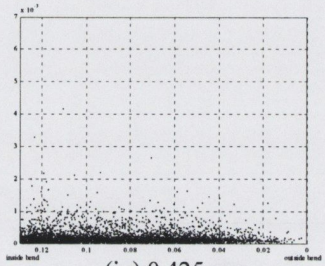

(iv) 0.425 mm

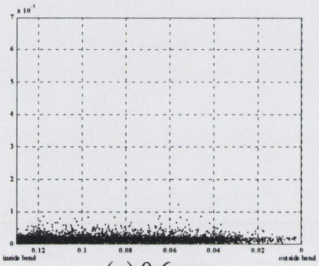

(v) 0.6 mm

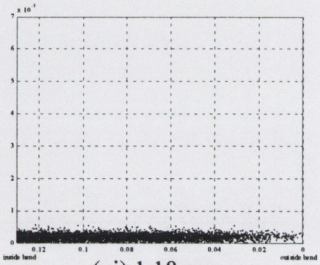

(vi) 1.18 mm

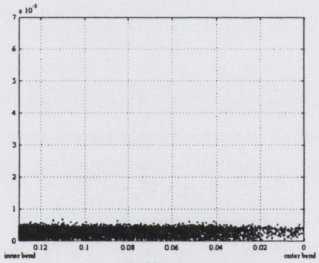

(vii) 2 mm

Figure B.2 (a): Scatter Plot of Particles hitting the plane θ = 15° at Q = 5l/s

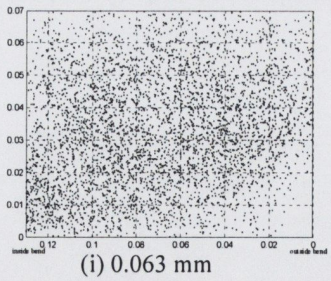

(i) 0.063 mm

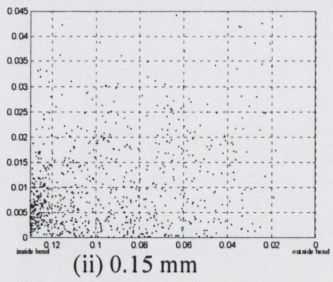

(ii) 0.15 mm

Figure B.2 (b): Remaining Particles not Entering into the Sump

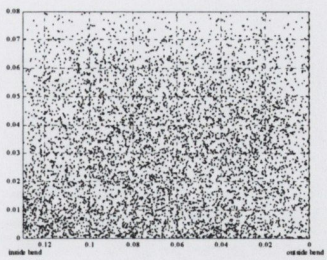

(i) 0.063 mm

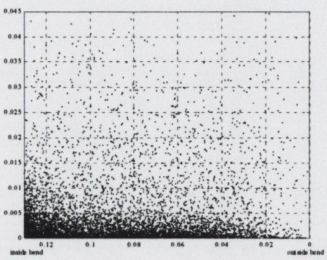

(ii) 0.15 mm

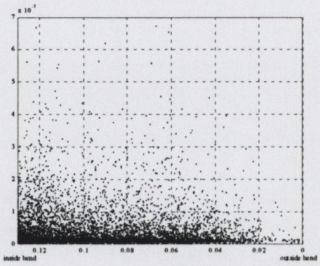

(iii) 0.3 mm

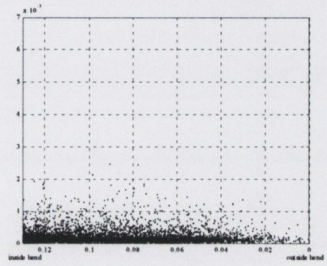

(iv) 0.425 mm

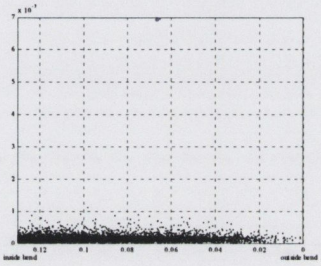

(v) 0.6 mm

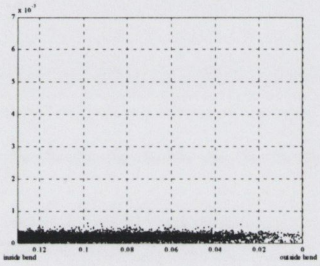

(vi) 1.18 mm

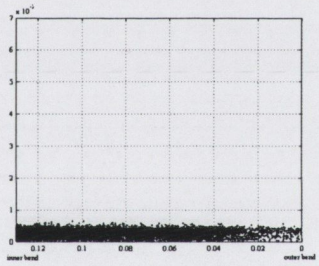

(vii) 2 mm

Figure B.3 (a): Scatter Plot of Particles hitting the plane θ = 15° at Q = 6l/s

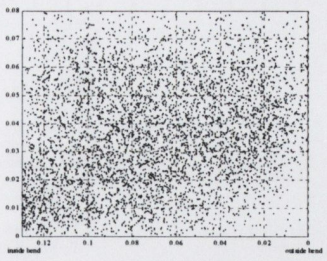

(i) 0.063 mm

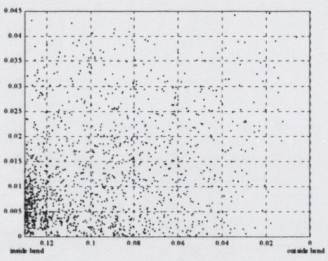

(ii) 0.15 mm

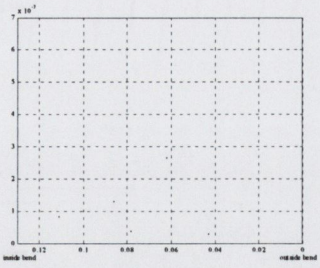

(iii) 0.3 mm

Figure B.3 (b): Remaining Particles not Entering into the Sump

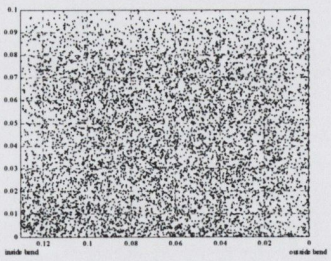

(i) 0.063 mm

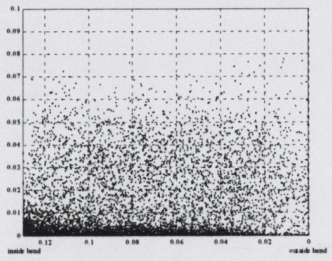

(ii) 0.15 mm

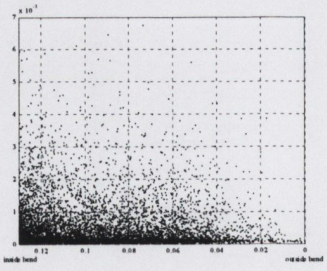

(iii) 0.3 mm

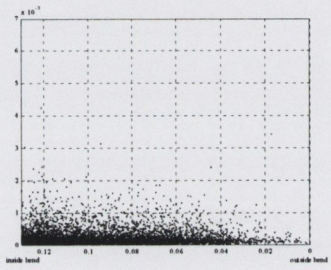

(iv) 0.425 mm

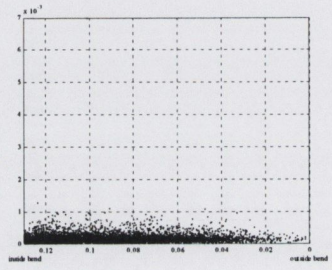

(v) 0.6 mm

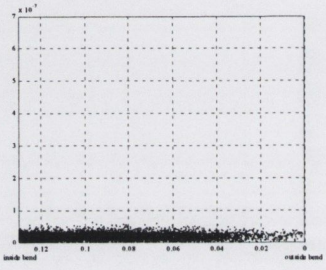

(vi) 1.18 mm

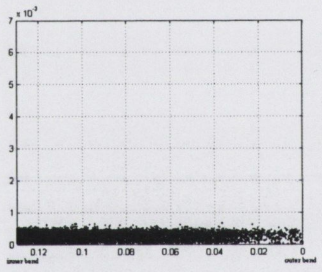

(vii) 2 mm

Figure B.4 (a): Scatter Plot of Particles hitting the plane θ = 15° at Q = 8l/s

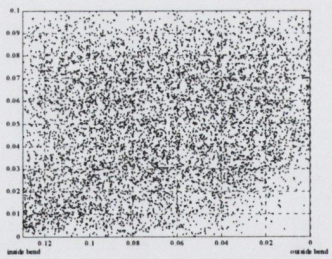

(i) 0.063 mm

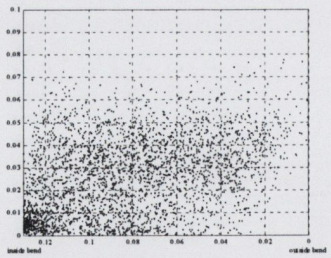

(ii) 0.15 mm

Figure B.4 (b): Remaining Particles not Entering into the Sump

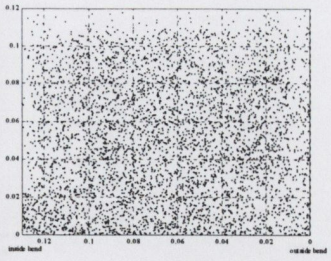

(i) 0.063 mm

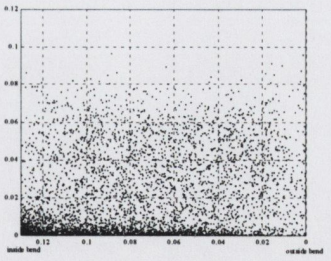

(ii) 0.15 mm

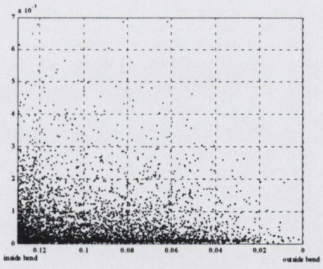

(iii) 0.3 mm

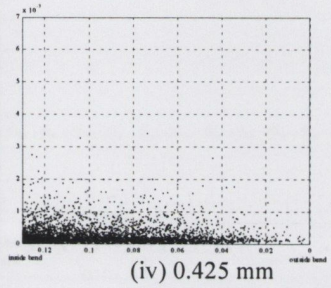

(iv) 0.425 mm

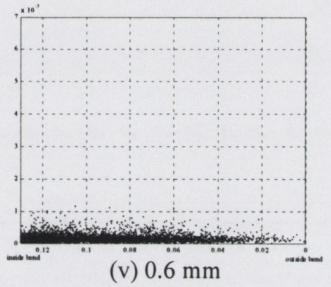

(v) 0.6 mm

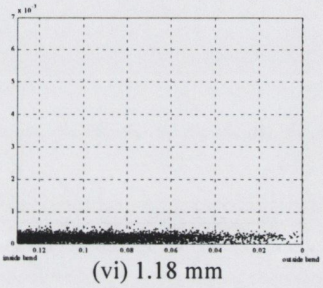

(vi) 1.18 mm

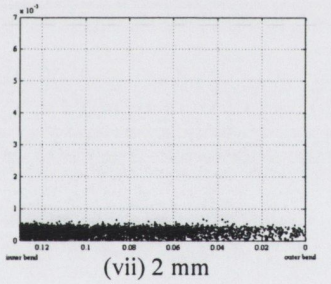

(vii) 2 mm

Figure B.5 (a): Scatter Plot of Particles hitting the plane θ = 15° at Q =10l/s

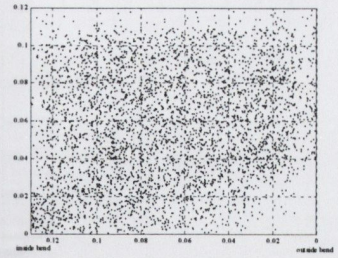

(i) 0.063 mm

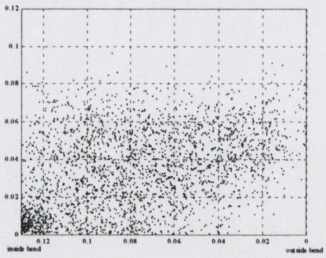

(ii) 0.15 mm

Figure B.5 (b): Remaining Particles not Entering into the Sump

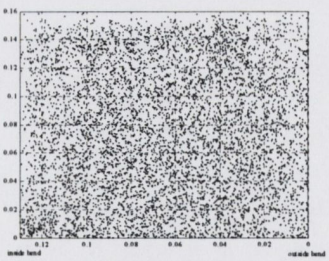

(i) 0.063 mm

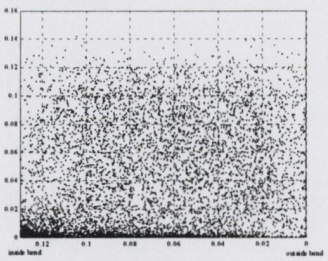

(ii) 0.15 mm

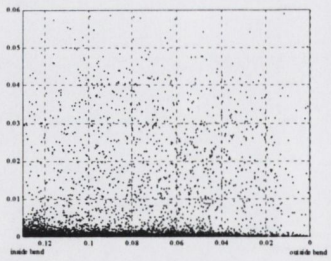

(iii) 0.3 mm

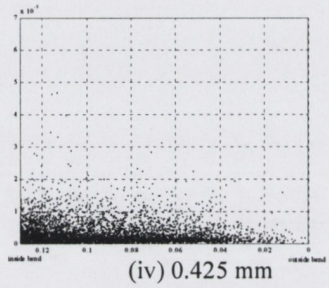

(iv) 0.425 mm

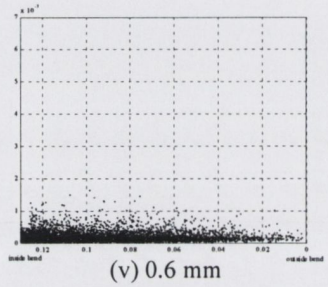

(v) 0.6 mm

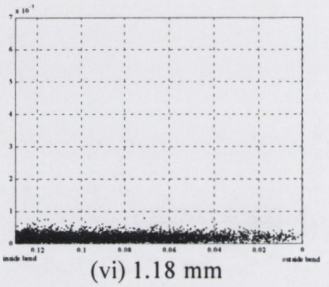

(vi) 1.18 mm

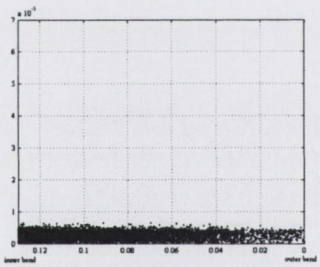

(vii) 2 mm

Figure B.6 (a): Scatter Plot of Particles hitting the plane θ = 15° at Q = 15l/s

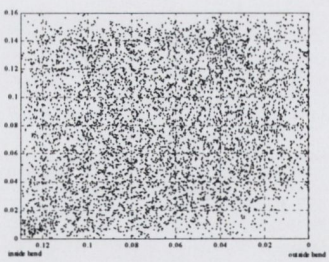

(i) 0.063 mm

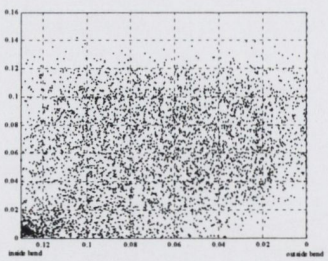

(ii) 0.15 mm

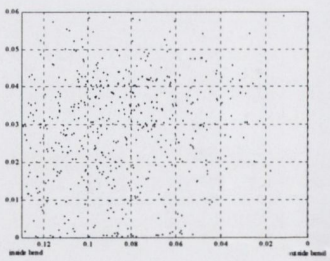

(iii) 0.3 mm

Figure B.6 (b): Remaining Particles not Entering into the Sump

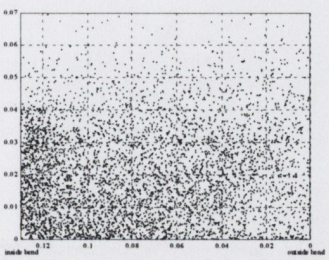

(i) 0.063 mm

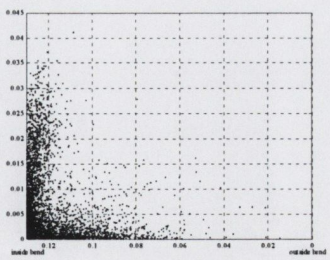

(ii) 0.15 mm

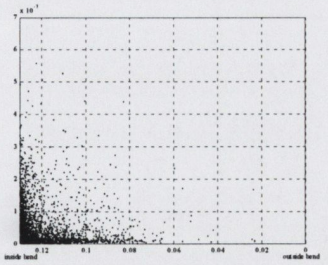

(iii) 0.3 mm

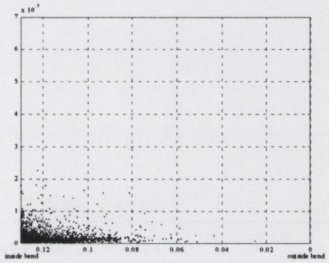

(iv) 0.425 mm

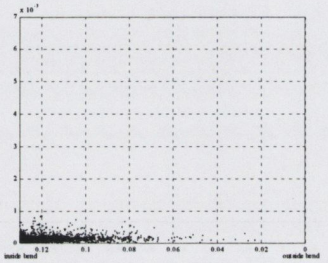

(v) 0.6 mm

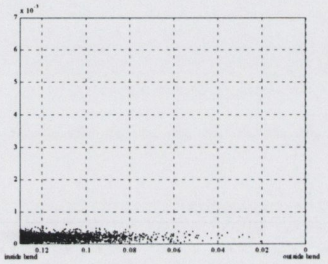

(vi) 1.18 mm

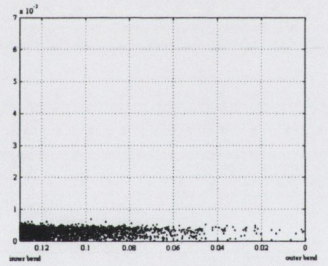

(vii) 2 mm

Figure B.7 (a): Scatter Plot of Particles hitting the plane θ = 30° at Q = 4l/s

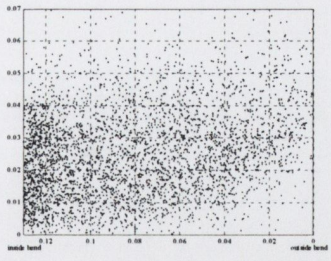

(i) 0.063 mm

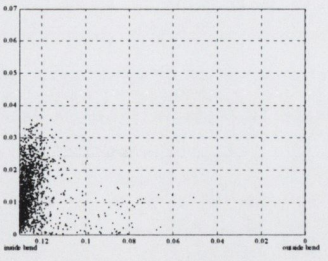

(ii) 0.15 mm

Figure B.7 (b): Remaining Particles not Entering into the Sump

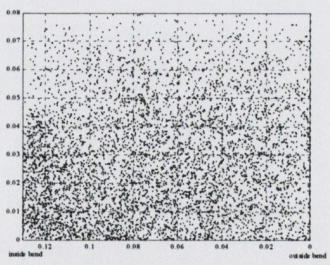

(i) 0.063 mm

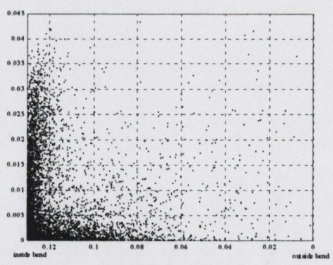

(ii) 0.15 mm

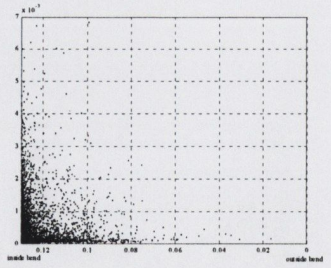

(iii) 0.3 mm

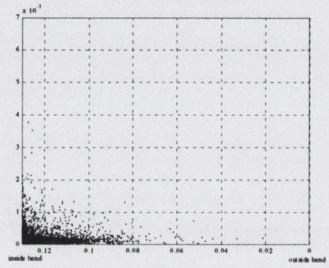

(iv) 0.425 mm

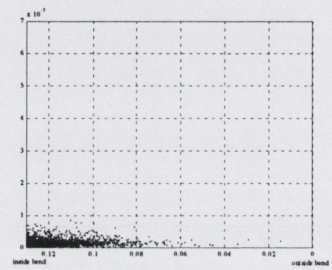

(v) 0.6 mm

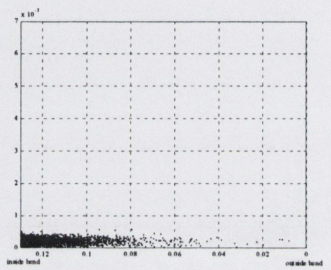

(vi) 1.18 mm

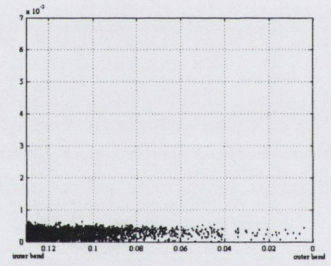

(vii) 2 mm

Figure B.8 (a): Scatter Plot of Particles hitting the plane θ = 30° at Q = 5l/s

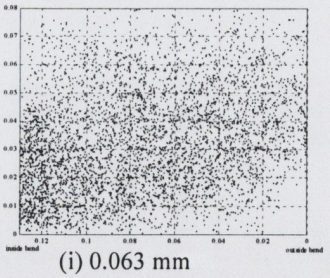

(i) 0.063 mm

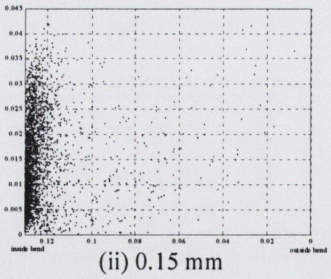

(ii) 0.15 mm

Figure B.8 (b): Remaining Particles not Entering into the Sump

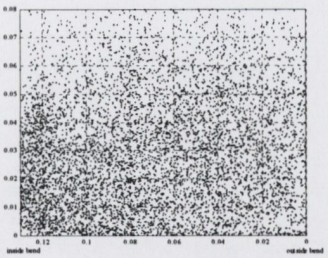

(i) 0.063 mm

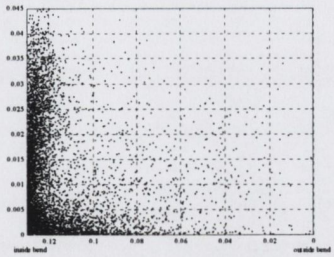

(ii) 0.15 mm

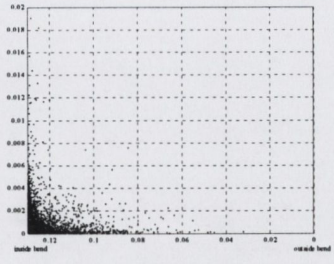

(iii) 0.3 mm

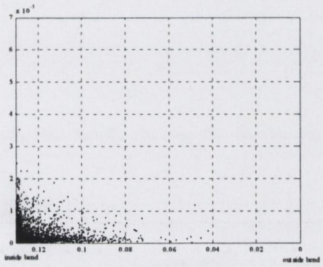

(iv) 0.425 mm

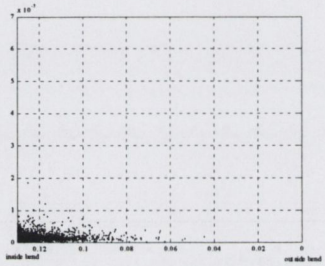

(v) 0.6 mm

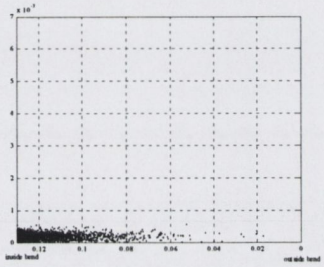

(vi) 1.18 mm

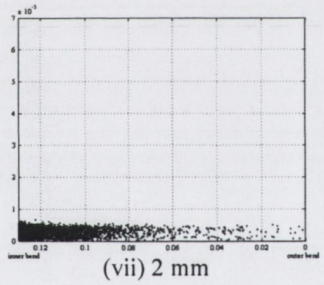

(vii) 2 mm

Figure B.9 (a): Scatter Plot of Particles hitting the plane θ = 30° at Q = 6l/s

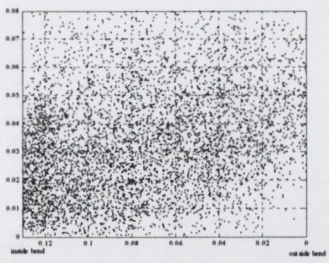

(i) 0.063 mm

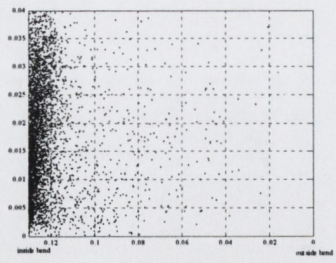

(ii) 0.15 mm

Figure B.9 (b): Remaining Particles not Entering into the Sump

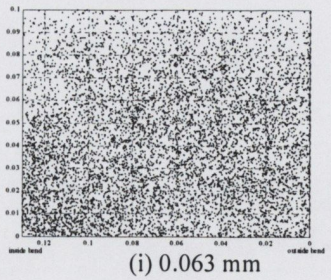

(i) 0.063 mm

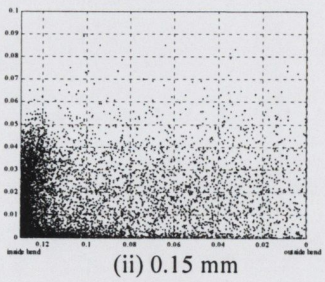

(ii) 0.15 mm

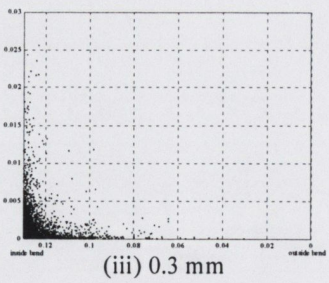

(iii) 0.3 mm

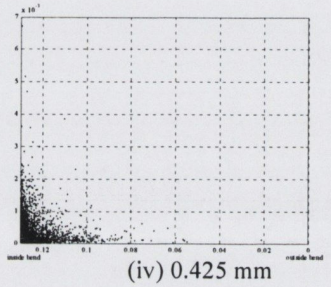

(iv) 0.425 mm

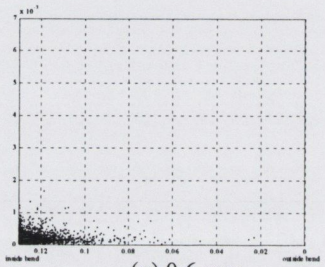

(v) 0.6 mm

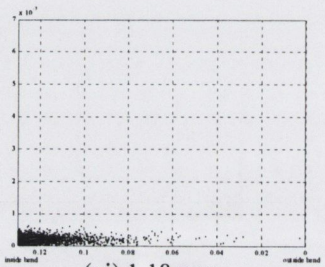

(vi) 1.18 mm

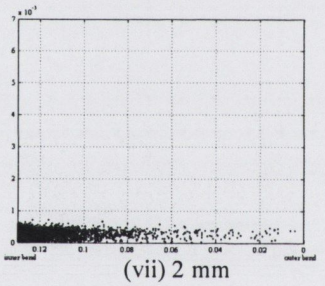

(vii) 2 mm

Figure B.10 (a): Scatter Plot of Particles hitting the plane θ = 30° at Q = 8l/s

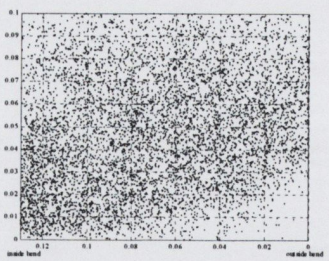

(i) 0.063 mm

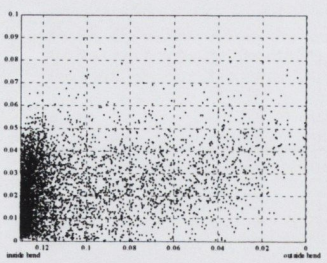

(ii) 0.15 mm

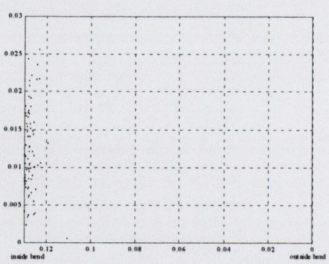

(iii) 0.3 mm

Figure B.10 (b): Remaining Particles not Entering into the Sump

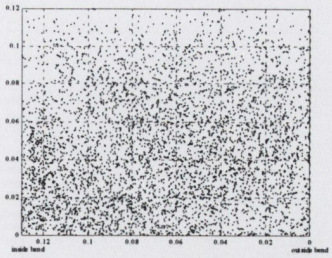

(i) 0.063 mm

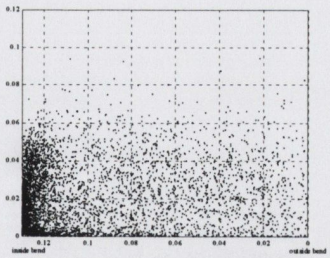

(ii) 0.15 mm

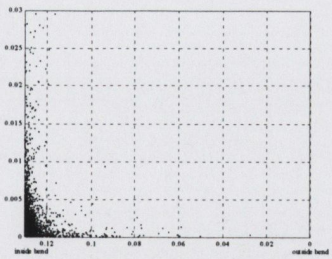

(iii) 0.3 mm

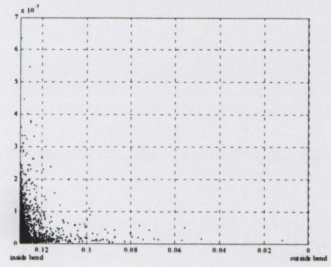

(iv) 0.425 mm

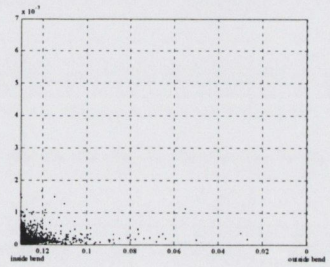

(v) 0.6 mm

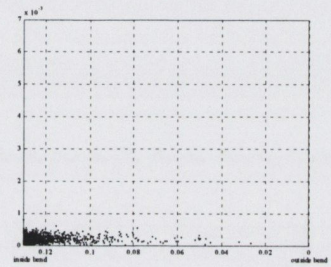

(vi) 1.18 mm

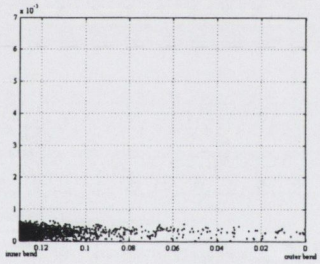

(vii) 2 mm

Figure B.11 (a): Scatter Plot of Particles hitting the plane θ = 30° at Q = 10l/s

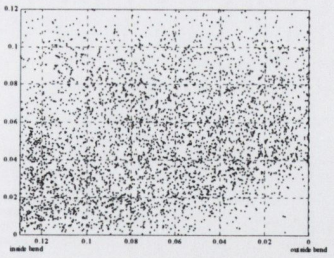

(i) 0.063 mm

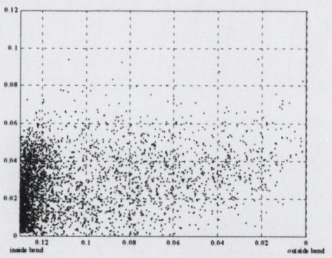

(ii) 0.15 mm

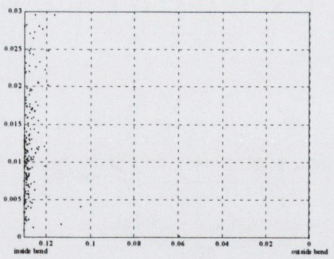

Figure B.11 (b): Remaining Particles not Entering into the Sump

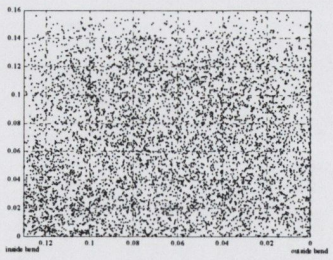

(i) 0.063 mm

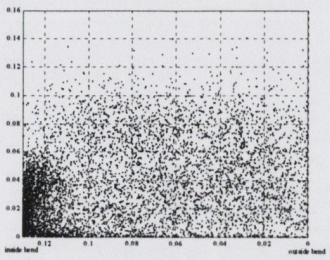

(ii) 0.15 mm

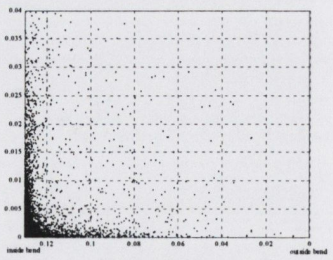

(iii) 0.3 mm

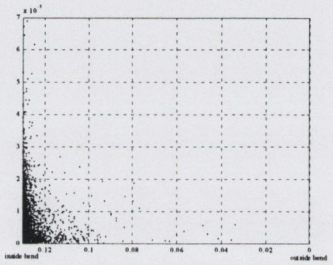

(iv) 0.425 mm

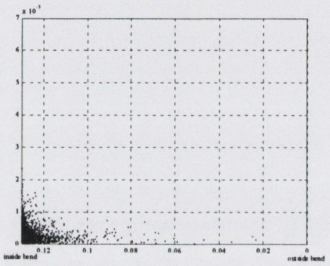

(v) 0.6 mm

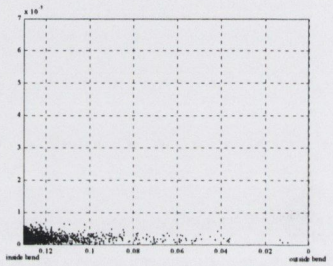

(vi) 1.18 mm

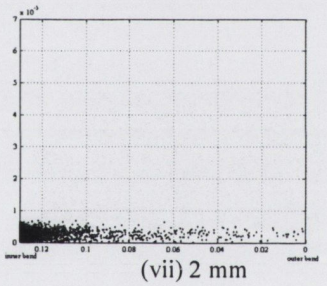

(vii) 2 mm

Figure B.12 (a): Scatter Plot of Particles hitting the plane θ = 30° at Q = 15l/s

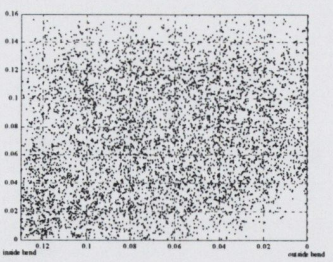

(i) 0.063 mm

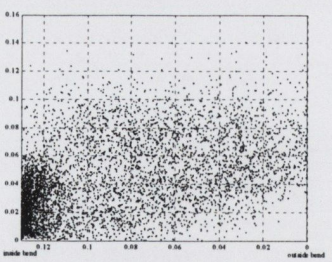

(ii) 0.15 mm

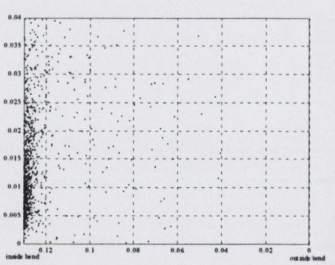

(iii) 0.3 mm

Figure B.12 (b): Remaining Particles not Entering into the Sump

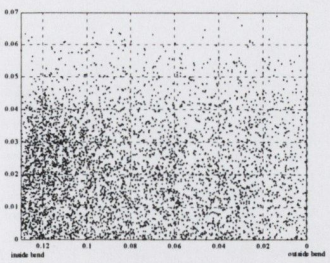

(i) 0.063 mm

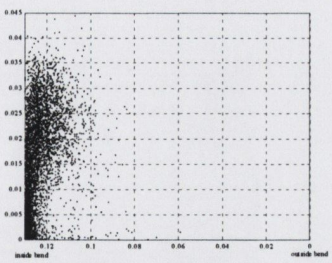

(ii) 0.15 mm

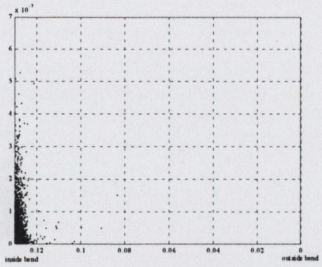

(iii) 0.3 mm

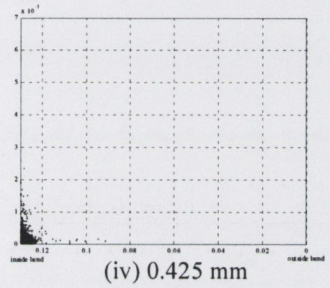

(iv) 0.425 mm

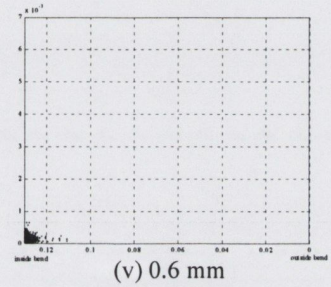

(v) 0.6 mm

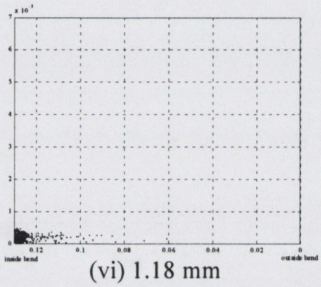

(vi) 1.18 mm

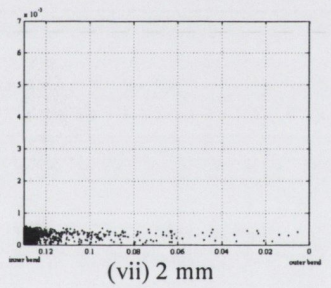

(vii) 2 mm

Figure B.13 (a): Scatter Plot of Particles hitting the plane θ = 45° at Q = 4l/s

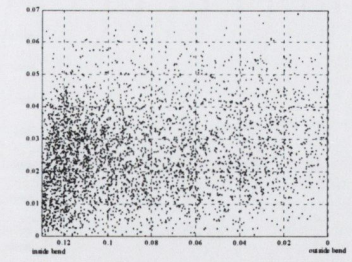

(i) 0.063 mm

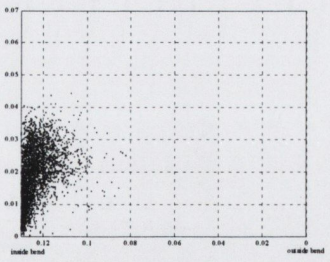

(ii) 0.15 mm

Figure B.13 (b): Remaining Particles not Entering into the Sump

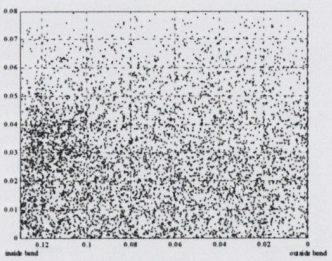

(i) 0.063 mm

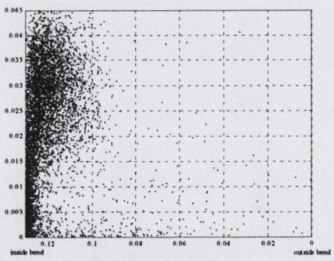

(ii) 0.15 mm

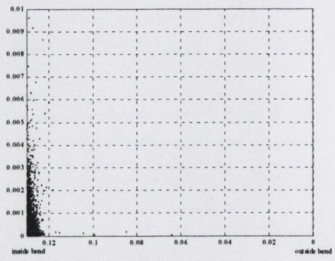

(iii) 0.3 mm

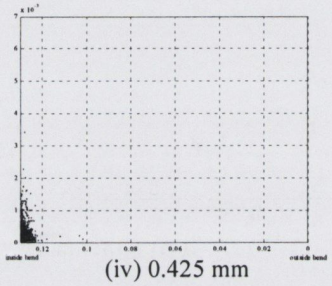

(iv) 0.425 mm

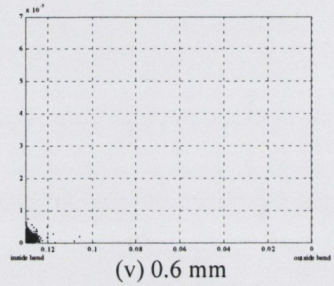

(v) 0.6 mm

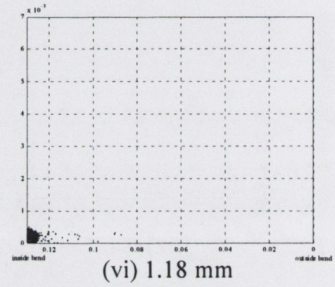

(vi) 1.18 mm

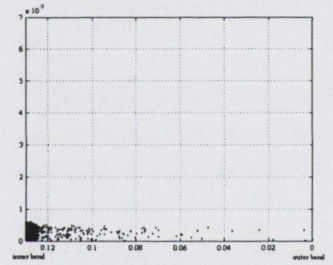

(vii) 2 mm

Figure B.14 (a): Scatter Plot of Particles hitting the plane θ = 45° at Q = 5l/s

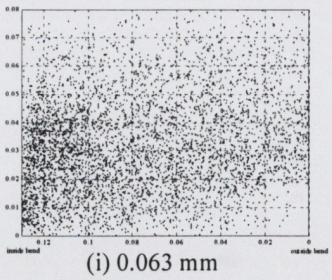

(i) 0.063 mm

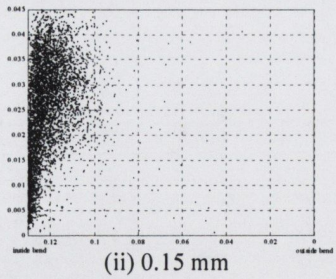

(ii) 0.15 mm

Figure B.14 (b): Remaining Particles not Entering into the Sump

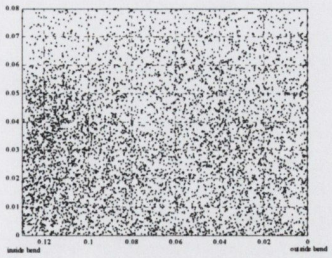

(i) 0.063 mm

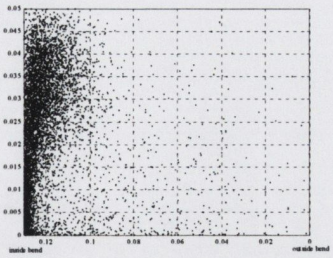

(ii) 0.15 mm

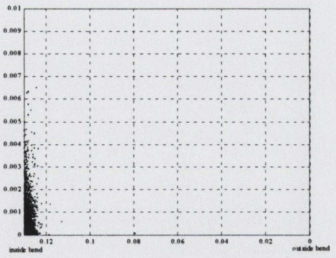

(iii) 0.3 mm

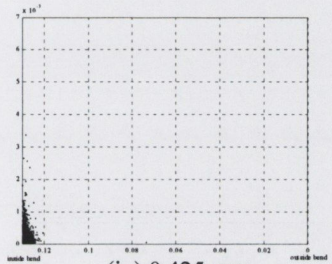

(iv) 0.425 mm

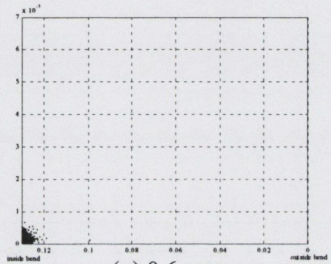

(v) 0.6 mm

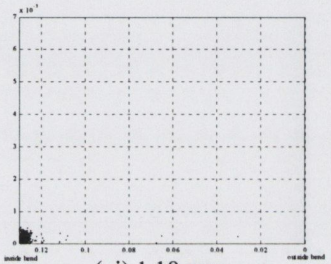

(vi) 1.18 mm

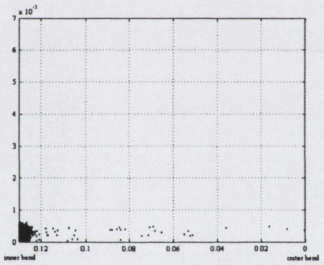

(vii) 2 mm

Figure B.15 (a): Scatter Plot of Particles hitting the plane θ = 45° at Q = 6l/s

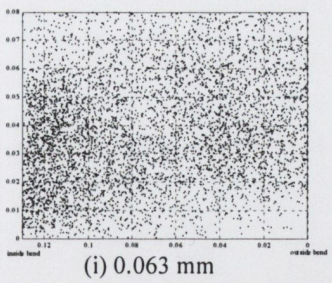

(i) 0.063 mm

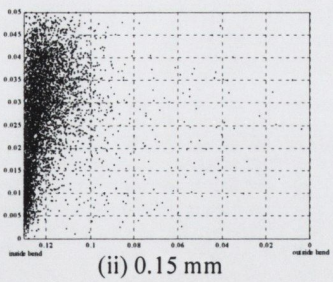

(ii) 0.15 mm

Figure B.15 (b): Remaining Particles not Entering into the Sump

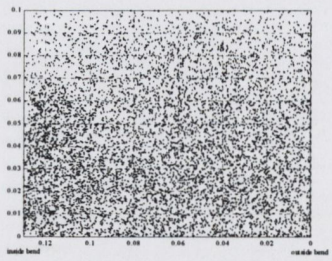

(i) 0.063 mm

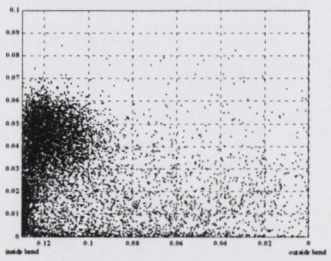

(ii) 0.15 mm

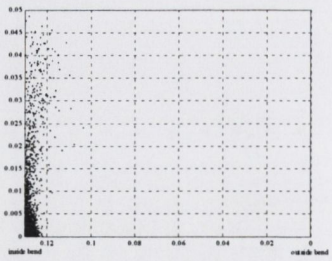

(iii) 0.3 mm

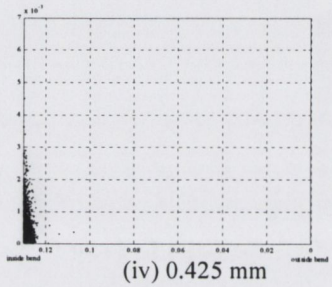

(iv) 0.425 mm

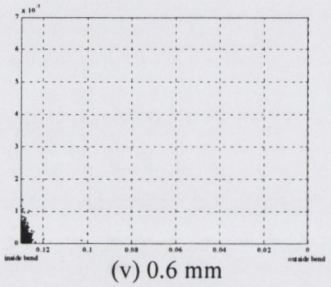

(v) 0.6 mm

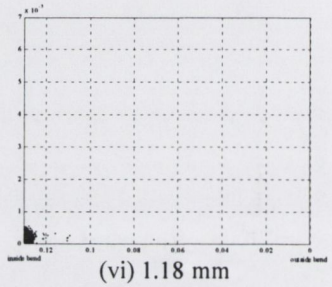

(vi) 1.18 mm

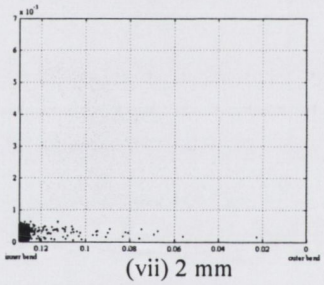

(vii) 2 mm

Figure B.16 (a): Scatter Plot of Particles hitting the plane θ = 45° at Q = 8l/s

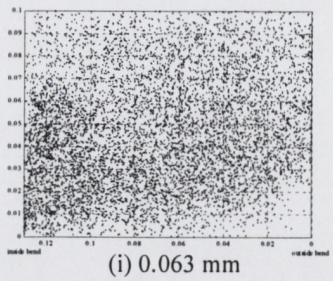

(i) 0.063 mm

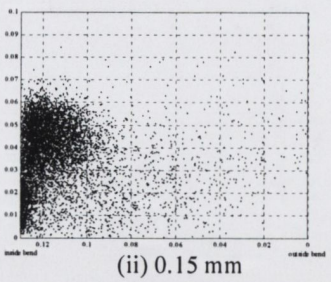

(ii) 0.15 mm

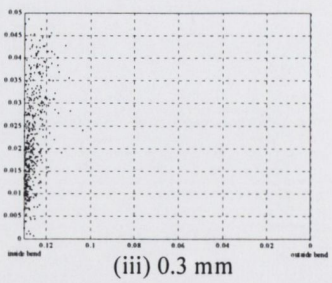

(iii) 0.3 mm

Figure B.16 (b): Remaining Particles not Entering into the Sump

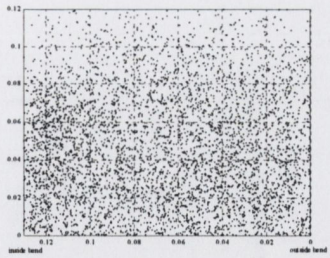

(i) 0.063 mm

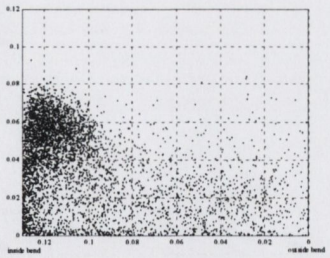

(ii) 0.15 mm

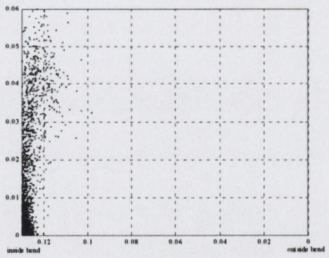

(iii) 0.3 mm

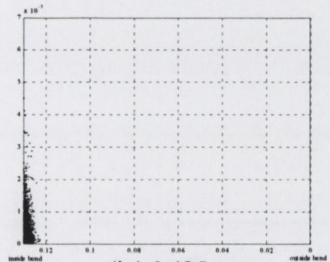

(iv) 0.425 mm

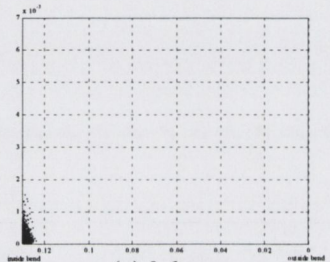

(v) 0.6 mm

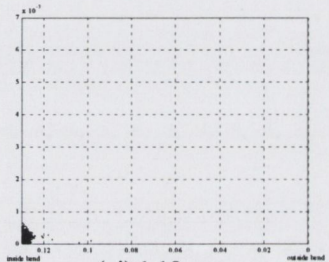

(vi) 1.18 mm

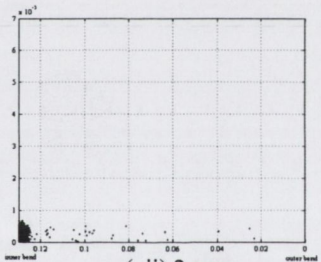

(vii) 2 mm

Figure B.17 (a): Scatter Plot of Particles hitting the plane θ = 45° at Q = 10l/s

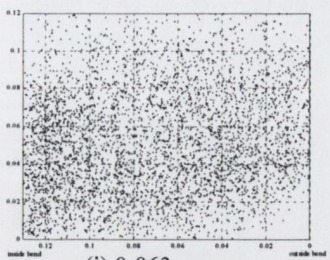

(i) 0.063 mm

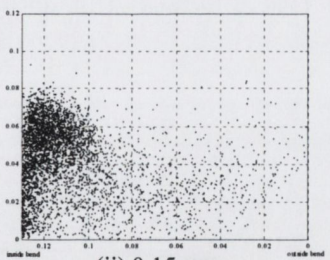

(ii) 0.15 mm

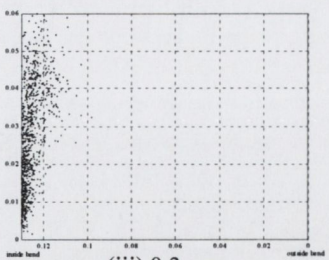

(iii) 0.3 mm

Figure B.17 (b): Remaining Particles not Entering into the Sump

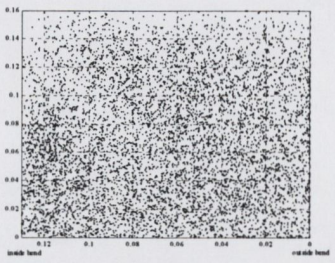

(i) 0.063 mm

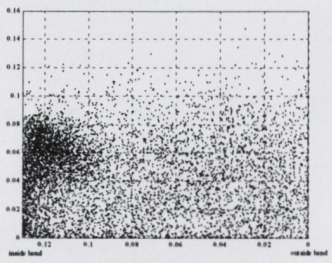

(ii) 0.15 mm

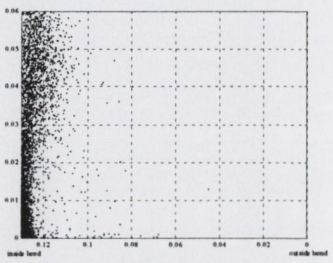

(iii) 0.3 mm

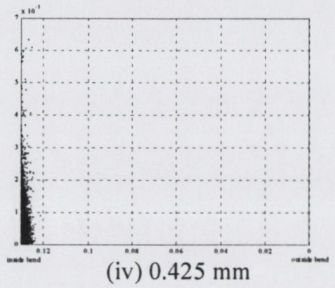

(iv) 0.425 mm

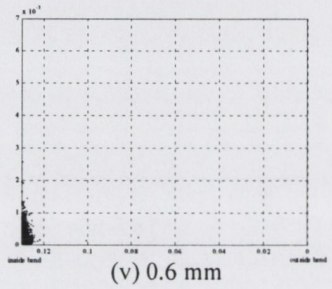

(v) 0.6 mm

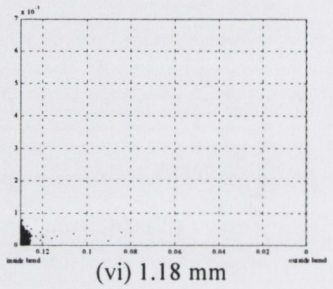

(vi) 1.18 mm

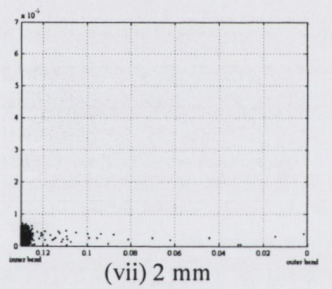

(vii) 2 mm

Figure B.18 (a): Scatter Plot of Particles hitting the plane θ = 45° at Q = 15l/s

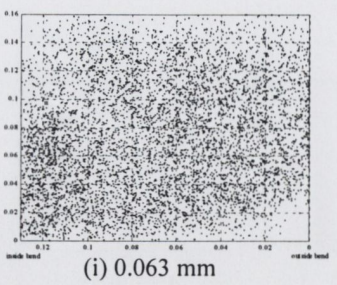

(i) 0.063 mm

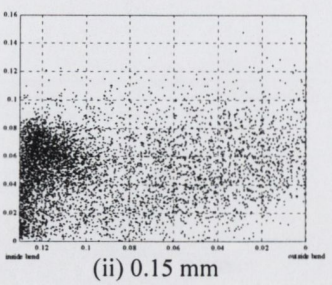

(ii) 0.15 mm

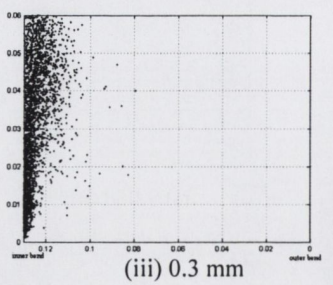

(iii) 0.3 mm

Figure B.18 (b): Remaining Particles not Entering into the Sump

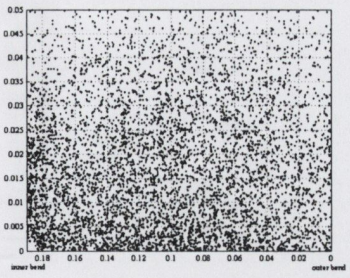

(i) 0.063 mm

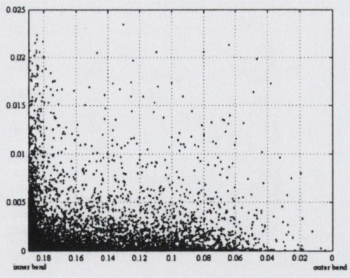

(ii) 0.15 mm

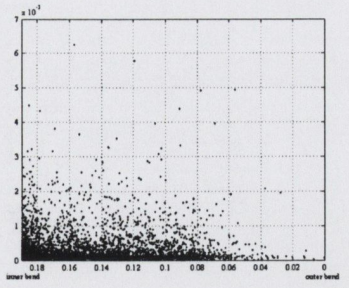

(iii) 0.3 mm

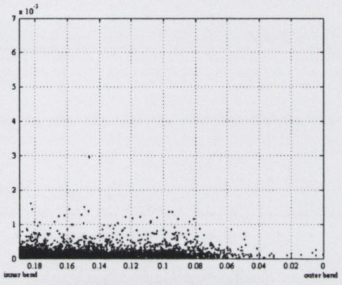

(iv) 0.425 mm

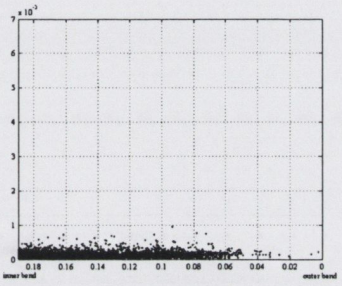

(v) 0.6 mm

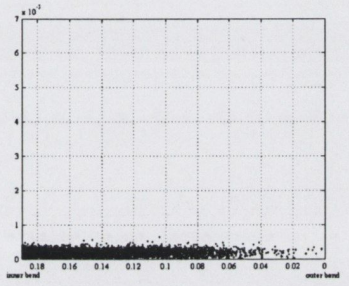

(vi) 1.18 mm

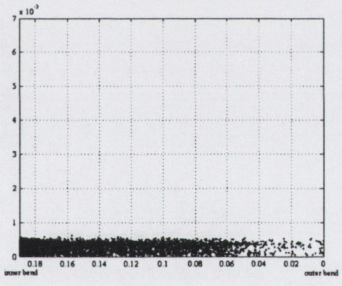

(vii) 2 mm

Figure B.19 (a): Scatter Plot of Particles hitting the plane θ = 30° at Q = 4l/s for channel width = 0.19m

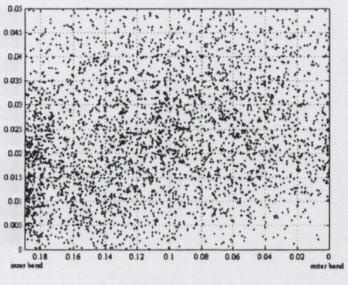

(i) 0.063 mm

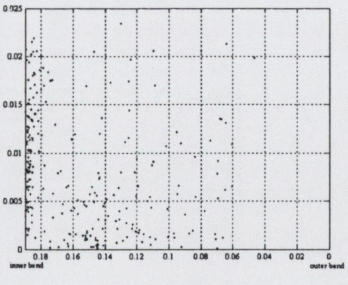

(ii) 0.15 mm

Figure B.19 (b): Remaining Particles not Entering into the Sump

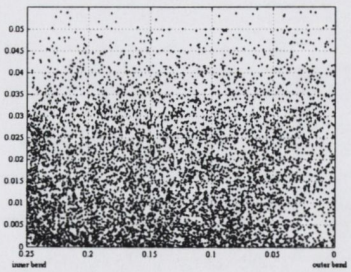

(i) 0.063 mm

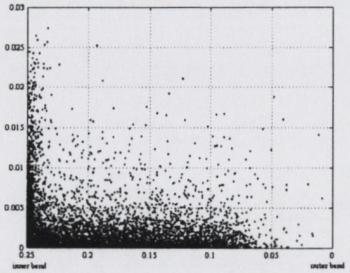

(ii) 0.15 mm

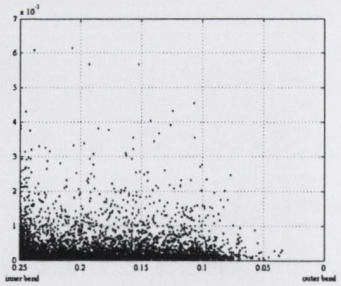

(iii) 0.3 mm

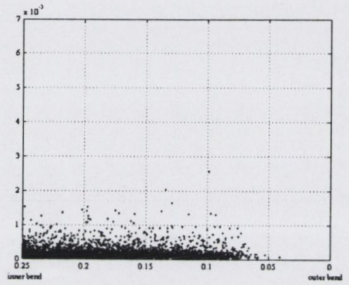

(iv) 0.425 mm

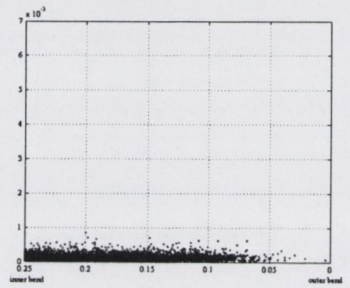

(v) 0.6 mm

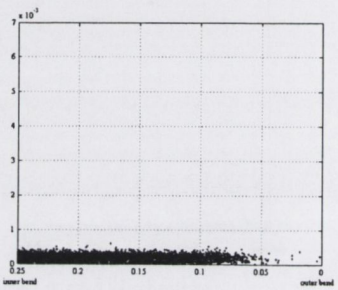

(vi) 1.18 mm

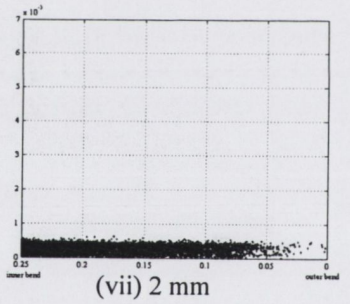

(vii) 2 mm

Figure B.20 (a): Scatter Plot of Particles hitting the plane θ = 30° at Q = 4l/s for channel width = 0.25m

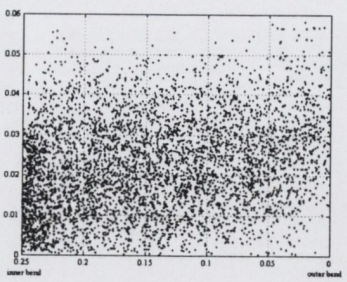

(i) 0.063 mm

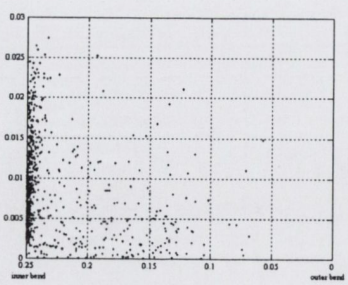

(ii) 0.15 mm

Figure B.20 (b): Remaining Particles not Entering into the Sump

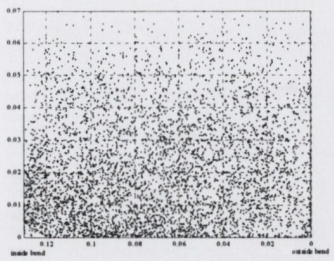

(i) 0.063 mm

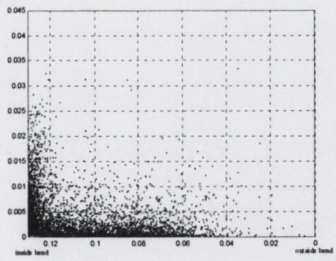

(ii) 0.15 mm

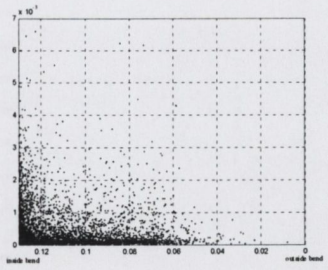

(iii) 0.3 mm

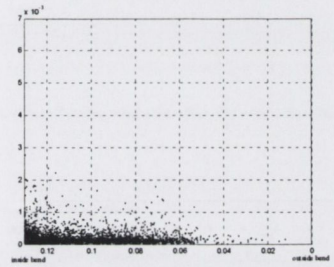

(iv) 0.425 mm

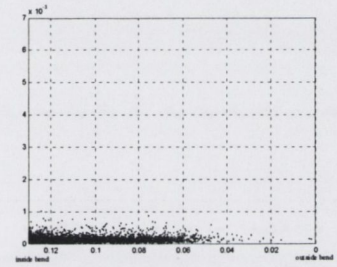

(v) 0.6 mm

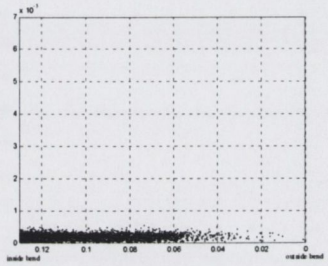

(vi) 1.18 mm

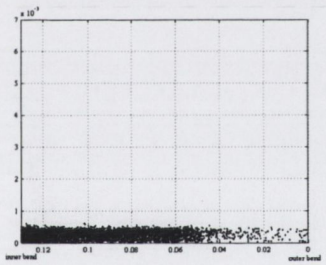

(vii) 2 mm

Figure B.21 (a): Scatter Plot of Particles hitting the plane θ = 30° at Q = 4l/s for $R_c/B = 6$

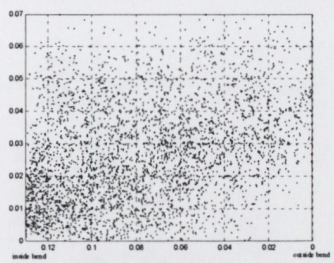

(i) 0.063 mm

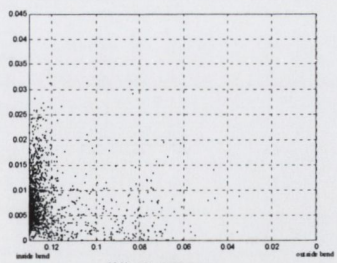

(ii) 0.15 mm

Figure B.21 (b): Remaining Particles not Entering into the Sump

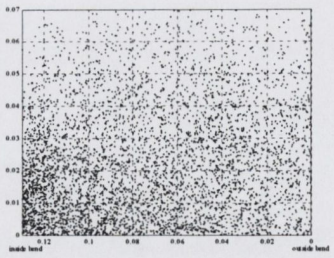

(i) 0.063 mm

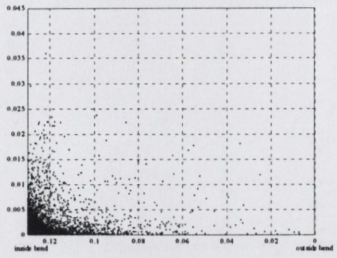

(ii) 0.15 mm

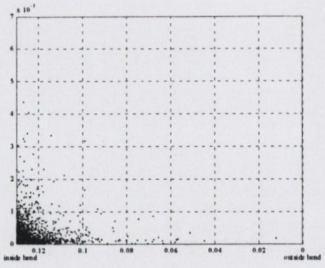

(iii) 0.3 mm

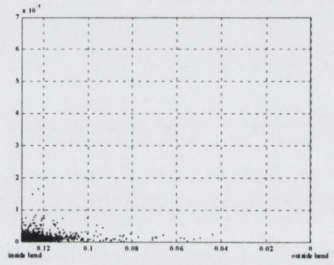

(iv) 0.425 mm

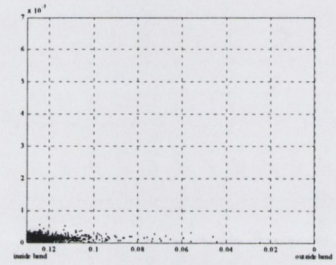

(v) 0.6 mm

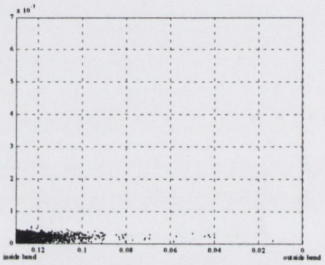

(vi) 1.18 mm

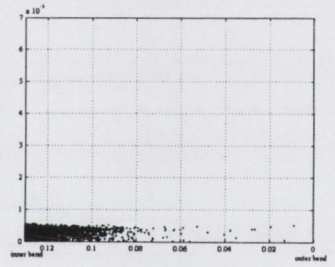

(vii) 2 mm

Figure B.22 (a): Scatter Plot of Particles hitting the plane $\theta = 30^{o}$ at Q = 4l/s for $R_c/B = 18$

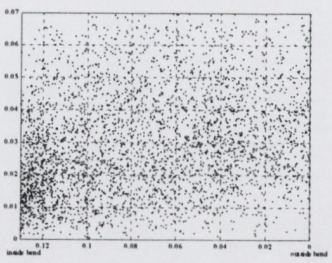

(i) 0.063 mm

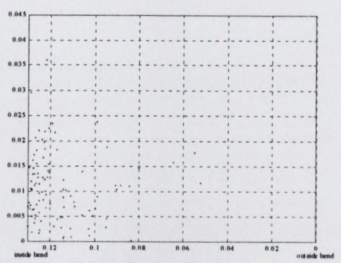

(ii) 0.15 mm

Figure B.22 (b): Remaining Particles not Entering into the Sump

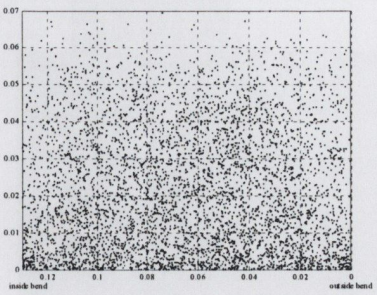

(i) 0.063 mm

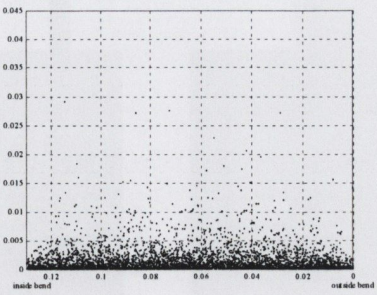

(ii) 0.15 mm

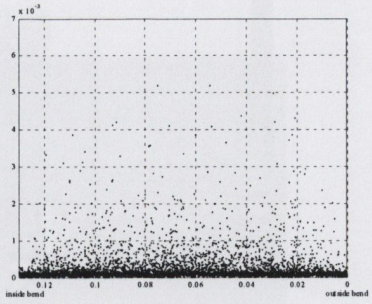

(iii) 0.3 mm

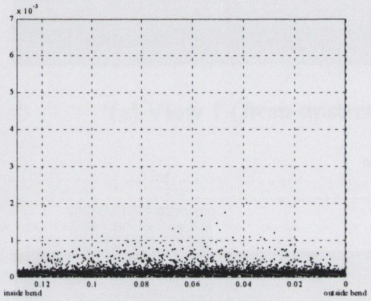

(iv) 0.425 mm

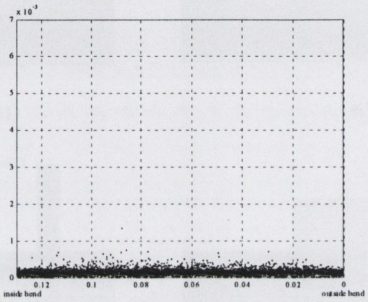

(v) 0.6 mm

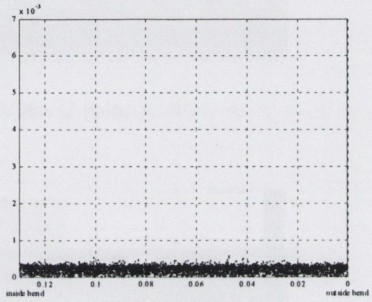

(vi) 1.18 mm

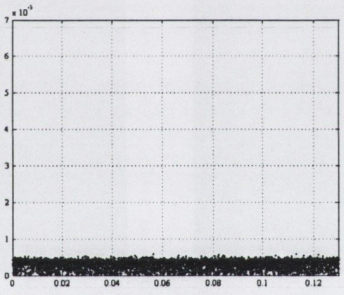

(vii) 2 mm

Figure B.23 (a): Scatter Plot of Particles hitting the plane $\theta = 0^o$ at Q = 4l/s; $R_c/B=\infty$

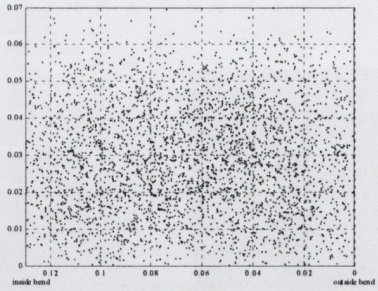

(i) 0.063 mm

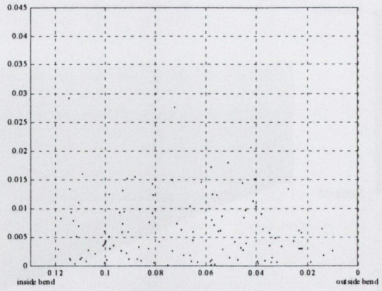

(ii) 0.15 mm

Figure B.23 (b): Remaining Particles not Entering into the Sump

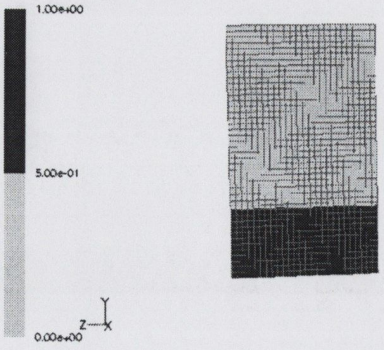

(a) Volume Fraction - 0°

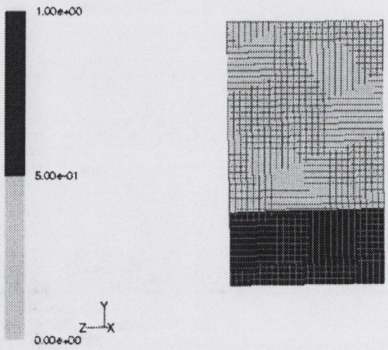

(b) Volume Fraction - 15°

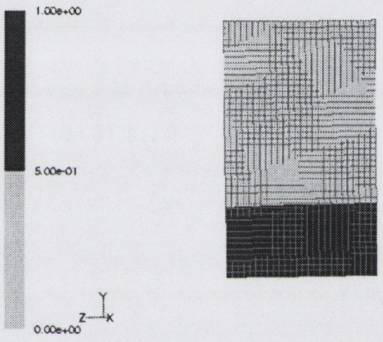

(c) Volume Fraction - 30°

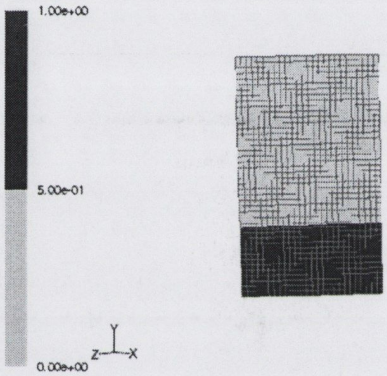

(d) Volume Fraction - 45°

Figure B.24 (a-d): Volume Fraction (water-red coloured) for different Angles of Bend - Curve grit Channel

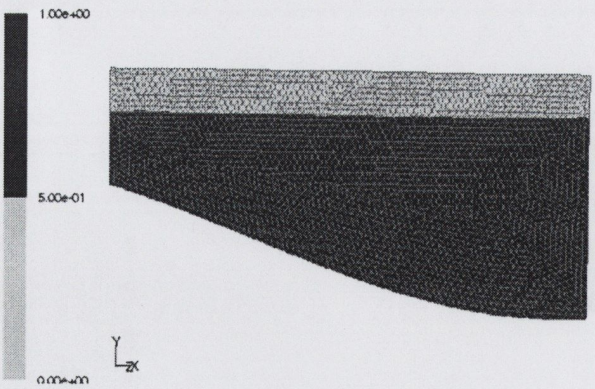

Figure B.25: Volume Fraction (water-red coloured) - Case Study at 60°

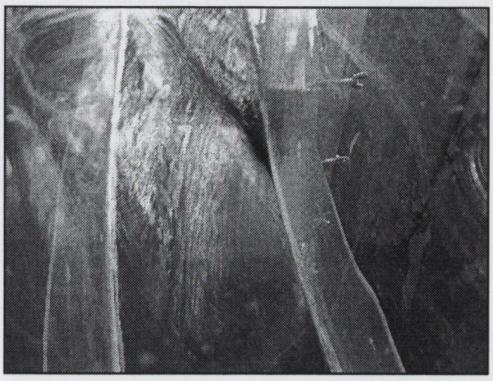

(a) View 1 (from upstream)

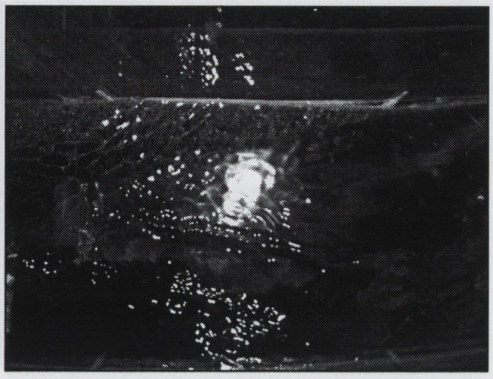

(b) View 2 (plan)

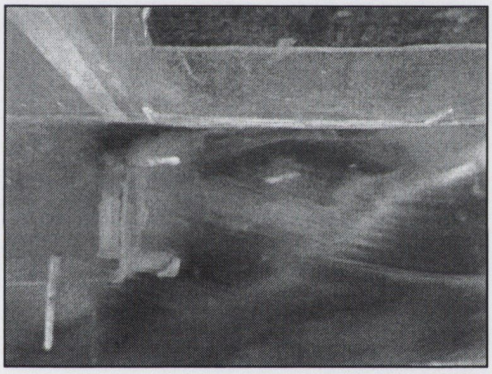

(c) View 3 (plan)

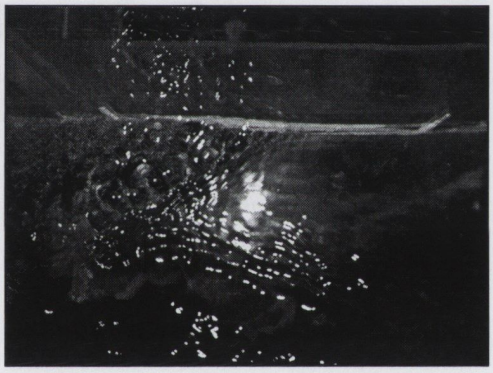

(d) View 4 (plan)

Figure B.26: Movement of Grit Particles in Curved Grit Channel